Development of an Integrated SPECT-CmT Dedicated Breast Imaging System

Incorporating Novel Data Acquisition and Patient Bed Designs

by

Dominic Joseph Crotty

Department of Biomedical Engineering
Duke University

Date:_____
Approved:

_____
Martin P. Tornai, Ph. D., Supervisor

_____
R. Edward Coleman, M.D.

_____
Ehsan Samei, Ph. D.

_____
Timothy G. Turkington, Ph. D.

_____
Gregg E. Trahey, Ph. D.

Dissertation submitted in partial fulfillment of
the requirements for the degree of
Doctor of Philosophy
in the Department of Biomedical Engineering
in the Graduate School of Duke University

2010

ABSTRACT

Development of an Integrated SPECT-CmT Dedicated Breast Imaging System

Incorporating Novel Data Acquisition and Patient Bed Designs

by

Dominic Joseph Crotty

Department of Biomedical Engineering
Duke University

Date:_____
Approved:

_____
Martin P. Tornai, Ph. D., Supervisor

_____
R. Edward Coleman, M. D.

_____
Ehsan Samei, Ph. D.

_____
Timothy G. Turkington, Ph. D.

_____
Gregg E. Trahey, Ph. D.

An abstract of a dissertation submitted in partial
fulfillment of the requirements for the degree of
Doctor of Philosophy
in the Department of Biomedical Engineering
in the Graduate School of Duke University

2010

Abstract

This thesis research builds upon prior work that developed separate SPECT and CT (computed mammotomography, or breast CT) devices that were independently capable of imaging an uncompressed breast in 3D space. To further develop the system as a clinically viable device, it was necessary to integrate the separate imaging systems onto a single gantry, and to simultaneously design a patient-friendly bed that could routinely and effectively position the patient during dual-modality imaging of her uncompressed breast in the system's common field of view. This thesis describes this process and also investigates practical challenges associated with dedicated breast imaging of a prone patient using the integrated SPECT-CT device.

We initially characterized the practicability of implementing the novel x-ray beam ultra-thick K-edge filtration scheme designed for routine use with the breast CT system. Extensive computer simulations and physical measurements were performed to characterize the x-ray beam produced using K-edge filtration with cerium and to compare it to beams produced using other filtration methods and materials. The advantages of using this heavily filtered x-ray beam for uncompressed breast CT imaging were then further evaluated by measuring the dose absorbed by an uncompressed cadaver breast during the course of a routine tomographic scan. It was found that the breast CT device is indeed capable of imaging uncompressed breasts at dose levels below that of the maximum utilized for dual-view screening mammography.

To prepare the separate SPECT and CT systems for integration onto a single platform, the cross contamination of the image of one modality by primary and scattered photons of the complementary modality was quantified. It was found that contamination levels of the emission (SPECT) image by the x-ray transmission source were generally far less than 2% when using photopeak energy windows up to ±8%. In addition, while there was some quantifiable evidence of a variation in the transmission image in response to the presence of ^{99m}Tc photons in the patient, the effect of primary and scattered ^{99m}Tc photons on the visibility of 5 mm acrylic photons in a low contrast x-ray transmission environment was negligible.

A novel, tiered, stainless steel patient bed was then designed to allow dual-modality imaging using the integrated SPECT-CT system. The performance of the hybrid SPECT-CT system was evaluated during early stage dual-modality patient imaging trials with particular emphasis placed on the performance of the patient bed. The bed was successful in its primary task of enabling dual-modality imaging of a patient's breast in the common field of view, but practical challenges to more effective patient imaging were identified as well as some novel solutions to these challenges.

In the final section of the thesis research, the feasibility of using two of these solutions was investigated with a view to imaging more of the patient's posterior breast volume. Limited angle tomographic trajectories and trajectories that involve raising or lowering the patient bed in mid tomographic acquisition were initially investigated using various geometric phantoms. A very low contrast imaging task was then tested using an observer

study to quantify the effect of these trajectories on the ability of observers to maintain visibility of small geometric objects.

This initial integrated SPECT-CT imaging system has demonstrated its ability to successfully perform low dose, dual-modality imaging of the uncompressed breast. Challenges and solutions have been identified here that will make future SPECT-CT designs even more powerful and a clinically relevant technique for molecular imaging of the breast.

Contents

List of Tables

List of Figures

xiv

xviii

Acknowledgements

I would initially like to thank all sources of funding for my thesis work, especially the Department of Defense Breast Cancer Research Program under grant number W81XWH-08-1-0352, the National Institutes of Health under grant R01-CA096821, and I would also like to thank the support given by the Department of Biomedical Engineering and the Department of Radiology at Duke University, the Malek Foundation, the Duke Endowment and the James B. Duke Fellowship Program.

I would like to thank my advisor, Dr. Martin Tornai for his enthusiasm, support, and creativity over the last five and a half years of my doctoral research work. I am indebted to him for his willingness to give me a chance as a retired professional rugby player in the world of science. Despite the long road to this point, I have never regretted taking this path and Martin has helped open doors for me that would have remained closed.

I also want to thank my committee members. I appreciate greatly your taking time from your busy work lives to help me graduate from this wonderful university. I stand in admiration of your academic and clinical work, and, as I start on my postdoctoral career, I wish you continued success in yours.

I would also like to sincerely thank my labmates in the Multi Modality Imaging Laboratory, Spencer Cutler, Priti Madhav, and Kristy Perez for your constant good humor and cheerfulness that helped me through the hard times. You are the best labmates that I could ever have wished for. To Brooke, Kirsten, Hannah and Thomas

Cutler, thank you for your friendship and generosity over these last years, you have become true friends of my family, and I will remain ever indebted to you for your friendship to Karen and I, and to our kids.

I would like to thank others that have been such a great source of help in my time at Duke. Chief among these is Don Pearce with whom I have shared many a laugh and who has been very generous with his time and expertise. I would not have been able to complete many tasks without his help. To Kathy Barbour who is an administrator without equal, thank you. To Teri Mills and Kelly Crace, you must know how helpful you have been to me. There are too many others at Duke whose paths have crossed mine to thank individually but I greatly appreciate all the help and friendship I have experienced over my time here.

Finally to Karen, to James, and to Niamh. To put you on the same page as everyone else is doing you a disservice because you are more important to me than I can adequately express. From the very bottom of my heart, I thank you. You have taken this chance and this road with me, and I hope I can repay your kindness and trust in me one day. I am blessed to know you and even more blessed to spend my days with you.

Go raibh míle maith agaibh.

Chapter 1

1. Introduction and Theory

Breast cancer is the most common non-skin cancer among US women, causing the deaths of over 40,000 women in 2009 [1]. It is estimated that over 192,000 women will be diagnosed with invasive breast cancer in the US this year, while the chances of a woman developing invasive breast cancer at some time in her life remain about 12% [1]. Recently however, there has been a decline in death rates from breast cancer. This encouraging trend is believed to be the result of increased awareness, earlier detection of some cancers through improvements in breast cancer imaging technology, and improvements in treatment [1-3].

1.1. Contemporary Breast Imaging Modalities

X-ray mammography (XRM) is the current mainstay technology for breast imaging and has long been considered the "gold standard" for breast cancer screening of asymptomatic women [3-5]. Current screening recommendations from the American Cancer Society are for women to begin a yearly mammography screening protocol from the age of 40; no upper age limit is advised [6]. Analyses of several randomized clinical trials across different geographic regions has shown that mammography is effective in reducing the mortality rate by between 20-35% for women aged 50-69 years [3]. The benefit of screening women in their 40s, who generally have denser breasts and faster growing tumors, is less clear than that of women aged 50 or older [7]. Recently published results from a systematic review of screening studies using mammography by

the U.S. Preventative Services Task Force showed an overall sensitivity for mammography across all groups of between 77% and 95% and an overall specificity between 94% and 97% [7]. With a relatively low cost, sustainable patient risk and high availability, mammography has proven its clinical value over many years, especially in the detection of non-palpable lesions[3].

Full field digital mammography (FFDM) is steadily replacing conventional screen film mammography as the preferred method for breast cancer screening [5, 8]. FFDM uses flat panel digital detector systems that provide both greater dynamic image range and access to digital archiving. As of 2008, 36% of all mammography units in the US were FFDM units with the number increasing every year [5], despite the fact that the systems are more costly to install [3].

Mammography is a 2D imaging technique that acquires projection images of the 3D breast volume from the cranial-caudal (CC, top-bottom) and mediolateral oblique (MLO, from the side) viewpoints while the breast is under compression [9] (see Figure 1.1). Compression aids in reducing scatter in the image, absorbed dose to the breast, and also allows the lower energy photons used in mammography to more uniformly penetrate the breast. By projecting the 3D breast volume onto a 2D image, mammography can often miss the presence of subtle, diffuse cancers that are occluded by radiographically similar tissue. The chest wall may lie outside the limited field of view (FOV) of the mammogram, missing the presence of lesions that reside close to, or in, this region. By using breast compression, mammography additionally causes discomfort to those that are

being imaged [10], potentially discouraging compliance with recommended screening

guidelines. Detection of cancer in mammography relies on the observation of masses and
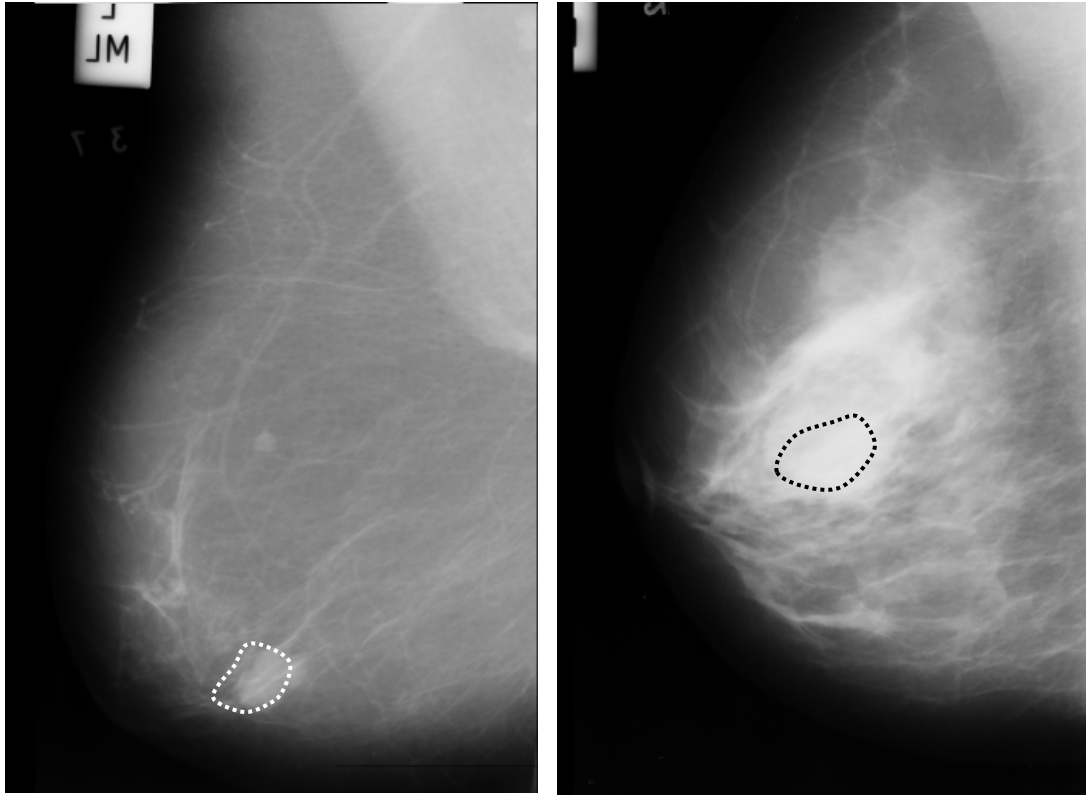
Figure 1.1: (Left) MLO mammogram of a highly adipose left breast with well circumscribed mass indicated. (Right) MLO mammogram of a heterogeneously dense breast with a mass underlying the dense glandular tissue. The image on the right indicates the difficulty of visualizing cancerous lesions in dense tissue when using 2D mammography. Images courtesy of the MIAS Database (http://peipa.essex.ac.uk/info/mias.html).

microcalcifications. Signatures of cancerous masses may be radiographically similar to

non-malignant lesions, especially in younger women with predominantly dense breast

tissue. Breast density and age are important predictors of accuracy for mammography as

can be seen when the results of screening trials using mammography are sub-divided into

different age and breast density cohorts. Statistical analysis of results from other

previous clinical trials demonstrates an adjusted sensitivity and specificity of 69% and

3

91%, respectively, for women aged between 40 and 49, compared to 83% and 94% in women aged 80 to 89 years. Adjusted sensitivity and specificity for women with extremely dense breasts was 63% and 89%, respectively, compared to 87% and 97% for women with almost entirely fatty breasts [11].

All these preceding factors continue to drive the search to find complementary and potentially competing 3D imaging techniques to improve the breast cancer screening paradigm.

The Multi-Modality Imaging (MMI) Laboratory at Duke is one of several research groups involved in developing dedicated 3D breast computed tomography (breast CT or computed mammotomography, CmT) [12-21] (see Figure 1.2). The integration of a CT system dedicated to breast cancer imaging into a hybrid SPECT-CT system forms the main subject of this thesis research. The concept common to breast CT devices is to tomographically image the uncompressed and pendant breast of a prone patient using a combination of a cone beam x-ray source and a fine-resolution digital flat panel detector. One advantage of the tomographic nature of breast CT is that it removes layers of overlapping tissue from reconstructed images to elucidate smaller lesions with isotropic resolution, or lesions that may otherwise remain undetected in mammography. Another advantage of the technique is that, unlike other imaging modalities, the inherent physical principles behind x-ray CT mean that the attenuation coefficients of different objects may be gleaned from reconstructed images. Thus, *in vivo* tissue differentiation between normal glandular tissue and cancerous lesions may theoretically be possible with breast CT. Compared to mammography, breast CT may improve visualization of cancers in

patients with breast implants.   However, microcalcifications remain more visible in

mammograms than in breast CT [18] and the ability to routinely image a patient's chest

wall and axilla region has yet to be demonstrated for dedicated breast CT systems.
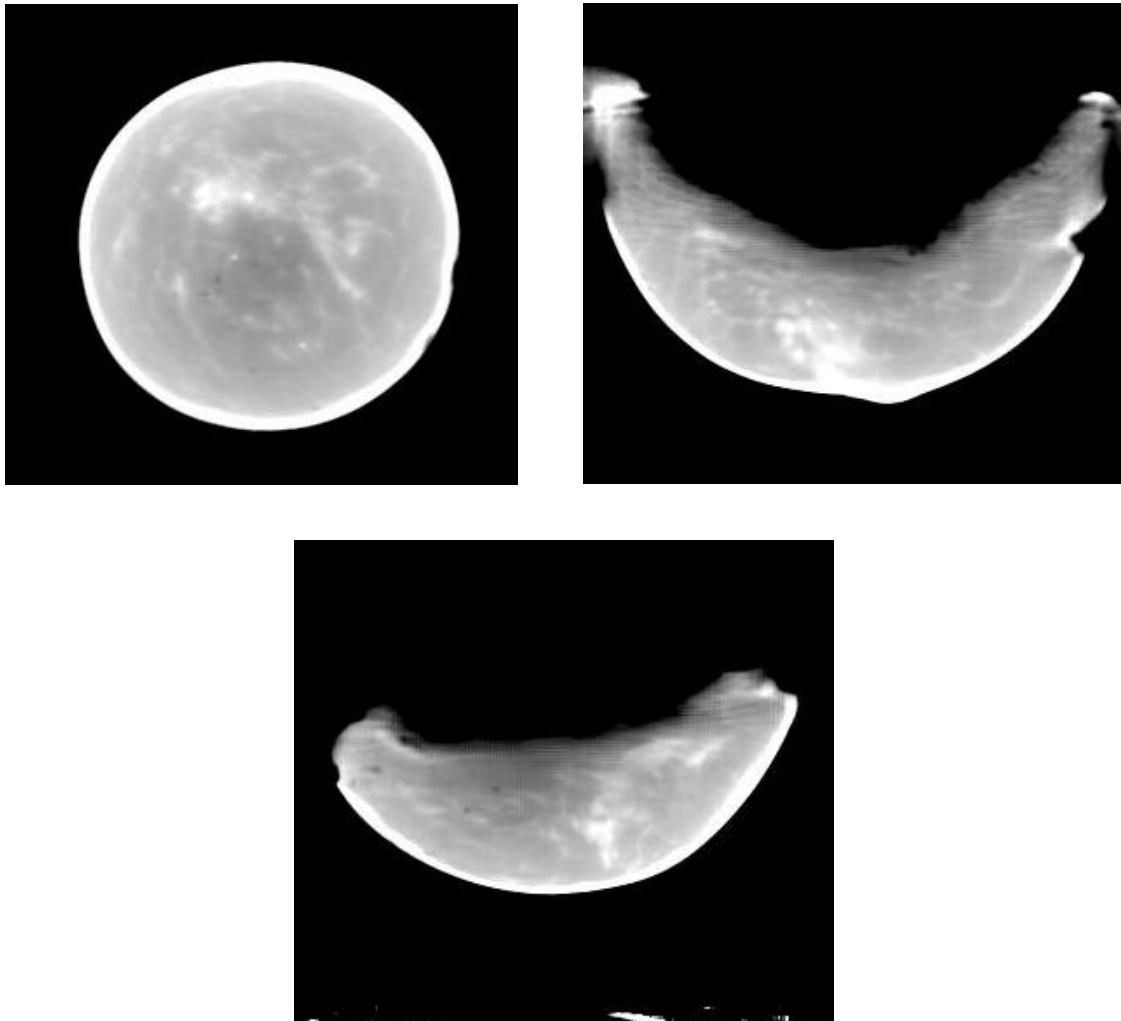
Figure 1.2: (Top left) Coronal, (top right) sagittal, and (bottom) transverse reconstructed slices. Slices illustrate the value of tomography in removing overlapping structure and enabling visualization of breast structure from orthogonal perspectives and not just from 2 views as is the case in mammography.

It is also imperative that any developed CT device does not significantly increase patient radiation dose, given the orders-of-magnitude increase in the number of projection views necessary to form the tomographic image; such an issue is investigated in this thesis research in detail in Chapter 3. Overall, it is hoped that breast CT devices will provide several benefits including: (1) improved detection of breast lesions by removing overlapping tissue, especially in women with radiographically dense breasts; (2) uncompressed breast imaging leading to improved patient comfort, with potentially (3) a resultant increase in breast screening compliance; and (4) an absorbed radiation dose to the breast equal to or less than that of the current standards of dual-view screening mammography.

Recently, the American Cancer Society recommended that women with high risk of developing breast cancer, for instance those with a family history of breast cancer, those that carry the BRCA1 or BRCA2 genetic mutation, and those younger women with extremely dense breasts should undergo regular breast cancer screening follow-up with contrast-enhanced magnetic resonance imaging (MRI) [6]. Unlike mammography, MRI is insensitive to breast density and MRI does not use ionizing radiation. In a recent systematic review of 11 prospective studies conducted between 1995 and 2007 using a combination of MRI and mammography to screen women at high risk for breast cancer, the sensitivity of the combined MRI-mammography protocol was reported to be between 80-100%, higher than that for mammography alone [22]. The specificity of the combined breast MRI-mammography protocol was reported to be between 73-93%, while the specificity of MRI alone was lower than that of mammography alone. Despite the

apparent advantages of using MRI as an adjunct to screening mammography for this population, its lower specificity, high cost per scan and limited availability hinder the widespread adoption of MRI to the general population.

For women with an elevated risk of breast cancer, breast ultrasound may also be a very useful tool as an adjunct to screening mammography, especially in discriminating between benign and malignant cysts [5, 23]. In a recently reported study, over 2800 women underwent mammography and radiologist-performed ultrasound examination [24]. The results indicated increased sensitivity in breast cancer detection when using mammography and ultrasound in combination versus using mammography alone (77.5% vs. 50%) but with reduced specificity (89% vs. 95%). This increased sensitivity mirrors previous results using breast US [25]. The real-time nature of US examinations also makes it an attractive adjunct to mammography. However, the low positive predictive value (8.9%) of ultrasound examination alone is one potential reason for the reduced likelihood of US gaining widespread acceptability as a screening tool [24]. Another consideration is the fact that the median time required to perform a bilateral screening breast ultrasound exam was 19 minutes, and 9 minutes for a unilateral exam [24], reducing patient throughput and impacting physician revenues; an earlier report had timed the physician examination at approximately 4 minutes [25]. The technique is also operator-dependant, although great strides are being made in producing exciting new automated imaging devices [26-27] using ultrasound technology, which may increase ultrasound's clinical role.

Digital breast tomosynthesis (DBT), a technique that acquires multiple x-ray images in a short arc around the breast, has, when used in a trial with mammography, been shown to reduce recall rates versus using mammography only [28-30]. Early indications are encouraging for the use of DBT alongside mammography, but with new commercial DBT devices on the horizon, the near future will more clearly demonstrate if the subjectively improved visibility of anatomy associated with DBT translates to changes in patient management and outcomes [31-32].

Along with improvements and innovations in anatomical imaging techniques for breast cancer, there has been a concomitant development of innovative 2D and 3D nuclear medicine (NM) techniques for breast cancer imaging as adjuncts to mammography. Due to their relatively poor image resolution, NM techniques are not used in screening for the presence of breast cancer but are used in the diagnosis and staging of the disease. NM techniques are additionally used to analyze the response of patients to breast cancer therapy.

One of the most common forms of 2D NM imaging of the breast is scintimammography, the planar complement to 3D SPECT imaging and the functional imaging equivalent of mammography. Scintimammography, in conjunction with mammography, has been shown to improve the diagnosis of breast cancer and is recommended in situations where results from mammography and ultrasound are equivocal. One study has indicated that breast density does not affect the accuracy of scintimammography and that indeed women with dense breasts may benefit most from this complementary imaging technique [33]. One reported meta-analysis of scintimammography indicated sensitivities and

specificities of approximately 85% and 84%, respectively [34]. Another meta-analysis of over 5300 patients using scintimammography reported a sensitivity and specificity of 85% and 87%, respectively, for palpable lesions. However, the sensitivity dropped to 67% for non-palpable lesions [35]; another series of earlier studies found that the sensitivity dropped to 55% for small lesions [36]. These studies used contemporary, large format clinical gamma cameras.

A promising development on the concept of scintimammography using a compact gamma camera for the diagnosis of breast cancer is molecular breast imaging (MBI) [37-40]. This 2D planar imaging technique uses two CZT-based compact gamma cameras that simultaneously acquire opposing views of the breast that reduce the lesion to detector distance. It has been demonstrated, in limited trials using volunteer subjects with suspected breast cancer, that MBI possesses an improved ability to detect lesions 5mm or less in size compared to the single headed imaging system used in scintimammography. Sensitivity improved from 85% for scintimammography to 91% for MBI. Another study using the same technology for detecting lesions in volunteers with suspected breast cancer showed a sensitivity of 90% for lesions <2cm in size and 82% for lesions <1cm in size. Average specificity for the MBI techniques for detecting small lesions in this study was reported as 69%.

3D SPECT generates improved image information content and characteristics and may further enhance the diagnostic accuracy of NM imaging techniques. SPECT has already been used for breast imaging, normally in staging of the disease, but the large, bulky, single or dual-headed cameras normally associated with SPECT impede imaging close to

the breast surface with a resulting negative impact on resolution and detectability. The MMI Laboratory at Duke is developing an innovative small compact gamma camera SPECT system that employs complex 3D trajectories and close contouring of the breast surface to improve the reconstructed 3D image quality of the pendant breast, and may permit viewing of the patient's breast and chest wall. This thesis deals with the integration of the SPECT imaging system with a complementary dedicated breast CT system.

Clinical whole-body positron emission tomography (PET) systems have traditionally been used to detect metastasis of breast cancer to other organs but not to detect primary breast cancer, due to its limited resolution and consequent limited ability to depict small (<1 cm) lesions. Overall, the sensitivity of 18F-Flurodeoxyglucose (18F-FDG) PET in detecting primary breast cancer was reported to be between 64% and 96%, while specificity has been reported to be between 73% and 100% [41]. PET using FDG has an important role in the assessment of the staging of breast cancer and in the prediction of tumor response in patients with locally advanced breast cancer receiving neoadjuvant chemotherapy.

Dedicated positron emission mammography (PEM) devices, a device consisting of two opposing planar PET detectors using mild compression and developed on a imaging platform physically similar to mammography, have been developed that improve upon whole-body PET imaging for breast cancer in terms of image resolution, reduced attenuation, shorter imaging time, and higher sensitivity [42-46]. Early indications are that PEM can improve the ability to visualize smaller cancers than PET [47], with one

study of 77 women with known or suspected breast cancer reporting a sensitivity and specificity of 91% and 93%, respectively. However, difficulties in imaging posterior lesions in the posterior breast due to the limited FOV of the detector, variable uptake of FDG in small tumors and false-positive findings from prior biopsy are some of the issues facing PEM [48], and so the clinical significance of PEM has not yet been established.

Paralleling major advances in the capabilities of independent imaging modalities are advances in the design and availability of dual-modality imaging systems that combine an anatomical imaging system (e.g. CT) with a complementary functional imaging modality (e.g. SPECT or PET) on a single gantry. While the dual-modality research imaging system described in this thesis shares a common field of view, this system is unusual in that clinical dual imaging systems are generally staggered axially and do not share a common field of view [49-50]. The combined information acquired from the integrated anatomical/functional imaging systems is considered to be superior to that of the independent systems alone and has been shown to influence clinical decision making [50-51]. The noisy functional imaging data, generally lacking a clearly structured outline, benefits from having the co-registered anatomical information to more accurately localize areas of increased activity uptake. A further advantage is that the anatomical data from CT can often be used to provide attenuation correction information for the PET and SPECT systems [52-53]. Co-registration of the functional and anatomical images is also made easier when the patient is imaged by both CT and NM systems with the patient remaining stationary rather than two separate imaging procedures in separate imaging suites. To optimize the development of dual-modality systems, there are efforts to

combine the two systems so that both structural and functional information can be acquired simultaneously and/or that the imaging detector used in the system is capable of acquiring and processing data from both modalities at once [49, 54-55]. Indeed, Chapter 4 of this thesis deals with the question of cross-contamination of one modality by the other if SPECT and CT data is acquired simultaneously.

SPECT-CT is a close counterpart of PET-CT and has been in development for many years [49, 56]. In order to reduce the possibility of image contamination issues such as pulse pile up in the SPECT system due to scattered x-rays from CT, clinical SPECT and CT systems are currently axially staggered and do not share the same FOV [49, 56-57]. For SPECT-CT breast cancer imaging, the SPECT system is composed of a single camera or dual bulky cameras with large FOVs whose size physically limits their ability to closely contour the breast surface of the supine patient. The MMI Laboratory is the first research site in the world to investigate a common field of view SPECT-CT device dedicated to breast cancer imaging with a small gamma camera that can closely contour the breast surface, thus potentially improving image resolution. Recent research has indicated the value of hybrid SPECT-CT for accurately localizing the sentinel nodes and in mapping the lymphatic system for patients with breast cancer [58-59].

Whole-body PET-CT is arguably the most well known dual-modality system for breast cancer imaging. Generally, 18F-FDG PET-CT is used for detecting metastatic or recurrent disease, for restaging [60] and in evaluation of response to therapy, and as a problem-solving method when results of conventional imaging are equivocal [48]. Combined PET-CT devices have shown to increase diagnostic accuracy and confidence

compared to PET alone [48]. Research-based PET-CT devices dedicated to breast cancer imaging are also in development and hold promise for improved detection and diagnosis of breast cancer in 3D, although its true role in the clinical management of breast cancer has yet to be found [61-62]. A table summarizing some clinically relevant technologies for breast cancer imaging is shown in Table 1.1.

1.2. Theory

1.2.1. X-ray production

X-rays for conventional diagnostic imaging systems are produced when electrons lose energy while coming into close contact with atoms of the target material inside the anode. The x-ray tube insert is composed of a cathode filament and a metal target anode in an evacuated container. A very high-strength electric potential is applied across the anode-cathode junction by an external power source and, under the influence of the electric field, thermionic electrons are 'boiled off' the cathode filament, accelerated across the junction and strike the anode target material at the focal spot of the tube. The kinetic energy of the electrons incident on the anode target is then converted into both heat (~99%) and electromagnetic radiation in the form of x-rays [63]. Two types of x-rays are particularly relevant for this research: *bremsstrahlung* and characteristic x-rays (see Figure 1.3).

When the negatively charged incident electron interacts with the positively charged nucleus of the target material, Coulombic forces attract and decelerate the electron, causing it to lose energy and produce an x-ray photon with energy equal to this loss in

Table 1.1 Summary table of the main clinical and other research-based breast imaging devices with reported sensitivities and specificities.

Modality	Clinical role	Sensitivity (%)	Specificity (%)	Notes	Refs
Mammography	• Screen asymptomatic women • Diagnosis	77 - 95[1] 63[2] 69[3]	94 - 97[1] 89[2] 91[3]	[1] - Systematic review across all demographics, USPTF [2] – Figure adjusted for women with ext. dense breasts [3] – Figure adjusted for women aged between 40-49	[7, 11]
MRI	• Adjunct to mammography • Screen high risk women • Disease staging • Therapeutic response	73-93[1] 80-100[2]	75-98[1] 73-97[2]	BIRADs 4 or 5 High risk women [1] – MRI alone [2] – MRI with mammography	[22]
Ultrasound	• Adjunct to mammography • Diagnosis • Differentiating benign from malignant lesions	50[1] 77.5[2]	92[1] 89[2]	BIRADS 4 or 5 [1] – US alone in high risk patients [2] – Mammography with US in high risk patients	[24]
Scintimammography	• Adjunct to mammography • Response to therapy	69-90[1] 67[2]	71-94[1] 87[2]	[1]Diagnosis of primary breast cancer [1]Meta-analysis study [2]Non-palpable cancers	[34-35]
PEM	Not yet defined	91[1] 86[2]	93[1] 33[2]	[1] – Known breast cancer [2] – BIRADs 5, results correlated with mammography	[45, 47]
MBI	Not yet defined	90[1] 82[2]	69%[1] Not reported	BIRADS 4,5, previously seen on mammography or US [1] – lesions <2cm [2] – lesions <1cm	[37]
PET	• Not used to detect primary breast cancer. • Used for restaging, complementary to other staging modalities, distant metastases, therapeutic response.	64-96	73-100		[48]
SPECT/CT	• Not used for primary breast cancer detection. • Used in lymph node staging, esp. in overweight patients.	Not reported	Not reported		[60, 64]
PET/CT	• Not used for primary breast cancer detection. • Used to image distant metastases, treatment planning, disease recurrence, staging.	90	71	Disease recurrence	[60]

kinetic energy.   Such radiation is termed *bremsstrahlung*, a German word meaning 'braking radiation'. The energy of each produced x-ray is proportional to the distance of the interaction of the incident electron from the nucleus; the closer the interaction the more pronounced the deceleration and the greater the energy of the generated *bremsstrahlung* x-ray.   Since the probability of direct interaction with the nucleus is extremely small, far more low energy x-rays are produced compared to x-rays with the maximum potential energy of the electric field. In this dedicated breast imaging system, the x-ray tube uses a target made from tungsten (Z=74). In addition to its higher x-ray generating efficiency (x-ray production efficiency increases with the atomic number of the target material), the high heat capacity of tungsten (C_p = 130 J/Kg-K) helps it to cope with the production of unwanted heat.

Characteristic x-rays are so termed since their energies are unique to the anode material from which they emanate. Characteristic x-rays are produced when an electron, with incident energy greater than the binding energy of a target atoms' inner shell orbiting electrons, interacts directly with an electron in the K shell of the target (and to a lesser extent the L, M and higher shells). This direct interaction ejects the orbiting electron from the K shell. Electrons from higher shells, seeking a lower energy state, cascade down to the lower energy shells closer to the nucleus. In moving from the higher to the lower shell, x-ray photons are produced with energy equal to the difference in binding energies between the shells. Each target material has unique shell binding energies and thus x-rays characteristic of the target material are produced. For Tungsten, K-shell

characteristic x-rays are produced at energies above 69.5 keV, the binding energy of the tungsten K shell.
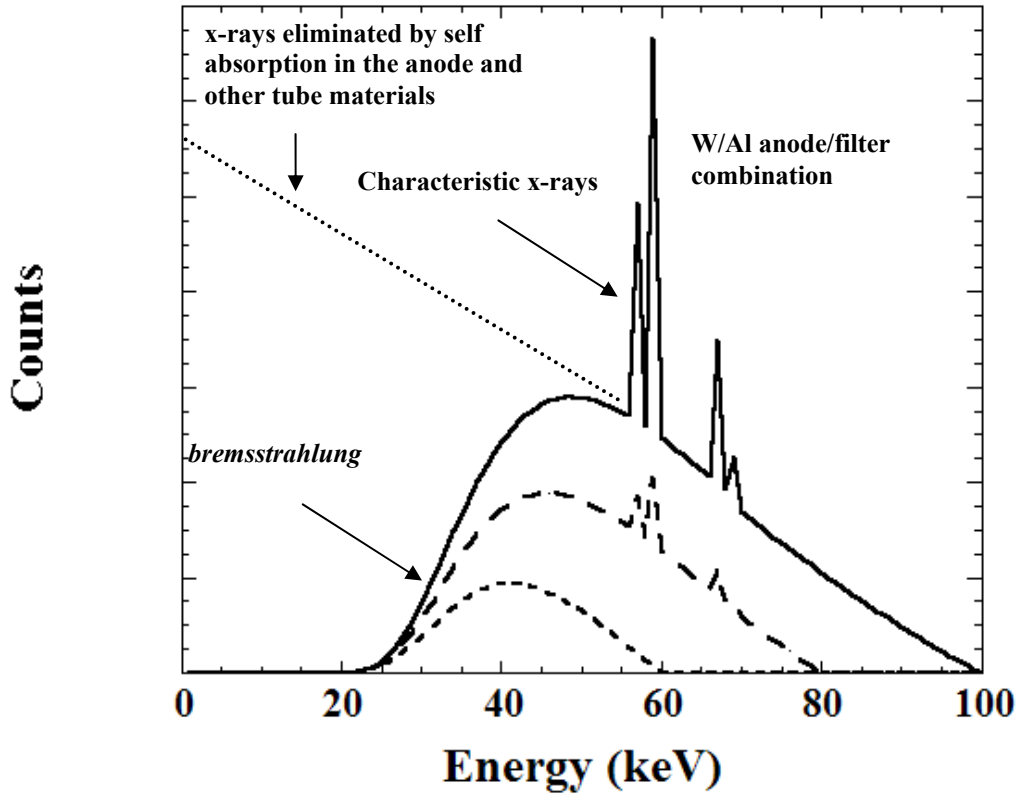
Figure 1.3: Simulated illustration of a W-anode x-ray spectrum at tube potentials of 60, 80 and 100kVp with 1 mm Aluminum filtration. The *bremsstrahlung* and characteristic x-rays are indicated on the spectrum.

1.2.2. ^{99m}Tc production

^{99m}Tc, a metastable isomer of technitium-99 is a daughter radionuclide of its parent ^{99}Mo, an unstable isotope of molybdenum. Produced in a generator, the ^{99m}TcO^{-4} (pertechnetate) is weakly bonded to the alumina column and is eluted from the column using an aqueous saline solution. The half-life of ^{99m}Tc is 6.02 hours, making it suitable for wide use in nuclear medical procedures. Other factors that make ^{99m}Tc the most

widely used radionuclide today for nuclear medical studies include the fact that it can be used to label many agents and the 140.6 keV γ-ray possesses high enough energy to exit the body without excessive interaction, thus reducing dose to the patient and enabling external detection by a suitable imaging detector. The US Federal Drug Administration has licensed ^{99m}Tc-sestamibi (^{99m}Tc -hexakis-2-methoxyisobutyl isonitrile), originally a cardiac imaging agent (Cardiolite®), for breast imaging (Miraluma®). Uptake of the radiopharmaceutical is facilitated by passive diffusion through the tumor cell membrane with subsequent concentration inside the mitochondria. ^{99m}Tc-sestamibi concentrates in breast tumors with a reported average 6:1 to 9:1 activity contrast ratio compared to surrounding tissue [65-66].
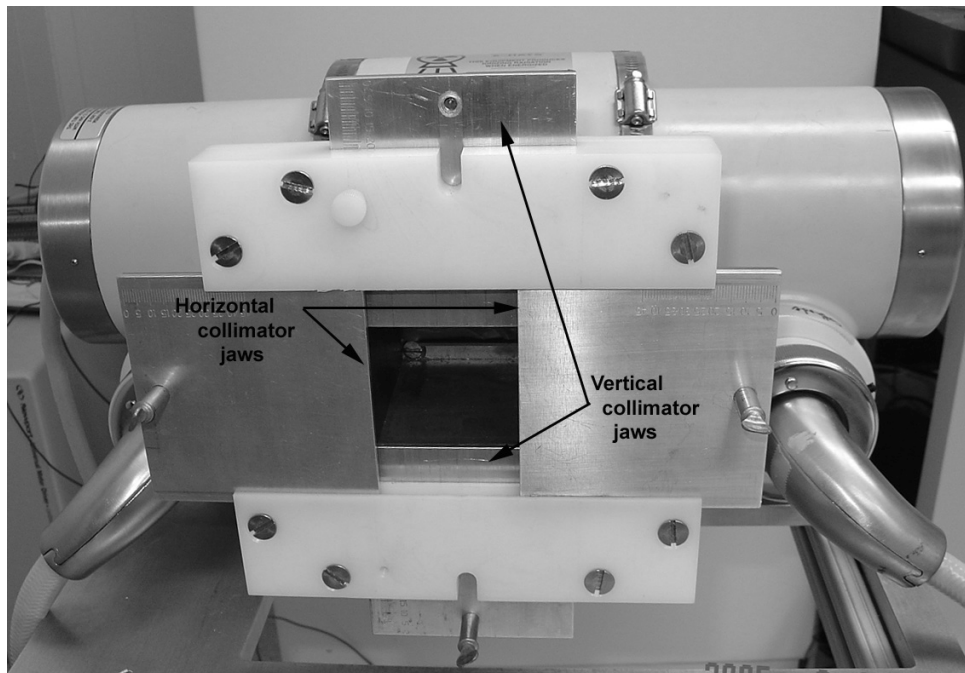
Figure 1.4: Photograph of the Varian x-ray tube with adjustable vertical and horizontal jaws indicated on the image. (Photograph courtesy of Dr. Randolph McKinley)

1.2.3. Beam Collimation

In diagnostic x-ray imaging, off-focal radiation or x-rays scattered from other parts of the tube all contribute to geometric blur in acquired projections, modifying object signal to noise ratio (SNR) and contrast. Image quality is increased and patient dose is also minimized by confining the x-ray beam to the smallest possible area needed to accomplish the required imaging task [67]. Spatial confinement of the x-ray beam is accomplished by collimating the beam near the focal spot of the x-ray tube, often accomplished by using fixed or mobile apertures. In this thesis, the collimator is sized using the mobile collimator jaws on the x-ray tube to restrict the maximum size of the FOV of the cone beam to just beyond the boundaries of the active FOV of the detector (see Figure 1.4). The minimum size of the FOV can then be modified by adjusting the gap between the jaws all the way down to zero.

Collimators play a vital role in the generation of SPECT images, selectively allowing γ-ray photons emitted only in the direct line of sight of the camera to be detected by the SPECT system. Collimators stop approximately 99.5% of photons from reaching the detector surface [68]. Collimators in SPECT thus establish the line of sight of the camera to the emission source and are the limiting factor in resolution for a SPECT system. Collimators also determine the sensitivity of the camera to the incoming source of radiation. Although there are many different types of collimator shapes in use, including pinhole, diverging and cone beam, in this system design we use a parallel-hole collimator (Figure 1.5). Parallel hole collimators generate an unmagnified image of the source distribution in the same orientation. Both converging and pinhole collimators generate

magnified images of the object but pinhole collimators generate an inverted image while other converging collimators generate an image in the same orientation. Diverging collimators generate a reduced image of the object in the same orientation as the object.
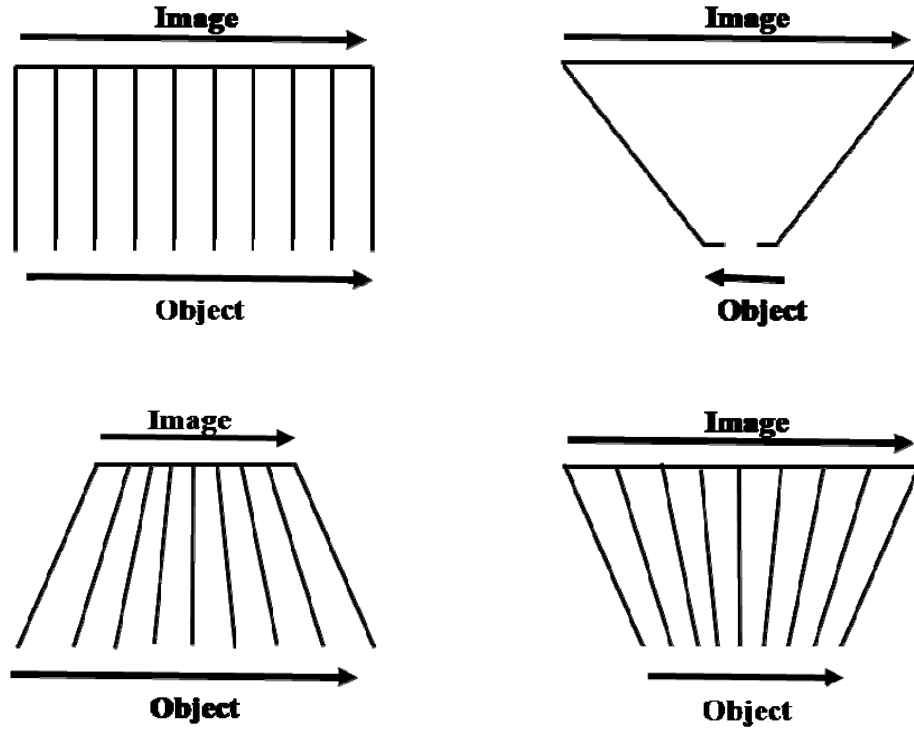
Figure 1.5: Illustration of the different collimator designs: (top left) parallel holed, (top right) pinhole, (bottom left) diverging, and (bottom right) converging collimators. Also indicated are the orientation and magnification of the object and its image.

Some other important parameters of the collimator design are the material composition, the shape, the thickness, and the length of the collimator septa, and the collimator hole size. Design tradeoffs exist for all these parameters. The most popular design for the holes is in a hexagonal close-packed array as it gives a very efficient packing fraction, provides good symmetry and allows for foil fabrication of the hexagonal septa [69]. A close-packed hexagonal array is the design used in this system. The attenuation

coefficient of the material used in the collimator design (in our case Pb) must be matched to the energy of the radiopharmaceutical being imaged so that the thickness of the septa walls is sufficient to absorb photons not travelling in the direction of the holes, but not so thick as to seriously degrade the performance (resolution vs. sensitivity) of the gamma camera [70].

Collimator resolution for a parallel holed collimator is described by:

$$R_{col} = \frac{d(l_{eff} + b + c)}{l_{eff}} \qquad (1.1)$$

where d is the hole diameter, l_{eff} is the 'effective length' of the collimator holes, b is the distance from the collimator to the source object, and c is the distance from the collimator to the detector. As resolution degrades for all types of collimators as the object to collimator distance increases, one objective in this system is to use the powerful 3D positioning capability of the SPECT system to position the gamma camera close to the surface of the breast. However, as the camera approaches the object, the sensitivity of the collimator for all photons, primary and scattered, also increases which may cause an increase in the detection of scattered photons transmitted by external photon sources such as an x-ray tube. This trend in increased scatter has relevance for the system designed in this thesis since it is composed of an integrated x-ray tube and gamma camera in close proximity. Transmitting x-ray photons while simultaneously acquiring SPECT data may increase the amount of detected scatter in the resulting SPECT image, thus hampering lesion detection. This is investigated in more detail in Chapter 3.

1.2.4. X-ray Beam Filtration

The energy spectrum of the x-ray beam incident on the object of interest is central to the ability of a CT system to successfully perform an imaging task [71-75].

1.2.4.1. Photon attenuation in an absorbing material

Photons are attenuated in intensity when passing through a material according to Beer's Law. Beer's law is energy dependent, since the attenuation coefficient of a material is itself energy dependent:

$$I(E) = I_o(E)e^{-\mu(E,Z,\rho)x} \tag{1.2}$$

where I is the transmitted photon beam intensity post-absorbing material, I_O is the incident photon beam intensity, x is the thickness of the absorber expressed in centimeters (cm), and μ is the linear attenuation of the material of the absorbing material expressed in cm^{-1}.

At a specific energy, the total attenuation coefficient of an absorber is the sum of the individual coefficients of each of the interaction processes at that energy:

$$\mu_{TOT} = \mu_{RAY} + \mu_{COMP} + \mu_{PHOTO} + \mu_{PAIR} \tag{1.3}$$

where μ_{TOT} (or more commonly, μ) is the cumulative attenuation coefficient, and μ_{RAY}, μ_{COMP}, μ_{PHOTO} and μ_{PAIR} are the Rayleigh, Compton, photoelectric absorption and the pair production sub-components, respectively, of the total attenuation coefficient at that energy. To normalize the effects of the physical density of the material the x-rays pass

through, the linear attenuation coefficient is often specified in terms of the mass attenuation coefficient or, μ/ρ, where ρ is the density of the absorbing material. The units of mass attenuation coefficient are then given by cm^2/g. For reference, the attenuation coefficient of Cerium, the filter material used in this system, is shown in Figure 1.6.
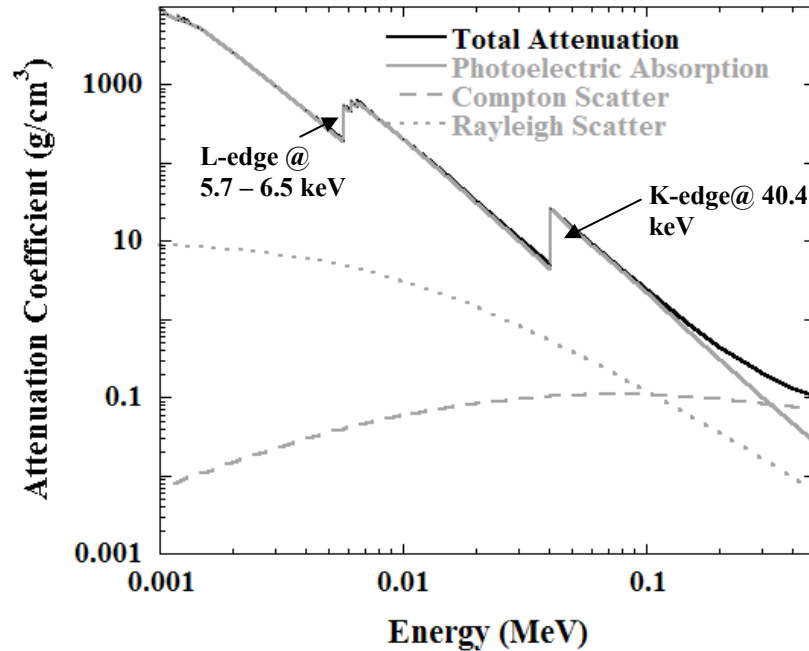
Figure 1.6: Illustration of the characteristic attenuation coefficient curve for Cerium, indicating the discontinuous jump in attenuation of the cerium absorber at energies around the characteristic absorption edges of cerium at 40.4 keV. In this CT system, we take advantage of the K-edge energy to selectively absorb x-ray photons at or around this energy.

The attenuation coefficient of an absorber decreases continuously with increasing photon energy, except at the K shell absorption edge, and to a lesser extent the L and M shell edges, of a material where it increases in a discontinuous manner. Filter materials preferentially absorb photons at energies where the attenuation coefficient of the filter material is greatest. For low-Z absorbing materials such as breast tissue, the K-edge energies are relatively low with a proportionally small change in attenuation coefficient.

For higher-Z filter materials, such as cerium, lead or tungsten based filters, the attenuating effect at these absorption energies is more dramatic and the filtered spectrum becomes more discontinuous around the K-edge energies of the absorber. This effect will be clearly seen in the filtered spectra in Chapter 2.

1.2.4.2. Intrinsic Filtration

Some of the lowest energy photons are initially filtered by self-absorption in the target material,. These photons do not contribute to the formation of an image but increase heat in the anode target. Low energy x-ray photons are attenuated further when passing through the intrinsic filtration of the tube, often made of aluminum or a similar attenuating material.

1.2.4.3. Extrinsic Filtration

Extrinsic filtration is normally added to 'harden' the beam by removing low energy (0-10 keV) x-rays that do not add information to the image but are absorbed in the body, causing an unnecessary increase in patient dose. Extrinsic filtration in mammography is used to enhance the characteristic x-rays of the anode material, e.g. for a Molybdenum (Mo) anode, a Mo filter is used to enhance the characteristic x-rays of Mo at 17.9 and 19.3 keV [76-77]. In addition to a change in the tube potential, the optimum anode/filter material combination for mammography varies as the size and composition of the breast in the detector FOV changes e.g. for a thicker denser breast a higher beam energy using another anode/filter combination is more optimal, e.g. Mo/Rh [78]. Examples of several thicknesses of Mo added to the raw x-ray beam from a Mo target are shown in Figure 1.7.

Tomographic imaging of an uncompressed breast presents a far different task than that of mammography and so different anode/filter combinations are required to optimize low-dose breast CT imaging for different breast sizes, and tissue compositions [17, 73, 79-80].
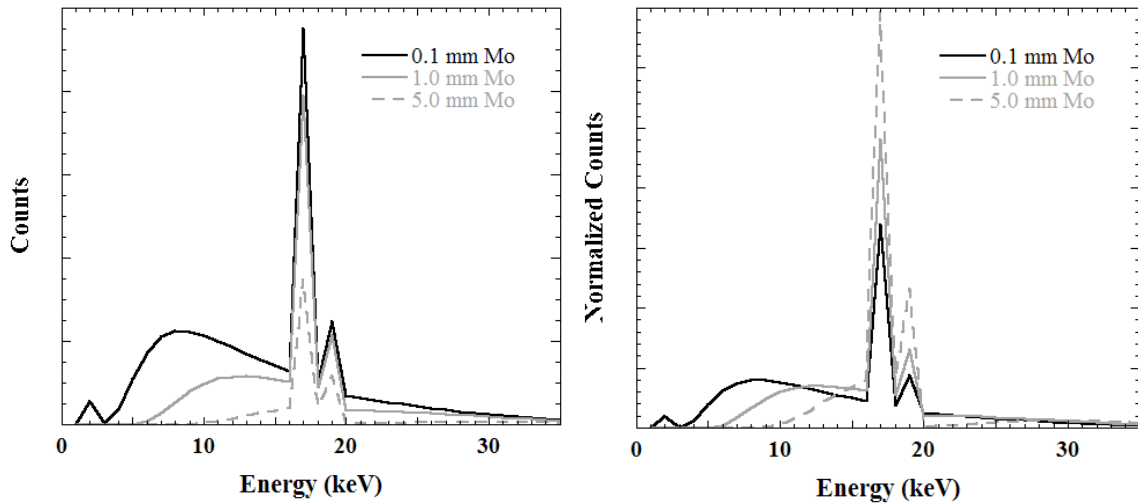
Figure 1.7: (Left) Plots of the simulated output spectrum of a Mo-anode x-ray tube with progressively increasing amounts of Mo material acting as extrinsic filtration. (Right) These plots are the same as those on the left except they are normalized to the same total number of counts to emphasize the increasingly monochromatic nature of the filtered beam with diminished flux as the thickness of the extrinsic filtration material layer is increased.

Extensive simulation based work was completed in the development of the independent breast CT system to optimize the spectral shape of the x-ray beam for low-dose, uncompressed breast imaging [79, 81-84]. It was found that a novel filtration method using ultra-thick K-edge beam filtration optimized the x-ray beam in terms of maximizing the dose efficiency of the system (SNR^2/dose). Validation of these simulation results is the subject of Chapter 2 in this thesis [75, 79-80, 82, 85-86].

The diverging nature of the x-ray cone beam and the non-uniform nature of the pendant breast [87] mean that a flat sheet of metal (a standard shape for an x-ray beam filter) may not be the optimal physical shape of a filter for cone beam imaging. Boone *et al.* found that using an ideal bowtie filter for dedicated breast CT imaging could reduce glandular breast dose by an average of 38% [88]. The shape of a bowtie filter becomes progressively thicker as the periphery of the beam is approached. The shape of the bowtie filter then attempts to equalize the intensity of the x-ray beam across the profile of the object being imaged, reducing flux to the thinner peripheral sections of the object. A recent study found that the absorbed dose was reduced at both the periphery and the center of uniform and irregularly shaped phantoms when using a bowtie filter compared to the setup without [89]. In this study, image quality improved with a concomitant reduction in scatter to primary ratio both in the center and towards the periphery of the phantom used in the study. However, the non-uniform and unique 3D shape of each breast makes the task designing an optimal 3D bowtie filter for tomographic imaging very difficult. It is also believed that further reducing the photon flux in this system by using a bowtie may degrade the SNR of the tomographic projections. It is further believed that the thick filter implemented in the CT system may perform a role similar to a bowtie filter since the path length of x-rays through the high-Z cerium filter towards the edge of the filter is longer than that of the central ray, thus reducing exposure and dose towards the periphery of the beam's field of view. For all these foregoing reasons, a bowtie filter has not been implemented in this system design and instead a filter made from flat sheet of metal is used instead.

1.2.5. Interaction of x-rays with matter

At the energy levels encountered in this thesis research (30 - 140 keV) , x- and γ-ray interact with matter through photoelectric absorption, Compton, or incoherent, scattering, and Rayleigh, or coherent, scattering.

1.2.5.1.   Photoelectric Absorption

In photoelectric absorption, all the energy of the incident photon is transferred to the electron, normally an electron in the inner K or L shell of the atom. The electron is then ejected with kinetic energy equal to the energy of the incident photon minus the binding shell energy of the ejected electron i.e.

$$E_e = E_\gamma - E_B \qquad\qquad (1.4)$$

where E_e, E_γ and E_B are the energies of the liberated electron, the incident photon and the binding energy of the liberated electron, respectively, expressed in electron volts.

Once a vacancy occurs in the inner shell of the ionized atom, photons from outer shells drop out of their outer orbits and occupy the vacant inner shells, releasing a cascade of characteristic x-ray photons, each with an energy characteristic of the difference between the binding energies of the constituent outer to inner shells. Another potential byproduct of photoelectric absorption is an Auger electron where the energy of the characteristic x-ray photon is transferred to an orbital electron whose kinetic energy upon liberation is the difference between the binding energy of the electron and the energy of the incident radiation. Auger electron yield decreases as the Z of the absorbing material increases.

Photoelectric absorption occurs in proportion to Z^5/E_O^3 where E_O is the energy of the incident photon [90]. This relationship shows that the lower the incident energy of the photon and the higher the Z of the interacting material, the more likely the interaction process will be photoelectric absorption. At the 40 keV energies encountered in this thesis, photoelectric absorption is the predominant interaction of the primary x-ray beam with the metal beam filter [63]. For SPECT imaging, the high-Z material of the CZT camera ($Z_{eff} = 49.3$) ensures that there is a high efficiency for photoelectric absorption at the 140 keV energy of the ^{99m}Tc γ-ray.

The kinetic energy of the photoelectron is fully deposited very close to the site of interaction, leading to an increase in dose in close proximity to the photoelectric event [91]. The emitted characteristic x-ray may also interact with other atoms, leading to a further increase in dose deposited in the uncompressed breast [63, 92].

1.2.5.2. Incoherent/Compton scattering

In Compton scattering, incident photons interact with outer shell or 'valence' electrons, rather than the inner shell electrons as occurs in the photoelectric event. Through conservation of energy and momentum, the energy of the scattered photon can be calculated as:

$$E_{sc} = \frac{E_o}{1 + \left(\frac{E_o}{511 \text{ keV}}\right)(1 - \cos\theta)} \tag{1.5}$$

where E_{sc} and E_o are the energies of the scattered and incident photons, respectively, expressed in electron volts, eV and θ is the angle of the scattered photon, in degrees.

The Klein-Nishina formula describes the probability of angular distribution of Compton scattered photons. The equation was classically derived as:

$$\frac{d\sigma}{d\Omega} = Zr_0^2 \left(\frac{1}{1+\alpha(1-\cos\theta)}\right)^2 \left(\frac{1+\cos^2\theta}{2}\right) \left(1+\frac{\alpha^2(1-\cos\theta)^2}{(1+\cos^2\theta)[1+\alpha(1-\cos\theta)]}\right) \qquad (1.6)$$

where $d\sigma/d\Omega$ is the differential scattering cross section as a function of the 4π solid angle, or probability of interaction, Z is the atomic number of the material, r_0 is the classical electron radius, θ is the scattering angle and α is a ratio of the photon's incident energy to the rest energy of the electron (511 keV).

At low energies, the Klein-Nishina model predicts there is a relatively uniform likelihood of a photon being scattered in any direction. As the energy of the incident photon increases, the incident photon is more likely to be scattered in the original direction of travel of the primary photon. This is illustrated in Figure 1.8 that shows the differential scattering cross section for scattered photons in soft tissue ($Z_{eff} = 7.4$) at 36 keV, the mean energy of the x-ray cone beam, and at 140 keV, the energy of the ^{99m}Tc γ-ray photon.

Compton scattering occurs when the incident photon energy is far greater than that of the binding energy of the electron, and so the likelihood of Compton scattering occurring increases with increasing incident photon energy [92]. Additionally, Compton scattering is also linearly dependent on the Z of the interacting material.
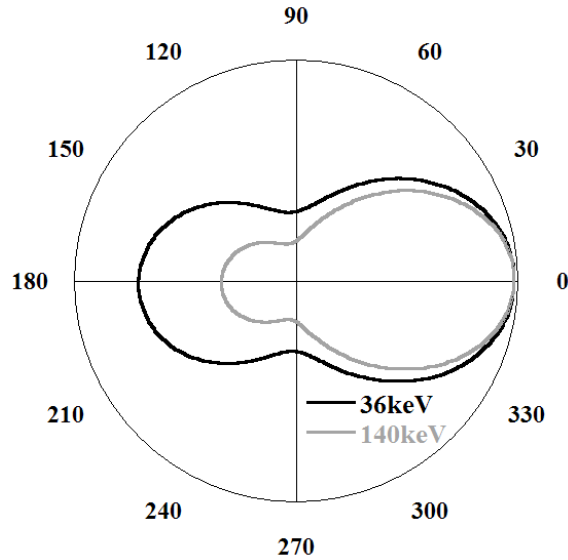
Figure 1.8: Klein Nishina-derived angular distribution probability for scattered x- and γ-ray photons in soft tissue (Z_{eff} = 7.4) from incident (black line) 36 keV x-ray photons and from (light gray) 140 keV γ-rays. The lower energy (36 keV) photons, typical of the mean beam energy of the x-ray beam used in this thesis, have a more symmetric angular distribution compared to the more forward oriented higher energy 140 keV photons.

1.2.5.3.   Compton scattering and image cross contamination

The compact, dual-modality system in this thesis possesses a common imaging FOV, and therefore, the potential for scatter from either the x-ray source or the emission source in the patient to contaminate the image of the complementary modality exists. Scattered photons produce a low frequency (slowly varying) signal in the reconstructed image, adding no information to the image but leading to a reduction in image contrast [93-98].

In this imaging system, forward scattered x-ray photons are likely to impact the x-ray detector, especially since the object to image distance in the compact CT system is between 20-22 cm. Energy integrating x-ray detectors, like one used in the current breast CT system, have no inherent ability to discriminate between the energy of a scattered or

primary photon. Scattered ^{99m}Tc photons may therefore be detected in the same way as x-ray photons and so add to scatter in the x-ray image.

The compact gamma CZT camera is designed to closely contour the breast surface and is therefore in close proximity to the edge of the cone beam x-ray. The flux of the x-ray source, orders of magnitude larger than the flux of γ-ray photons emitted from the patients' breast, may generate scatter in the SPECT image, especially since the compact gamma camera contours the patient's breast so closely [99-100]. Energy discriminating detectors, like the CZT-based detector used in the SPECT subsystem, can use the fact that scattered photons possess lower energies than their primary counterparts to remove unwanted scatter from acquired SPECT data. This is accomplished by using energy windowing, a process where photons possessing only certain energies are allowed to form the resulting SPECT image. The energy window is implemented using pulse height discriminators, electronic components that form part of the gamma camera signal processing chain. These discriminators accept only those event energies that lie between a preset lower and/or upper threshold [92]. Events whose energies lie outside these limits are rejected in the final image.

Image cross contamination is investigated in detail in Chapter 4 of this thesis. The contribution of Compton scattered 36 keV (or lower energy) x-ray photons to the acquired SPECT data in energy windows of different sizes about the 140 keV photopeak is measured, in addition to the effect of primary and scattered 140 keV γ-ray photons to the CT projections and reconstructed images.

1.2.5.4.   Other forms of interaction in matter

A third form of interaction is coherent or Rayleigh scattering, an elastic interaction that conserves the energy of the scattered photon. Although coherent scattering is a more common component of interactions in cerium at 36 keV than incoherent scattering (see Figure 1.6), coherent interactions form a lower proportion of interactions in soft tissue compared to incoherent interactions at the same energy. At the energy of the ^{99m}Tc γ-ray photon, 140 keV, coherent interactions play only a very minor role compared to incoherent interactions[101-102].   In addition, since the energy of the photon is conserved in a Rayleigh interaction and the detector used in our system is an energy integrating detector, Rayleigh interactions cannot be separated from other forms of interaction. For these reasons, coherent scattering was not considered in this thesis.

Pair production requires the incident photon to possess an energy twice that of the rest mass of an electron, i.e. at least 1.02 MeV. Pair production derives from the interaction of a photon with the nucleus and results in the generation of a positron and an electron. Pair production is of no consequence at the energies encountered in this thesis.

1.2.6. Dosimetry theory

There is a small but significant risk of radiation induced cancer associated with breast x-ray examinations [103]. Guidelines from the American College of Radiology (ACR) suggest that the average dose to the breast from dual-view mammography of a 4.2 cm

thick compressed breast, consisting of 50-50% adipose-glandular tissue, must not exceed 6mGy[104]; the ACR's European counterpart [105] has issued similar recommendations. Since the protocol for our proposed breast CT scan involves acquiring hundreds of individual projection images of the pendant breast, minimizing the amount of dose delivered to the breast while maintaining image quality is central to the successful design of the imaging system described in this thesis [106-107].

Dose to the breast is intimately tied in with the interactions of photons in matter. When ionizing radiation interacts with breast material at the energies typically encountered in this thesis, electrons are liberated from atoms of the breast tissue mainly through photoelectric absorption and Compton interaction [90]. Electrons liberated in the processes deposit their kinetic energy along their track in the area surrounding the interaction site through collisional energy loss or radiative loss. Only collisional energy loss is considered to add to absorbed dose [90-91]. The scattered photon may travel and ionize other atoms, thus increasing the deposition of dose through further Compton scattering. Absorbed dose to the uncompressed breast during a tomographic scan is measured in Chapter 3.

The amount of dose absorbed by the breast is dependent on several factors: the material composition of the breast (absorbed dose increases with increasing glandularity of the breast tissue) [108], by the mass of the breast, and by the energy and fluence of the incident x-rays (influenced by the spectrum of the x-ray beam). The choice of detector material for the specific imaging task is also important since the photon detection efficiency of the detector is related to the energy of the x-rays that exit the breast and

impinge on the detector surface. In this breast CT system, the x-ray beam incident on the pendant breast in the FOV has been designed specifically to maximize the dose efficiency for uncompressed breast imaging, i.e. maximizing the SNR of the reconstructed image while minimizing dose to the breast [109-110].

Absolute dose is defined as the average amount of energy imparted by ionizing radiation to a mass of material [91, 111], i.e.

$$\text{Dose} = \frac{\Delta\varepsilon}{\Delta m} \qquad\qquad (1.7)$$

where ε is the imparted energy in Joules, J and m is the mass of the medium, expressed in kg. There are a number of standard measurement units for dose. The international standard unit is the Gray [111] (Gy) which is equal to 1J/kg. 1Gy is also equal to 100rad, another popular unit of measurement. Dose is closely related to the concept of x-ray exposure which measures the amount of charge (electrons) liberated by ionizing radiation per unit mass of air. Exposure is measured in Roentgens(R) where $1R = 2.58 \times 10^{-4}$ C/kg. Other factors that influence the dose to a material are the fluence of the x-ray beam passing through the volume of material represented by Δm, the mass energy transfer of the constituent materials of the medium, and the average energy of the x-ray beam.

1.2.6.1.   Dose measurement techniques

Dosimetric techniques for breast imaging span both simulation based [15, 112-113] and empirical techniques [108, 114]. For mammography, a common technique is to measure the exposure in air at the surface of the breast and to use simulation derived conversion

factors to convert the entrance exposure to absorbed dose in the breast. Monte Carlo

based simulation techniques are also used in breast CT dosimetry [88, 115] to estimate

dose to uncompressed breasts of different shapes and compositions.
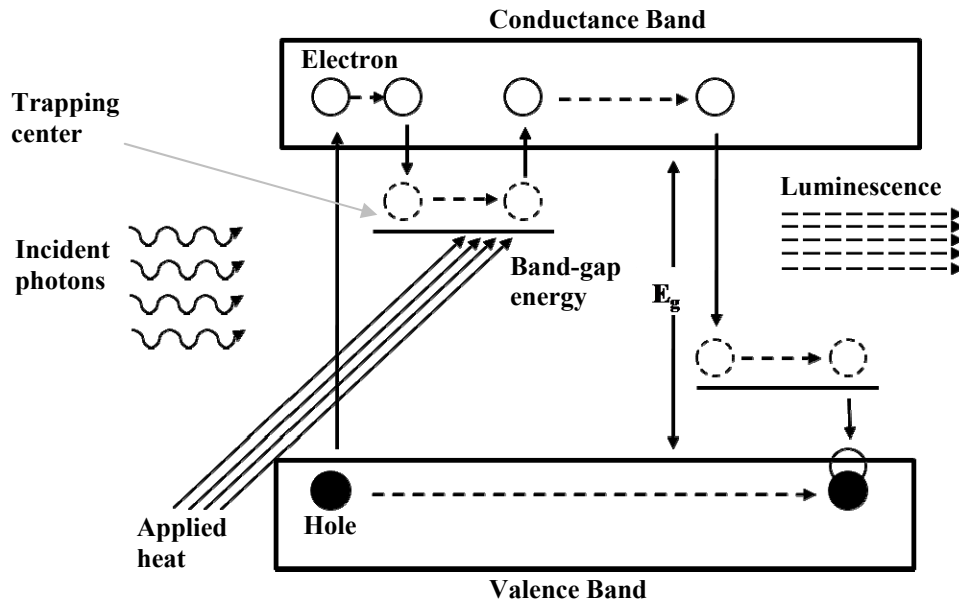
Figure 1.9: Simplified illustration of the thermoluminescent process whereby incident radiation creates electron hole pairs and elevates the electrons (clear circles) from the valence band to the conduction band. The electron drops from the conduction band to the intermediate electron trap layer, caused by adding dopant material to the TLD material. Upon heating, the electron gathers enough energy to raise itself out of the luminescence layer into the conduction band but it then drops down to the valence band to recombine with a hole (solid black circle), releasing light in the process.

One popular method to empirically measure dose is with thermoluminescent dosimeters

(TLDs). In the thermoluminescence process, the TLD material, commonly an inorganic

crystal, absorbs energy from the ionizing radiation, in the process elevating an electron

from its valence band to the conduction band (Figure 1.9) [92]. Normally, these electrons

quickly recombine with the holes remaining in the valence band, emitting a photon in a

process termed fluorescence ($T_{1/2}$ < μsec.). In TLDs however, the main TLD crystal

material is infused with impurities that create charge trapping centers between the

valence and conduction bands [111]. These centers trap returning electrons where they (and their accompanying energy) are stored until heat is applied to the crystal ($T_{1/2} \gg$ msec.). Upon heating to a specified temperature range (which varies by TLD material), the trapped electrons are re-elevated to the conduction band and fall again to the valence band, emitting visible light photons. This delayed light-producing process is called phosphorescence. If the manufacturing process does not include a doping step, the light emitted upon heating will be minimal. Although there is a continuous band of temperatures where different intensities of luminescence occurs, called the characteristic 'glow curve' of the material (Figure 1.10), each TLD material has been characterized so that the area of the curve under the main peak is proportional to the accumulated exposure.
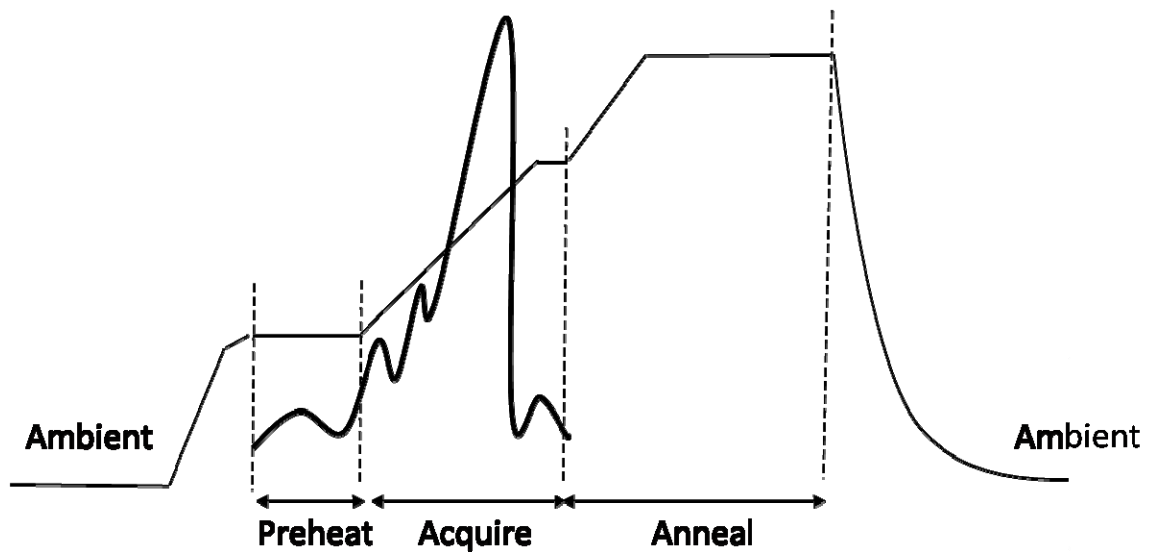
Figure 1.10: Glow curve typical of the LiF:Mg,Ti TLDs used in the dose experiments. The piecewise straight line illustrates the temperature gradient, and the smooth curve a typical light intensity curve versus temperature for the LiF:MgTi material. The various stages of heat treatment and TLD readout status are also indicated on the graph.

Lithium Fluoride (LiF) is one of the main materials used to make TLDs for medical dosimetry and it is the TLD material used in this thesis. To increase their thermoluminescence, LiF crystals are doped using small amounts of magnesium and titanium impurities [92]. LiF:Mg,Ti TLDs were used in this thesis research due to their tissue equivalence ($Z_{eff,LiF}$ = 8.2 vs. 7.4 for soft tissue) small size, dose linearity (up to ~4 Gy), and sensitivity to small doses (minimum sensitivity is ~100 µGy) [92, 111, 116].

Although TLDs are the gold standard for dosimetry, another more recently developed method to measure dose is with radiochromic film, materials that have a high sensitivity for ionizing radiation [91, 117]. Radiochromic film possesses fine spatial resolution, limited by the grain size of the constituent material, for generating 2D profiles of absorbed dose, a large dynamic range of sensitivity (0.1 – 20 cGy for the film used in this thesis) and a near-linear response to incident radiation [111, 118]. Radiochromic film consists of a colorless thin layer (7-23 µm) of radiosensitive monomer crystals between plastic layers [119]. The film undergoes solid-state polymerization in real time in reaction to incident radiation [120]. The polymerization creates a dye-complex darker in color compared to unexposed portions of the film, and is subsequently digitized after a 24 hour period needed to allow stabilization to occur. The polymerization in the film yields an absorption spectrum with a maximum at 635 nm [121], which is most sensitively detected with optical digitization using red light.

1.2.7. Image generation

1.2.7.1. X-ray detection

The x-ray CT system in this thesis, in common with other breast CT systems, uses an indirect image detection mechanism [122-125]. In such a system, incident x-ray photons initially interact with a layer of scintillator material to fluorescently produce a shower of visible light photons centered about a specific wavelength of light [92]. The system in this thesis uses thallium-doped cesium iodide (CsI:Tl, Z_{eff}=54, ρ = 4.51 g/cm^3), a scintillator material that produces an emission spectrum of visible light photons that is maximized at a wavelength of 550 nm. The number of light photons emitted by the scintillator is proportional to the integral energy of the incident radiation (66k photons per MeV). The CsI:Tl scintillator material is either grown directly on or affixed to the glass substrate of the underlying semiconductor photodiode material, in this case hydrogenated amorphous silicon (aSi:H) [126]. To maximize the efficiency of signal generation, it is important to match the emission spectrum of the scintillator with the absorption spectrum of the photodiode material – such is the case with CsI:Tl and aSi:H where the light absorption efficiency of aSi:H is approximately 80% at 550 nm [127].

The fluorescent light emitted during the x-ray exposure illuminates the underlying photodiode array and frees up electrons in the pixels of the photodiode. During an exposure the integral charge induced in the pixel is stored at a capacitor formed at the junctions of the photodiodes. These charge packets are then read out sequentially by application specific integrated circuits connected to the capacitors.
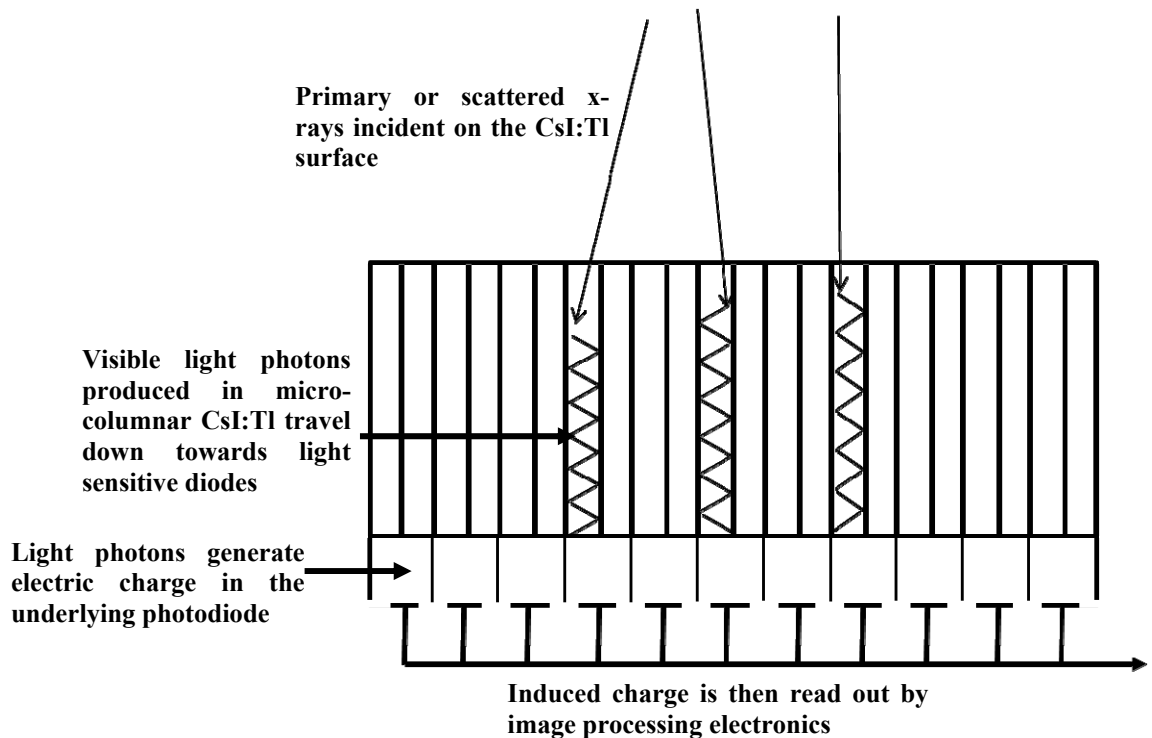
Figure 1.11: Illustration of the process of transforming x-rays to electronic signals in the indirect x-ray detection process of CsI:Tl. Incoming x-rays are turned into visible light that induces charge in photodiodes and the charge is read out by electronics (not shown). Note the columnar shape of the CsI:Tl scintillator that allows the detector maintain resolution.

The popularity of CsI:Tl is thanks to its impressive light yield, its high absorption efficiency due to the high Z of its constituent materials (Z_{Cs} = 55, Z_I = 53) and the high packing density of the scintillator needles that increases absorption efficiency. Another advantage to CsI:Tl as a scintillator is its needle-like structure that guides the generated light photons to the underlying photodiodes, reducing the lateral diffusion of the light photons and retaining good spatial resolution. The primary scintillation decay time of CsI:Tl is 800 ns , longer than other competing scintillators. One other major issue when using CsI:Tl as a scintillator is a problem with afterglow, which can be upwards of 5% of the peak light value 2ms after exposure, depending on the intensity and duration of the

excitation pulse [128]. This causes problems in high speed imaging, such as pulse pileup in high count rate applications, reconstruction artifacts in CT, and reduced contrast and blurring in other imaging environments [92, 129]. By co-doping CsI:Tl using materials such as Eu^{2+}, the afterglow can be reduced considerably [128].

Direct detector systems rely on the direct creation of electron-hole pairs in the semiconductor material (e.g. amorphous selenium, a-Se, mercuric iodide (HgI_2), cadmium telluride (CdTe) amongst others) in response to incident x-ray photons [130]. The layer of photoconducting material, e.g. a-Se is superimposed on an underlying thin film transistor (TFT) layer. Incident x-rays directly induce the creation of electron-hole pairs that accumulate upon one plate of a charge storage capacitor. In contrast to the indirect system, there is generally no intermediate light generation step between incident photon and electron-hole generation. The strong electric field placed across the a-Se layer makes the carriers flow towards the electrodes with minimal lateral diffusion. This mechanism results in improved spatial resolution compared to other technologies [126]. In addition, the tendency of induced carriers to travel straight to the electrodes means that thicker layers of photoconducting material can be superimposed on the TFT array, thus improving absorption efficiency. However, direct detector materials are currently not widely used in commercial full CT systems owing to poor temporal characteristics (image lag) and other dynamic capabilities [130-132].

1.2.7.2.   SPECT detection

The compact gamma camera used in the SPECT subsystem is composed of 6mm thick modules, each 5x5 cm^2, made from monolithic cadmium zinc telluride (CdZnTe or CZT) crystals, a commercially available semiconductor detector material.   The crystal is pixilated with 2.3x2.3 mm^2 electric contacts. The actual properties of CZT depend on the concentration of zinc in the bulk as well as the surface of the material. With its high effective atomic number (Z_{eff} = 49.5, ρ = 5.78 g/cm^3), CZT has good stopping efficiency for detecting ^{99m}Tc γ-rays at 140.6 keV, the energy of the incident ^{99m}Tc primary γ-rays [133].

Semiconductor materials have energy bands that separate electrons in the lower energy valence band from those in the conduction band at a higher energy level. The valence and conduction bands are separated by an energy gap that is 1.56 eV for CZT, at room temperature. This relatively large band gap potential reduces the intrinsic charge carriers in the material, thereby reducing the thermally induced leakage current in the CZT modules. The low leakage current, in addition to its high detection efficiency, high charge collection due to electron-hole mobility bandwidth leading to fine energy resolution and high signal to noise ratio make CZT highly suitable for operation at room temperature [70].

In CZT, electron-hole (e-h) pairs are produced by an ionization mechanism in response to the energy of the incident photons along the path of the photon (~31k e-h pairs produced per 140.6 keV photon) [70, 133]. When e-h pairs are created, electrons from the valence

band are raised to the conduction band where they migrate to the anode under the influence of an applied external voltage potential. This is the signal that is processed by the detector electronics. Recombination of energized electrons with holes within the semiconductor material before the electrons reach the anode leads to errors in the accuracy of the detected energy versus the true energy of the incident photon.

The movement of electrons produces a charge at the anode in proportion to the energy of the incident photon. Application specific integrated circuits connected to the anode process the anode signal so that the energy and pixel location of the signal is digitized, buffered, and interfaced to a computer. If 'list-mode' data acquisition is employed, the chronological order of incoming events is preserved in addition to the energy and spatial location of the events. Although this increases the size of the acquired data set, list mode data enables post processing of the raw data to model different setups e.g. varying the noise characteristics of the data. List mode data acquisition is employed in Chapter 3 to enable modeling the effect of acquiring SPECT in the presence of x-ray photons using different sized energy windows.

1.2.8. Image reconstruction methods

1.2.8.1.   The Radon transform

Take the simplified, hypothetical case of imaging a 2D object f(x,y) in the detector FOV (Figure 1.12), which can be a 2D distribution of attenuation coefficients for CT imaging. The Radon transform in the 2D case is the set of line integrals in a frame of reference, rotated at angles θ through the object, and can be written as:

$$p(X_r,\theta)= \int_{-FOV}^{+FOV} f(x,y)dY_r \qquad (1.8)$$

where the integration occurs parallel to the rotated line Y_r.
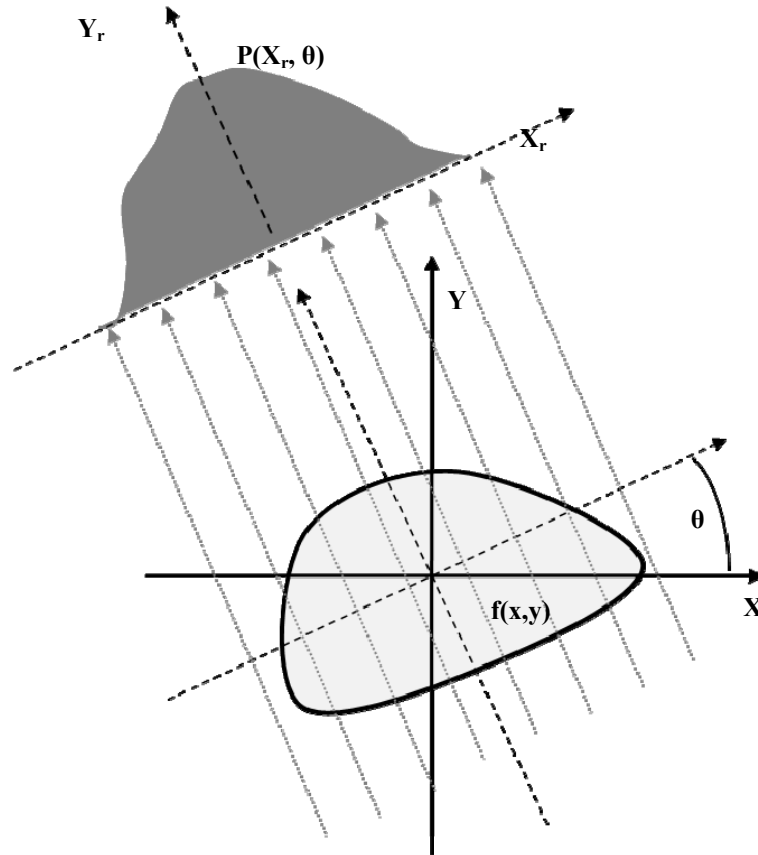
Figure 1.12: Illustration of the principle of Radon transform with line integrals through a 2D distribution f(x,y) of either attenuation coefficients or source activity.

Co-ordinates (x_r, y_r) in the rotated frame of reference are related to the co-ordinates (x,y) in the object frame of reference by the following co-ordinate transformation (see Figure 1.12):

$$\begin{bmatrix} x \\ y \end{bmatrix} = \begin{bmatrix} \cos\theta & -\sin\theta \\ \sin\theta & \cos\theta \end{bmatrix} \begin{bmatrix} x_r \\ y_r \end{bmatrix} \qquad (1.9)$$

This is called the X-ray transform, which in 2D is the same as the Radon transform. The relationship between the X-ray and Radon transforms does not extend to an object or activity volume in 3D, as the 3D Radon is the set of all 2D plane integrals whereas the X-ray transform is still the set of all line integrals through the object.

1.2.8.2.   Filtered backprojection

Due to its relative ease of implementation and speed of reconstruction, filtered back projection (FBP) methods are some of the most common methods in use for commercial CT scanners. Inversion of the Radon transform forms the basis for 3D reconstruction using FBP [134]. For cone beam imaging, many FBP-based reconstruction algorithms are based on the Feldkamp-Davis-Kress (FDK) algorithm, originally developed for CT machines that acquired data only in a circular orbit [135]. Using this algorithm, an exact solution existed only for the central plane of the orbit and reconstructed image quality degraded as you moved farther from this central plane, and especially degraded at large cone beam angles. This algorithm was best used for systems that have a small cone beam angle, and was not able to accommodate arbitrarily complex 3D orbits. More recently, there has been great progress in deriving novel FBP algorithms that accommodate non-circular orbits, some of them developed specifically for breast imaging an uncompressed pendant breast [136-139].

1.2.8.3.   Iterative reconstruction

The CT and SPECT images shown in this thesis work were reconstructed using statistically based iterative reconstruction techniques. Statistical iterative reconstruction

methods do not invert the Radon transform but instead maximize the probability or the likelihood of, for CT, an attenuation coefficient being present in a particular element of the reconstructed volume (or voxel, the 3D equivalent of a pixel) given the projection data that were acquired. For SPECT this extends to maximizing the likelihood that a particular voxel contains a certain level of activity. Iterative reconstruction techniques allow for improved reconstruction with reduced image artifacts when complex or incomplete 3D x-ray source-detector trajectories are used to generate the projection data in CT, or when the SPECT gamma camera uses complex 3D orbits to acquire SPECT projection data. Such is the case with both modalities in this system [100, 140-142]. In addition, iterative methods perform well when the projection data is acquired using low x-ray exposures or quantum limited SPECT data i.e. it has a high noise component, and when other system characteristics need to be modeled such as the detector point spread function or focal spot shape.

Iterative algorithms start with an assumed image, calculate forward projections from the assumed image, $p^{(j)}$ for the jth iteration, compare these with the original measured projection data acquired during the CT scan, p, and iteratively update the estimated image, $\mu^{(j)}$, based upon a comparison between the forward projected and measured projections. This workflow can be summarized by the following equation for a 2D projection of an object:

$$p^{(j)}=A\mu^{(j)}+ e \qquad\qquad (1.10)$$

where A is the system matrix or model of the CT system that can include many important system characteristics such as the system geometry and detector response, and e is the error vector accounting for such aspects of the system like additive noise and measurement bias.

The reconstruction algorithm used in this thesis work was developed by Dr. James E. Bowsher at the Duke University Medical Center. The CT reconstruction algorithm incorporates an ordered subset transmission reconstruction (OSTR) method that uses subsets of projections to accelerate convergence of the likelihood [143-144] while the SPECT algorithm incorporates an ordered subset expectation maximization (OSEM) algorithm that, similar to the CT algorithm, uses subsets of projections to accelerate the maximization process of the maximum likelihood expectation maximization algorithm. Ordered subsets methods process each subset of grouped projections at once. It is best to order the subsets such that the projections corresponding to angles with maximum angular distance from previously used angles are chosen at each step [143]. This accelerates convergence as compared to random or sequential ordering of the subsets. In addition to accelerating reconstruction for both modalities, an advantage of both ordered subset codes is that they were designed to allow complex 3D source-detector data acquisition trajectories about the pendant breast that enable improved image quality with reduced distortion of reconstructed objects [99-100, 141-142].

In OSTR, the estimates of the attenuation coefficients are made so that the probability of the measured attenuation coefficients is maximized. Updated estimates for the

attenuation coefficients in subset S+1, based on the estimates in subset S for iteration n in voxel k of the object is given by [144]:

$$\mu_{s+1}^n(k) = \mu_s^n(k) + \mu_s^n(k) \frac{\sum_{i \in S(s)} l_{ik}(\bar{y}_i(\mu_s^n) - Y_i)}{\sum_{i \in S(s)} l_{ik}\langle l_i, \mu_s^n \rangle \bar{y}_i(\mu_s^n)} \qquad (1.11)$$

where:

$\bar{y}_i(\mu_S^n) = d_i e^{-\langle l_i, \mu_s^n \rangle}$ is the expected number of counts in detector bin i ,

$\langle l_i, \mu_s^n \rangle = \sum_i l_{ij} \mu_s^n(j)$,

Y_i is the measured transmission in bin i,

l_{ij} is the length of projection line i through voxel j,

$S(s)$ contains the projections in subset s.

In the course of developing the independent CT system, it was found that the optimal number of reconstruction iterations with respect to a tradeoff between object SNR and contrast varied as a function of the diameter of the spherical objects under reconstruction [123]. Despite the quantative and qualitative differences observed in the reconstructed objects, a followup observer study indicated that there was no difference in the number of spheres of varying diameter observed, regardless of the number of reconstruction iterations [123]. In light of this result such a test was not repeated during the course of this thesis and so, unless otherwise noted, all reconstructed images shown in this thesis were generated at the 10th iteration.

OSEM is a variation on the maximum likelihood expectation maximization (ML-EM) algorithm that tries to maximize the likelihood that the estimated, reconstructed source

46

distribution $\hat{f}$ is the actual true source distribution, f, given the measured projections of source distribution, g, i.e.

$$\hat{f} = \arg\max_f p(g{:}f) \qquad (1.12)$$

The OSEM algorithm is then:

$$\hat{f}_j^{new} = \frac{\hat{f}_j^{old}}{\sum_{i' \in S_n} h_{i'j}} \sum_{i \in S_n} h_{ij} \frac{g_i}{\sum_{i=1}^{N} h_{il}\hat{f}_l^{old}} \qquad (1.13)$$

where h_{ij} is an element of the system matrix representing the mean contribution of pixel j in the object to pixel i in the projections. Backprojections are only performed for projection bins belonging to the subset S_n [145].

1.3. The independent breast CT and SPECT systems

This thesis work straddles the end of the development phase of the independent SPECT and CT imaging systems and the beginning of the development and implementation of the first prototype combined SPECT-CT imaging device dedicated to breast cancer imaging. The independent SPECT and CT imaging subsystems use a combination of custom-designed and off-the-shelf hardware and software components. Detailed descriptions of the design, implementation, and capabilities of the independent SPECT and CT subsystems have been extensively presented elsewhere [75, 99-100, 123, 125, 142, 146-151], and what follows is an overview of the independent systems as they existed before this thesis work began, and during the early part of the thesis work.
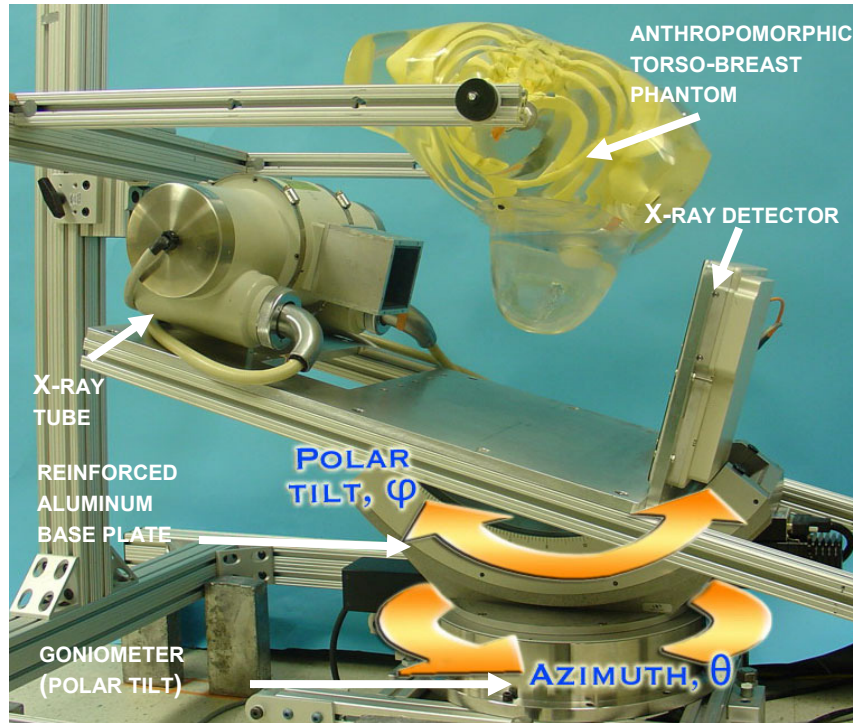
Figure 1.13: Photograph of the independent CT system imaging an isolated and combined anthropomorphic torso-breast phantom hanging pendant in the CT system FOV. The major mechanical components of the system and the available positioning capabilities of the independent CT system are noted in the photograph.

The integrated dual-modality SPECT-CT imaging system that was designed and developed during the course of this thesis work will be described in more detail beginning in Chapter 4.

1.3.1. Independent CT system

The independent breast CT system [125] (see Figure 1.13) components consist of a rotating tungsten (W) target cone beam x-ray source (model Rad-94, *Varian Medical Systems*, Salt Lake City, UT) with 0.4 or 0.8 mm focal spot size and a high heat capacity for repeat tomographic acquisitions. Tube potentials are provided by a powerful and versatile 60 kW generator (model CPX-160, *emd Technologies,* Montreal, Quebec,

Canada). The system uses a 600 μm thick CsI:Tl scintillator based amorphous silicon digital x-ray detector (*Varian Medical Systems*, Salt Lake City, UT) with a 1920x1536 pixel grid using a 127 μm pixel pitch. The source and detector were secured to a reinforced solid metal plate and attached to a goniometer (model BGM200PE, *Newport Corp.*, Irvine, CA) and rotation stage (model RV350CC, *Newport Corp.*, Irvine, CA). A Ce (Z = 58, ρ = 6.77 g/cm^3, K-edge = 40.4 keV) (*Santoku America, Inc.*, Tolleson, AZ) 100th value attenuating layer filter (0.0508 cm at 60 kVp) is used to produce an incident x-ray beam with a quasi-monochromatic energy spectrum with a FWHM of <15% according to simulation [80]. A custom built collimator attached to the x-ray source allows filters of different compositions and thicknesses to be inserted as the need arises. An SID of 55 cm was used for the independent breast CT set up with a magnification of 1.57 for an object located at the center of rotation of the system. The compact SID was used partially to ensure that the flux reaching the x-ray detector through the filter and pendant breast was adequate for signal generation. Custom designed software algorithms were implemented in C using the application program instruction software of the various imaging components to synchronize gantry motion, x-ray exposure, and image acquisition [123]. This semi-autonomous software (the initial setup is user-controlled but the image acquisition process is automated) enables various x-ray projection exposures levels to be chosen in addition to the total number of projection views, the azimuthal and polar angular separation between projections (symmetrical or asymmetrical angular separation is possible), and the temporal delay between acquired projections. Based on these user-specified parameters, a theoretically infinite number of imaging trajectories could be implemented by the independent CT system so that projection data can be

acquired at various azimuthal and polar orientations around a pendant uncompressed breast [141-142, 149].

Major findings from the initial development of the independent CT system included the use of complex 3D sampling trajectories to improve reconstructed image quality with reduced cone beam distortion of the uncompressed and pendant breast. These complex trajectories could also be used to overcome the geometrical limitations imposed by the imaging components and the patient lying prone on a bed [110, 142]. Development of novel trajectories to avoid the geometric limitations of the patient and the bed will be studied more closely in Chapter 6 of this thesis. In developing the independent CT system, simulations indicated that the dose efficiency of imaging the uncompressed breast could be optimized by using a quasi-monochromatic beam using thick Ce filtration; and such a beam filtration scheme was implemented in the system [80, 86]. Empirical measurement of the actual dose delivered by the quasi-monochromatic beam to the uncompressed breast will be the subject of Chapter 3 of this thesis. Lastly, an observer study that used Monte Carlo based dose calculations indicated that visualization of lesions less than 5 mm in diameter in a low-contrast cluttered background could be improved by using the 3D low-dose imaging capabilities of this breast CT system when compared with digital mammography [109].
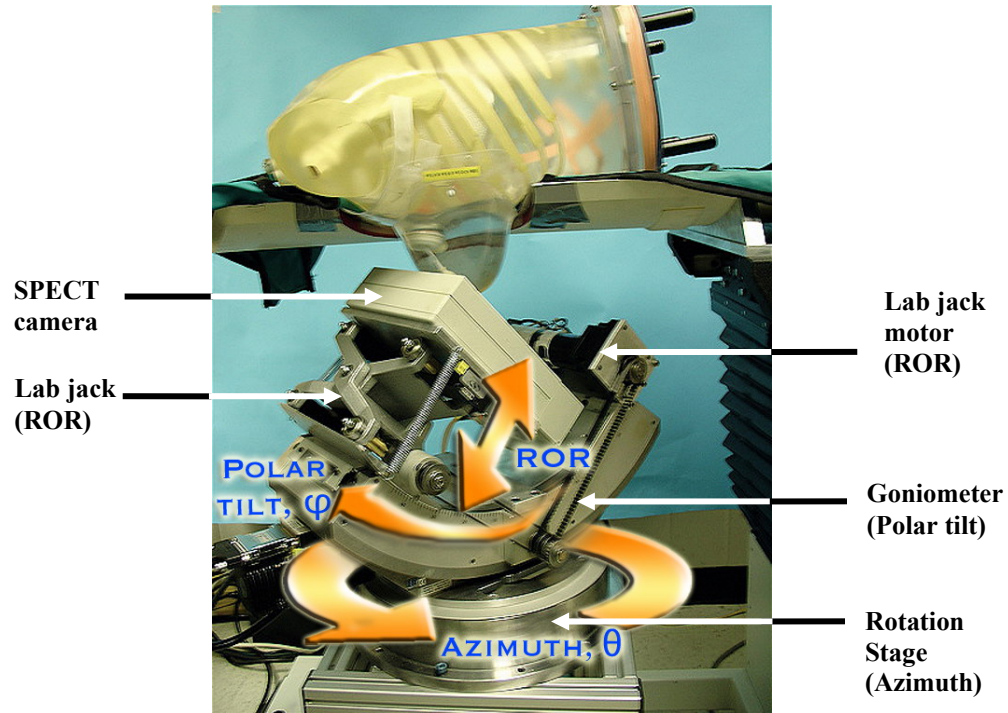
Figure 1.14: Photograph of the independent SPECT system seen closely contouring the combined anthropomorphic torso-breast phantom on an early prototype patient bed (see Chapter 5). The major components of the independent SPECT system are noted.

1.3.2. Independent SPECT system

The independent SPECT system [148] (Figure 1.14) uses a compact 16x20 cm^2 field of view Cadmium-Zinc-Telluride (CZT) *LumaGEM* 3200S^{TM} gamma camera (*Gamma Medica, Inc.*, Northridge, CA) with a 64x80 pixel array of discretized crystals, each 2.3x2.3x6 mm^3 on a 2.5 mm pitch. The mean energy resolution of the gamma camera measured at 140 keV is 6.7% FWHM and the measured sensitivity with a collimator is 37.9 cps/MBq. A parallel hole collimator with hexagonal holes (1.2 mm flat-to-flat (inner diameter), 0.2 mm lead septa, and 25.4 mm height) was used throughout the studies described in this thesis [147]. The gamma camera is attached to a laboratory jack (model

M-EL120, *Newport Corp.*, Irvine, CA) and a goniometric cradle (model BGM200PE, *Newport Corp.*, Irvine, CA) that permits varying distances (0-10 cm) to the center of rotation (radius of rotation, ROR) and further permits tilting from 0° to 90° in the polar direction. The independent SPECT system was attached to a rotation stage (model RV350CC, *Newport Corp.*, Irvine, CA) allowing a rotation of 360° around the vertical chest-nipple axis of the pendant, uncompressed breast. Currently, this system is controlled by software that semi-automatically synchronizes image acquisition and gantry motion in a fashion similar to that used in the CT system [146]. Custom-built software implemented during the initial phase of development enables the user to define a subset of camera orbits based upon the selection of polar and ROR parameters at pre-defined azimuthal or rotation set points. The system uses an iterative OSEM algorithm that is a modified and accelerated version of the maximum likelihood expectation maximization (ML-EL) algorithm. The algorithm enabled the modeling of complex 3D imaging orbits through the incorporation of 3 Euler angles into the reconstruction set up, and also enabled other aspects of the system to be modeled including attenuation and scatter components [146-147].

Accomplishments in the initial phase of the SPECT system design included developing the 3D positioning capability of the gantry to position the camera anywhere in a 2pi steridian hemisphere around a pendant, uncompressed breast. Simple and more complex 3D orbits were investigated that allowed imaging of breasts of various shapes and sizes and also demonstrated imaging deep into the chest wall and the axilla region of anthropomorphic breast phantoms [100, 148]. The ability to visualize lesions less than 1

cm in size at clinical count rates was also demonstrated, although no observer studies were performed in the initial phase of development. The flexibility of the developed positioning system further demonstrated the ability of the system to image breasts of all shapes and sizes underneath a patient bed [99]. This positioning flexibility was maintained in the research work completed in this thesis.

1.4. Organization of the Thesis

This rest of this thesis document is roughly divided into 2 sections: the first section (Chapters 2 & 3) deals with characterizing the independent CT system, and the second section (Chapters 4-6) investigates issues related to the development and enhancement of the integrated SPECT-CT imaging system. Specifically, Chapter 2 characterizes the implemented filtered x-ray beam. The dose delivered to the breast during a tomographic scan is empirically measured in Chapter 3. Chapter 4 investigates signal crosstalk between the SPECT and CT systems with a view to integrating the independent imaging systems into a single hybrid design on a single mechanical gantry. The design and performance of a new bed for volunteer patient imaging studies using the integrated dual-modality SPECT-CT breast imaging is described in detail in Chapter 5. Chapter 6 describes novel x-ray source-detector trajectories to facilitate imaging closer to the chest wall, with concluding remarks and future work described in Chapter 7.

Chapter 2

2. Heavily Filtered Beams for Uncompressed Breast Imaging

Prior simulation studies performed in the MMI Lab modeled the imaging of an uncompressed 15cm breast composed of 50-50% adipose-glandular with a 5mm embedded lesion using a monochromatic x-ray beam and a CsI-based detector with a W target anode tube [80]. The results of these studies indicated that the dose efficiency (SNR^2/dose) for uncompressed breast imaging is optimized when using an x-ray beam with a mean energy between 30-40 keV [80].

In contrast to conventional x-ray systems that use extrinsic filters in the 1-3 half-value layer range, the thickness of Cerium (Ce, Z=58, ρ=6.89 g/cm^3) that simulations found shaped the x-ray beam to maximize dose efficiency for breast CT imaging was in the hundreds of value layers [80]. Cerium belongs to the lanthanide group and readily oxidizes when exposed to air, making its handling a potential concern for everyday use in the laboratory. However, the metal possesses an attractive 40.4 keV K-edge absorption energy (shown in Figure 1.6 and repeated in Figure 2.6) that was shown in simulations to generate a filtered x-ray beam with a mean beam energy in the optimum range for uncompressed breast CT imaging over a wide range of tube potentials and breast sizes [80].

There are then several purposes to the experiments described in this chapter: to demonstrate the practicability of implementing the heavy K-edge filtration scheme in our

system; to validate results of the earlier simulation study; to compare measured spectra for several different filter materials, some common and other more novel materials for x-ray imaging; to compare measured and simulated results for the novel ultra-thick K-edge filtration scheme; and, to experimentally quantify important beam metrics for breast imaging using our implemented beam filtration method. Partial results of this work were presented in an oral presentation at the 2006 *SPIE Medical Imaging Conference* in San Diego, California, and published therein, and more complete results were also published in the journal *Physics in Medicine and Biology* [152].

Each breast tissue type possesses a unique x-ray attenuation coefficient that varies continuously with energy. These tissues may in principle therefore be finely differentiated using monochromatic x-ray beams at different energies [153-154]. The value of a monochromatic x-ray beam for 3D breast imaging lies in its anticipated ability to enable improved discrimination between low-contrast tissues (1-2% difference) such as cancerous lesions embedded in surrounding normal breast tissue [108]. Separation of such small intrinsic contrast differences with the spectrally narrow beam may also enable the possibility for absolute tissue attenuation coefficient quantification, hence *in vivo* tissue characterization. Patients, for whom 2D x-ray mammography has proven to be inconclusive, such as those with large and radiographically dense breasts, may thus receive earlier and improved detection of tumors that might otherwise progress untreated. This characteristic of a monochromatic beam is in addition to its ability to reduce the absolute dose delivered to the patient, helping to maximize dose efficiency.

Other methods of producing quasi-monochromatic x-ray beams exist, for example using synchrotron light sources or Bragg diffraction [155-160]. Synchrotron light sources have so far proven to be too expensive and impractical for routine clinical medical imaging applications, although there are ongoing efforts to make synchrotron research clinically viable for routine medical imaging [161]. Devices implementing Bragg diffraction techniques produce a fan beam of x-rays that introduce other complexities in the design of a breast CT system including the necessity to move the object relative to the beam. This can increase patient scan times and the likelihood of image artifacts due to combined mechanical and patient motion.

2.1. Pre-Breast Spectra

2.1.1. Spectrum Analyzer

In this study, the spectrum of the x-ray cone beam was measured using a high performance x-ray and γ-ray spectrum analyzer (Amptek Inc., model *XR-100T-CdTe*, Bedford, MA) with a 3x3x1 mm^3 cadmium telluride (CdTe) detector mounted on a peltier cooler, and possessing high detection efficiencies at close to 100% for beam energies between 15-70 keV (see Figure 2.1). The analyzer was placed on a tripod base on the lab floor approximately 15' from the x-ray focal spot in order to reduce the flux incident on the detector face of the spectrum analyzer and to avoid saturating the detector electronics (see Figure 2.2). The 15'separation between focal spot and detector face had the effect of minimizing the detection of scattered x-rays, although it increased the attenuation of the beam through the intervening air mass. Using figures derived from NIST tables, it was

estimated that there was an approximate 20% attenuation of the beam in this air gap [154] (at an assumed beam energy of 35 keV, μ/ρ_{air} = 3.02x10^{-1} cm^2/g and ρ_{air} = 1.21x10^{-3} g/cm^3).
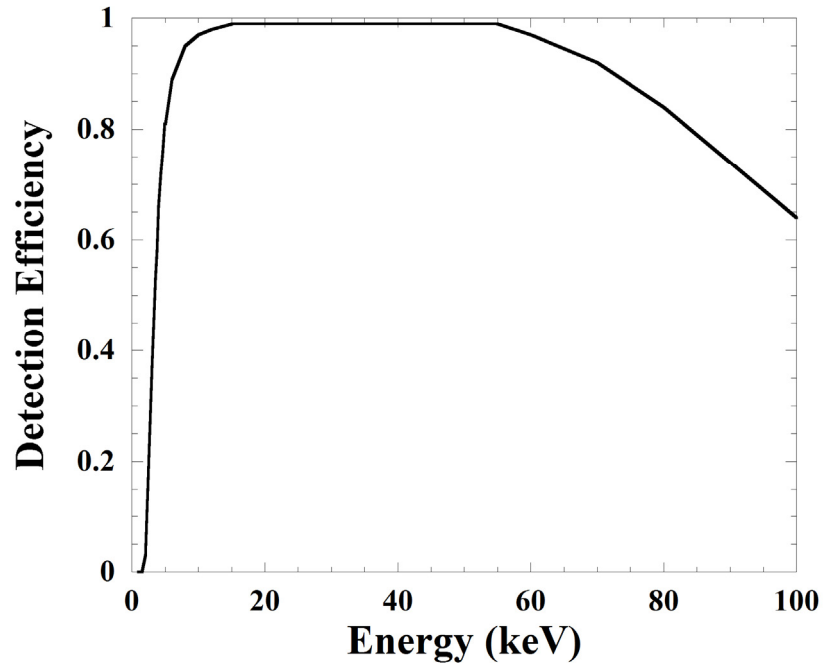
Figure 2.1: Detection efficiency of the CdTe spectrometer used in the experiments showing close to 100% efficiency in the 15-55 keV energy range. (Adapted from Amptek's website: www.amptek.com))

2.1.2. X-ray spectra simulation

X-ray spectra were simulated using *xSpect*, an x-ray system simulation code developed at Henry Ford Health Systems (Detroit, MI) and based on a semi-empirical x-ray generation model [162-163]. While there are several outputs from an *xSpect* simulation, the transmitted x-ray beam energy spectra and accompanying x-ray exposures were the most

pertinent *xSpect* outputs for this particular study. The simulation model is described in detail elsewhere [123], and the software has recently been updated to a newer version [164].

Briefly, the simulation program models the output of x-ray tube targets under various operating parameters such as tube potential, anode material and anode angle. The precise thicknesses and physical composition of absorbing materials can be modeled and added to the path of the simulated beam to model both intrinsic and extrinsic filtration for the x-ray beam. In addition, adipose and glandular breast tissue can also be modeled to simulate breasts of varying thicknesses composed of different proportions of glandular-adipose tissue in the beam path. The properties of detector materials, e.g. the efficiency of the detector material, can furthermore be modeled to complete a comprehensive simulation of the x-ray imaging system.

Studies with an exposure meter (RadCal Corp, *model 1515*, Monrovia, CA) initially measured the exposure at the CT system's isocenter. Scatter-free spectra were then simulated using a modeled tungsten anode target having nominal intrinsic filtration, the thickness of which was adjusted to match the exposure at isocenter measured using the exposure meter. Spectra were generated with and without filter materials in the beam path to mimic the x-ray tube output at the 55 cm SID of the independent x-ray system. For each of the seven filtration materials modeled in the experiment and detailed in Table 2.1, the thickness of the modeled filter material was modified until the simulated unfiltered tube exposure at 60 kVp was reduced by a factor of 200 and then 500. These

particular filter thicknesses are termed the 200th and 500th value attenuating layers (VL) of the filter material. The output spectrum for each of the seven materials at the 200th and 500th VL was generated using tube potentials from 40-100 kVp in 20 kV increments. These operating voltages span a range that includes the low voltage more typical of current x-ray mammography (25-33 kVp for Mo/Mo and Mo/Rh and less than 35 kVp for W/Mo) , to a higher tube voltage that could provide higher mean beam energies and higher overall x-ray flux to image breasts with thicker diameter. The simulated spectrum output was generated on a per-mAs/cm^2 basis in 1 keV energy bins at the independent system SID.

Table 2.1 Filter materials and actual thicknesses used to acquire pre-breast spectra.

Element	Z	Purity (%)	Density (g/cm^3)	K-edge Energy (keV)	200th VL (mm)	Actual Atten. VL @ 60 kVp	500th VL (mm)	Actual Atten. VL @ 60 kVp
Aluminum[a]	13	97.9	2.70	1.56	23.96	192	30.62	454
Copper[b]	29	99.9	8.92	8.98	1.02	227	1.30	447
Silver[b]	47	99.9	10.49	25.51	0.30	134	0.40	437
Cerium[c]	58	99.9	6.89	40.44	0.71	196	0.91	536
Neodynium[c]	60	99.9	6.80	43.57	0.70	185	0.93	515
Europium[c]	63	99.9	5.24	48.52	1.00	222	1.25	476
Tungsten[b]	74	99.95	19.25	69.53	0.20	200	0.25	384

a. 6061 Aluminum
b. *Alfa Aesar*, Ward Hill, MA.
c. *Santoku America Inc.,* Tolleson, AZ.

2.1.3. Pre-Breast Spectra Measurement

Pre-breast spectra were empirically measured using the materials detailed in Table 2.1 according to the setup in Figure 2.2, without the breast slabs along the beam path.
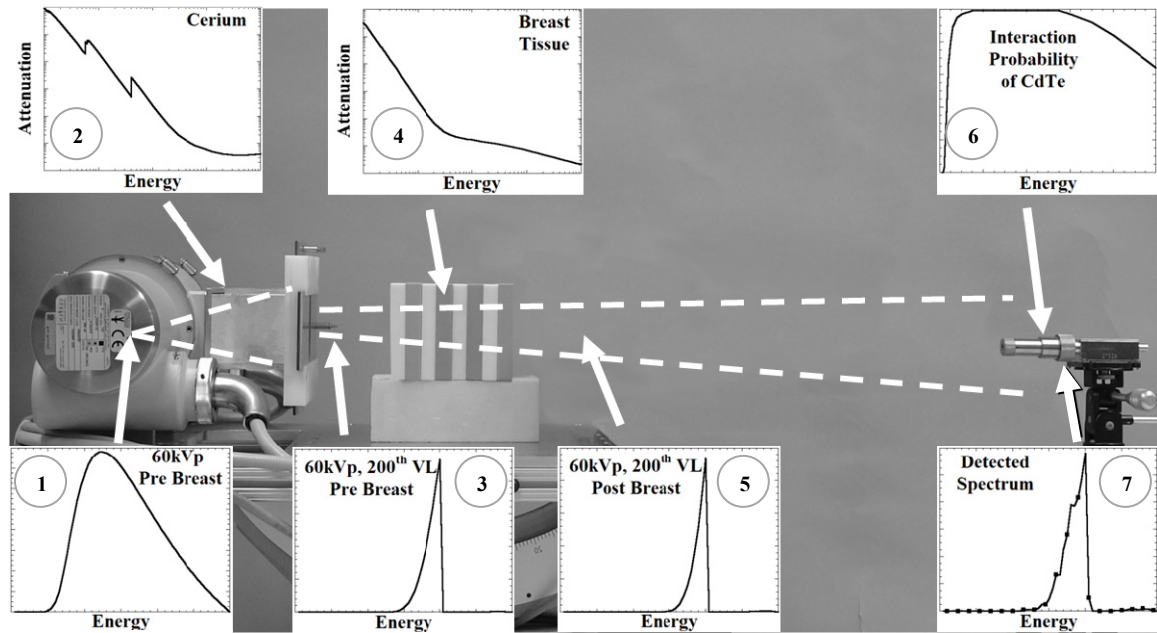
Figure 2.2: Experimental setup showing the x-ray source and collimated cone beam passing through slabs of breast equivalent tissue (resting on styrofoam) towards the spectrum analyzer. The various absorption, emission, and transmission spectra and system parameters encountered at different points in the experimental workflow are noted. The distance from the focal spot (at left) to the detector (at far right) was 15 feet. The photograph is for illustration purposes and the horizontal distances are not shown to scale.

The illustrations accompanying Figure 2.2 graphically explain the experimental method. The intrinsically filtered cone beam that exits the Tungsten-anode x-ray tube, figure #1, was further filtered by the various extrinsic filter materials (the discontinuous attenuation coefficient curve of cerium is illustrated in figure #2) to produce the heavily filtered beams (figure #3 illustrates the case of a cerium-filtered beam at a 200th VL thickness and

60 kVp). The resultant filtered beam takes on a narrow, quasi-monochromatic characteristic. The x-ray tube collimator jaws were closed substantially to reduce the output x-ray beam flux, as indicated by the dashed lines that trace out the bounds of the cone beam. No breast equivalent material is present in the beam path in the measurement of pre-breast spectra, although the slabs were replaced for the post-breast spectra, described in more detail later in this chapter. The detection efficiency of the CdTe spectrum analyzer and a sample of an experimentally detected spectrum are illustrated in figures #6 and 7, respectively.
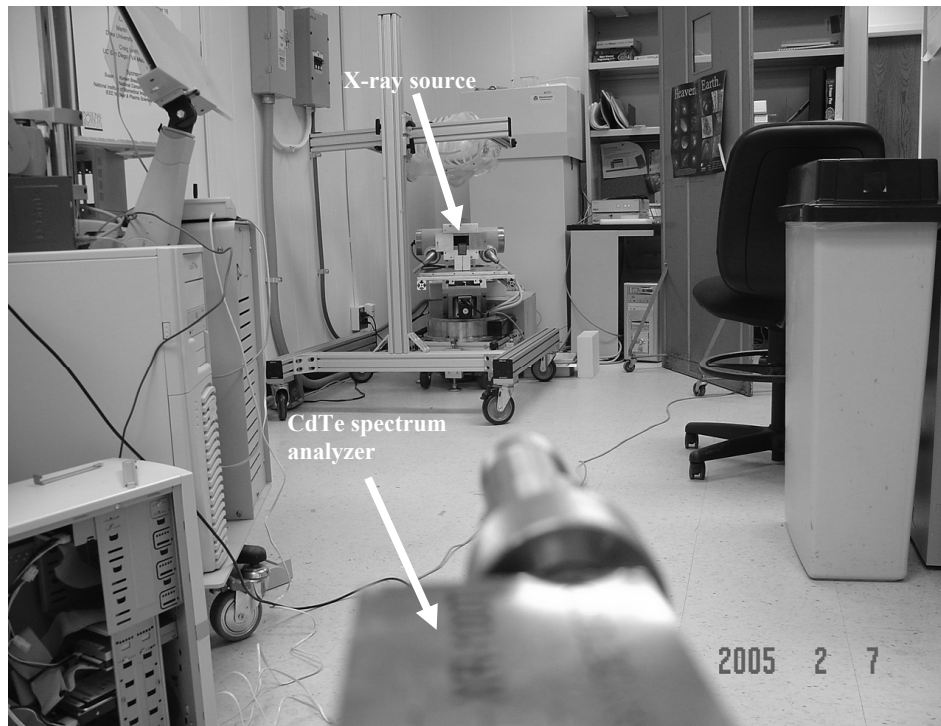
Figure 2.3: Photograph of the CdTe spectrometer pointed in the direction of the x-ray source, with the 15 feet separation more obvious in this photograph.

Aligning the CdTe detector face to the x-ray tube anode and focal spot was accomplished visually using a narrow beam laser inserted into the detector collimator housing. The direction of the laser was adjusted until the laser shone directly onto the anode (see Figure 2.3 for a line of sight view from the spectrum analyzer towards the anode of the x-ray tube). To further limit the possibilities of detector saturation during the counting procedure, 2 mm thick tungsten disks with apertures of varying diameters (25-2000 μm, cut by laser) were placed in front of the beryllium window of the spectrum analyzer. This was in addition to a 4cm long brass collimator inserted into the shaft of the spectrum analyzer that collimated the incident x-ray beam.

Four separate x-ray tube operating voltages, 40 to 100 kVp in 20 kV increments, were tested in these pre-breast spectral measurements, similar to the voltages used in the *xSpect* simulations. To standardize output flux, a constant x-ray source exposure of 0.4mAs was used for these pre-breast spectral studies. At each voltage setting and for each filter material and thickness, the x-ray source was exposed multiple times until approximately 100 detected events were present in the peak of the spectrum detected by the analyzer. The combination of the low mAs, the heavily filtered x-ray beams, the 15' separation distance, and the x-ray tube and CdTe collimators limited the observed count rate to well the reported maximum detection rate of the CdTe detector (20 kcps). In fact, observed count rates were normally kept below 2 kcps.

A schematic of the electronic setup from the spectrum analyzer to the PC is shown in Figure 2.4. The uncalibrated output of the spectrum analyzer is a histogram of detected

events versus a number of data bins, a number that varies depending on the number of

bits selected in the analog to digital converter of the multi channel analyzer and the gain

of the amplifier that powers the detector. An ^{125}I source with observable 27, 31 and 35.5

keV peaks was used to calibrate the observed x-ray system spectrum versus photon

energy. This calibration spectrum is shown in Figure 2.5.
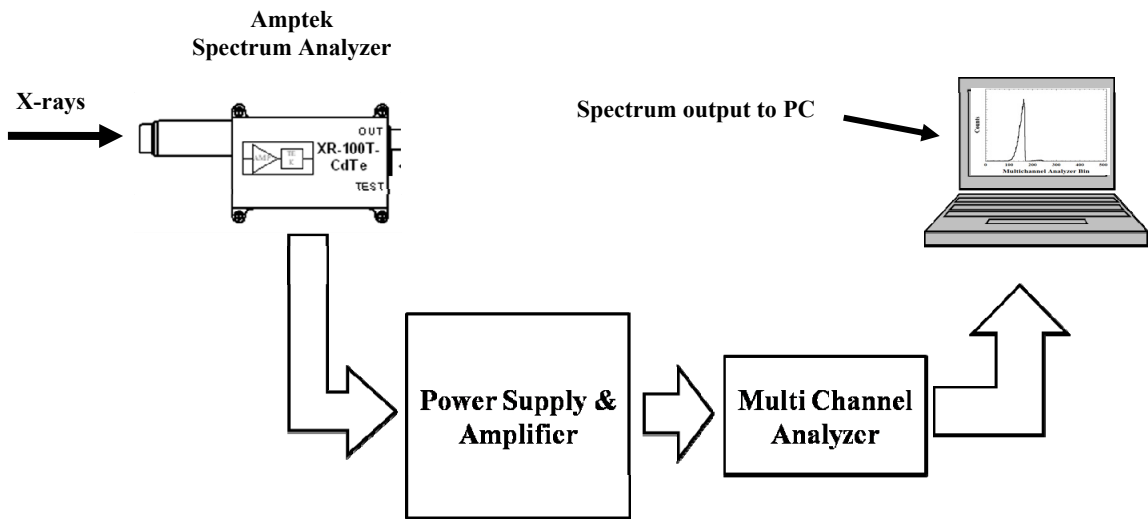
Figure 2.4: Block level schematic of the data acquisition process from incident x-rays to output spectral data.

The characteristic mass attenuation curves of each of the 7 filter materials are compared

in Figure 2.6. Aluminum and copper are filter materials commonly used for beam

filtration in commercial x-ray systems, and have relatively low K-edges compared to the

other tested filter materials. Silver acted as a surrogate material for molybdenum (Mo)

and rhodium (Rh), two commonly used filter materials in x-ray mammography, since

Silver has a K-edge absorption energy that is near to that of Mo and Rh. Cerium has a K-edge at an energy that was previously shown in simulation to be advantageous for dedicated breast CT [75, 80]. Two more rare earth metals, europium and neodymium, possess K-edge absorption energies that are close to cerium and were included as practical alternatives to cerium for different breast imaging tasks, e.g. thicker breasts, different glandular breast tissue fraction. Tungsten, another common filter material, with a K-edge much higher than that of cerium, was also included for the purposes of comparison, similar to aluminum and copper. Aluminum and copper provided a lower bound on k-edge absorption energies while tungsten provided the higher bound.
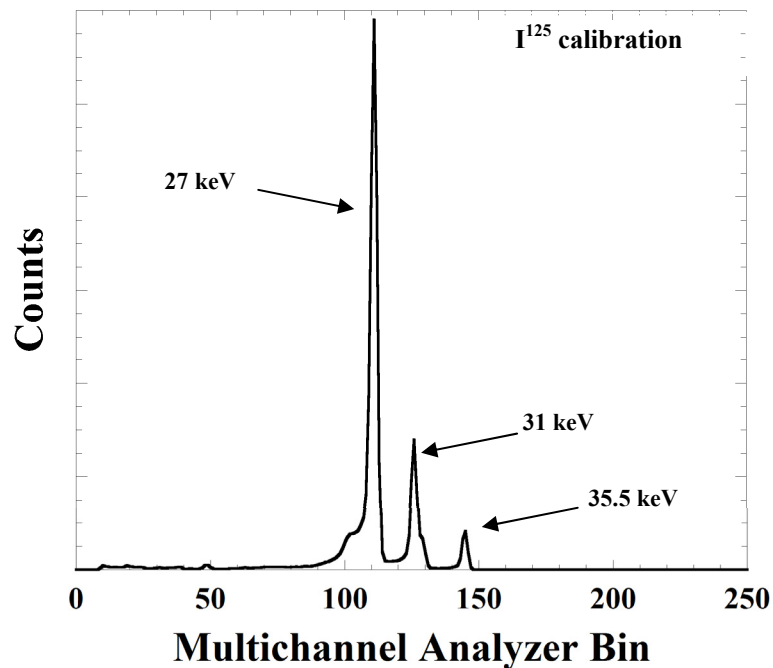
Figure 2.5: Raw measured Iodine-125 calibration spectrum showing recognizable 27, 31 and 35.5 keV peaks.

.
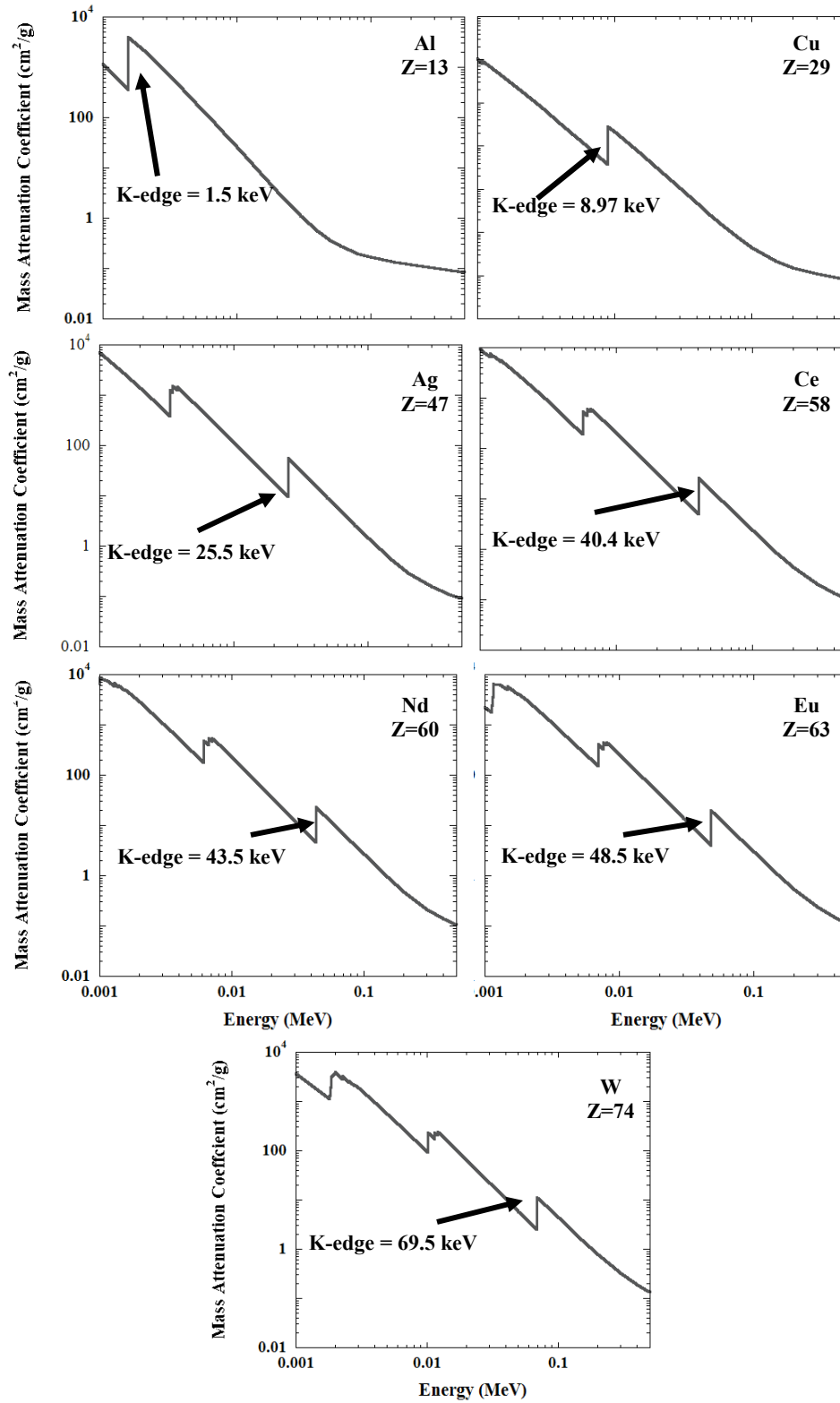
Figure 2.6: Plots of the mass attenuation coefficient of each of the filter materials used in the pre-breast experiments. Note how the K-absorption edge energy increases for increasing Z of the absorbing material.

65

The individual filter thicknesses empirically tested in this section of the study correspond approximately to the 200th and 500th attenuation value layer (VL) of each filter material. These attenuating value layer thicknesses are energy dependent, and the specific thicknesses were determined using *xSpect* with an operating tube voltage of 60 kVp. This tube voltage was chosen since it lies in a relatively smooth region of the attenuation coefficient curves of all of the above materials, away from any K-edge discontinuities that might otherwise bias the resultant material thicknesses. 60 kVp was also one of the proposed operating tube voltages for the breast CT system. Practical limitations in obtaining exact metal thicknesses meant that the values in Table 2.1 approximated the stated attenuation value layer at 60 kVp.

Actual attenuation values for these filter materials are also indicated in the table and are calculated based on simulation outputs. The particular implemented filter value layers were chosen by considering tube heating effects, where a 500th VL represents the upper limit of filter material thickness for this system under expected clinical operating conditions for full breast tomography using >200 sequential exposures per breast [123]. A 200th VL filter, or thinner, then represented one of the possible filter thickness for practical daily clinical use, although a 100th VL filter is now used in practice [165].

Comparisons between different filter materials were made possible by normalizing the x-ray exposure, the cumulative number of exposures and the aperture diameter in front of the spectrum analyzer.

2.1.4. Metrics used for spectral data analysis

Common figures of merit (FOMs) for both pre- and post-breast spectra are mean beam energy and full width at tenth-maximum (FWTM), similar to metrics used previously [80]. Mean beam energy, $\bar{E}$, is calculated using the first moment, or weighted mean of the spectral distribution of the x-ray beam, i.e.

$$\bar{E} = \frac{\sum_0^{E_{max}} I(E)*E}{\sum_0^{E_{max}} I(E)} \tag{2.1}$$

where I(E) is the beam intensity at energy, E, with a maximum x-ray energy of E_{max}.

The FWTM is used to indicate the degree of monochromaticity of the x-ray beam incident on the breast. Full width at half maximum (FWHM) is the traditional metric for spectral resolution, but this metric may neglect the presence of other features (e.g. a low intensity, yet broad energy distribution) that may otherwise bias the spectrum. For example, while a traditional mammography spectrum may have sharp (i.e. narrow FWHM) characteristic x-rays, the integral intensity of these characteristic x-rays is usually lower than the integral intensity of any broader underlying *bremsstrahlung* spectrum from the same tube. Thus, a higher overall degree of monochromaticity could be expected with a spectrum having a lower FWTM metric.

2.1.5. Pre-breast spectra results

Figures 2.7 – 2.14 show plots of simulated and measured spectra at a 200th VL filter thickness between 40-100 kVp for the unfiltered beam and all 7 filter materials described

in Table 2.1. To make the plots clearer, the simulated spectra have been normalized to the same maximum measured value within each filter material. The plots illustrate the wide range of possible beam spectra that can be generated when any of the tube operating parameters or the filter material is varied. Note the broad polychromatic spectra associated with the unfiltered beam and the beams filtered by low-Z materials such as Al and Cu (Figures 2.8, 2.9), especially as the peak tube voltage increases. Silver (Figure 2.10) possesses a narrow quasi-monochromatic spectrum at a 40 kVp tube potential. Its resultant low mean beam energy, concentrated around the 25.5 keV K-edge energy, makes it a suitable filter for standard x-ray mammography [166-167]. However, as the tube potential increases, the Ag spectrum becomes increasingly bimodal in appearance. The broad polychromatic spectra of Al and Cu can be contrasted with the pronounced quasi-monochromatic spectra of the lanthanide filters (cerium, europium and neodymium in Figures 2.11, 2.12 and 2.13, respectively) at tube potentials above the K-edge absorption energies of the respective metals. The mean energies of beams filtered using the lanthanide materials are concentrated around the K-edges of the respective filter materials. This quasi-monochromatic beam spectral shape and the resultant mean beam energies make these materials suitable filter candidates for breast CT [73, 80].

Both 200th and 500th VL filtered beams were investigated for each filter material. Thicker filters were previously shown to provide greater beam quasi-monochromaticity with an accompanying improvement in dose efficiency [123]. While acquiring spectra, however, and through other experiments, it was determined that tube heating concerns bias against routine use of the 500th VL filter for multiple breast CT acquisitions [123].
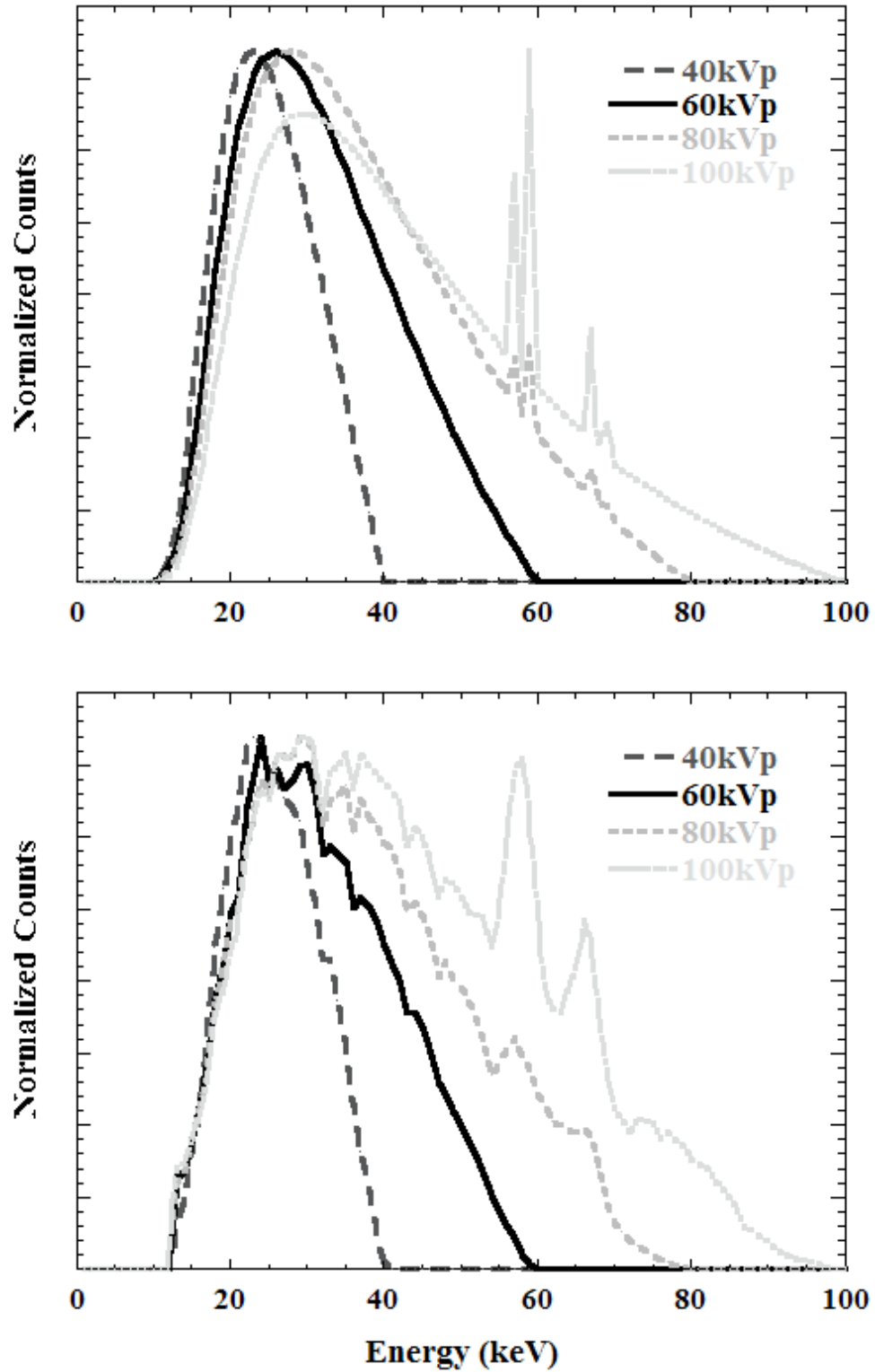
Figure 2.7: Superimposed plots of (top) the simulated and (bottom) measured unfiltered beam spectra from 40-100kVp, normalized to the peak values.
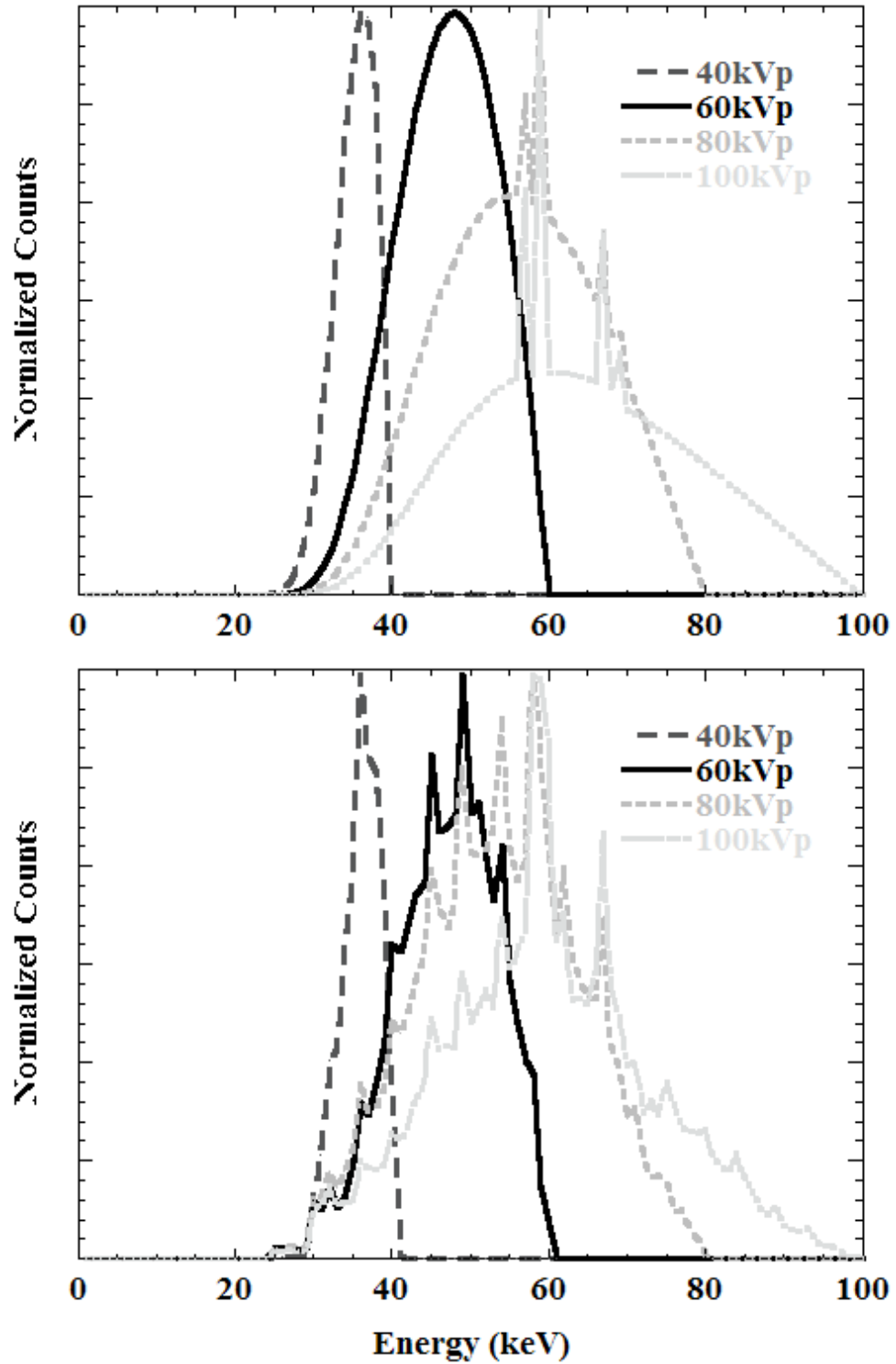
Figure 2.8: Superimposed plots of (top) the simulated and (bottom) measured 200th VL Al-filtered spectra from 40-100kVp, normalized to the peak values.
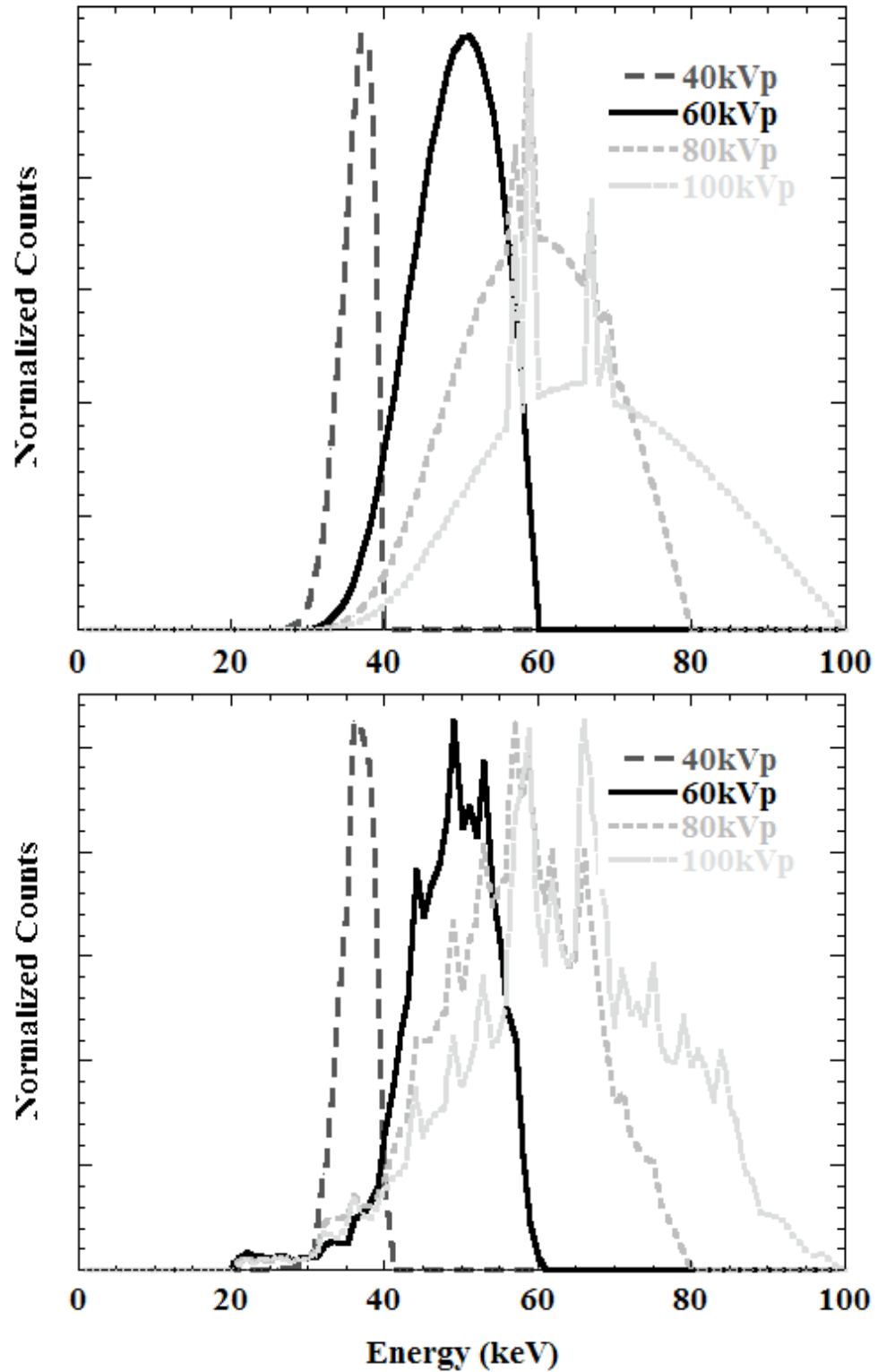
Figure 2.9: Superimposed plots of (top) the simulated and (bottom) measured 200th VL Cu-filtered beam spectra from 40-100kVp, normalized to the peak values.
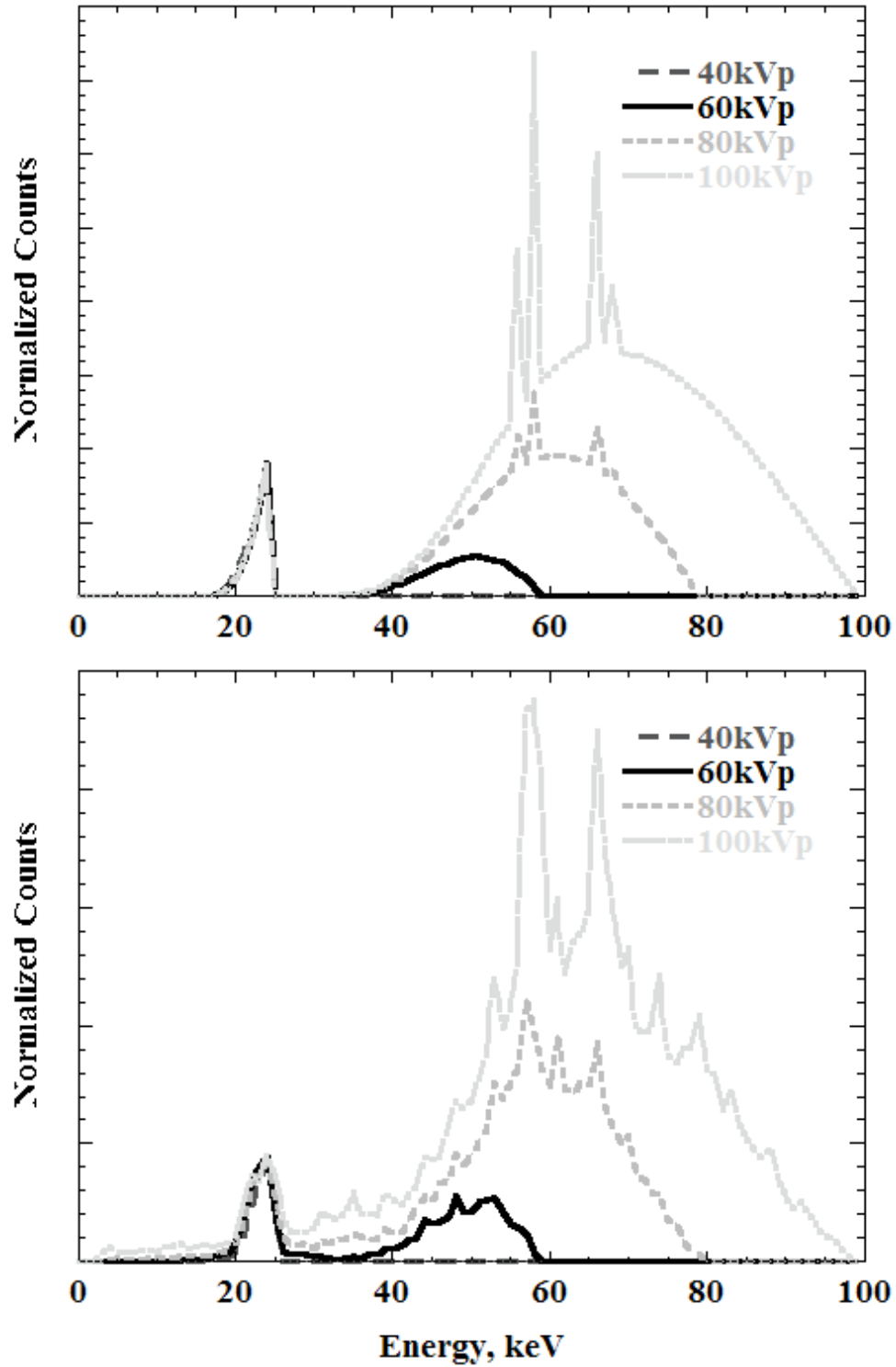
Figure 2.10: Superimposed plots of (top) the simulated and (bottom) measured 200th VL Ag-filtered beam spectra from 40-100kVp. Spectra are normalized to the height of the spectra before the K-edge of Ag (25.5 keV).
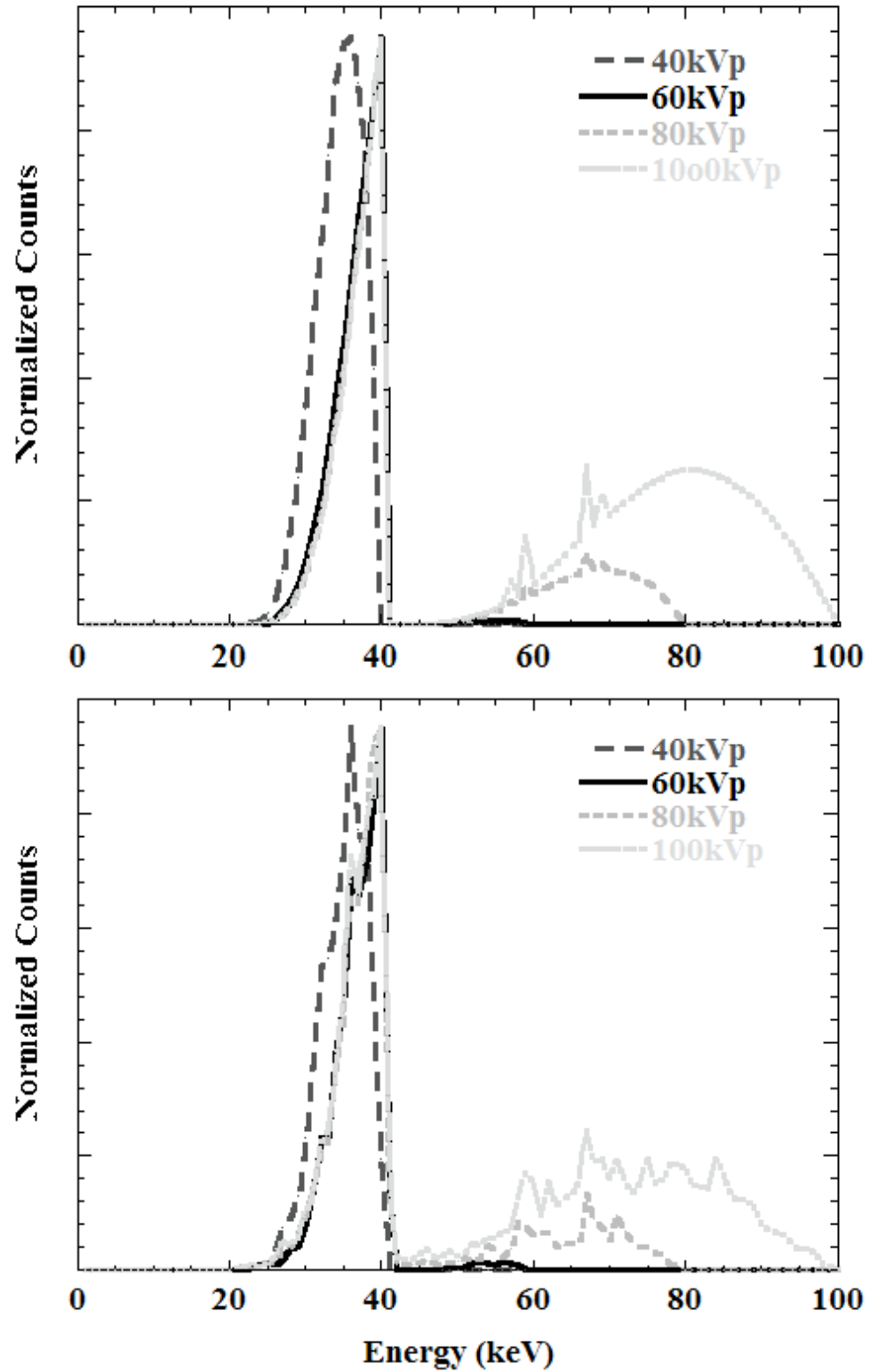
Figure 2.11: Superimposed plots of (top) the simulated and (bottom) measured 200th VL Ce-filtered beam spectra from 40-100kVp, normalized to the peak values.
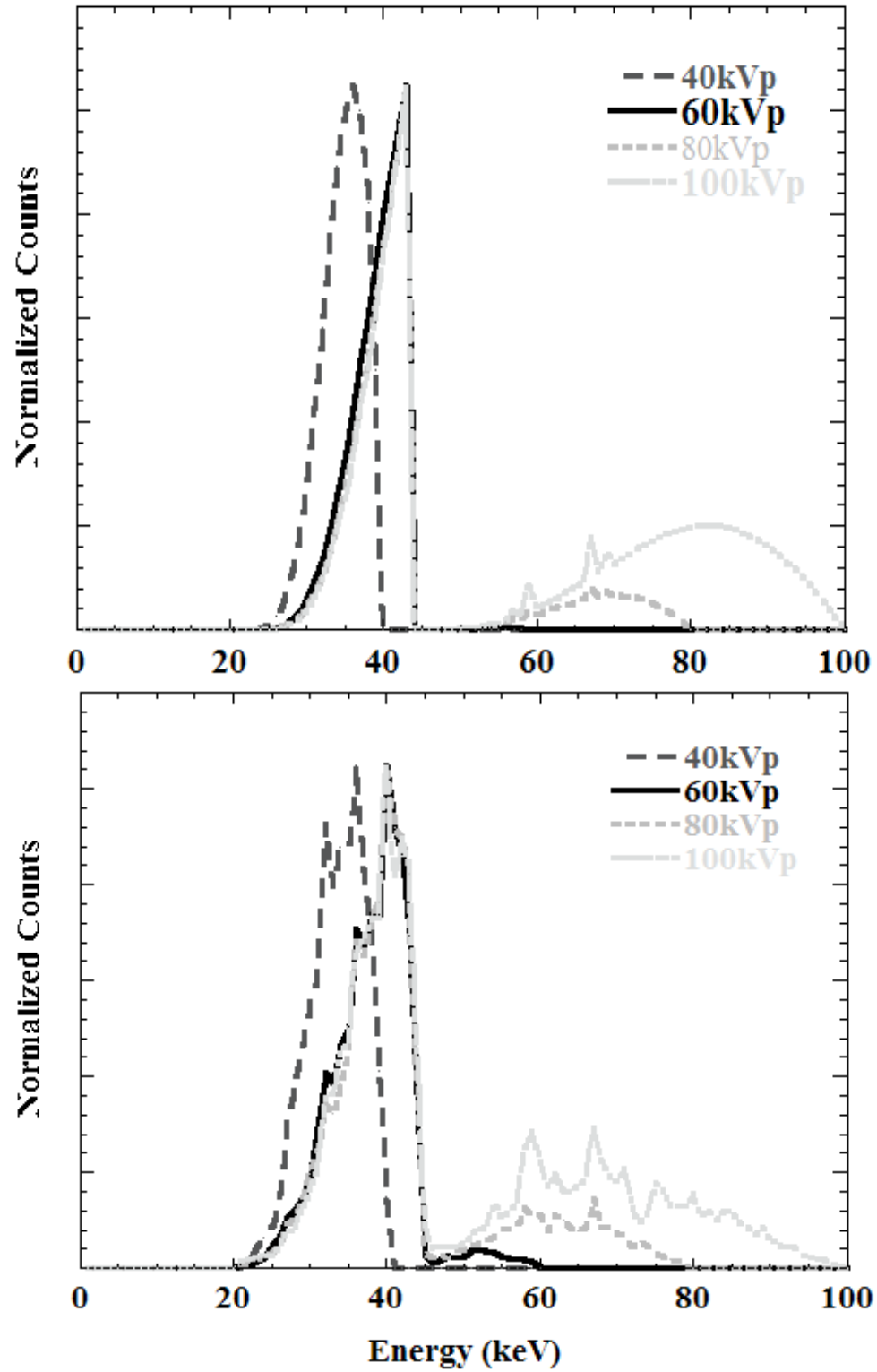
Figure 2.12: Superimposed plots of (top) the simulated and (bottom) measured 200th VL Nd-filtered beam spectra from 40-100kVp, normalized to the peak values.

74
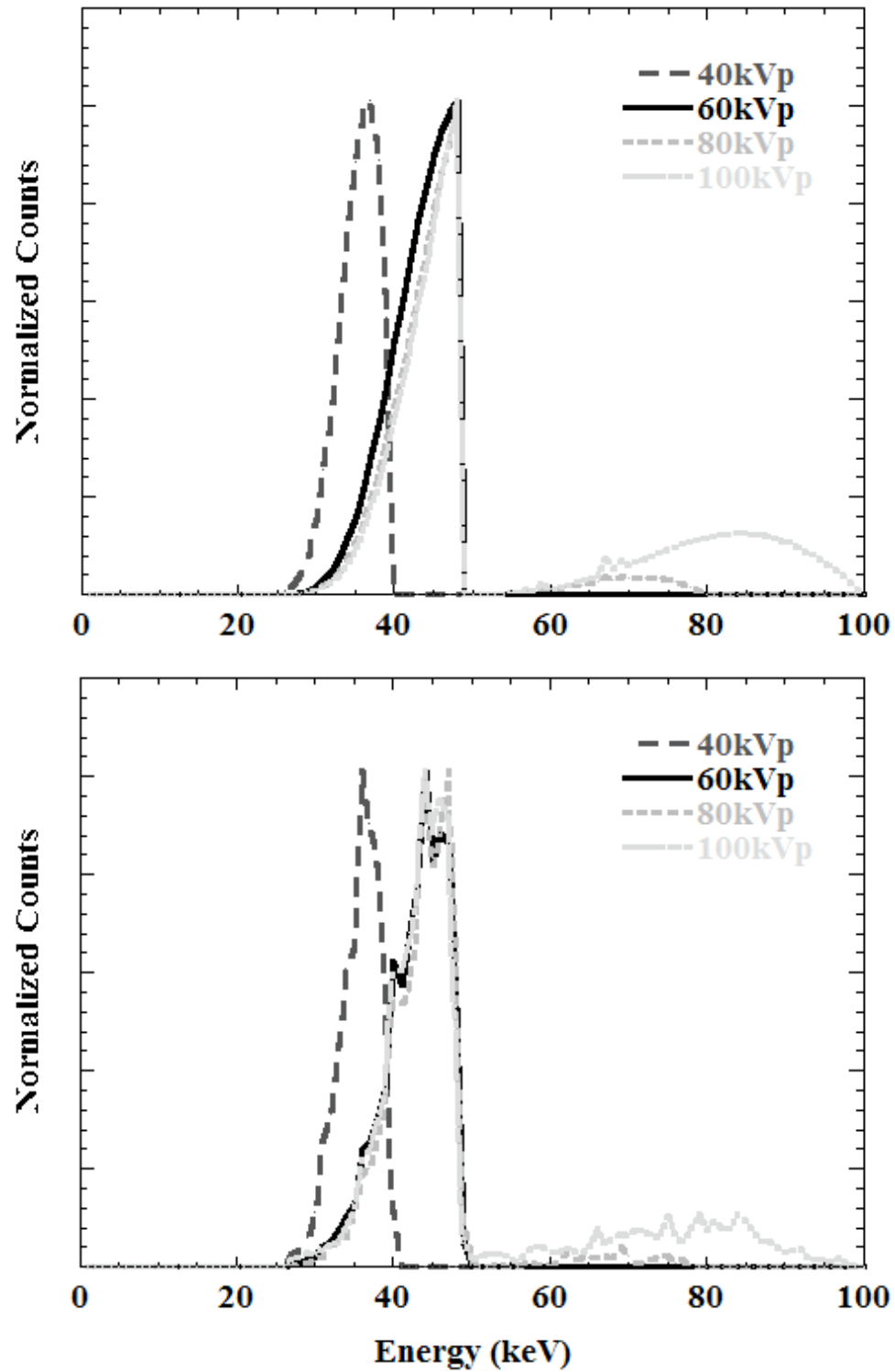
Figure 2.13: Superimposed plots of (top) the simulated and (bottom) measured 200th VL Eu-filtered beam spectra from 40-100kVp, normalized to the peak values.
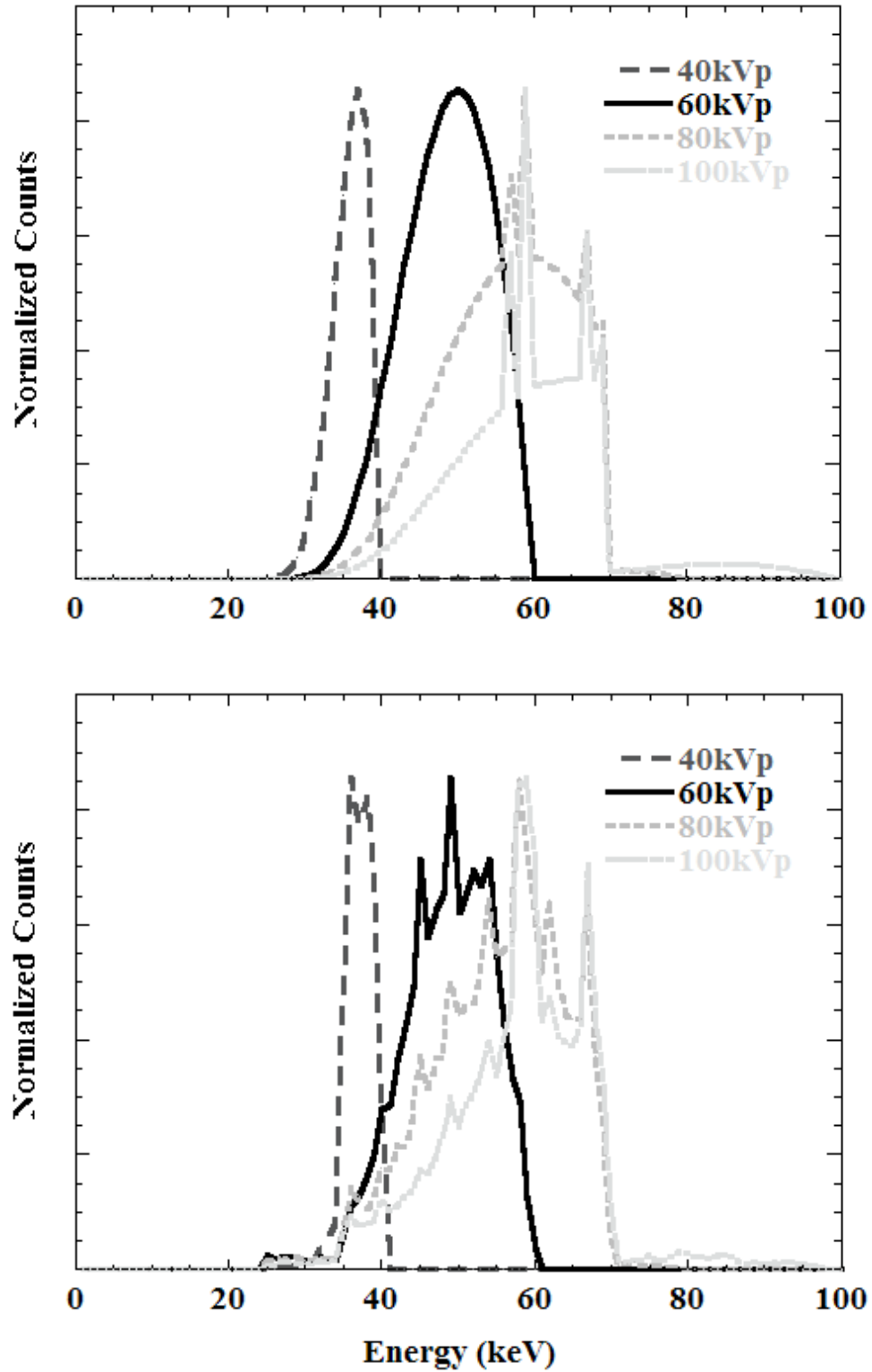
Figure 2.14: Superimposed plots of (top) the simulated and (bottom) measured 200th VL W-filtered beam spectra from 40-100kVp, normalized to the peak values.

Figure 2.15 is a comparison plot of pre-breast spectra acquired using all 7 filters in the study at a tube voltage of 60 kVp and a 200th VL (cf. Table 2.1) filter thickness. This plot more clearly illustrates the distinct differences in beam spectral shapes at a single tube voltage and filter thickness than the spectra shown across all tube voltages in Figures 2.7-2.14. A sharp cutoff is evident in detected photons at energies higher than the K-edges of the respective lanthanide filters, leading to more quasi-monochromatic spectra when compared to the filter materials with both lower and higher K-edge energies. The mean energies of the respective spectra, indicated by dashed lines superimposed on the spectra, illustrate the wide range of mean beam energies for uncompressed breast imaging that can be generated by using different beam filtration techniques.

A comparison of simulated and measured average pre-breast beam energy as a function of atomic number of the filter material is shown in Figure 2.16 for combinations of a 200th and 500th VL filtered beam at 60 and 80 kVp. At 60 kVp, the measured mean beam energy for the cerium filter with either a 200th or 500th VL is approximately 36.5 keV, which lies in the range of beam energies for optimum dose efficiency described earlier. The average beam energies of the other lanthanide metals, europium and neodynium, are situated close to that of cerium. Since optimum dose efficiency is affected by breast and lesion size [123] (more so than by breast composition), these other metals may also be appropriate for dedicated breast CT as alternatives to cerium, especially for larger breasted women where higher mean beam energies may aid with increased signal transmission through the thicker breasts.
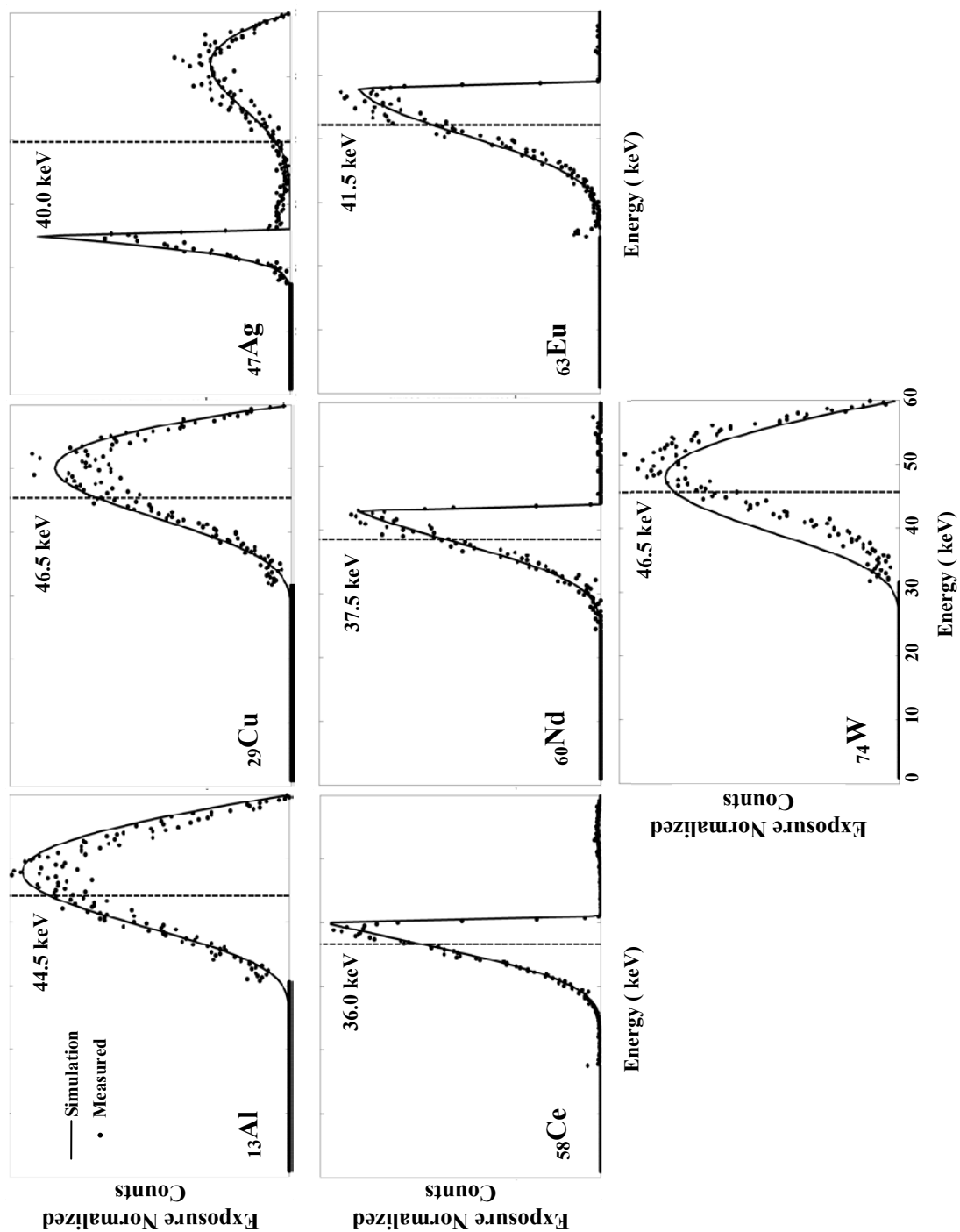
Figure 2.15: Exposure normalized pre-breast measured spectra for the 7 filters superimposed with simulated spectra. Spectra are acquired at 60 kVp and 200th VL. The weighted mean beam energy for each filter is illustrated with a vertical dashed line.

78
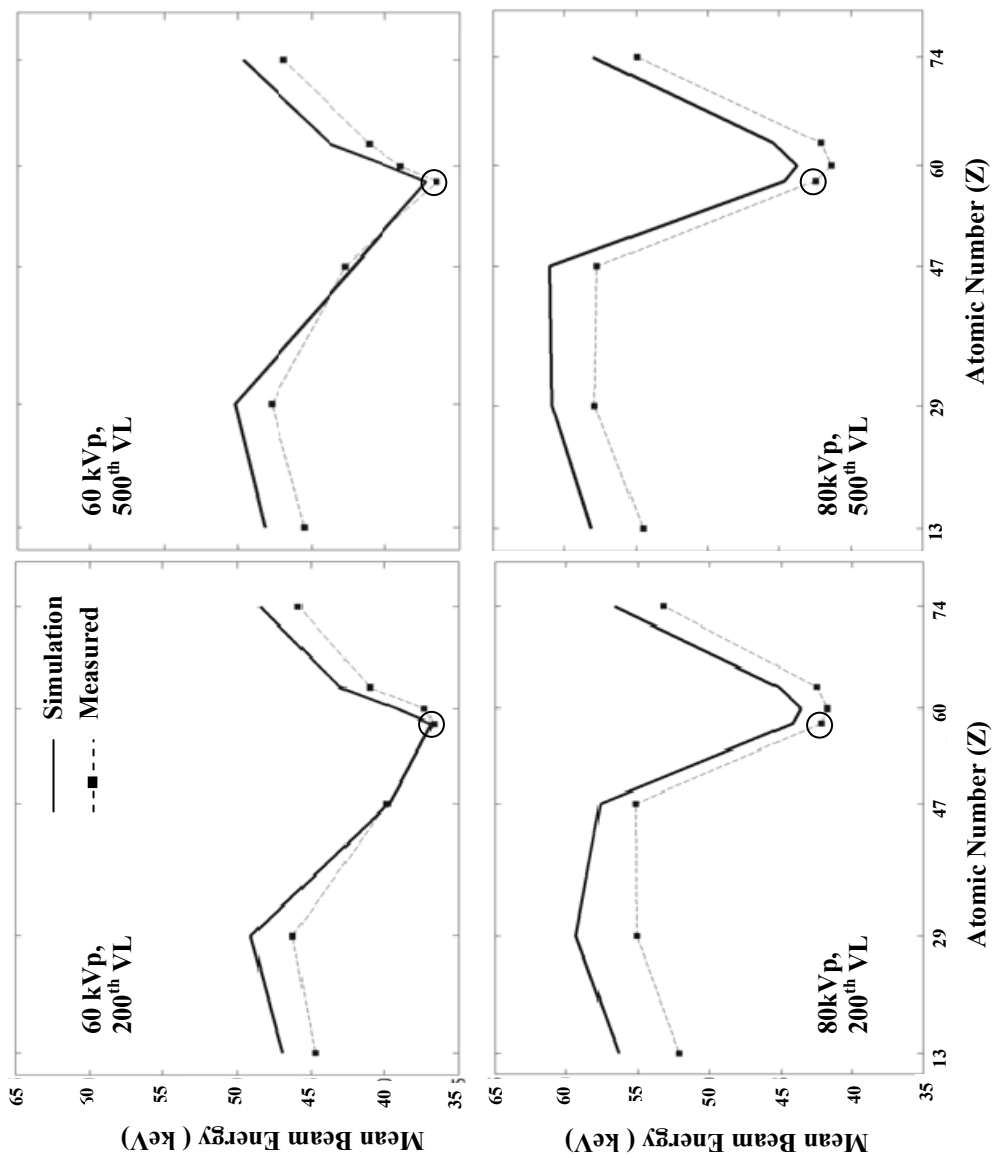
Figure 2.16: Simulated (solid lines) and measured (broken line with data points) weighted average beam energy for pre-breast filters at given atomic numbers for various listed conditions.

Another interesting feature is the ability of the lathanide metal filters to maintain average beam energies close to the optimal range for breast CT even when the tube potential is raised to 80 kVp (Figure 2.16). This maintenance of average beam energy is in contrast to the simple non-K-edge heavy filtration methods using other filter metals whose average energy shifts away from their lower kVp means when tube potential is increased. The ability to maintain optimal mean beam energies is another advantage for using K-edge filtration methods over simple heavy filtration using other materials, e.g. silver, since it allows for potentially using a higher tube potential for greater flux if the need arises when imaging thicker, denser breasts.
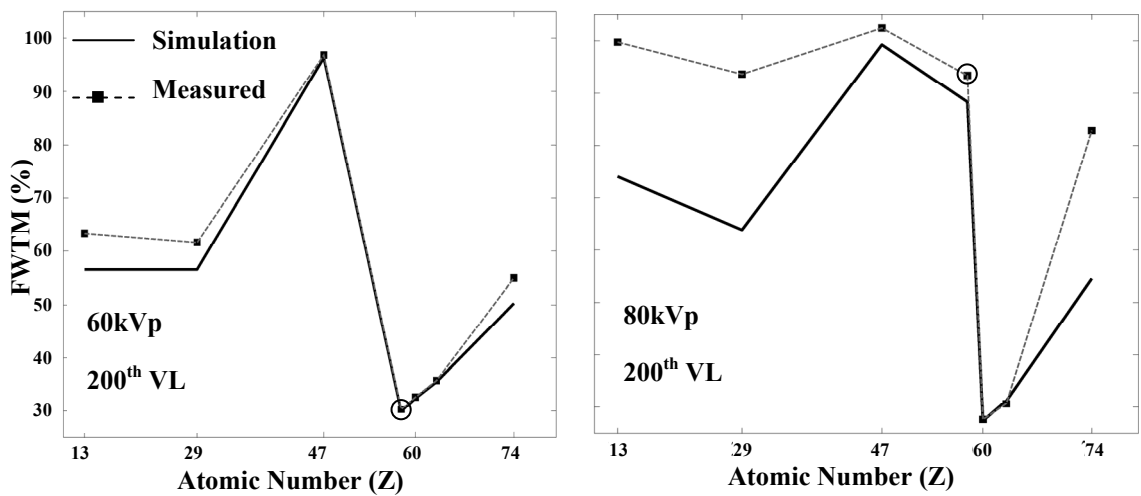
Figure 2.17: Measured and simulated FWTM values plotted as a function of atomic number of the filter materials. Cerium (circled), Z=58, exhibits the minimum FWTM of this set of metals at 60kVp but, due to the bimodal spectral shape seen in Figure2.11, has much greater spectral broadening at 80kVp.

As a measure of monochromaticity, a comparison of FWTM results for each of the measured and simulated pre-breast filter materials is plotted in Figure 2.17 for a 200[th]VL

attenuation layer and tube voltages of 60 and 80 kVp. Close agreement between measured and simulated data is observed for most filter materials. At 60 kVp, the highest degree of monochromaticity, i.e. lowest FWTM, is seen for the cerium filter where the effect of the K-edge is to essentially eliminate photons beyond approximately 40 keV. At the higher tube voltage of 80 kVp, the constraining effect of the cerium K-edge is reduced which allows some higher energy photons to break through, as seen in Figure 2.11, thus broadening the cerium spectrum. For higher tube voltages such as these, it may be that neodymium (Figure 2.12), possessing a slightly higher K-edge than cerium, is a better choice of filter material for larger breast diameters.

Focusing more specifically on the characteristics of the cerium-filtered beam, Figure 2.18 plots simulated and measured spectra for a 60 kVp unfiltered (0th VL) x-ray beam and with an equivalent 200th and 500th VL cerium-filtered beam. The plots illustrate the dramatic change in spectral quality when ultra-thick K-edge filtering is used. The most obvious visual characteristic, most clearly seen in the superimposed simulation curves, is the increasing monochromaticity of the filtered beam compared to the more polychromatic, unfiltered beam. The effect of the ultra thick filter is to eliminate lower energy photons, with the higher energy photons eliminated by the K-edge absorption. Consequently the mean filtered beam energy is concentrated around the K-edge of the filter material.

Figure 2.19 illustrates the simulated and experimental results of using a 200th VL Cerium filter on the raw x-ray beam at three tube operating voltages: 40, 60 and 80 kVp.

Agreement of experimental and simulated data is excellent. Comparing the filtered beams at 60 and 80 kVp, the excess high-energy photons at the higher operating voltage gives a bimodal quality to the spectrum that modestly degrades the monochromatic nature of the x-ray beam.

In conjunction with Figure 2.19, Figure 2.20 plots the response of the beam to the 200th VL Ce filter for varying peak tube voltages. The measured spectra have been normalized to the same number of x-ray exposures used to acquire each spectrum, mAs per exposure and spectrum analyzer collimator aperture. The plots then indicate the increase in beam flux possible when increased voltages are used. This may be advantageous when imaging larger-breasted women that need increased beam flux to improve the noise quality of projections. The increase in beam flux is readily apparent for the higher tube voltages, as is the evolution of the beam from quasi-monochromatic at 60 kVp to a more bimodal shaped spectrum when the tube voltage reaches and surpasses 80 kVp.

While for CT a higher voltage on an unfiltered beam may be preferable for minimizing dose to the patient, the resulting higher energy photons may reduce object contrast. In addition, while higher tube voltages increase overall photon flux, the mean beam energies of the filtered beams are also driven outside the optimum range for uncompressed tomographic breast imaging. Therefore, to preserve a narrow energy band, an operating tube voltage of 60 kVp is preferred for dedicated breast imaging.
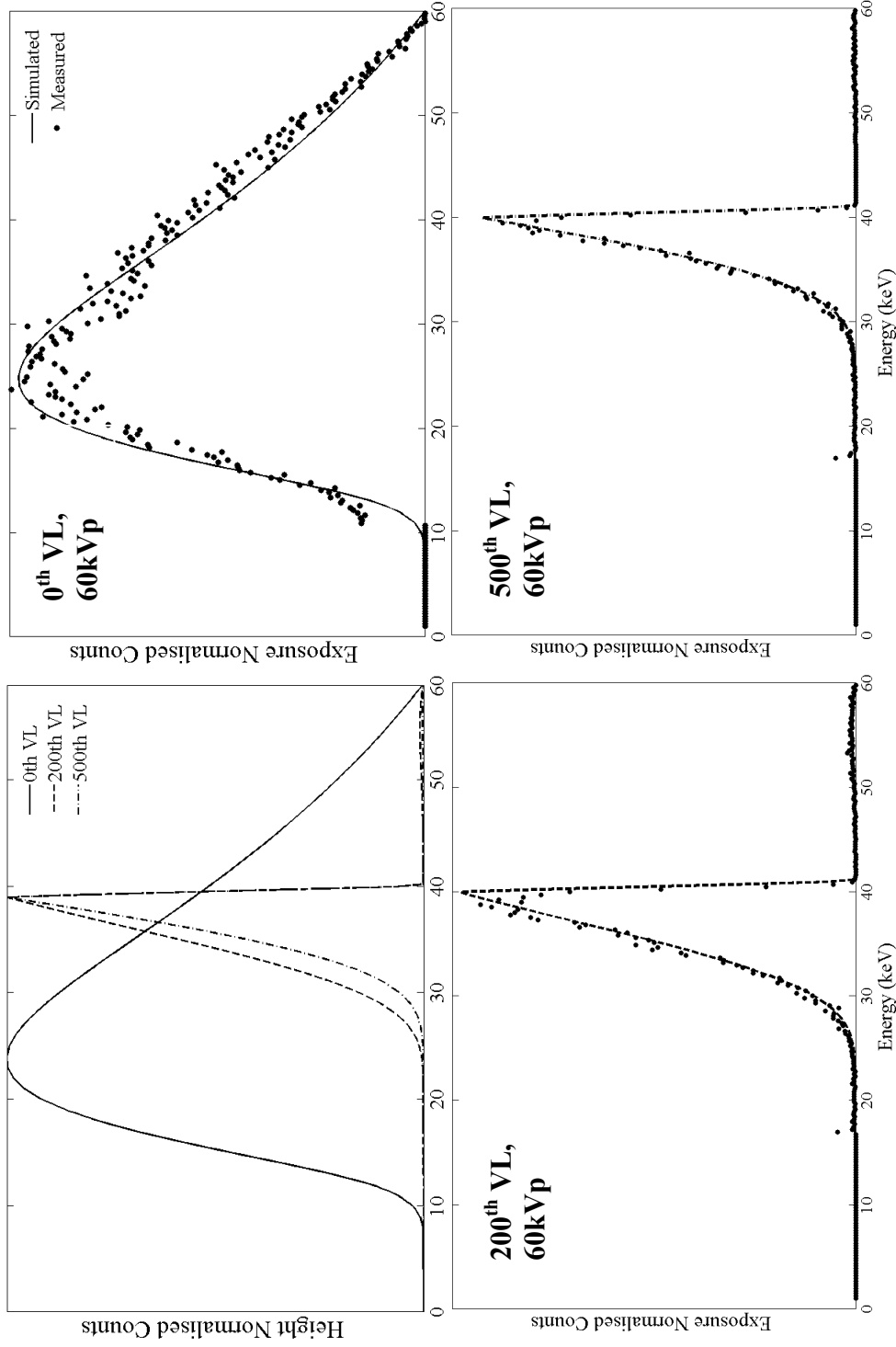
Figure 2.18: Plots of simulated and measured spectra at 60 kVp for 0th VL (unfiltered beam), 200th VL and 500th VL Ce-filtered spectra showing an increased monochromaticity appearance as the filtration increases.

83
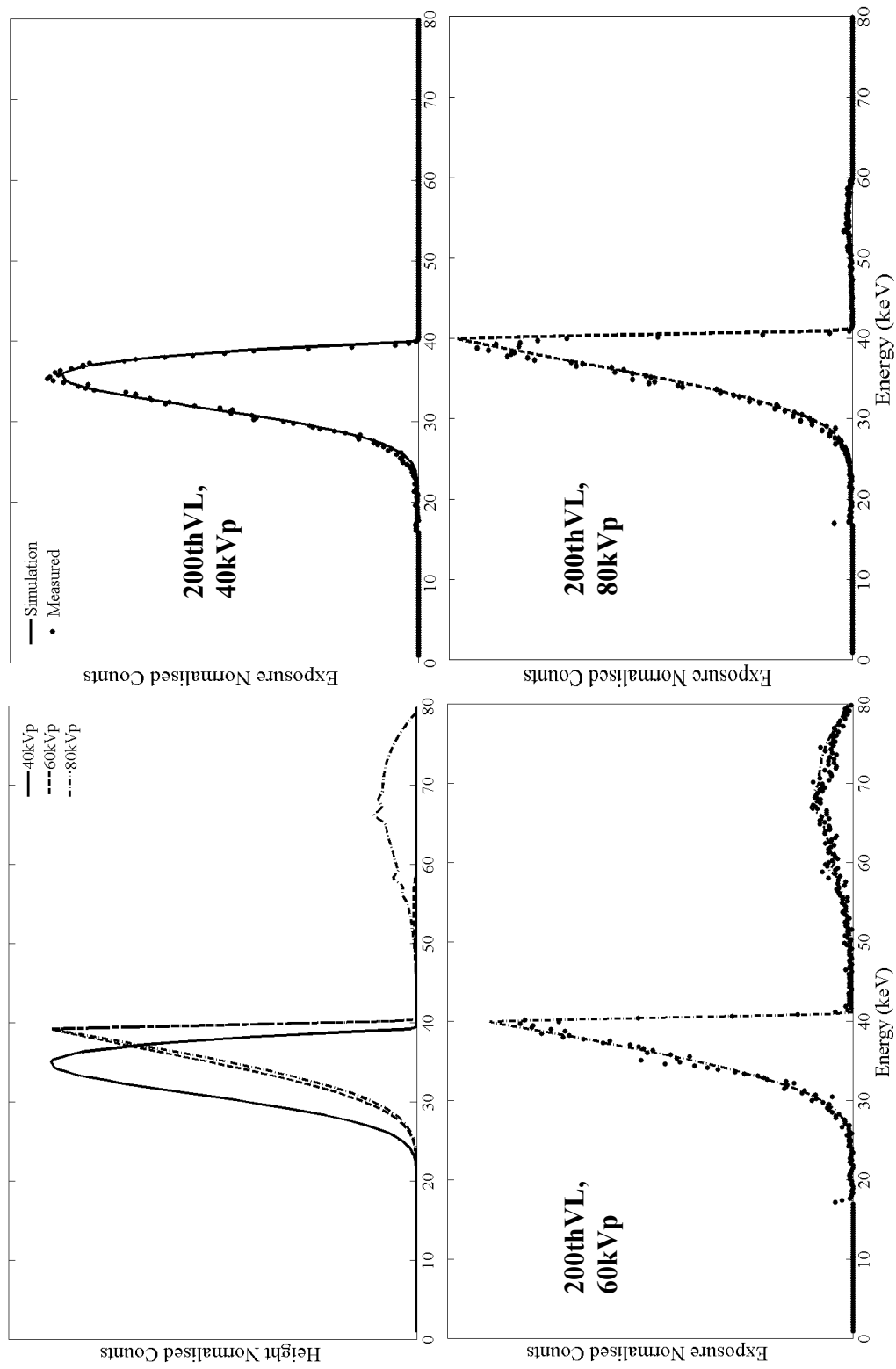
Figure 2.19: Plots of simulated and measured 200th VL Ce filtered spectra for 40, 60 and 80 kVp spectra showing changes in spectral quality as the tube voltage increases.

84
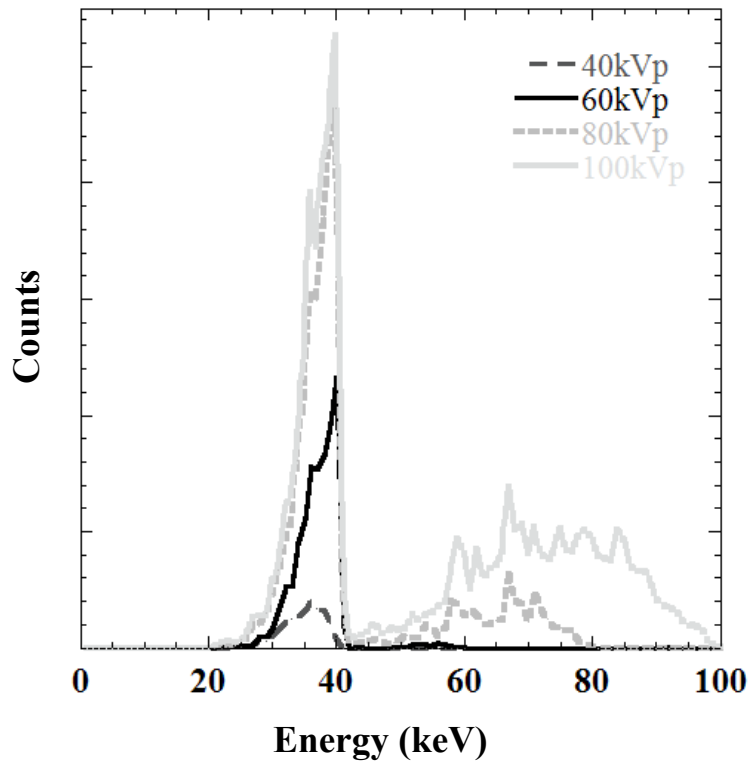
Figure 2.20: Plot measured spectra for a 200th VL Ce-filtered beam and varying tube potential. Note the increase in photon flux as tube potential increases.

2.2. Post-breast Spectra

The effect on the filtered x-ray spectrum after it passes through breast materials of varying densities and thicknesses was also measured. It is this beam that impinges on the flat-panel imaging detector, so determining and then optimizing the characteristics of this post-breast beam is vital for ensuring the best possible image. Based on the overall

results of the first section of this study and on previous studies done in the lab [80, 123], cerium was chosen as the filter material to further test.

Stacks of breast tissue equivalent plates (CIRS Inc., Norfolk, VA), each 2 cm thick and having either 100% glandular or 100% adipose composition (ICRU-44 specifications) were centered at the system isocenter (35 cm from the focal spot) to represent uncompressed breasts of various thicknesses and densities in the beam path. Figure 2.1 shows a 16 cm 50-50% glandular-adipose breast equivalent tissue setup with the center of the composite breast equivalent material placed at the isocenter of the CmT system. The energy-dependent characteristic attenuation coefficient of the breast slabs are shown in figure #4 in Figure 2.1. A typical x-ray beam after having passed through the breast slabs is illustrated in figure #5 in Figure 2.1. The total number of equivalent breast material slabs was varied to create breast tissue of thickness ranging from 8 to 18 cm. These two breast diameters bound the majority of breast sizes seen clinically [168], and results for breast diameters outside this range could be extrapolated from those investigated here. Composition of breast material along the beam path was also varied to span the range of possible breast tissue densities, from 100% glandular to 50-50% and 100% adipose tissue.

A 200th and 500th VL cerium filter were tested in this setup, in addition to the unfiltered beam. Tube operating voltages spanned 40 to 80 kVp in 20 kV increments. In order to get higher count rates through the breast slabs, larger x-ray exposures, ranging from 1.6 and 10 mAs, were used compared with the earlier pre-breast filter measurements. The

spectrum analyzer was exposed to 100 pulses of the x-ray source to inherently normalize spectra across different set ups in this section of experiments.

An additional FOM calculated in the post-breast spectrum analysis section of the study was an index of beam hardening, calculated as the ratio of weighted mean energies of the pre-breast and post-breast x-ray beams. Beam hardening is caused when a broad based or polychromatic energy spectrum with a substantial low energy component is incident on an object. The low energy components of the beam are progressively attenuated as the beam penetrates the object further and the average energy of the beam increases, increasing the degree of beam hardening. Although image processing techniques can minimize the effects of beam hardening (e.g. seen as cupping in CT images), these artifacts still reduce the intrinsic quality of projection images and may subsequently impact the differentiation of low contrast objects and the ability to perform quantative analysis on reconstructed CT images [101]. Pre-hardening the beam by removing low energy components before it is incident on the breast surface is one way to minimize the degree of beam hardening.

While alternative approaches are to model the energy spectrum during the reconstruction process [169-170], our approach to breast CT is to use a quasi-monochromatic beam for minimal beam hardening in acquired projections with the added benefit of potentially reduced dose to the object. Beam hardening is thus an indication of the monochromaticity of the beam and an indication of the intrinsic quality of the acquired projections.

Figure 2.21 shows exposure-normalized, unfiltered and 200th VL filtered pre- and post-breast measured spectra at 60 kVp, along with *xSpect*-generated spectra for a 16 cm breast of 100% glandular composition. Though the unfiltered spectra are generally noisy due to the broad spectrum and exposure normalization, overall agreement is excellent between measured and simulated data. Note the dramatic change in average energy, indicated by straight lines on the plots, of the post-breast beam for the unfiltered beam as opposed to the relatively minor change for the heavily filtered beam. The shift in mean beam energy of the post-breast spectrum for the unfiltered beam indicates a high degree of beam hardening. Contrast this with the relatively small change in mean beam energy for the heavily cerium-filtered beam. A low value of beam hardening emphasizes the improvement in mononchromaticity. This result illustrates one of the potential advantages of using such a heavily filtered beam in order to reduce image artifacts caused by beam hardening in a dedicated breast CmT imaging system.
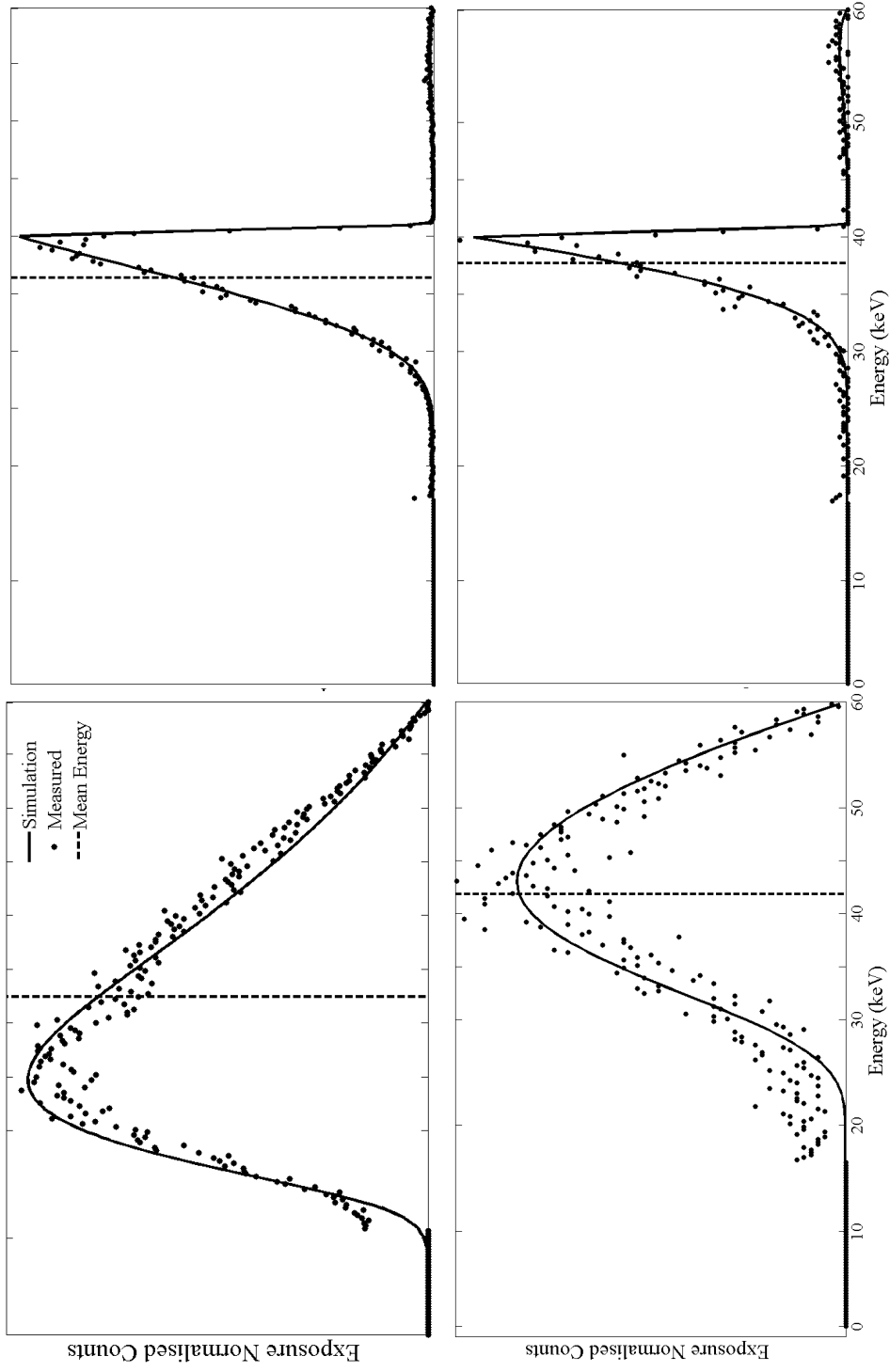
Figure 2.21: Simulated and measured spectra for (top row) pre-breast and (bottom row) post-breast (left column) unfiltered and (right column) 200th VL Ce filtered beam through a 16cm thick breast of 100% glandular composition. Vertical dashed line indicates the weighted mean beam energy.

Figure 2.22 illustrates the effect of different 16 cm breast tissue compositions on the filtered (200th VL) post-breast beam spectrum. The plots, normalized to the same exposure, detector collimator aperture size and number of x-ray projections indicate only slight beam hardening with increasing breast tissue glandularity and a concurrent noticeable decrease in the overall available photon flux compared to more fatty breast tissue. When the 200th VL spectra are compared against the 500th VL spectra, there is a noticeable spectral narrowing for the 500th VL spectra, indicating the more monochromatic nature of the 500th VL beam compared to the 200th VL beam.

Figure 2.23 compares spectra acquired using the same 100% glandular equivalent breast tissue composition under different conditions of tube voltage and beam filtration with varying breast size. Thicker breasts increase beam hardening and reduce the available photon flux through the uncompressed breast. The large apparent decrease in post-breast photon intensity between the 12 cm and 16 cm breast is consistent with the exponential nature of Beer's Law, where there is a near-threefold decrease in photon transmission factor for a 16 cm thick breast compared to a 12 cm breast, all other factors remaining constant. There is a further two-fold decrease in transmission when an 18 cm breast is used, compared to the 16 cm breast. The more monochromatic nature of the 500th VL beam is apparent compared to the 200th VL beam.
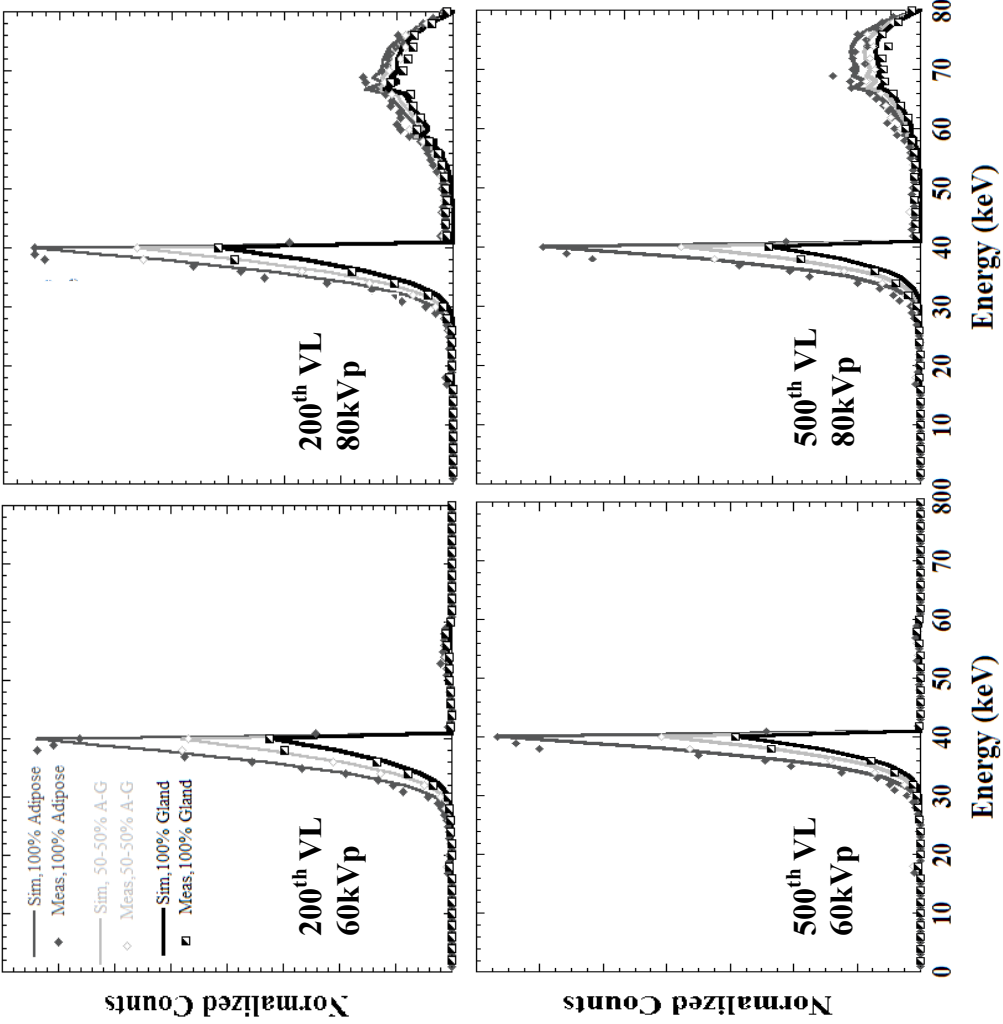
Figure 2.22: Simulated and measured spectra for a Ce-filtered beam at (top row) 200th VL and (bottom row) 500th VL at a tube potential of (left column) 60kVp and (right column) 80kVp. Note the decrease in photon flux for a 16cm breast as the glandularity of the breast is increased. Note also the spectral narrowing for the 500th VL compared to the 200th VL under both conditions.
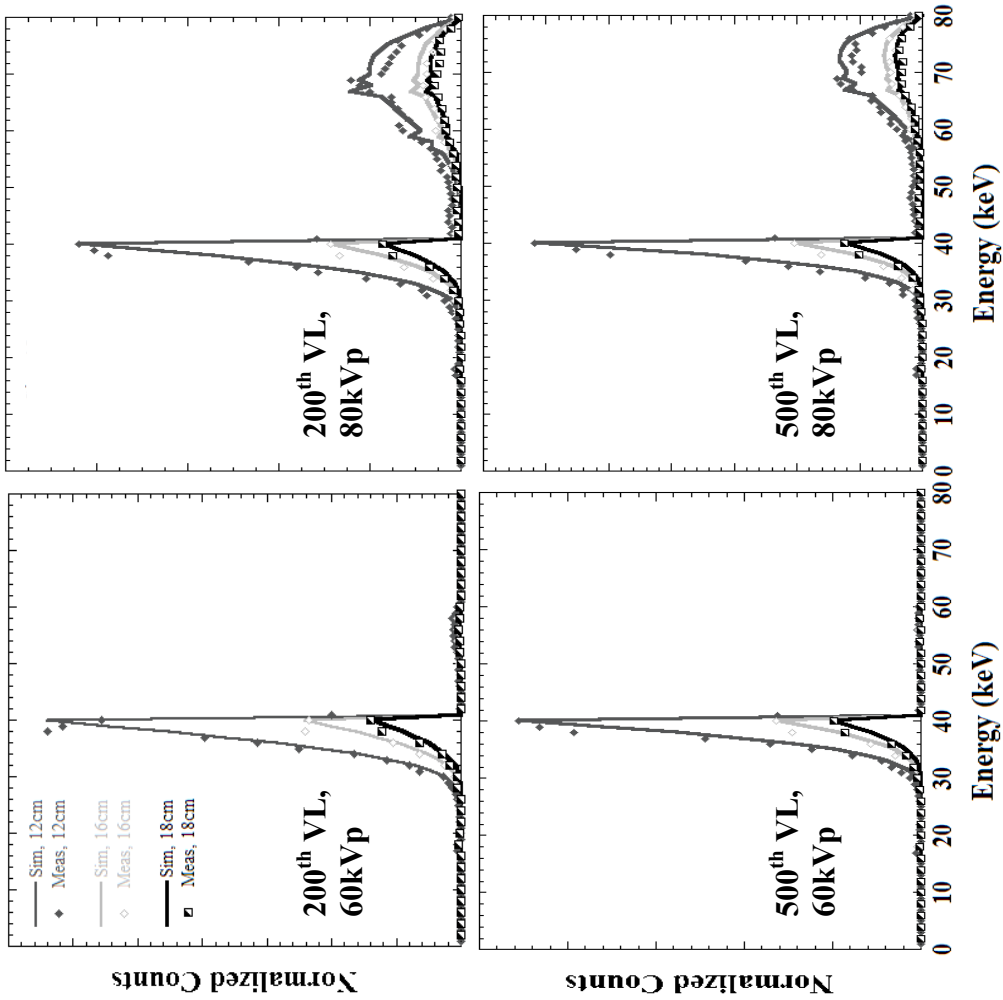
Figure 2.23: Simulated and measured spectra acquired for a 200th VL Ce-filtered beam for 100% glandular breast equivalent tissues of different diameters. Note again the sharp decrease in spectral intensity with a thicker breast.

The trends in reduced photon flux, apparent from the acquired spectral measurements, illustrate the potentially increased difficulty in imaging large diameter, uncompressed, dense breasts in breast CT, given the need to restrict breast dose to be comparable to that of mammography.

Table 2.2 Measured beam hardening (%) at 60 kVp across all experimental Ce filter setups.

Breast Thickness (cm)	Beam Attenuation Value Layer								
	Unfiltered			200th VL			500th VL		
	Glandular Tissue(%)			Glandular Tissue(%)			Glandular Tissue(%)		
	0	50	100	0	50	100	0	50	100
8	19.1	17.5	14.2	3.00	1.34	3.99	0.98	1.41	1.25
12	17.0	20.0	22.7	1.78	2.35	2.68	0.74	1.11	1.42
16	19.6	23.0	25.8	2.25	2.78	3.71	0.86	1.12	1.82
18	20.1	24.4	26.1	2.18	2.70	4.44	0.78	1.09	1.95

Table 2.2 lists the minimum degrees of measured beam hardening across all breast compositions and thicknesses under all operating voltages and filter thicknesses. In agreement with the previous plots, beam hardening is seen to increase with increasing thickness of breast tissue and also with increasing glandular composition. Results are best for the thickest filter, but the proportional improvement between the 200th and 500th VL filter is dwarfed by the improvement between the unfiltered and the 200th VL filtered beam.

The FWTM of the post-breast spectrum for a 16 cm thick breast across all breast densities and filter thicknesses at tube voltages of 60 and 80 kVp are shown in Figure

2.24. There is good agreement between simulated and measured results for the heavily filtered cases but not for the unfiltered beam case, due to the noisy nature of the unfiltered beam. At 60 kVp, there is a three to four fold reduction in spectral broadening for the 200th VL Ce-filtered beam as compared to the unfiltered beam (~25% for the 200thVL beam vs. ~85% for the unfiltered beam), indicating much greater monochromaticity in the beam incident on the x-ray imaging detector.

Improvement in FWTM figures for 80 kVp are not as pronounced, with the FWTM improving from ~100% for the unfiltered case to just over 80% for the 200th VL. This trend in increased spectral broadening reinforces the suggestion that higher voltages may not be ideal for routine tube operation. The difference between measured and simulated values is most pronounced for the unfiltered beam, where noise in the measured beam spectra is highest. Though measured results in the 80 kVp case follow simulated results less closely than those at 60 kVp, the trend in results is comparable.
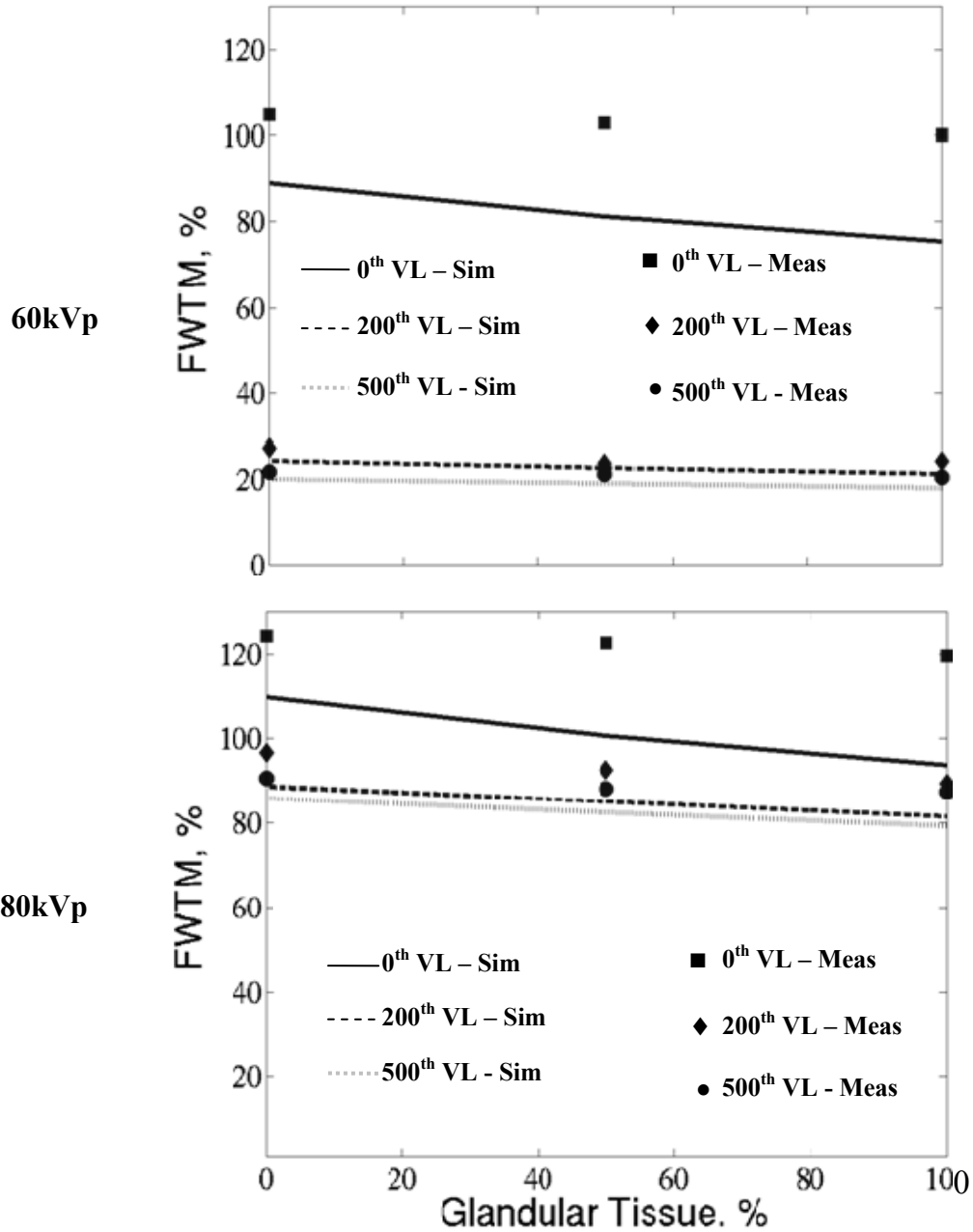
Figure 2.24: Simulated (lines) and measured (data points) FWTM at 60 and 80kVp for 16cm breasts of varying density for 0th VL (unfiltered beam), 200th VL and 500th VL Cerium filtration. There is close agreement between simulated and measured data for the heavily filtered spectra but agreement for the noisier unfiltered data (solid line and square mark) is not as good. FWTM increases with tube voltage due to the more apparent bimodal appearance of the spectra at higher voltages (cf. Figures 2.11, 2.19, 2.22).

2.3. Escape Events in the CdTe Detector

During the course of the experiments it was noted that an unusual number of low energy 'events' were being detected by the spectrum analyzer as highlighted in Figure 2.25. Strong evidence pointed to the detector being at fault and a number of experiments were undertaken to isolate the source of the error but were unsuccessful in solving the issue. These experiments included shielding the spectrometer external housing with extra layers of thick Pb bricks, or using a double collimator. It was also thought that the 'events' were simply noise from the detector electronics.
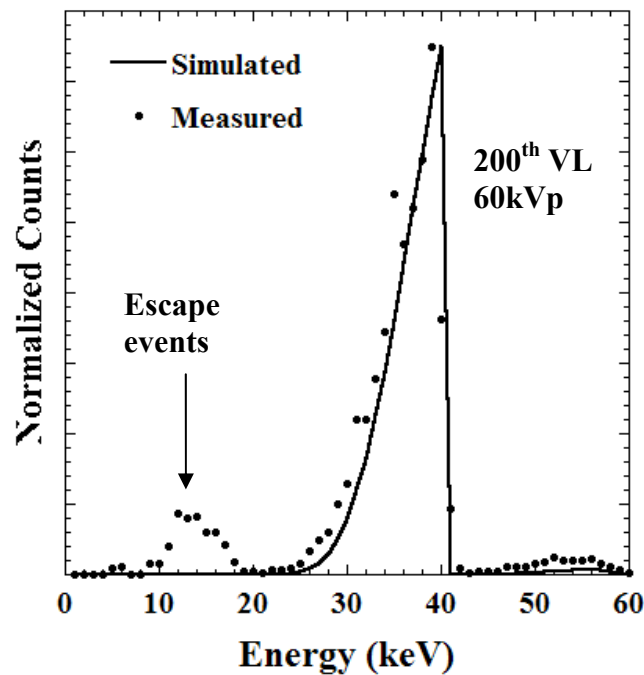
Figure 2.25: Height normalized simulated and measured, Ce-filtered spectrum (60 kVp, 200th VL) showing a region of escape events in the measured spectrum, not present in the equivalent simulated spectrum.

However the company that manufactures the spectrum analyzer (*Amptek Inc.,* Bedford, MA) , subsequently indicated in a published Application Note that the events were likely escape events from the Cd and Te detector materials [171]. Due to the escape phenomena, a proportion of characteristic Cd or Te x-rays (K-edge of Ce = 26.7 keV, Td = 31.8 keV) leave the small detector volume and do not deposit their full energies in the detector. This situation is illustrated in Figure 2.26.
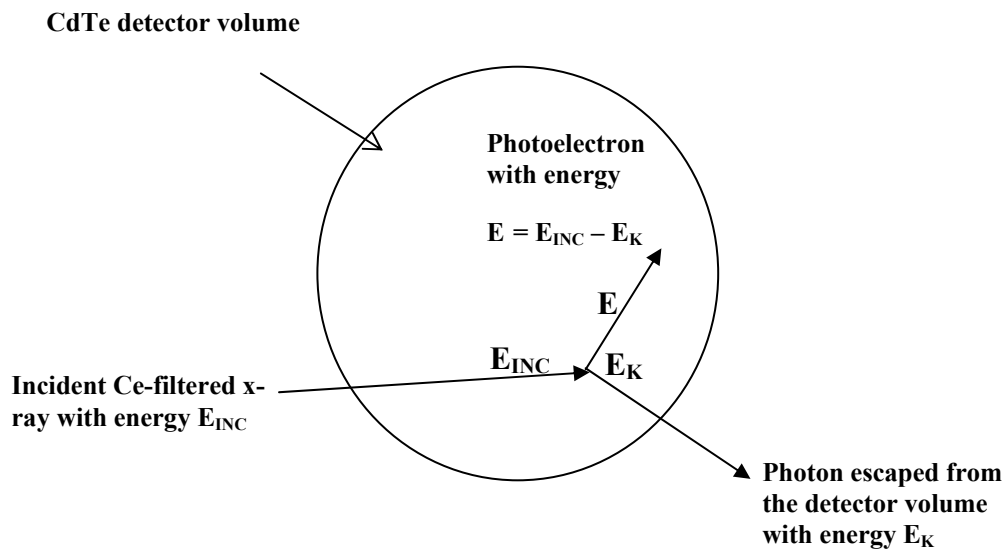
Figure 2.26: Illustration of the escape peak phenomenon in the small CdTe detector. The measured residual energy deposited in the detector volume is approximately equal to the difference between the energy of the incident x-ray and binding energy of the Cd or Te electron.

Thus, more lower energy events than would normally occur are detected, at energies below which the filters should, in theory, attenuate practically all photons. Some of the x-rays in the Ce-filtered beam interact with the K-shell electrons of the CdTe in the detector volume. These interactions result in the release of a photoelectron and a characteristic x-ray that escapes from the detector volume. Therefore the deposited

energy is equal to the difference between the incident x-ray and the binding energy of the K-shell electron.

Software to correct the error was not available at the time of these experiments. The erroneous events were simply discarded from the spectrum whenever a clear boundary existed between the appearance of the detected events and the underlying true spectrum. Due to their continuous nature, erroneous events are likely included in the remaining spectrum even after discarding clearly visible events.

However, absolute quantative accuracy in measuring the generated spectra exposures was not the main point of the experiments and so small sources of error were considered acceptable. In addition, it was believed that the magnitude of the remaining error in the heavily filtered beams was not considered a serious impediment to the overall accuracy and reliability of the trends seen in results for this set of experiments.

2.4. Discussion

In this chapter, a series of polychromatic spectra generated by common x-ray filter materials and quasi-monochromatic x-ray cone beam spectra generated using ultra-thick K-edge filter materials were experimentally measured and compared to simulated scatter-free spectra.

Operating the CT system within an optimal mean beam energy range is important to reducing the absorbed dose to the breast while maintaining image signal quality. Earlier studies led to the conclusion of using cerium as a near-ideal filter for breast CT under

most imaging conditions, and based on our measurement metrics, the results of the current study further corroborate these earlier conclusions [123]. Pre-breast and post-breast spectra were acquired using various filter materials under a range of operating conditions that mimic those seen clinically for a large variation in uncompressed breastthicknesses and of breast equivalent material compositions. Agreement exists between measured and simulated data, suggesting that this simulation engine can be used with confidence when optimizing future imaging tasks.

Comparisons of spectral FOMs generally showed significant improvement for ultra-thick filtered beams over spectra generated solely with intrinsic beam filtration. It has been possible to implement such an ultra-thick filtration scheme in our lab without undue distress on the prototype CmT system [75, 123, 125]. This is the technique now used as standard in the breast CT imaging system.

One of the advantages of using the ultra-thick K-edge filtration scheme is the reduction in absorbed dose to the breast of the patient during breast CT. A necessity that arises from the experiments outlined in this chapter is to then calculate the absorbed dose to the breast when employing the Ce-filtered beam. This question is answered in the next chapter, a chapter that further characterizes the breast CT system and describes a couple of techniques used to estimate and measure the dose to the uncompressed breast during a standard tomographic scan.

Chapter 3

3. Dose Distribution in the Uncompressed Breast

This chapter characterizes the absorbed dose to the pendant, uncompressed breast during a tomographic scan acquired using the prototype breast CT system and quasi-monochromatic x-ray spectrum described in Chapter 2. Since the dose imparted to an object is intimately tied up with the energy spectrum of the x-ray beam incident on that object, this chapter relies on the extensive spectral measurements performed in Chapter 2.

Guidelines from the American College of Radiology recommend that the average absorbed dose from dual-view mammography to a 4.2 cm-thick compressed breast consisting of 50-50% adipose-glandular tissue not exceed 6 mGy [104]. As a technology, uncompressed breast CT imaging is still in its infancy and so it lacks an equivalent standard. Since breast CT acquires many hundreds of individual 2D projection images, the cumulative dose absorbed by the breast during a tomographic scan is of paramount importance to imaging system design [123]. A consistent aim in the optimization of this breast CT system has been to confine the cumulative absorbed dose for a breast CT scan to that of dual-view screening mammography, or even lower. When previously compared against dual-view mammography in a phantom-based observer study, this CT subsystem demonstrated an improved ability to visualize small (<5 mm) spherical 'lesions' in low-contrast images containing structured background material at doses comparable to or less than that of dual-view mammography [109].

Early Monte-Carlo-based dosimetry studies demonstrated the ability of breast CT to successfully image the uncompressed breast at doses equivalent to that of mammography [15, 20]. Two subsequent simulation-based studies generated dose conversion factors specific to breast CT as a function of various imaging techniques and breast compositions [88, 115]. Indeed, the results from one of the studies were used to estimate the dose for the independent CT system developed in the MMI Lab. In that observer study, the dose imparted to the breast from breast CT was estimated using the dose conversion factors previously described, since no experimental validation of the absolute dose estimates was available [88, 109].

In addition to generating the conversion factors and additionally estimating the cumulative absolute dose to simulated uncompressed breasts, the early studies simulated the spatial dose distribution for breast CT at different beam energies and tube potentials [88, 115]. One study, using mean beam energies of 20-40 keV in the simulated system, similar to those employed in our breast CT system, showed that the resulting dose profiles across the breast phantom were highly non-uniform, with dose absorbed at the periphery of the phantom being far higher than in the center [115]. Dose profiles across the phantom were shown to become increasingly uniform as the simulated mean beam energy increased above approximately 60 keV. In a different study by Boone *et al* [15] using tungsten tube potentials from 80-120 kVp, a much more uniform dose profile for breast CT was demonstrated at these higher tube potentials. A recent study employed embedded TLDs to study the dose distribution in a 14 cm diameter PMMA half-ellipsoid phantom [172]. By varying tungsten target x-ray tube potentials from 60-80 kVp, the

dose was seen to increase appreciably towards the periphery both radially (towards the skin) and axially (towards the anterior breast). However, a more recent followup study by the same investigators using radiochromic film and the same imaging system at 80 kVp indicated a fall off in dose towards the nipple [12].

There were three main objectives to this set of studies: (1) to characterize the distribution of the dose within the various breast volumes using the radiochromic film technique; (2) to empirically measure, using calibrated radiochromic film, the dose imparted to the uncompressed breast using a breast cadaver during a scan using the regular tomographic scan protocol developed for the breast CT system; (3) to empirically measure, using calibrated thermoluminescent dosimeters (TLDs) and ionization chamber-calibrated radiochromic film, the absolute absorbed dose imparted to geometric and anthropomorphic breast phantoms and an uncompressed breast cavader.

This was a highly collaborative piece of interdepartmental research that could not have been completed without the expertise of Dr. Samuel Brady, a colleague in the Medical Physics Graduate program at Duke University. While it is difficult to draw clean borders between the responsibilities of the various researchers in the course of the research, I was responsible for the experimental concept and design, the acquisition of the calibration and experimental data, and the analysis of the processed dosimetry data. Dr. Brady was primarily responsible for preparation and handling of the radiochromic film and thermoluminescent dosimeters, and for processing the raw calibration and experimental data into its final form. However, these are not clean lines, and at various points in the course of the work we discussed all matters of the research together. I am also first author

in any presentations or articles that deal with this research. This work was presented at the *2010 Duke University Comprehensive Cancer Conference* and at the *2010 SPIE Medical Imaging Conference* in San Diego. The conference proceedings paper detailing this work was a finalist in the Michael B. Merickel student paper awards at the *2010 SPIE Medical Imaging Conference,* was published in the *2010 SPIE Medical Imaging Conference Proceedings,* and has been submitted for peer-review to *Medical Physics*.

3.1. Dose Estimates Derived from Dose Conversion Coefficients

Dose conversion factors [173] had been previously generated to simulate uncompressed breast CT imaging using our system. These dose conversion factors were used in the course of the filter experiments described in Chapter 2 to characterize the dose from beam spectra empirically acquired for all the various tested filter materials.

To do this, pre-breast spectra (spectra acquired without any breast slabs in the beam path) were acquired using the method described in Chapter 2. The parameters used to acquire the different spectra across the various filter materials, e.g. aperture size, number of exposures, mAs per exposure, were normalized to each other. The dose conversion factors were generated in terms of $\mu Gy/10^6$ photons/keV, and so the total number of photons in each 1 keV energy bin for each normalized filter spectrum was calculated, and the resultant cumulative dose per exposure was quantified by aggregating the dose across each energy bin for each filter material.
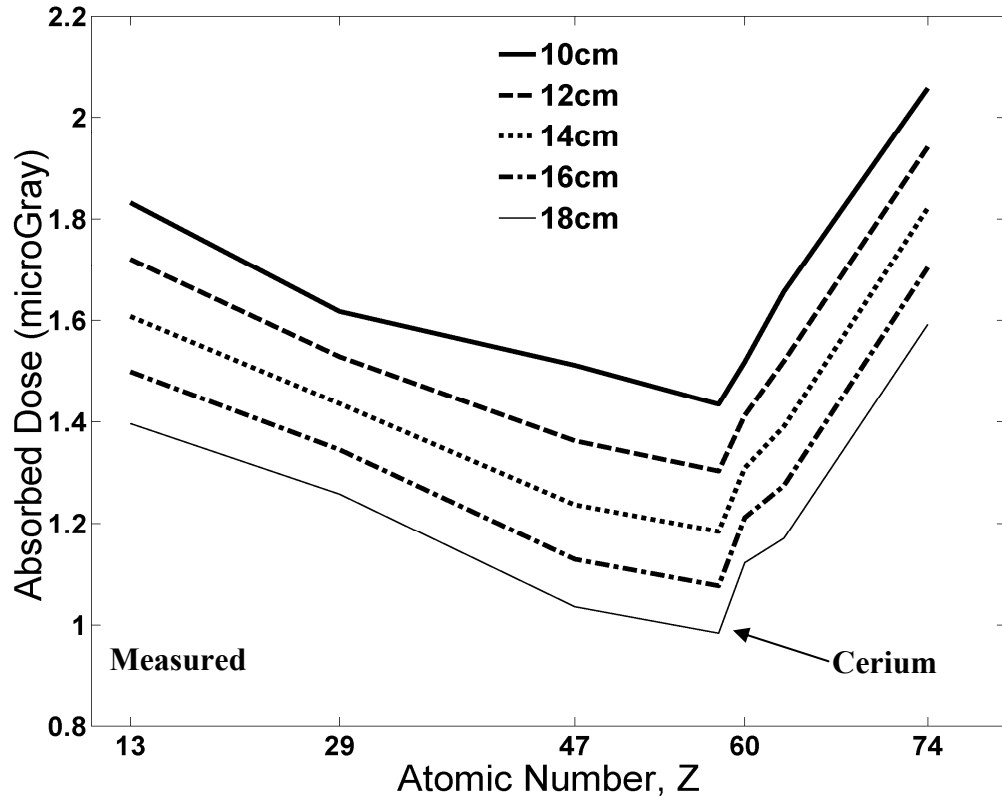
Figure 3.1: Plots of dose calculated from exposure-normalized measured energy spectra for filters operating at 60kVp and 200th VL for a range of breast sizes from 10-18cm with a 50-50% adipose-glandular breast tissue composition. Trends illustrate a minimum in absorbed dose for heavy K-edge filtration using Cerium.

A plot of absorbed dose (in μGy) for a range of breast thicknesses from 10 cm to 18 cm is shown in Figure 3.1 for all tested filter materials. The modeled breast composition is 50-50% adipose-glandular across a range of uncompressed breast thicknesses. The plots are from measured data generated using a tube voltage of 60 kVp at filter thicknesses equivalent to a 200th VL filter. The results indicate that Cerium has the lowest absorbed dose for breasts of all thicknesses under these particular operating conditions. These results were taken as an early empirical confirmation of the benefits of using a Ce-filtered beam for uncompressed breast imaging.

3.2. Dosimeter Preparation and Calibration

3.2.1. Radiochromic Film Preparation and Readout

The 3 layer structure of the XRQA film (GafChromic[TM], *International Specialty Products,* Wayne, NJ) used in the experiment consists of a 50 μm active monomer layer sandwiched between layers of polyester, each 100 μm in thickness. The film undergoes solid-state polymerization in real time in reaction to incident radiation [120]. The polymerization creates a dye-complex darker in color compared to unexposed portions of the film, and is digitized after a 24 hour period needed to allow stabilization to occur. The polymerization in the film yields an absorption spectrum with a maximum at 635 nm [121], which is most sensitively detected with optical digitization using red light. A typical characteristic response curve of radiochromic film is shown in Figure 3.2.

XRQA films were digitized using reflection densitometry on a flatbed scanner (Expression 10000XL, *Epson America*, Long Beach, CA) [174-175]. The scanner employed a xenon gas fluorescent source light and a linear charged coupled device (CCD) array for film readout [176]. The scanner's source light illuminates only during previewing and scanning; so to "warm-up" the scanner, ten blank scans were performed in succession and then discarded. Warming up the scanner provided a more stable light source and more consistent optical density (OD) readings [177]. The films were placed on the scanner in an area of high source-light uniformity, which corresponds to the center of the scanner. Each exposed film was scanned five times [177] at a resolution of 72 pixels/in (0.4 mm pixels), with no color corrections, and image files were saved in uncompressed format.
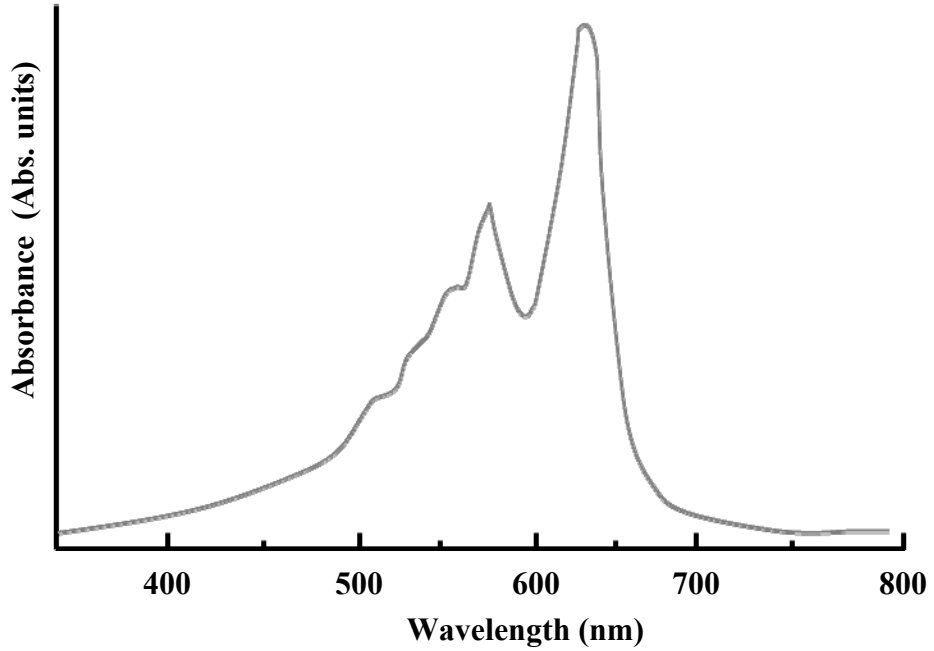
Figure 3.2: Typical absorption spectrum response curve of the radiochromic film used in the dosimetry experiments, showing a peak absorption at approximately 632 nm.

The final image consisted of an average of the five scans smoothed with a 3x3 pixel kernel. The films were scanned prior to being exposed and then carefully realigned on the scanner for post-exposure scans (alignment error measured to be ~1 mm). Once irradiated, the films darkened such that their OD quadratically increased with exposure [118, 120]. A net OD (OD_{net}) was calculated as the log transformation of the ratio of pre-(I_{pre}) and post-exposed (I_{post}) scanner light intensity value [178]:

$$OD_{net} = OD_{post} - OD_{pre} = \log_{10}\left(\frac{I_0}{I_{post}}\right) - \log_{10}\left(\frac{I_0}{I_{pre}}\right) = \log_{10}\left(\frac{I_{pre}}{I_{post}}\right) \qquad (3.1)$$

where I_0 was the measured light intensity of the flat field scan performed at the same time of the pre- and post-exposure film scans. All films were digitized using 48-bit color

depth with RGB file format (16-bit per color channel) and the red (R) channel was extracted for analysis in MATLAB (R2007a, *Mathworks Inc*., Natick, MA) [179]. The script in MATLAB used the results of the dosimeter calibrations (described in Section 3.2.3) to convert the observed optical density to a calculated dose.

3.2.2. TLD Preparation and Readout

All TLDs used in the experiment (3x3x1 mm^3 Harshaw TLD-100 (LiF:MgTi) chips, *Thermo Eberline, LLC*, Franklin MA) were first tested for batch uniformity by being exposed to a cumulative exposure of 1R. All chips that deviated greater than 2 standard deviations from the batch mean were discarded. The TLDs were annealed using a TLD-annealing furnace (168-300, *Radiation Products Design, Inc.*, Albertville, MN), and read using a TLD reader (Harshaw 5500, *Thermo Fisher Scientific, Inc*., Waltham, MA) with WinREMS software. Nitrogen gas was introduced during the readout cycle to reduce non-radiation-induced signals [180]. A typical response curve for TLDs is shown in Figure 1.9.

3.2.3. Dosimeter Calibrations

The TLDs and XRQA film were cross-calibrated with a 6 cm^3 ionization chamber (Mammochamber, Model 10x5-6M-3, *RadCal*, Monrovia, CA). The ion chamber was calibrated by the University of Wisconsin's Accredited Dosimetry Calibration Laboratory. Four separate sets of dosimeters including one piece of film, two TLDs, and the ion chamber were exposed in air to four separate exposure levels with the quasi-monochromatic x-ray beam, ranging from 0.659 to 1.915 R. The dosimeters were located

approximately 38 cm from the x-ray focal spot (on the tomographic system's current isocenter) and localized along a vertical line near the center of the x-ray cone beam field of view to eliminate the heel effect due to the tube's orientation. One set of TLDs and one section of film were set aside elsewhere in the laboratory for background measurements. Absorbed dose was calculated by multiplying the ion chamber exposure reading by the energy dependent water and oil f-factors (0.88 cGy/R and 0.74 cGy/R, respectively for 36 keV) and Wisconsin's provided calibration factor for 60 kVp. Both dosimeter calibration plots were fit using least-squares regression techniques. Due to uncertainty in the results of the initial set of TLD results, a second TLD calibration was obtained one week after the first. The results of calibrations are shown in Figure 3.3.

Quasi-quadratic fitting functions, using a Levenberg-Marquardt algorithm [178], were obtained to calibrate the ionization chamber to the radiochromic film measurements in water and oil (R^2 = 0.99 in both cases). A linear fitting function was derived for both calibration runs for the TLDs in water (R^2 = 0.99 in both cases). The shapes of these curves are consistent with the known characteristics of the dose-response of these dosimeters. Given that dosimetry with radiochromic film is still relatively new, the various measurements and appropriate least squares fits to the data can be used to calibrate one set of measurements from the other. In this case, the TLD and ion chamber measurements are considered the gold standard to which the radiochromic film is being calibrated and evaluated.
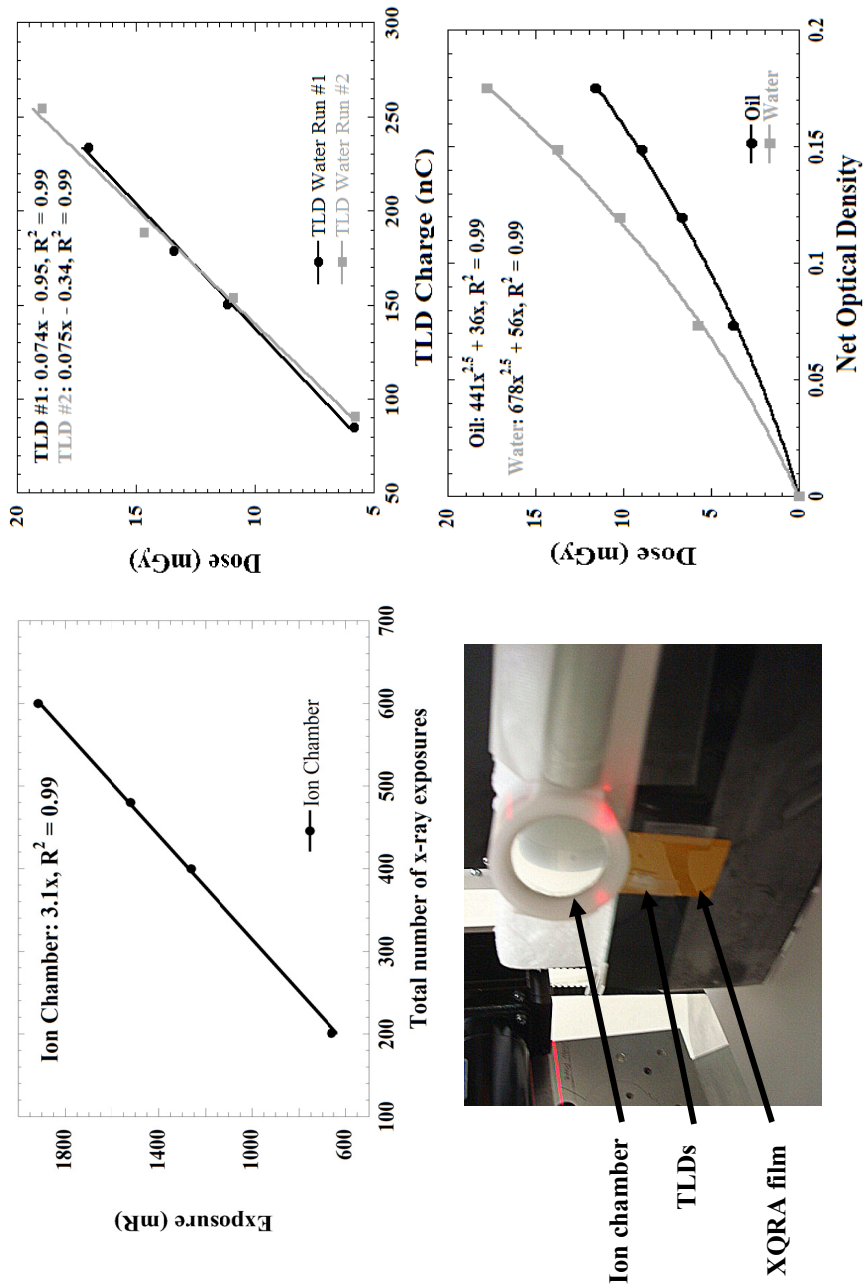
Figure 3.3: Calibration curves for; (top left) ion chamber exposure as a function of the number of x-ray exposures, (top right) generated TLD charge for water for both calibration runs. (Bottom right) Calibrated radiochromic film net optical density for oil (black) and water (gray). Also shown is a photo of the ion chamber, TLDs and radiochromic film (orange) placed along the central vertical line of the cone beam plane in the FOV of the CT system, aligned to avoid the heel effect of the x-ray tube.

109

3.3. Geometric and Anthropomorphic Phantom Dose Measurements using Radiochromic Film

Three phantom volumes were used to measure the absorbed dose using our CT system: two geometric phantoms in the shapes of a cylinder and a cone, and an anthropomorphically shaped breast phantom (Figure 3.4). The regular cylindrical phantom presents a constant cross section (radius = 12.5 cm) of absorbing material to the divergent x-ray cone beam, and mirrors the setup often used in Monte Carlo dose simulation studies. The conical shape mimics the decreasing effective diameter of the pendant breast from chest wall to nipple, but does so in a controlled fashion. From previous studies [168] we have estimated that approximately 15% of subjects have this conically shaped pendant breast. The anthropomorphic breast shape is then a natural progression from the prior geometric shapes and represents a 60% prevalent clinical geometric pendant breast dimension and volume [168].

Cross-sectional templates were cut out of the XRQA film of the phantom volumes (shown in Figure 3.4). With these given dimensions, the cone then simulates a large diameter breast at the upper edge of the cone, tapering to a smaller diameter breast towards the nipple. Due to the asymmetric 3D shape of the anthropomorphic breast phantom, separate templates of each axis (in sagittal and transverse orientations) were created by photographing the water-filled phantom from orthogonal perspectives. The orthogonal short axis film sections were sliced vertically through their centers to enable interlacing.
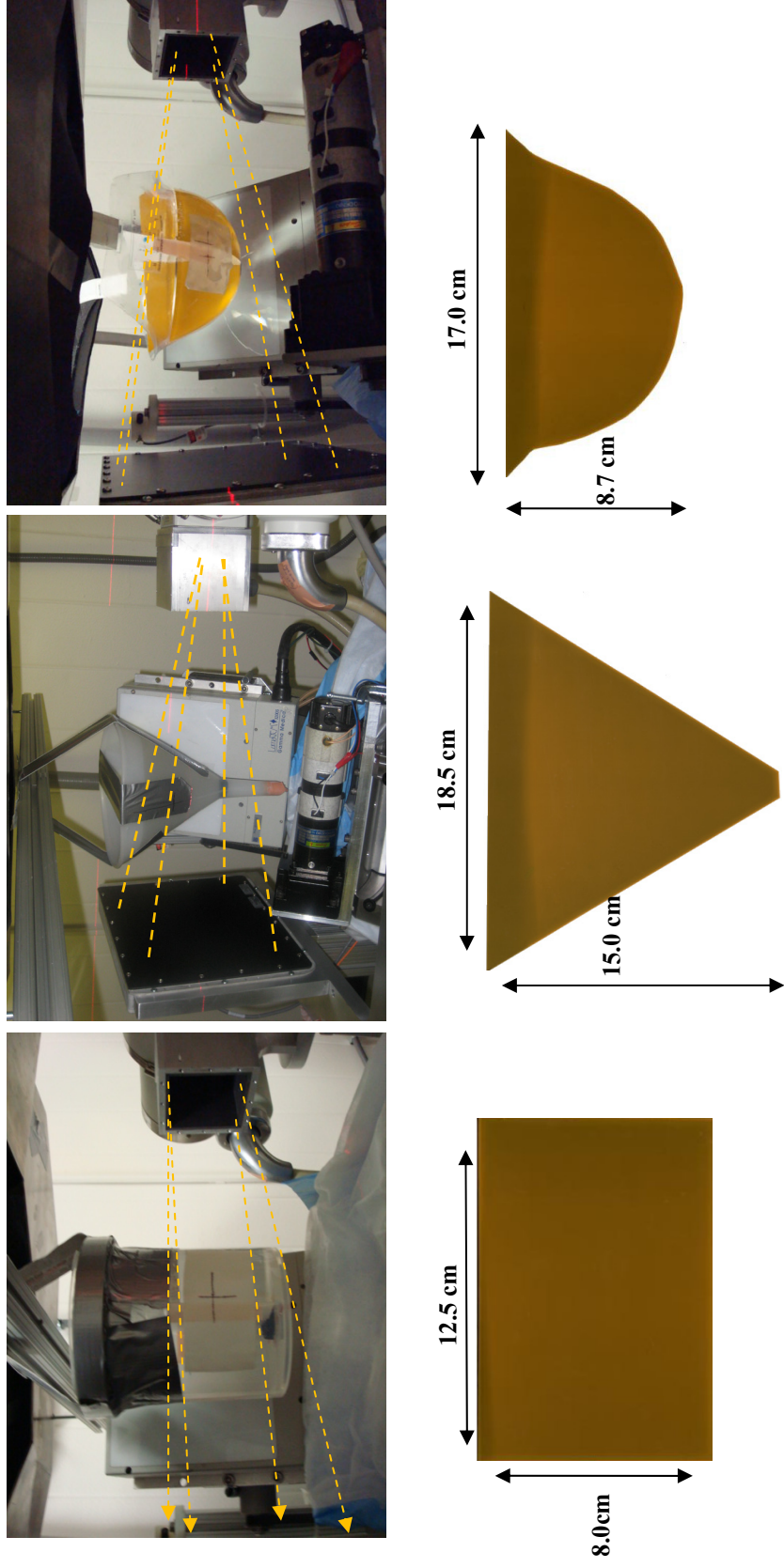
Figure 3.4: Photographs of the (left column, upper) cylinder suspended in the CT FOV with the outline of the x-ray cone beam superimposed on the image; (left column, lower row) the radiochromic film is shown below this photograph with accompanying dimensions. The same set up is shown for the (middle column) cone-shaped and (right column) anthropomorphic breast phantoms.

111

For each of the variously shaped phantoms, a single sheet of the film was attached with adhesive tape at several points to the inside surface of the phantom, ensuring minimal movement of the film during filling of the volumes with water or oil, and subsequent scanning. The central axes of the phantoms were positioned at the isocenter of the cone beam CT imaging system (raw projections of the setups are shown in Figure 3.5), and scanned using the tomographic imaging protocol described below. This enabled the absolute dose and dose profiles to be measured across the 2D central plane of each of the 3D breast phantom volumes. The phantoms were initially filled with 1000 mL of water (ρ = 1.0 g/cm^3) and tomographically irradiated. Using a new sheet of unexposed radiochromic film, the water was subsequently replaced by 1000 mL of mineral oil (ρ = 0.84 g/cm^3), and the tomographic exposure process repeated.

Water and oil were used to mimic the uniform tissue composition of breasts that form the boundaries of 100% glandular or adipose breast tissue composition, respectively. To ensure adequate exposure of the radiochromic film using the low flux CT scanning technique, each film dosimeter was exposed to three consecutive full tomographic scans acquired at 60 kVp, 2.5 mAs per projection for a total of 255 exposures (including 15 calibration projections) under each experimental setup. The dosimeter responses were scaled to represent a single scan measurement. Sections of each of the secured sheets of film projected above the upper edge of the liquid in the container and were then irradiated by the x-ray cone beam in air. These sections are not shown in processed images of the processed dosimetry data (see Figures 3.8, 3.10, 3.13, and 3.17).

Cylinder - Water

Cylinder - Oil

Cylinder – Pixel Intensity Profiles

Cone - Water

Cone - Oil

Cone – Pixel Intensity Profiles

Note: some parts of the film were exposed in air

Anthropomorphic - Water

Anthropomorphic - Oil

Anthropomorphic – Pixel Intensity Profiles
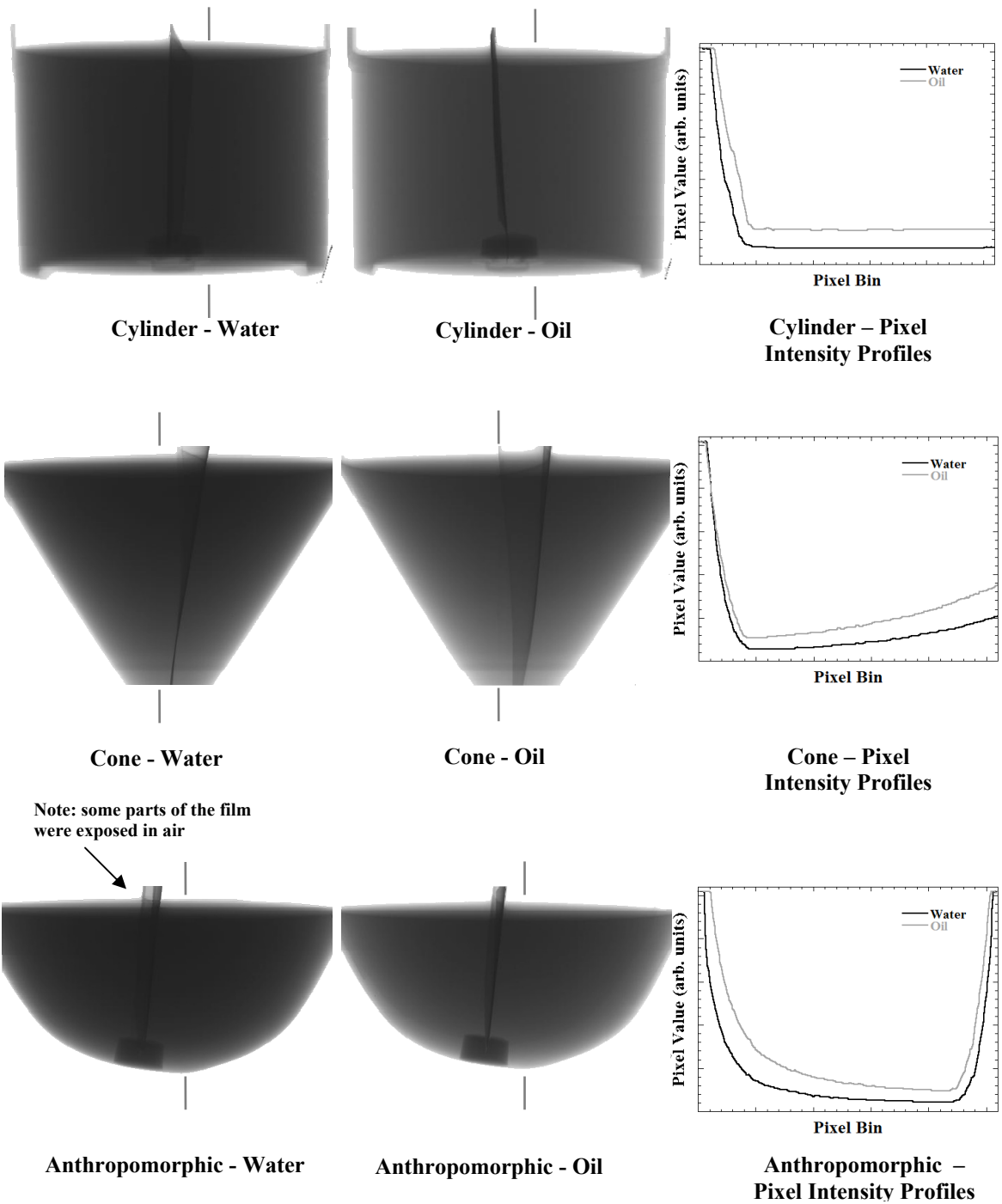
Figure 3.5: Raw projections of the radiochromic film in the various shaped phantoms in water and oil. The orthogonally orthogonally positioned film in the anthropomorphic phantom is not visible from this perspective. The accompanying profiles across the projections illustrate the greater attenuation of the x-ray beam by the water filled phantoms compared to that of the oil filled phantoms, as evidenced by the consistently higher pixel value for the oil based images than those of the corresponding water based images.

3.4. Validation of the Radiochromic Film Dose using TLDs

Results from the radiochromic film measurements in the conical breast phantom were cross-validated with dose measurements acquired using TLDs. Thirty seven TLDs (18 pairs and 1 single TLD, with pairs being used to ensure greater accuracy in the "point dose" measurements) were located on a regular array of points across the triangular template of the conical phantom (Figure 3.6), to measure the dose to the breast at varying distances from the breast surface to the center of the breast, and at different anterior distances from the "chest wall" towards the decreasing diameter at the nipple.

Each TLD pair was secured to a thin acrylic template of the conical phantom. Using a food vacuum sealer (*Foodsaver V2240BS*, Jarden Corp., Rye NY), the TLDs were first vacuum sealed in pairs and then the entire set of TLDs was additionally secured and vacuum-sealed to the acrylic template to isolate the TLDs from any liquid contamination, and to further secure them to the template surface. The entire TLD validation experiment was repeated twice, separated by a number of days to the first experiment using identically located pairs of TLDs on the template.

A comparison plot of TLD "point dose" measurements in the conical water-filled phantom compared to dose measurements extracted from identical regions of interest (ROIs) on the co-registered radiochromic film image is shown in Figure 3.7. Results from the 14 of 19 TLD pair locations that were immersed in the water and oil that filled the phantom are reported (see Figure 3.6). The measured TLD values are averaged from

four TLD measurements (2 TLD runs with pairs of TLDs located at each point, in each run). For comparison, the radiochromic film measurements were generated by overlaying a reconstructed maximum intensity image of the TLDs in water and comparing it to the processed image of the radiochromic film. An ROI of the same size as the TLDs were drawn on the film image at the corresponding positions of the TLDs and the mean and standard deviation of the dose was measured in that ROI.
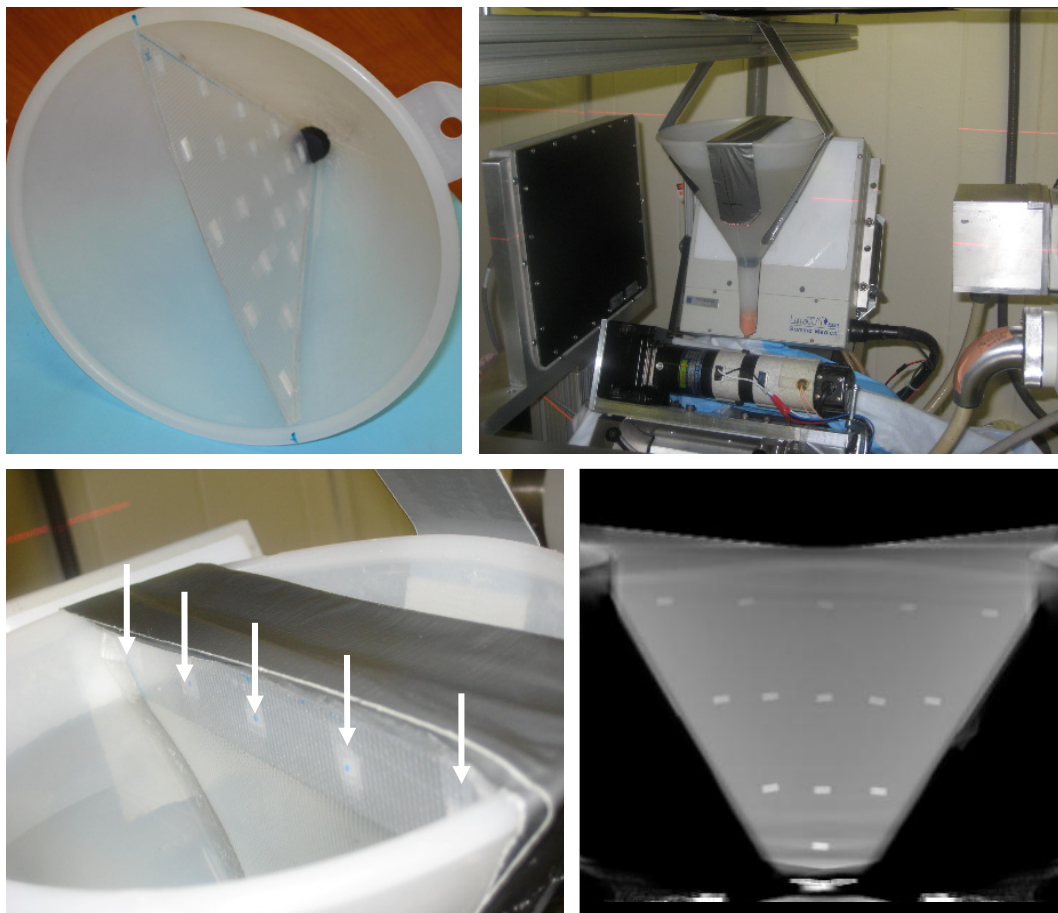
Figure 3.6: Photographs of the regular array of TLDs on the plastic template (upper left) secured in the cone shaped phantom, (upper right) in the CT FOV, (lower left) a close up view showing the water level in the cone, and (lower right) a reconstructed MIP image of the TLDs in the cone shaped phantom. The uppermost row of TLDs that are visible above the water line (at arrows) were not in the CT FOV, and so are not seen in the MIP image.
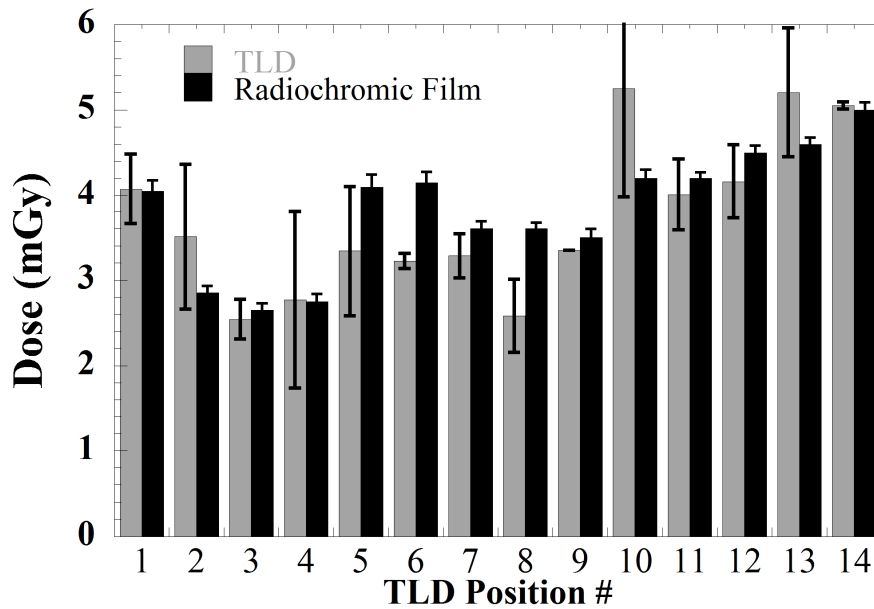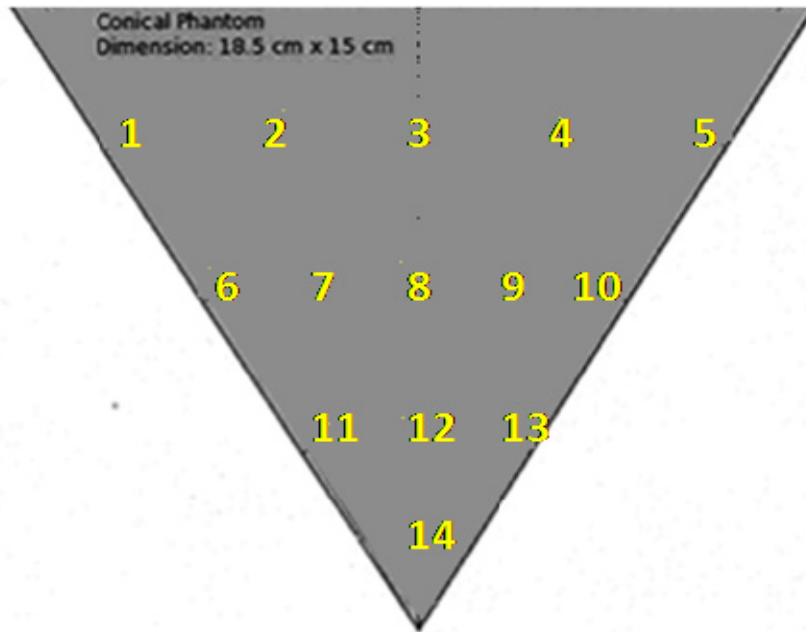
Figure 3.7: (Top) The conical template with the numbered positions of the visible TLD pairs (see Figure 3.6). (Bottom) The average and standard deviation of the "point doses" measured from the TLDs in water, compared to the dose at the equivalent ROI locations in the radiochromic film. Standard deviations for the radiochromic film were determined as the variation from the mean of the ROI in the film. Standard deviations of the TLDs were determined from 2 measurements of 2 TLDs at each location, or 4 trial measurements.

TLD doses range from 2.5 - 5.2 mGy with a mean dose of 3.7 ± 0.9 mGy, and the equivalent figures for the radiochromic film are 3.8 ± 0.7 mGy. The figures for TLDs and radiochromic film therefore track each other very well, with most results within 10% of each other. The greatest discrepancies between the TLD and film dosimeter measurements, however, are generally located towards the periphery of the triangular template. These differences can be attributed to slight inaccuracies during image registration, potential water seepage along the film edges, proximity to the water-air interface at that location, the fact that the TLDs were secured to a 2 mm plastic sheet, providing a slightly different local scatter environment, and differences in angular dependence (anisotropy) of response between the film and TLDs. While the calibration of the TLDs and the film was performed using a perpendicular exposure technique in air, any angular dependence of the responses was not explicitly characterized in this study. The overall close agreement between TLD and radiochromic film measurements serves to validate the film measurements that were evaluated throughout.

3.5. Cylindrical Phantom Dose Measurements

Figure 3.8 shows calibrated color plots of the absorbed dose to the cylindrical breast phantom in water and oil measured using the radiochromic film. Also shown in Figure 3.8 are horizontal and vertical profiles measured at different distances from the posterior to the anterior section of the phantom, i.e. from the top of the phantom near the 'chest wall' to the bottom of the phantom near the 'nipple'. A comparative plot of the three horizontal profiles is shown in Figure 3.8 also. The profiles indicate that the measured dose in water is consistently greater than that of the equivalent profile in oil. This can be

attributed to the greater mass energy absorption coefficient of water compared to oil at 36 keV, used to mimic the coefficients for glandular tissue and fatty tissue, respectively. The measured mean dose to the radiochromic film within the water filled cylindrical phantom for a single tomographic scan was measured to be 5.4 ± 0.4 mGy, ranging from 3.4 mGy to 7.1 mGy. The equivalent measurement for oil generated a mean dose to the oil filled phantom of 3.5 ± 0.3 mGy with a range between 2.5 to 4.5 mGy.

The horizontal dose profiles show a prominent cupping effect across the center of the cylinder for both water- and oil-filled phantoms. The measured cupping effect is similar to the cupping effects seen in others' simulation studies employing cylindrical phantoms at beam energies close to the mean beam energy of our breast CT system [115]. The cupping effect is not as prominent in the oil-filled phantom compared to the water-filled phantom. This is in part due to the greater mass energy absorption coefficient of water compared to oil at 36 keV. For the water phantom, peak dose levels measured at the periphery of the rectangular film are approximately 13% and 34% greater than at the center of the phantom for the left and right peripheries, respectively. For oil, the dose profile is relatively flat from one periphery to the center of the cylinder, but is approximately 20% higher on the other side than the center.

There is a small systematic variation (~1-4%) in the measured flat field light exposure across the calibrated radiochromic film scanner which may affect the processed radiochromic film. The horizontal asymmetry seen in the profiles may be also due to a slightly un-centered cylinder that received higher x-ray fluences while the CT system was rotating.
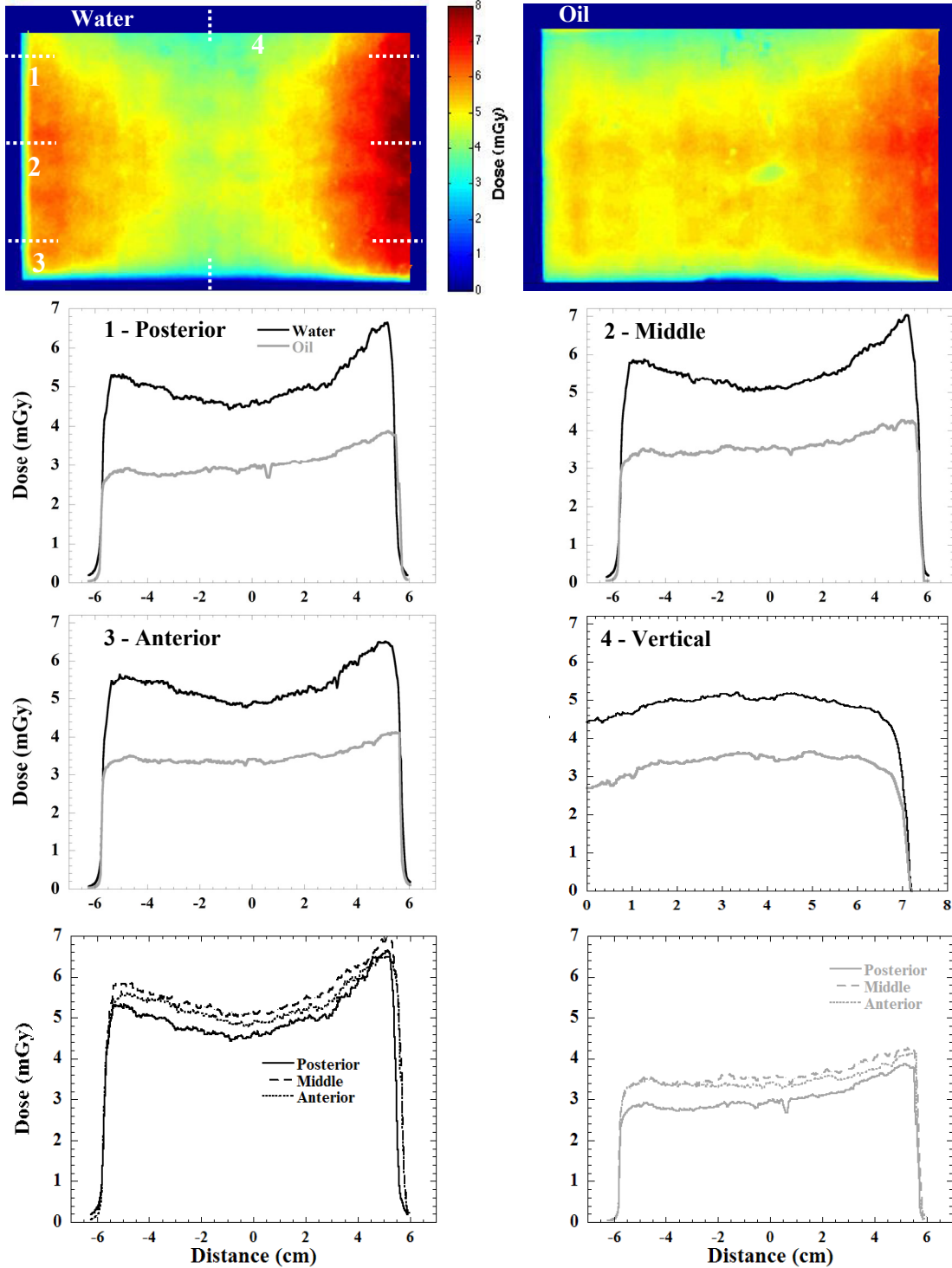
Figure 3.8: (Top row) Color calibrated distributions of the absorbed dose for the (top row, left) water filled and (top row, right) oil filled cylinder. The distance of the horizontal profiles are measured with respect to the centerline of the breast phantom. Dark red colors indicate areas of high absorbed dose. Dose profiles for the various indicated horizontal and vertical lines are shown in the middle two rows for both oil and water. The bottom row illustrates the three horizontal profiles superimposed on each other from posterior to the anterior breast (chest wall to nipple).

Given that the system obtains routine CT data with a full 360º scan, these sorts of asymmetries should be minimal. Other factors of the horizontal asymmetry were additionally interrogated. Some of the asymmetry may be caused by a larger number of "calibration images" occurring at one specific azimuthal location of the cylinder relative to the x-ray source during the scan; however the effect of the proportionally small number of calibration exposures (4% of the total number of exposures are for calibration) cannot explain the magnitude of the elevated dose levels. Nevertheless, careful patient breast centering would be recommended given the close geometrical configuration of this compact system, and especially if the subject is suspected of having very dense breasts.

The vertical dose profile from 'chest wall' to 'nipple' demonstrates an approximate 13% change between maximum and minimum absorbed dose values. The greater uniformity in vertical dose profile may be due to the constant diameter that the cylinder presents when intersected by the divergent but symmetric cone beam. If positioned exactly at isocenter, the constant diameter equalizes the path length of the x-rays incident on the cylinder, and so photons tend to deposit the energy in a likewise consistent manner. There is a slight peak in the absorbed dose profile approximately where the central x-ray of the beam is located. This may be explained by the greater photon fluence (less divergence) near the central ray of the beam, progressively reducing towards each periphery of the beam. The greater decrease in dose levels towards the upper edge of the cylinder may be attributable to the proximity of the edge to the air interface where the lack of chest-wall scatter-in processes decreases the overall dose to that point of the volume, especially when compared to the middle of the cylinder, which is closer to the central ray of the beam.
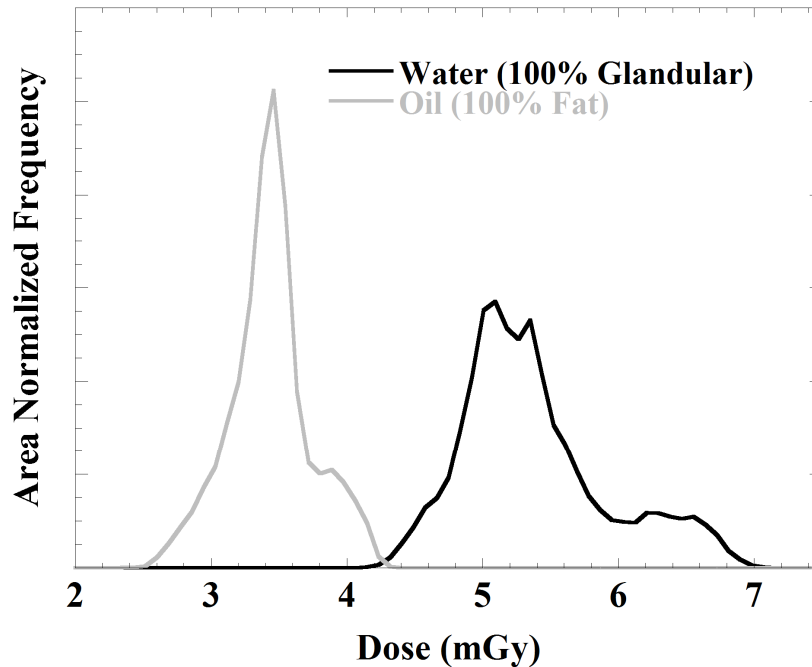
Figure 3.9: Normalized histogram for the oil (gray), and water (black) filled cylinder phantom showing a clear distinction in the dose characteristics between the oil and water filled phantoms.

A histogram of dose measured throughout the entire film area is shown in Figure 3.9. The histogram indicates a clear distinction between the dose levels in the oil and water filled phantoms. The histograms are normalized to the same area.

3.6. Cone Phantom Dose Measurements

The cone shaped phantom, while symmetric, more closely resembles the characteristic shape of a pendant breast, with a tapering of the effective diameter of the phantom from the thick 'chest wall' to the 'nipple' area. As mentioned earlier, approximately 15% of pendant breasts from MRI scanned subjects have been characterized to have this

geometry [168]. This dramatic tapering has an evident affect on the dose distributions, seen in the profiles in Figure 3.10.

There is a pronounced concavity in the water dose profile at the thickest section of the chest wall (profile #1 in Figure 3.10) with an approximate 50% difference between the peak periphery measured dose (~6 mGy) and the center of the phantom (~4 mGy). At this level the diameter of the cone is approximately 15 cm wide, slightly wider than the cylindrical phantom altogether. The peak peripheral dose in the equivalent oil dose profile is more uniform with only approximately 17% greater dose at the edges than that of the central section of the phantom (~2.9 mGy vs. 2.5 mGy). The dose profile for both the oil and water-filled conical phantom is more symmetrical about the vertical axis of rotation, potentially due to more uniform centering of the phantom. Horizontal dose profiles progressively flatten closer to the nipple (see profile #2, Figure 3.10, generated at 9.25 cm diameter). The underlying reason for this is that, as the breast diameter decreases, the cumulative absorbed dose in the center of the breast, aggregated over the tomographic scan, increasingly approaches that of the entrance dose. As an explanation, Figure 3.11 illustrates the aggregative effect of two conjugate projection views on the dose profile at different phantom radii. Indeed, the convex appearance of Profile #3 in Figure 3.10, generated at a diameter of approximately 3 cm, indicates that, very close to the nipple, the center of the phantom cumulatively absorbs more dose than the skin. The increasing nature of Profile #4 in going from the chest wall towards the nipple further illustrates the increasing overall dose with decreasing phantom diameter.

122
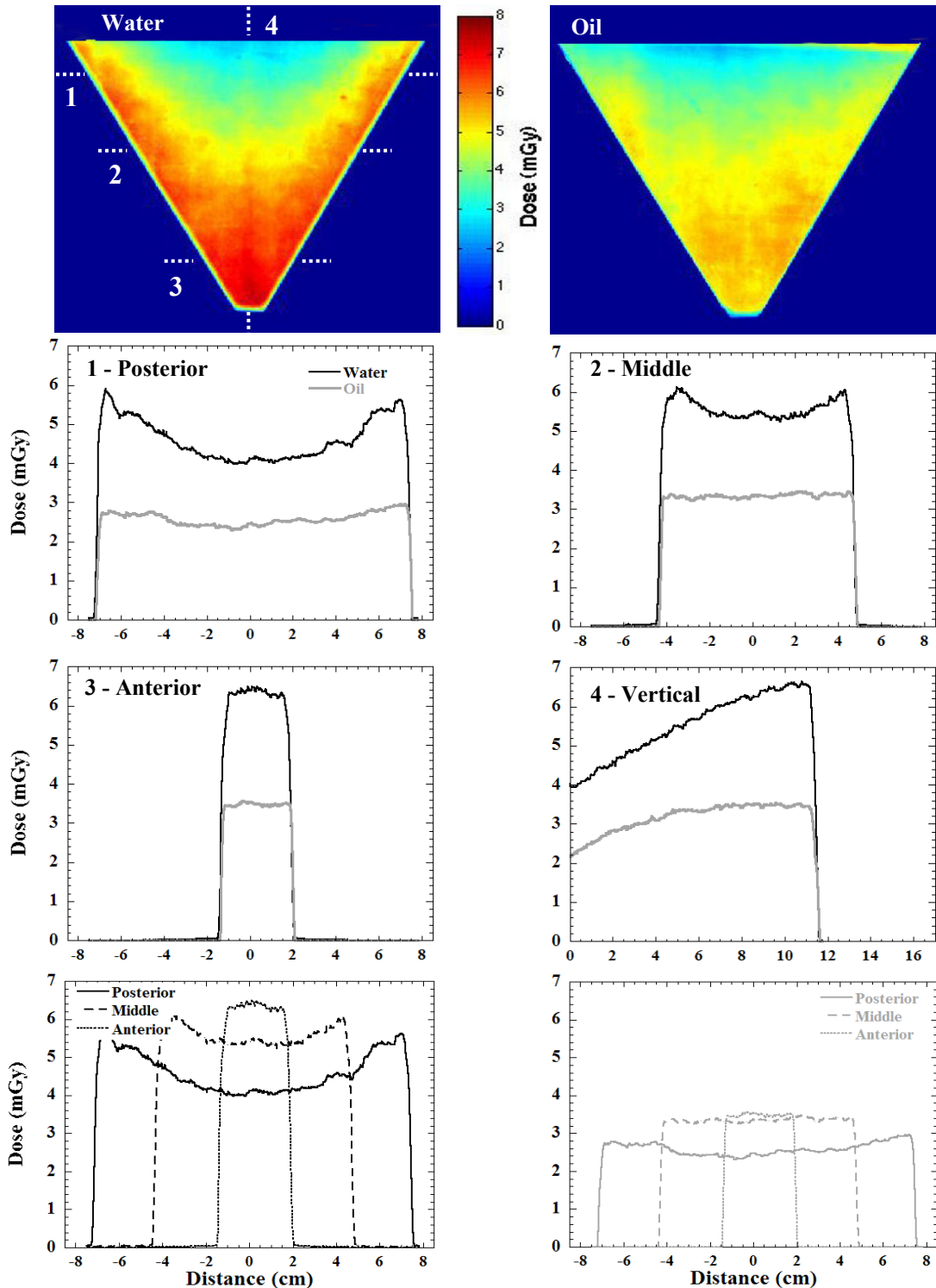
Figure 3.10: (Top row) Color calibrated distributions of the absorbed dose for the (top, left) water filled and (top, right) oil filled cone. Dose profiles for the various indicated horizontal and vertical lines are shown in the middle two rows for both oil and water. The bottom row illustrates the three horizontal profiles superimposed on each other from posterior to the anterior breast (chest wall to nipple). Note the progressively higher absorbed dose as the diameter of the cone decreases. The >60% increase in dose from the chest wall to the nipple is evidence of the influence that the object diameter has on absorbed dose.

123
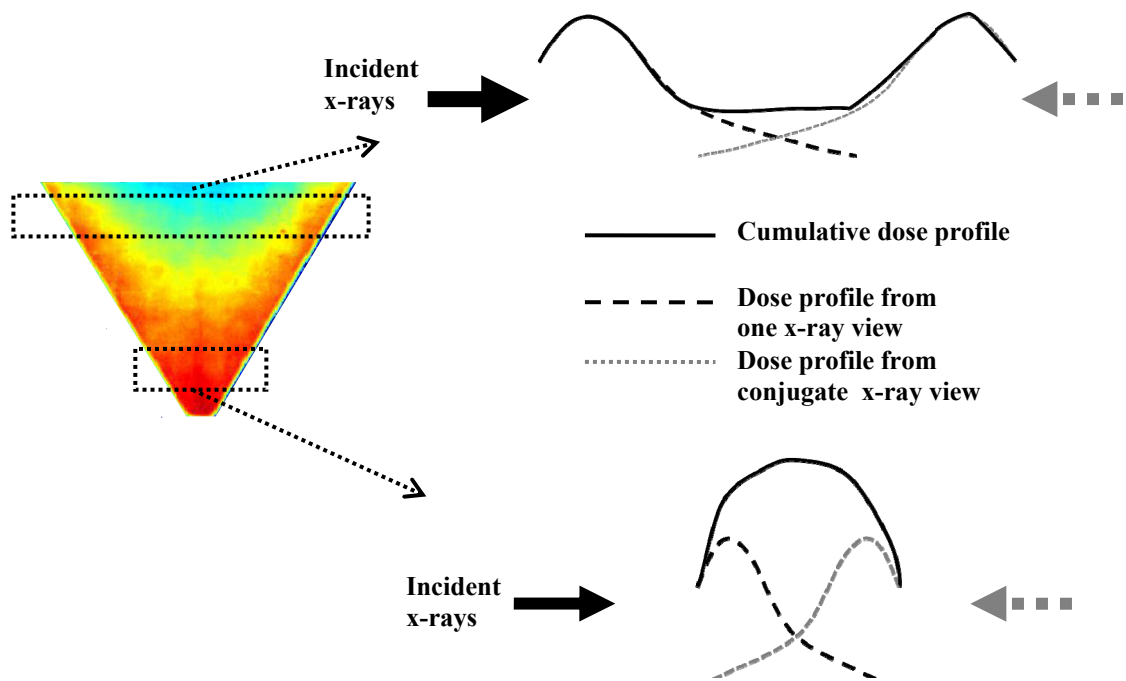
Figure 3.11: Illustration of the effect of conjugate views on the dose profile as the radius of the cone shaped phantom decreases. Towards the 'chest wall'(posterior breast), the radius is so large as to minimize the cumulative effect of the individual dose profiles, but as the radius reduces towards the 'nipple' (anterior breast), the profiles begin to acquire a convex shape.
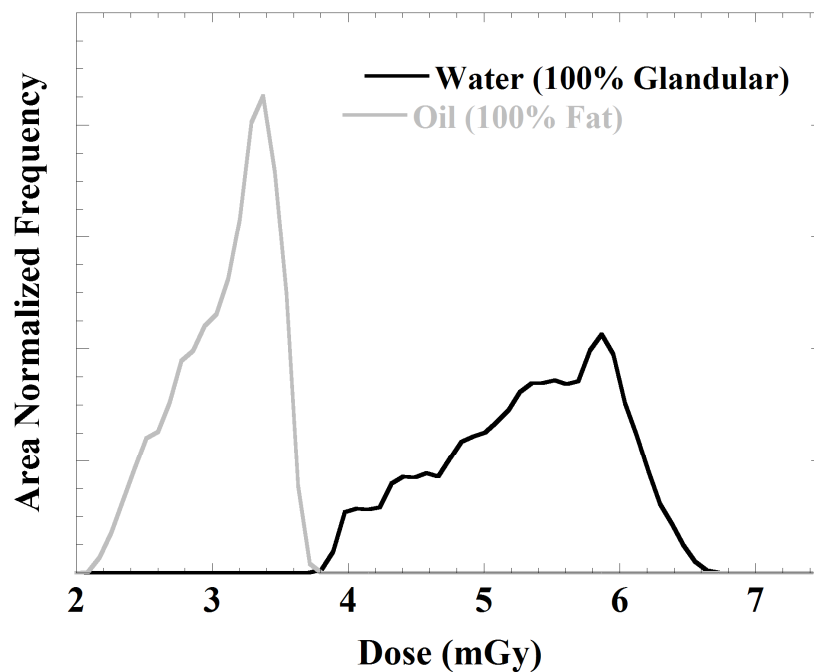
Figure 3.12: Area normalized histogram of the absorbed dose in the oil (gray) and water (black) filled cone phantom. The histogram shows a clear distinction between the levels of absorbed dose seen in both phantoms.

The skin (edge) dose remains relatively constant (~6 mGy), even as the breast diameter reduces, but the dose along the medial phantom increases from 4 mGy at the chest wall to approximately 6.5 mGy by the nipple region. The mean cumulative dose measured in the 2D conical cross section of the conical phantom is 5.3 ± 0.6 mGy, and that of the oil phantom is 3.1 ± 0.3 mGy. A histogram of absorbed dose for the cone phantom in both the oil and water-filled cone phantoms is shown in Figure 3.12. Similar to the cylinder, there is a clear distinction between the oil and water dose measurements with a strong bias in the water filled dose towards higher absorbed dose levels. The histograms are normalized to the same area.

3.7. Anthropomorphic Breast Phantom Dose Measurements

Figure 3.13 illustrates color calibrated images of the dose measured in the more clinically relevant anthropomorphic breast phantom, based on shape, size and density content. The mean dose measured in the water-filled phantom was 4.5 ± 0.4 mGy and that of the oil-filled volume is 3.8 ± 0.2 mGy. The results in Figure 3.13 also illustrate an increase in mean dose levels closer to the nipple, similar to the other geometric shapes. Evident in the profiles is the cupping close to the chest wall of the breast (profile #1 is generated at a breast diameter of 13.4 cm) and the gradual flattening of the profile as the nipple is approached, consistent with the more geometric phantoms shown earlier. However, the anthropomorphic breast does not taper near the nipple as sharply as the cone (the breast diameter for profile #3 is 6 cm) and so the convex shaped profile that was present close to the nipple in the conical phantom is not seen in the anthropomorphic breast phantom.

125
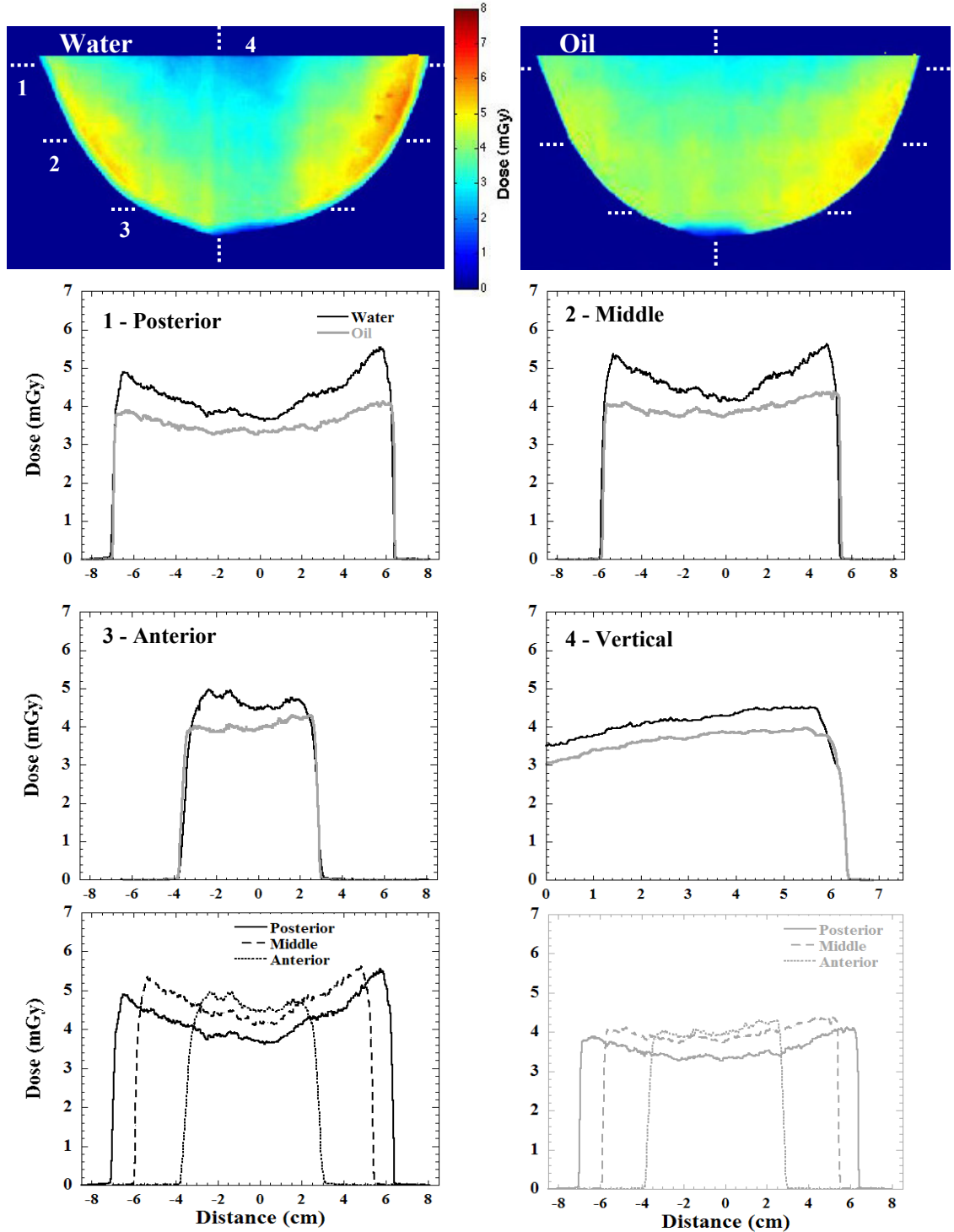
Figure 3.13: (Top row) Color calibrated images of the absorbed dose for the (top left) water filled and (top right) oil filled anthropomorphic phantom. The more rounded shape of the breast indicates that, unlike the conical phantom, the dose profile is not markedly convex at the nipple. The vertical dose profile indicates a 28% increase in dose along the center of the breast from the chest wall towards the nipple. The dose profile for water (equivalent 100% glandular tissue) is again consistently higher than that of the oil (equivalent 100% fatty tissue), but only nominally when compared with the more geometric phantoms.

Furthermore, the dose measured in oil, while consistently lower than the dose measured in water in the anthropomorphic phantom, is consistently higher than for the other geometric phantoms, and the reverse is true for the breast dose measured in water, making the point-wise differences between water and oil (glandular and adipose) smaller. All measurement procedures, preparation and immersion in the fluids, film calibration, 24 hour stabilization of the film post-exposure, and characterization procedures were identical to the earlier measurements. Thus, the greater similarity in the cumulative mean dose levels for both oil and water indicates that the breast geometry may play a larger role in overall absorbed dose than material content alone. It was already shown how dramatically dose can vary for different geometric configurations, (cf. Figures 3.8, 3.10).

Histograms of dose figures (Figure 3.14, left) acquired across the 2D cross sections of both the oil- and water-filled anthropomorphic breast phantoms show a broader spectrum of dose values for the water-filled phantom, whereas dose in the oil filled phantom is more tightly distributed about the mean. The separation between oil and water is not as clear as in the cone and cylinder histograms, although the reason for this is not clear.

A schematic plot of the variation in dose normalized to the center of the thickest section of the phantom (Figure 3.14, bottom) highlights the spatial trends seen in the profiles, where the periphery of the anthropomorphic phantom receives between 30-40% more dose than the central volume. Asymmetry is evident in the dose profile close to the chest wall of the phantom with the peak peripheral dose being between 20-30% greater than the mean dose in the center. This trend in increased periphery dose to the skin corroborates

previous simulated and measured dosimetry experiments for breast CT [115, 172], and is

consistent with generally accepted depth dose characteristics when irradiated with

ionizing radiation.
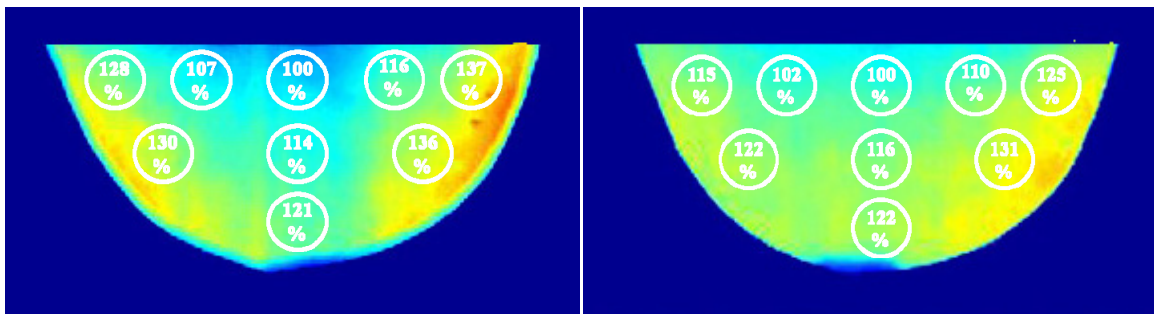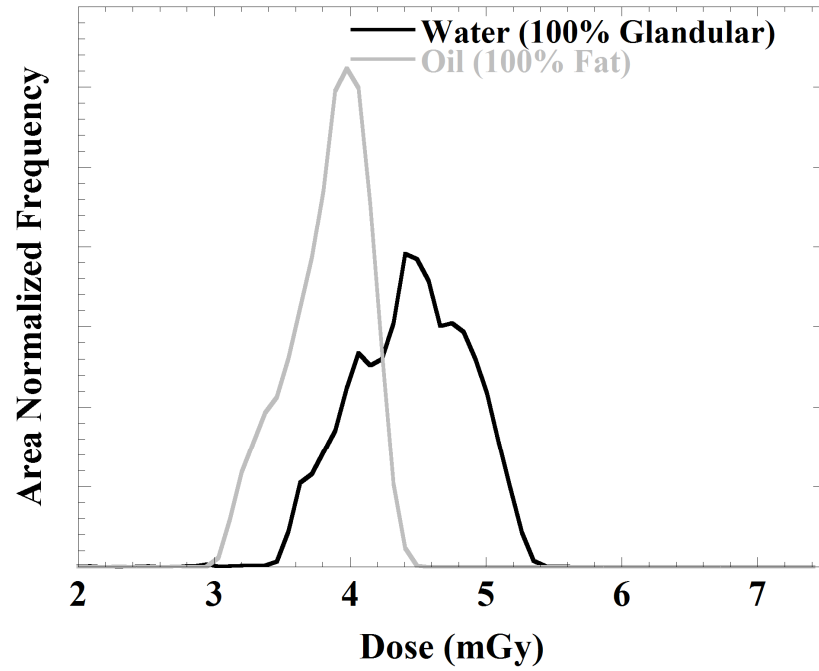
Figure 3.14: (Top) Histogram of dose measurements for the anthropomorphic volume filled with water (black) and oil (gray). The histograms illustrate the broader distribution of dose in the more 'glandular' simulated tissue compared to the 'fatty' simulated tissue. (Bottom) Percent dose normalized to the lowest dose in the center of the thickest part of the anthropomorphic phantom for water (left) and oil (right).

3.8. Cadaver Breast Dose Measurements

Cadaver breast experiments were undertaken a few months subsequent to the experiments involving the geometric phantoms and so another batch of radiochromic film was calibrated using the same technique used previously. The results of the film calibration, shown in Figure 3.15 and based on method the method used earlier [178], show a very close fit to the measured dose ($R^2 = 0.99$).
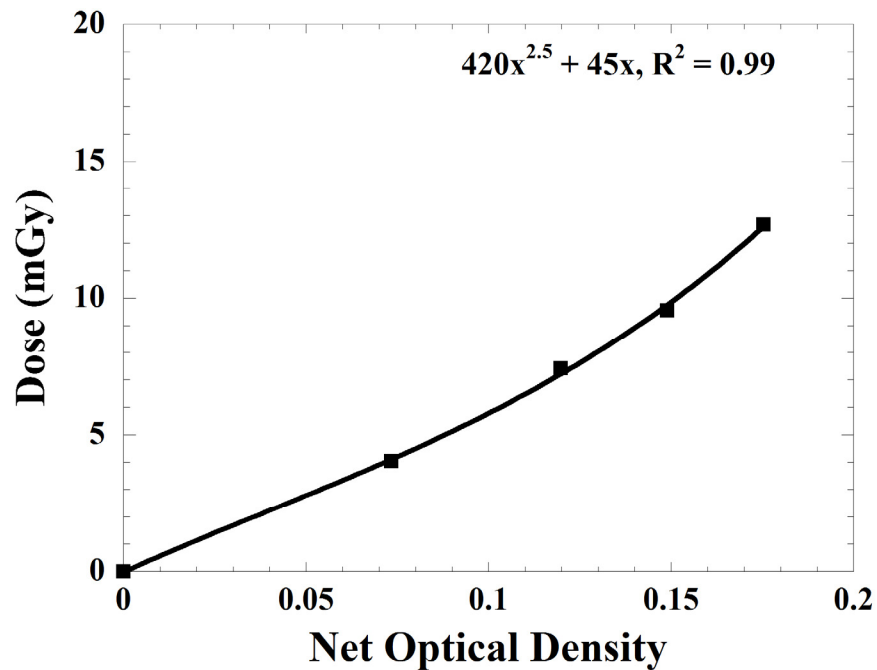
Figure 3.15: Plot of the calibration curve for the radiochromic film used to measure the dose absorbed by the uncompressed cadaver breast.

A breast cadaver excised from a 48-year old woman was used to estimate the dose to human breast tissue during a tomographic scan using the integrated breast CT system. The excised cadaver was placed in a 975 mL anthropomorphic breast phantom and the skin was attached to the sides of the phantom using small plastic and metal hair clips

(Figure 3.16). A sheet of radiochromic film was cut out and inserted between the cadaver breast halves in a manner similar to that for the geometric and anthropomorphic phantoms (see top row, right in Figure 3.16).

A photograph was acquired of the breast in the plastic anthropomorphic breast holder with a ruler placed next to the holder for scaling. The image was imported into image processing software where it was scaled to 100% and segmented to produce a clear outline of the plastic holder. A template was then printed and used to cut the radiochromic film to the correct proportions. An incision was initially made down the central medial-lateral dimension of the breast from the exposed breast tissue to the skin and the sheet of calibrated radiochromic film was inserted between the breast halves (middle left, Figure 3.16). The breast tissue naturally closed about the sheet of film to eliminate the air interface between the film and the breast tissue, and, as in past cadaver experiments, the isolated breast cadaver sagged in the middle of the breast phantom due to the lack of support from the absent patient chest wall. Therefore, 175 mL of mineral oil was added to the breast phantom to provide a realistic scatter medium at the margin of the posterior breast tissue (bottom, left, Figure 3.16). Three tomographic scans were acquired at 2.5 mAs per projection, for a total of 255 exposures (including 15 calibration projections) per tomographic scan.
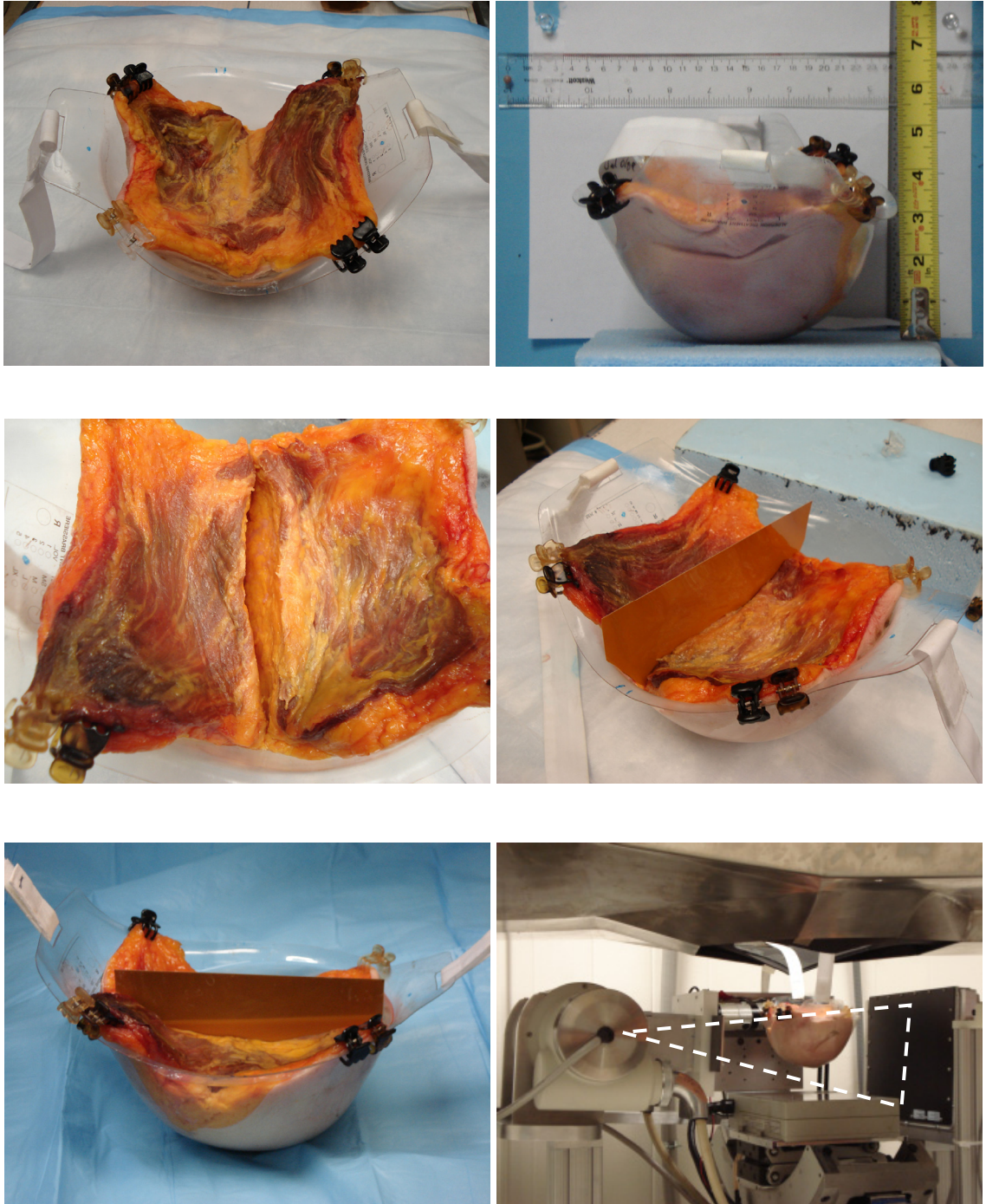
Figure 3.16: Photographs of the breast cadaver used in the experiments (top left) in the plastic volume. (Top right) The film template was made by photographing and scaling the photograph of the breast phantom using image processing software. (Middle row)The initial incision into the breast was made in the medial-lateral axis and the sheet was inserted between the halves. Note the (middle right) sagging evident in the middle of the breast phantom that prompted filling the breast phantom with 175 mL of oil (bottom left). (Bottom, right) A photo of the breast volume suspended in the FOV of the breast CT imaging system.

Color-calibrated images of the orthogonally positioned radiochromic films irradiated between the cadaver breast halves are shown in Figure 3.17. The locations of dose profiles across various planes of the radiochromic film are indicated on the images. Generally good symmetry exists in the absolute dose measurements and in the shape of the dose profile across the repeated studies, with a slight asymmetrical increase towards one side in the superior inferior film, potentially caused by asymmetrical placement of the film across the center of the breast tissue volume in that orientation. The average dose increases as the vertical profile approaches the nipple, with the dose at the nipple approximately 17% greater than that at the level of the posterior breast, in agreement with measurements using the anthropomorphic breast phantoms. At the posterior breast, peak peripheral dose figures at the sides are 20-30% greater than the minimum dose measured in the middle of the phantom.

The overall average doses measured for the cadaver tissue, not including the oil-filled regions, were 4.3 ± 0.3 mGy and 4.2 ± 0.3 mGy in the medial-lateral and superior-inferior directions, respectively. These dose measurements lie between the mean doses of 3.8 ± 0.2 mGy and 4.5 ± 0.4 mGy measured previously for the oil and water-filled breasts, respectively. Figure 3.18 includes a histogram of the dose values measured in the cadaver tissue for both the medial-lateral and superior-inferior templates, outside of the oil-filled regions. The histograms are normalized to the same area and show close agreement in terms of shape and distribution of measured dose in the cadaver breast across both orientations. Figure 3.18 also includes images of the mean measured dose in various indicated regions of interest in the cadaver breast.
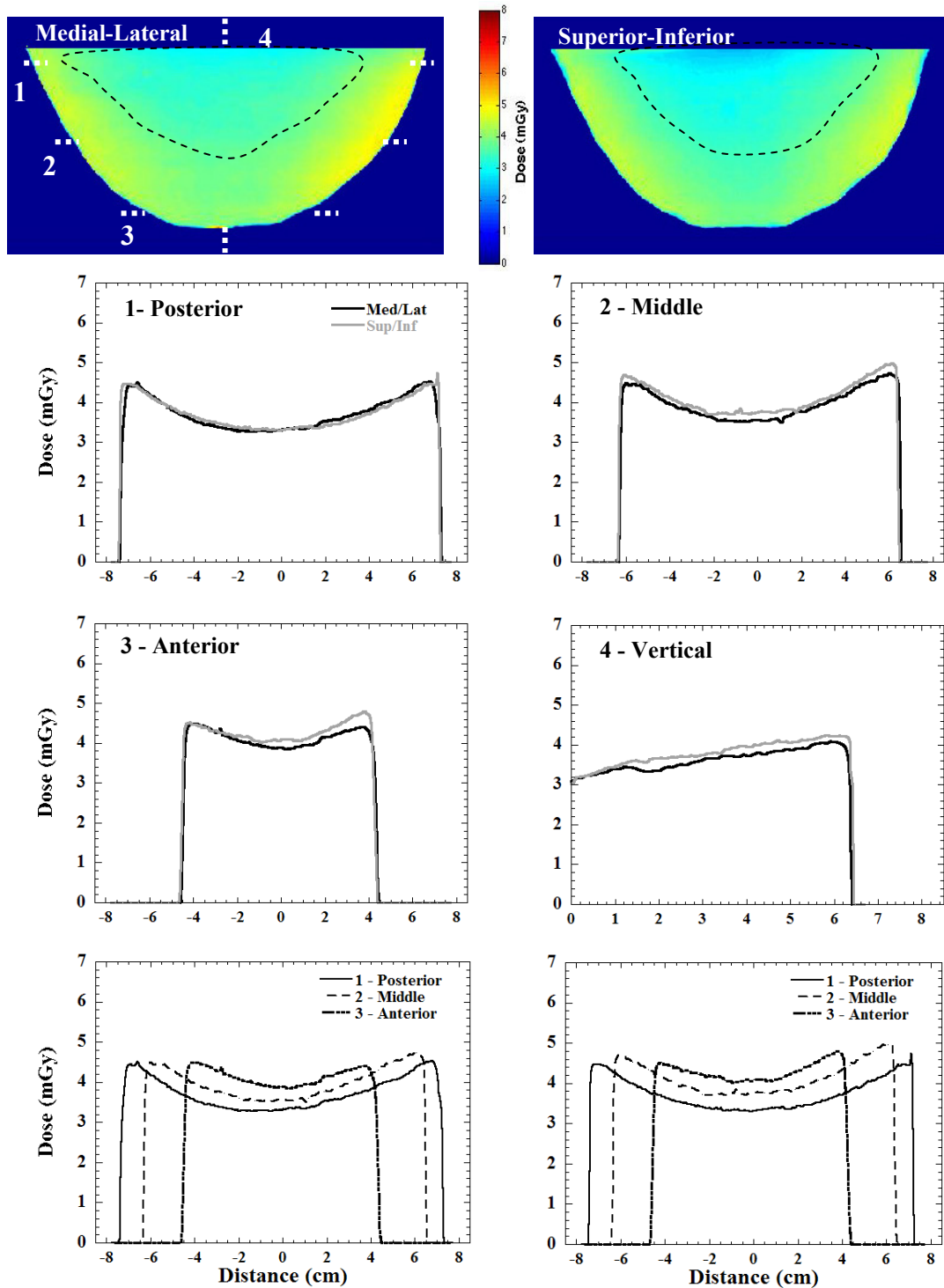
Figure 3.17: Color calibrated images of the absorbed dose in the cadaver breast for the (top left) medial-lateral and (top right) superior-inferior film templates. The accompanying dose profiles indicate good agreement for the templates across dose profiles, and also indicate an overall increase in measured dose as the nipple is approached, similar to the anthropomorphic phantom data in Figure 3.13. There is good agreement also between the radiochromic film results in the medial-lateral and superior-inferior orientations. The extent of the oil is approximated by the dashed line.

133
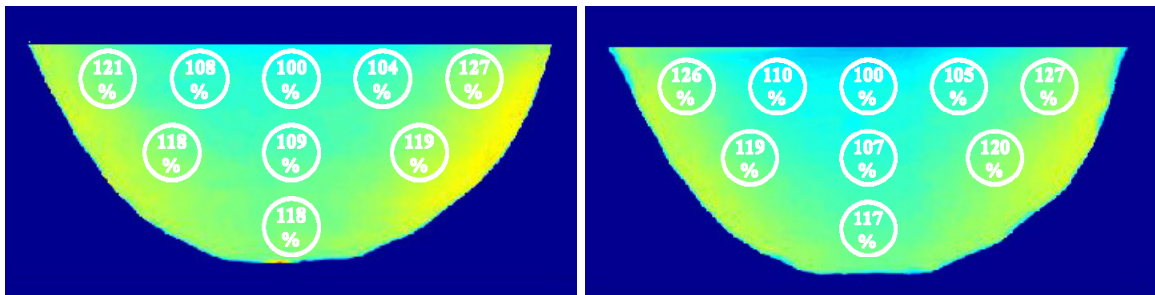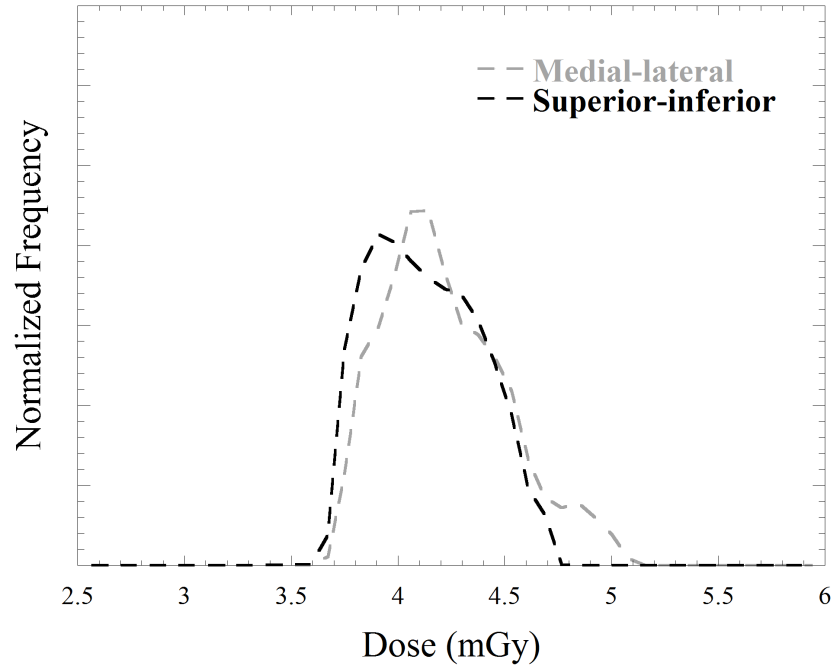
Figure 3.18: (Top) Normalized histograms of dose measurements for the cadaver breast films in the regions excluding the oil back fill. Histograms are shown for the medial-lateral (gray dashed line) and superior-inferior oriented film (black dashed line). (Bottom) Percent dose normalized to the lowest dose in the center of the thickest part of the cadaver breast volume for the medial-lateral (left) and superior-inferior oriented films (right), (c.f. Figure 3.14).

These dose levels are measured relative to the minimum measured mean dose level in the

thickest section of the breast volume (containing oil) and show a gradual increase in dose

to the peripheries compared to that in the center of the breast. This trend is as expected,

especially in light of previous results using the oil and water filled anthropomorphic breast phantoms (Figure 3.14).
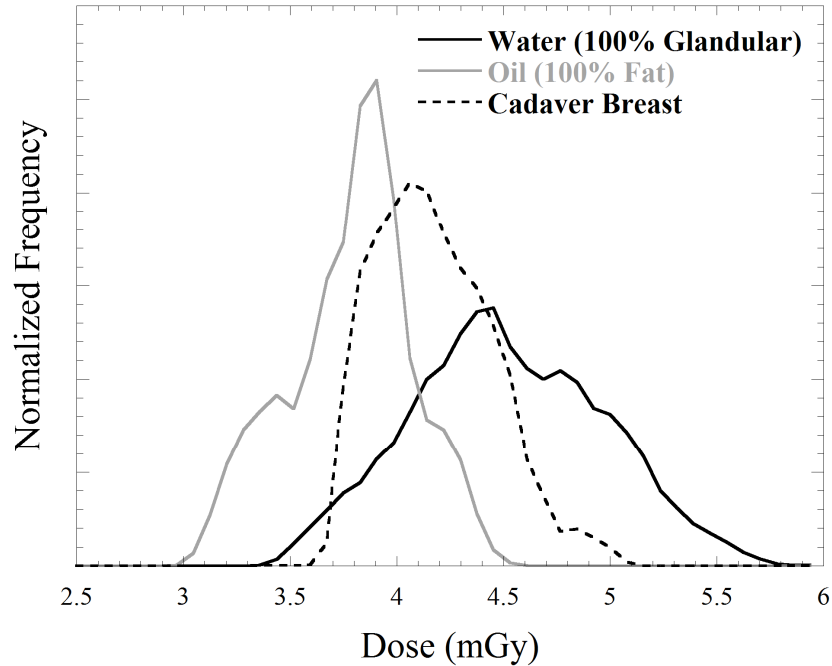
Figure 3.19: Superimposed histograms composed of the (black) water and (gray) oil-filled anthropomorphic breast phantom dose distribution (previously shown in Figure 3.11) along with the average dose distribution of the cadaver breast tissue (dashed). The histograms have been area normalized to each other. Also, the cadaver dose histogram is an average of both film orientations.

Figure 3.19 illustrates a composite histogram of the dose distribution of the cadaver breast tissue and those of the oil and water-filled anthropomorphic phantoms. The cadaver breast dose histogram is an average of the individual histograms in the medial-lateral and superior-inferior orientations. Results from the cadaver breast are indicated in the dashed line to distinguish it from the black and light gray lines of the water and oil-filled anthropomorphic breast phantoms, respectively. The three histograms have been further normalized to the same area. The histograms indicate that the dose distribution of the cadaver breast tissue, composed of adipose and glandular tissue is located between

the dose distributions of the oil and water-filled anthropomorphic phantoms. This result corroborates and validates the previous anthropomorphic data using the boundary materials of oil and water to simulate upper and lower dose limits.

3.9. Conclusions

Spectral-based studies using dose conversion coefficients indicated the advantages of using Ce as a filter material for uncompressed breast imaging. The studies described here followed prior studies using the independent CT system in an observer study [109], where CT was shown to outperform mammography in the task of imaging small, low contrast lesion-like spheres in a low contrast background at 0.8-2.4 mGy doses, which are far below the American College of Radiology recommended upper limit of 6 mGy dose for dual-view screening mammography.

In the first part of this current study, the doses deposited during tomographic scans of various geometric phantoms containing a wide range of simulated biological materials were measured using calibrated radiochromic film and TLDs fully immersed in the phantom volumes. The TLDs, a gold standard in dosimetry evaluation, were used to cross-validate the radiochromic film. Of particular interest was how the wide angle x-ray CT cone beam from the quasi-monochromatic source affected the dose distribution given various geometrical configurations, shapes and material contents of the 3D phantoms. The second main section of this study measured the absorbed dose in an uncompressed cadaver breast, a natural progression from the geometric and anthropomorphic phantoms of the first section of the study.

For the geometric and anthropomorphic phantoms, mean doses in oil (simulating 100% adipose tissue) and water (simulating 100% glandular) were 3.8 mGy and 4.5 mGy, respectively. The mean absorbed dose in the cadaver breast tissue was measured to be 4.2 mGy. This dose figure, averaged between two orthogonal orientations of the radiochromic film, is located between the upper and lower material bounds of the measurements made in water and oil. Previous measurements calculated via Monte Carlo simulation [15, 20, 109], are validated by these measurements.

The ACR upper limits were developed for a breast composition having a perceived 50-50% glandular-adipose tissue composition based on mammographic density measurements. The maximum mean absorbed dose in the anthropomorphic phantoms was generated using near equivalent 100% glandular and 100% adipose tissue materials. The results in this chapter, combined with previous observer study results [109], therefore suggest that the breast CT system and imaging protocol developed here is able to tomographically image the uncompressed breast using less than the maximum allowable dose for dual-view screening mammography.

Chapter 4

4. Investigating Image Cross Contamination in the SPECT-CT Device

The chapter quantifies the effects of image cross-contamination in the integrated SPECT-CT imaging system i.e. contamination of the SPECT (emission) image by photons from the x-ray (transmission) source, and its complement, contamination of the reconstructed transmission image by the emission source. The initial set of experiments described in the first section of this chapter empirically quantify the scattered X-ray contamination of the emission image due to the orientation of the SPECT gamma camera relative to the CT source-detector axis. The second section quantifies contamination of the transmission x-ray image by photons emitted from ^{99m}Tc in the patient.

Scattered x-ray photons pose a number of challenges for the SPECT imaging system, especially for systems having a common field of view, including the potential for significant degradation in image quality and errors in the quantitative accuracy of SPECT studies [49, 57, 181]. An increase in detected events exceeding the maximum count rate of the gamma camera due to the flux of scattered x-rays may additionally cause a transient paralyzing effect on pulse counting system electronics, as was the case for several prototype dual-modality systems [57, 182].

The problem of scattered x-ray transmission into the SPECT image exists only when a simultaneous dual-modality imaging protocol is desired to potentially achieve faster patient throughput, or to minimize the effects of patient motion on image registration. In the simultaneous protocol, an x-ray projection image is acquired at the same time that a

single SPECT projection is being acquired (Figure 4.1). In this way, scattered x-ray photons may impinge on the SPECT gamma camera, contaminating the resulting SPECT projection image. Under the interleaved and separate imaging protocols, SPECT gamma camera data acquisition can be turned off while the x-ray exposure is in process. In these modes of operation, contamination of the SPECT image is not an issue. Timing diagrams for the SPECT and CT systems under the planned imaging protocols are shown in Figure 4.1.
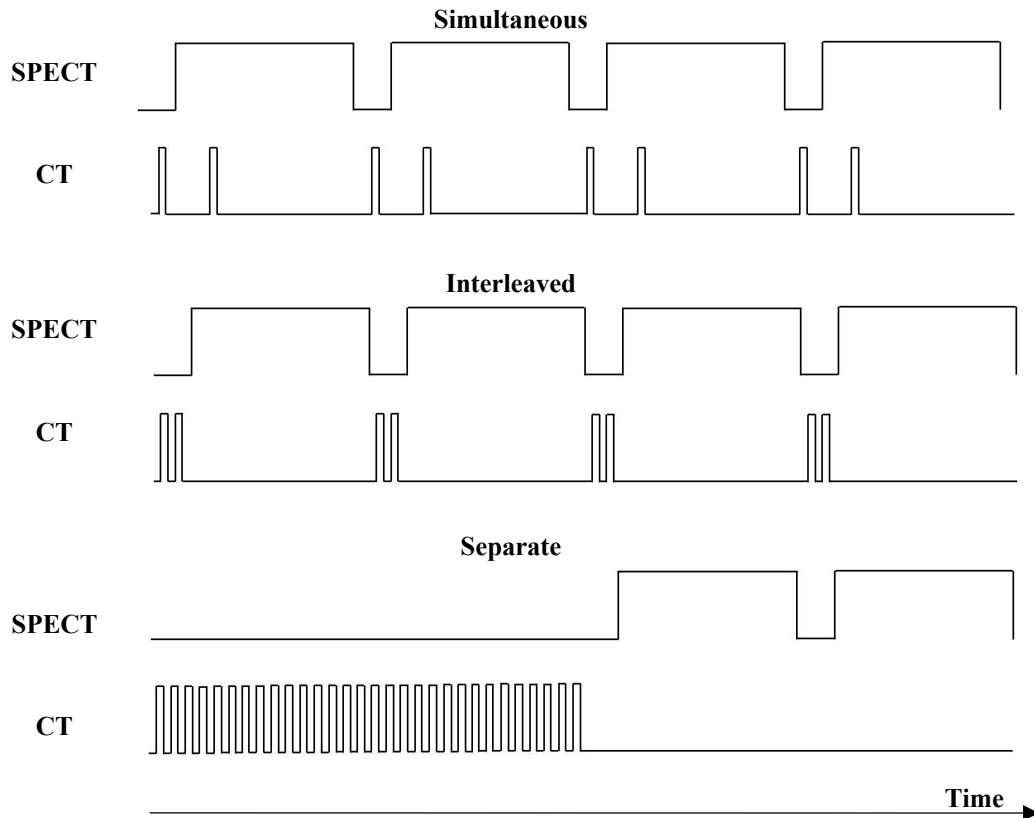
Figure 4.1: Timing diagrams for the proposed dual-modality imaging protocols. (Top) A simultaneous protocol will involve acquiring CT data while SPECT data is being acquired. (Middle) In an interleaved protocol, the CT system acquires data between SPECT data acquisition cycles. (Bottom) The CT system separately acquires a complete set of x-ray projection data, followed by a complete set of SPECT projection data. In the diagrams, a high signal indicates that the system is acquiring data. For each CT acquisition, there is a commensurate system motion since more angles are needed for CT than for SPECT. It is also understood in this diagram that the system will not move while SPECT data is being acquired.
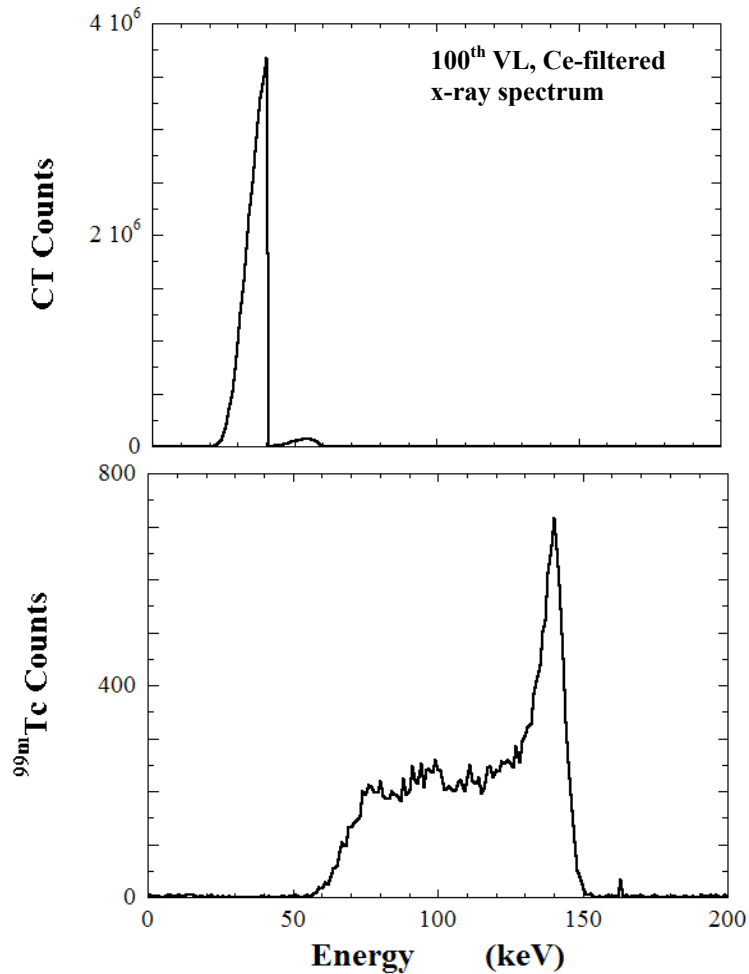
Figure 4.2: Spectra for (top) a single 1mAs x-ray exposure at 60 kVp tube potential using the Ce-metal 100th VL filtered x-ray beam, and (bottom) a 20 sec. acquisition at one projection of ^{99m}Tc activity (500 µCi) in a ~1000 mL breast.

Figure 4.2 compares a simulated spectrum of primary x-rays from a 1 mAs exposure at a tube potential of 60 kVp with a typical measured spectrum of emitted ^{99m}Tc activity acquired during a 20 sec. time interval (500 µCi of ^{99m}Tc activity in a ~1000 mL breast phantom). Note that the cumulative primary x-ray flux is orders of magnitude greater than the ^{99m}Tc flux emanating from the patient's breast. In addition, note that the mean and highest energies of the primary x-ray spectrum are widely separated from the

photopeak of the ^{99m}Tc spectrum. In addition, this x-ray spectrum is generated for a 1 mAs exposure, while the current CT system employs 2.5 mAs per x-ray exposure.

Given the relatively high x-ray flux from the transmission source, the compact source-image distance employed in the CT system, the common imaging FOV geometry, and the desirability of the SPECT system camera to closely contour the breast surface (increasing the sensitivity of the parallel-holed collimator of the gamma camera) it was proposed that the coincidental combination of multiple scattered x-ray photons and a scattered ^{99m}Tc gamma ray may be detected as aggregate events within the emission photopeak. This study empirically examines such a scenario with a view to optimizing the orientation of the SPECT camera relative to the x-ray transmission source in the integrated SPECT-CT system.

Current clinical dual-modality SPECT-CT imaging systems, including clinical whole body SPECT-CT systems used for breast imaging [59, 64], are implemented with their emission and transmission systems axially staggered by 50-60 cm [51, 183] to remove the potential for signal crosstalk, as well as to reduce equipment complexity [49]. This is similar to clinical whole body PET-CT systems currently in use [184-185]. One of the first common FOV combined PET and CT scanners [182] had a rotating coincident PET detector partial-ring with axially coplanar CT source-detector, but was abandoned due to severe cross-talk contamination between the emission and transmission systems. A similar concept SPECT-CT system was also abandoned for comparable reasons [57].

Dual-modality SPECT-CT small animal imaging systems have been developed that share a common FOV, and use pinhole collimation for increased emission sensitivity [186]. Pinhole collimators have low sensitivity for scattered x-rays, and the pyramidal support structure shields well against scattered radiation. Though pinhole SPECT has been investigated for dedicated breast imaging [187-188], the challenges of positioning close to the breast while using a pinhole collimator may be difficult to solve, and this approach has not yet been implemented for dedicated dual-modality breast imaging.

A potentially more difficult contamination problem exists for transmission imaging in the integrated system since the emission source (140 keV gamma rays emitted from the patient's body) cannot simply be turned off when the x-ray detector is acquiring projection data. In addition, unlike the collimated, energy-discriminating gamma camera used in SPECT, the un-collimated, energy-integrating x-ray detector aggregates the energy of all detected photon events, regardless of their individual energies. This means that primary and scattered γ-ray photons from the patient may contaminate each x-ray projection.

In these studies, anthropomorphic breast phantoms of various volumes were filled with water and ^{99m}Tc radioactivity, and exposed using various techniques by the x-ray source in various orientations relative to the x-ray source-detector axis. The effect of emission source contamination of the transmission x-ray projection image was then measured.
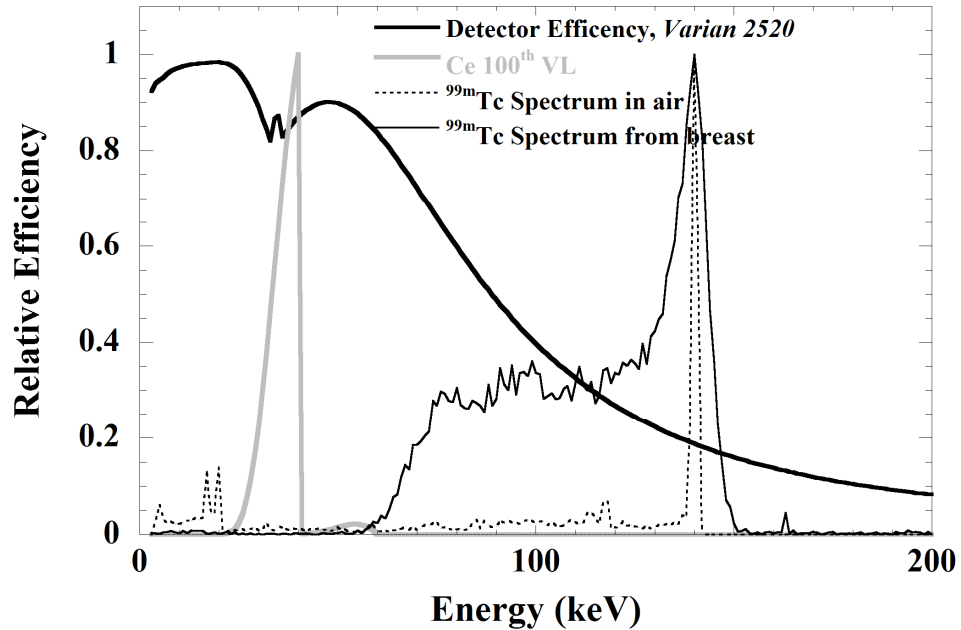
Figure 4.3: Plot of the detector efficiency of the Cs-I x-ray detector used in the experiments with superimposed representative spectra (height normalized) of the Ce-filtered x-ray cone beam at 60 kVp, a ^{99m}Tc spectrum in air, and the same ^{99m}Tc spectrum acquired through the breast.

Due to the effect of scatter in the breast and torso phantoms, the characteristic discrete emission of the ^{99m}Tc isotope is measured as a non-uniformly distributed energy spectrum of emitted photons. A proportion of these photons are, by virtue of the orientation of the x-ray detector to the breast and torso phantoms, incident on the uncollimated and otherwise unshielded x-ray detector.

A plot of the detection efficiency of the *Varian 2520* detector used in the CT system is shown in Figure 4.3. Superimposed on the plot are representative spectra of the filtered x-ray cone beam at a tube potential of 60 kVp, a ^{99m}Tc spectrum acquired in air and a ^{99m}Tc spectrum acquired after emission from a breast phantom. The plot indicates that while the detection efficiency of the 600 μm thick CsI(Tl) scintillator for the primary 140 keV gamma ray photons is relatively low (<20%), the efficiency increases substantially

as the energies of the incident (scattered) photons decrease and is close to 100% efficiency at low energies. The distributed probability of detection for the broad spectrum of ^{99m}Tc gamma rays fueled the need to study emission source contamination of the transmission image.

The x-ray detector efficiency shown in Figure 4.3 is accurate for ionizing radiation that is incident on the face of the detector. In the integrated SPECT-CT system design, the patient/emission source lies prone above and oblique to the detector, presenting a longer effective path length for any primary or scattered γ-ray incident on the scintillator surface. Longer effective photon interaction path lengths increase the likelihood of detection of the contaminating gamma rays by the x-ray detector and so the physical orientation of the digital x-ray detector relative to that of the patient may also play a role in the level of the observed contamination.

Transmission source contamination of the emission image was presented at the 2005 *IEEE Nuclear Science Symposium and Medical Imaging Conference* in San Juan, Puerto Rico, and published in the 2005 *Proceedings of the IEEE NSS and MIC*. Contamination of the transmission image by the emission source was presented at the *2006 SPIE Medical Imaging Conference* in San Diego and published in the 2006 *Proceedings of the SPIE*.

4.1. Contamination of the SPECT (emission) Image by the x-ray CT (transmission) Source

4.1.1. Methods

Since this research was conducted prior to the integration of the separate SPECT and CT systems, it was necessary to make modifications to the x-ray system gantry to enable dual-modality imaging with a common FOV. Figure 4.4 shows the setup that was used. The x-ray source and detector were attached to a cross beam (*80/20 Inc.*, Columbia, IN) that had been used previously in very early-stage CT experiments in the lab [123].
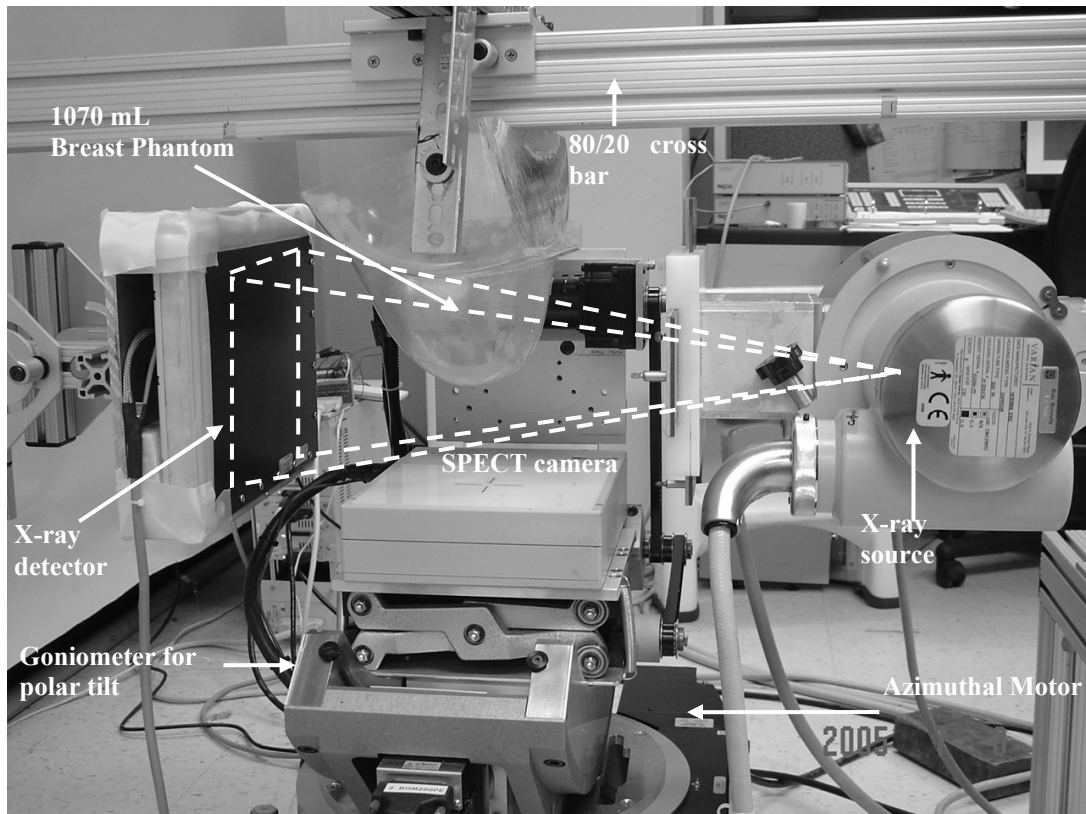
Figure 4.4: Photo of the x-ray source-detector (oriented right to left) and fully mobile SPECT systems positioned to have a common FOV for the purposes of these contamination studies. The x-ray system is attached to a modified cross-bar. The SPECT system is shown here with the camera directly below the pendant breast phantom volume that hangs in the common FOV of the modified systems. Various system components are indicated on the image.

The 55cm SID of the independent CT system was measured as accurately as possible, and the SPECT system was repositioned so that the SPECT system's center of rotation lay directly underneath the cross beam.

The SPECT and CT imaging systems were positioned relative to each other such that the central ray of the cone beam was laterally offset 5 cm from the anticipated center of rotation. This intentional offset configuration (Figure 4.5, top left) resulted in a half-cone beam acquisition, and was the standard positioning of the independent CT system before the CT and SPECT systems were integrated [149, 189]. Employing an offset geometry while allows imaging of larger breast volumes than are allowed when the central x-ray is centered. From the perspective of image contamination, one advantage associated with using an offset geometry is that the breast may provide some 'self- attenuation' of scattered x-ray photons incident on the SPECT detector, thus providing an advantage over a centered x-ray cone beam.

The SPECT camera was placed at three different azimuthal angles relative to the fixed central x-ray axis of the CT system (Figure 4.5, top left). Orientations were selected so that the gamma camera was closest to the anode of the x-ray source at -15º, perpendicular to the central x-ray axis at 0º, and positioned closest to the x-ray detector face at +10º. The x-ray cone beam geometry and short source to object distance of the CT imaging system dictated the limits of gamma camera orientation at -15° and +10°, to avoid the SPECT camera entering the x-ray cone beam FOV and physically truncating a section of the resulting CT transmission image.
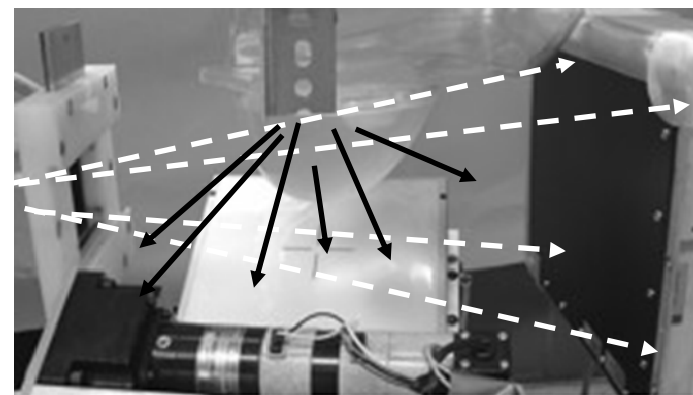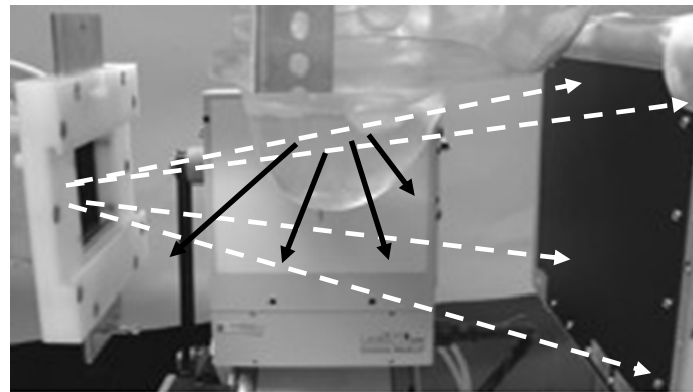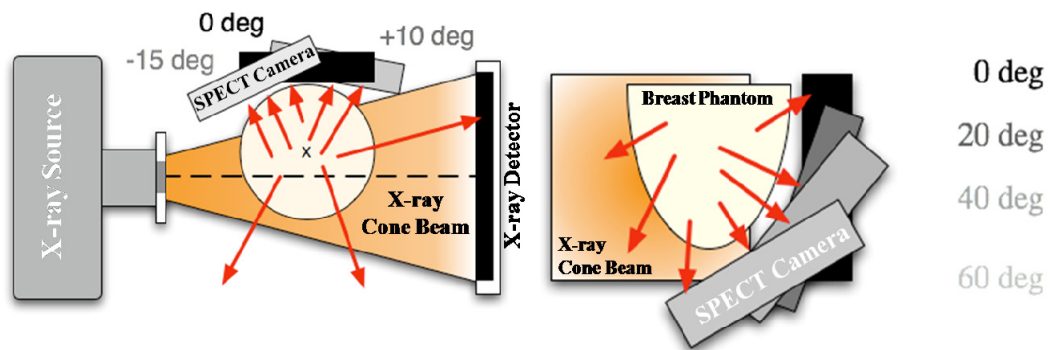
Figure 4.5: (Top row) Illustrations of the CT system's source and detector with visible x-ray cone beam (orange), pendant breast phantom, and SPECT camera from (top left) top-down and (top right) head on from the x-ray detector's viewpoint. Sample x-rays scattered from the breast volume in all directions are also illustrated (red arrows). Note the CT central ray (dashed line) laterally offset from the center of system rotation (marked by an X inside the breast). The illustrations show the SPECT camera contouring the phantom in three different azimuthal orientations (top left) in addition to the 4 polar orientations (top right) included in the study. (Middle row) Photograph of the x-ray system with superimposed x-ray cone beam footprint (dashed white lines) exposing the pendant breast phantom in the 0° azimuth angle and 0° polar angle orientation with x-rays scattered from the phantom (black arrows) impacting the gamma camera. (Bottom) Photograph of the SPECT system setup in the 0° azimuthal and 60° polar orientation.

Since the geometric efficiency of the SPECT camera to incident radiation changes as a function of polar tilt, four SPECT camera tilt angles were investigated at each of the azimuthal positions (Figure 4.5, top right). Given the various types of orbits already investigated with the SPECT system [100, 190], polar tilt angles ranging from 0-60° in 20° increments were selected and measured with respect to the vertical chest wall-to-nipple axis of the breast. To mirror intended clinical protocols, the separation of the SPECT camera face to the surface of the breast phantom was always less than 1cm.

Three fillable breast phantoms (*Radiology Support Devices, Inc.,* Newport Beach, CA) of various shapes and volumes were investigated, representing a wide range of breast sizes for clinical imaging [168]: small (325 mL), medium (1070 mL) and large (1500 mL) breasts [191].

Three levels of x-ray exposure were used to irradiate each phantom: 2.5, 5.0 and 10.0 mAs per projection (each level used 100 mA of tube current but varied the exposure time). The tomographic scan protocol routinely used in the MMI Lab employs a 2.5 mAs exposure per projection. Higher exposure levels were used to probe the effects of using such relatively high techniques in comparison to the routine x-ray exposure. Exposures lower than 2.5 mAs, while possible for breast CT techniques, were not measured since 2.5 mAs represents our routine x-ray exposure and an exposure lower than 2.5 mAs would be assumed to have a proportionally smaller scatter effect. Each acquired emission projection scan was 20 seconds long, which is twice what the routine SPECT acquisition time, with the x-ray exposures occurring during this time interval. The SPECT gamma camera uses a parallel hole collimator with hexagonal holes (1.2 mm flat-

to-flat (inner diameter), 0.2 mm lead septa, and 25.4 mm height). The camera has a

measured sensitivity of 37.9 cps/MBq using the collimator.
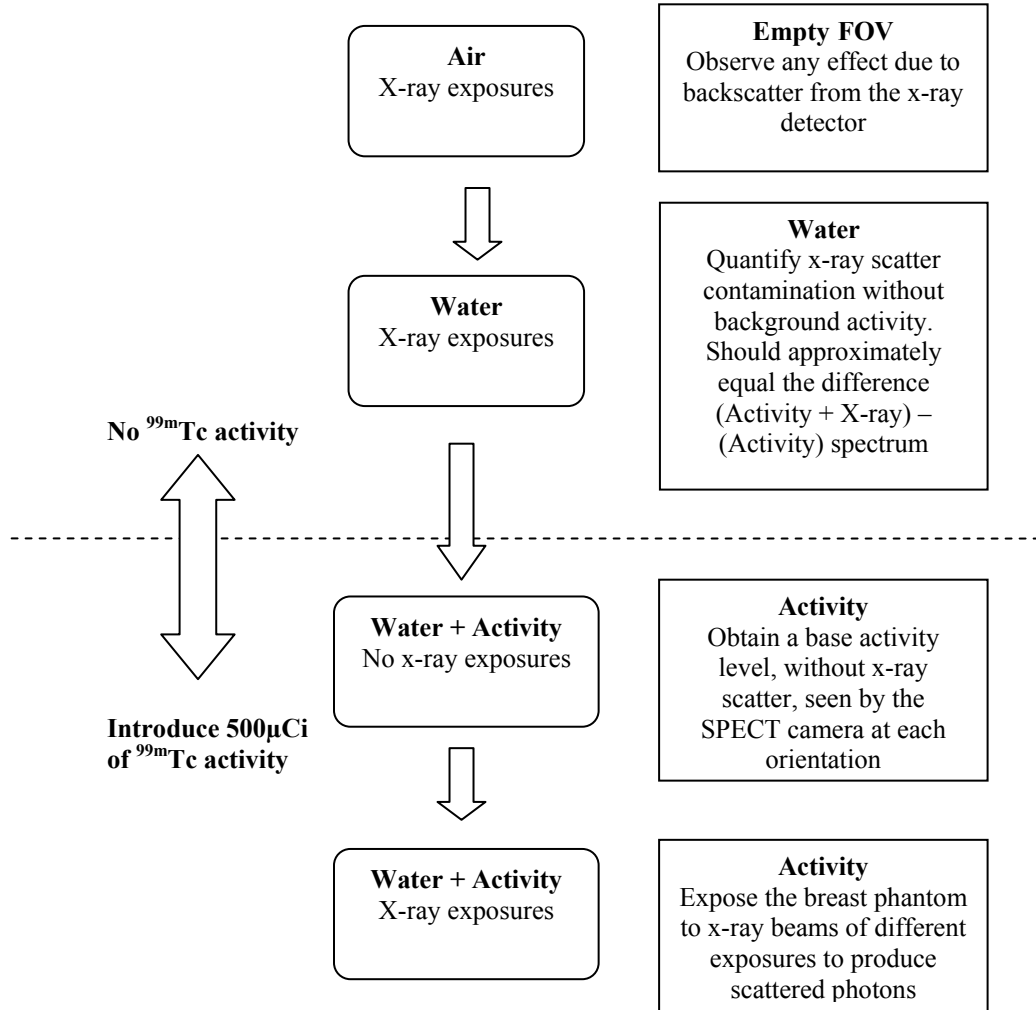
Figure 4.6: Flowchart of the protocol for each of the breast phantoms at each of the SPECT camera orientations.

The experimental protocol is illustrated in Figure 4.6. The SPECT camera initially

acquired data without a breast phantom in the common FOV of the imaging system – the

empty FOV was exposed to x-rays and the resultant backscattered image acquired on the

SPECT camera. This setup isolated the contribution of x-ray detector and other

component backscatter on contamination of the SPECT detector.

Each breast phantom was subsequently filled with water and irradiated in each camera position to investigate scatter contamination due to the presence of a material within the breast volume. Although the density of water (1.0 g/cm^3) is greater than that of fatty tissue and slightly less than that of fibrous breast tissue [153], water was used since the emission radionuclide-complex (^{99m}Tc-pertechnetate) could be dissolved and uniformly mixed throughout the breast volume, whereas it would not dissolve if oil (density $= 0.87$ g/cm^3) was used instead.

To observe the baseline emission spectrum from each breast, approximately 500 μCi of ^{99m}Tc-pertechnetate was next diluted in the water and multiple preliminary emission images and energy spectra were acquired, all without contaminative x-ray exposure. Lastly, a scan of each phantom (containing the ^{99m}Tc activity) was acquired by exposing the phantom to x-rays in order to observe and quantify transmission x-ray source contamination of the emission image for each gamma camera position. To ensure adequate variance and mirror the stochastic nature of the x-ray scatter, six exposures were applied during each 20sec. emission projection scan. Full list mode data files using an open energy window were acquired for all scans. Although lower hardware thresholds are possible with this CZT camera, a minimum hardware energy threshold was fixed at approximately 60 keV, the level routinely used in this lab for 140 keV imaging.

Retrospective energy windowing was used to quantify the photopeak contamination for each breast at each SPECT camera orientation and x-ray exposure level. In addition to

being time-normalized, the baseline emission scans were also decay-corrected to account for the time interval between data acquisition without and with x-ray exposure. The required decay time intervals were found from the time stamps on the original acquired data files.
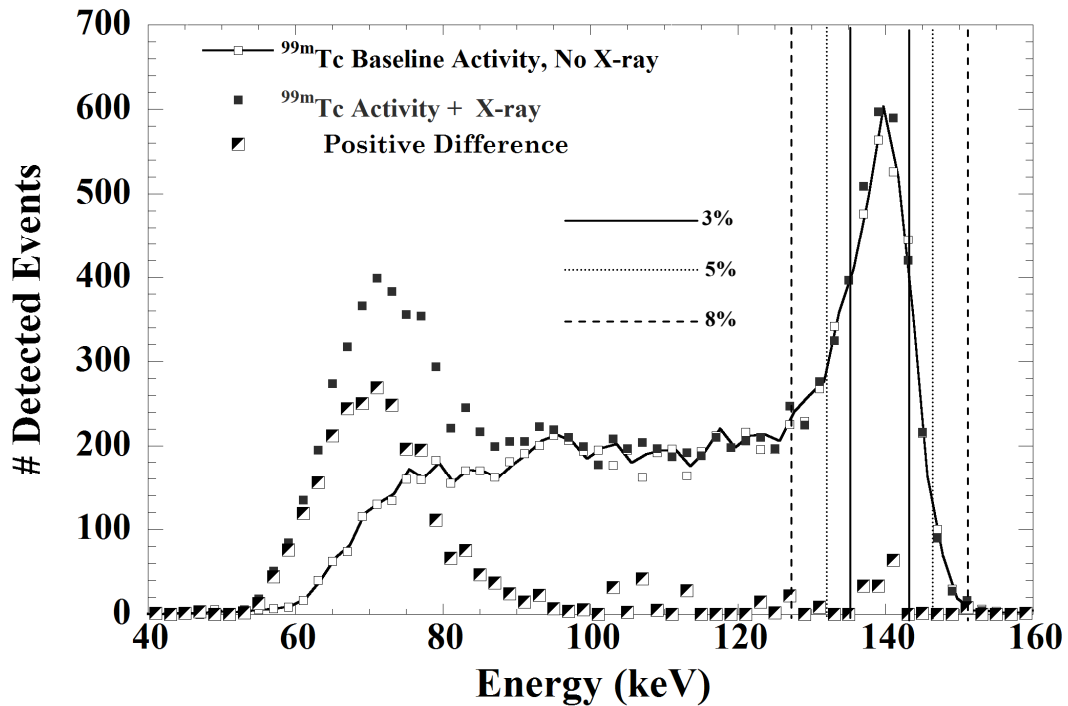
Figure 4.7: Sample energy spectra acquired for a single set up (1070mL breast, 0° azimuth, 40° tilt, 10mAs per exposure). Two conditions are illustrated: background or normal ^{99m}Tc emission spectrum from the pendant phantom without added x-rays, and the equivalent emission spectrum with included x-ray contamination. The positive-valued difference of the previous two spectra is also shown. This difference is used to calculate photopeak contamination using the illustrated energy windows pertinent to ^{99m}Tc breast imaging.

Contamination was quantified by initially calculating a difference spectrum between the decay-corrected baseline emission scan without x-ray exposure and data acquired with contaminating x-ray exposures. This difference spectrum was modified to include only positive difference values, since x-ray contamination adds detected events to the acquired emission data. Four energy windows about the photopeak were investigated in the data analysis: an open energy window and windows of ±3%, ±5% and ±8% (Figure 4.7). The

photopeak contamination for each energy window was then quantified by calculating the integral number of positive-truncated counts from the difference spectrum within the energy window as a percentage of the integral number of counts detected within the same energy window during the emission scan, acquired with the particular x-ray exposure.

Figure 4.7 shows energy spectra acquired during a 20 sec. baseline scan of ^{99m}Tc activity from the 1070 mL breast phantom without added x-ray exposure and an x-ray contaminated ^{99m}Tc spectrum. The absolute-valued difference calculated between the two acquired spectra is shown with the positions of the various energy windows used to quantify photopeak contamination indicated on the image (see also Tables 4.1 to 4.3).

4.1.2.   Results

4.1.2.1.   Acquired energy spectra

Contaminated emission image spectra for the 325 mL, 1070 mL and 1500 mL breast phantoms are shown in Figures 4.8 and 4.9. Figure 4.8 contains spectra from emission projections acquired at a fixed azimuthal angle of 0° relative to the central cone beam x-ray but with varying polar tilt angle. As the SPECT camera polar angle is increased, an increase in the total number of detected counts, specifically photopeak counts, is observed within the constant 20 sec. acquisition. This is consistent with the gamma camera viewing an increased volume of the breast, and is not due to x-ray scatter. Figure 4.9 illustrates x-ray contaminated energy spectra acquired at a constant camera polar tilt angle of 40° but with varying azimuthal angle relative to the central x-ray. In these figures there is also a trend of increasing scatter contamination with both increasing

breast size and x-ray exposure, consistent with the increased x-ray flux. Data for each orientation and exposure level presented here represent the cumulative effects of six x-ray exposures for that particular setup. Increased cumulative contamination of the emission spectra is readily apparent in the 60-85 keV region as x-ray exposure and polar tilt angle are increased. With an applied hardware threshold of 60 keV, scatter contamination at energies lower than this threshold may in fact be larger than what is apparent in these spectra. It is encouraging for practical considerations of the imaging protocol that the most obvious scatter is constrained to energies well below the 140 keV photopeak of ^{99m}Tc (Figures 4.8 and 4.9) since, in practice, SPECT images of the breast are generated using data windowed about the photopeak (see Figure 4.10).

Calculated percentage photopeak contamination of the various emission image energy spectra are reported in Tables 4.1, 4.2 and 4.3 for each of the three breast sizes. The results indicate barely measureable levels of photopeak scatter contamination, generally much less than 2% per x-ray exposure across all x-ray exposure levels and azimuthal and polar orientations of the camera. Indeed, there is no clearly identifiable trend in the contamination results seen with varying camera orientation. The highest levels of contamination occur in the case of an open energy window. Since using an open window is not practical in SPECT imaging, the result is not of concern and can be seen as a purely illustrative record of total x-ray scatter contamination.
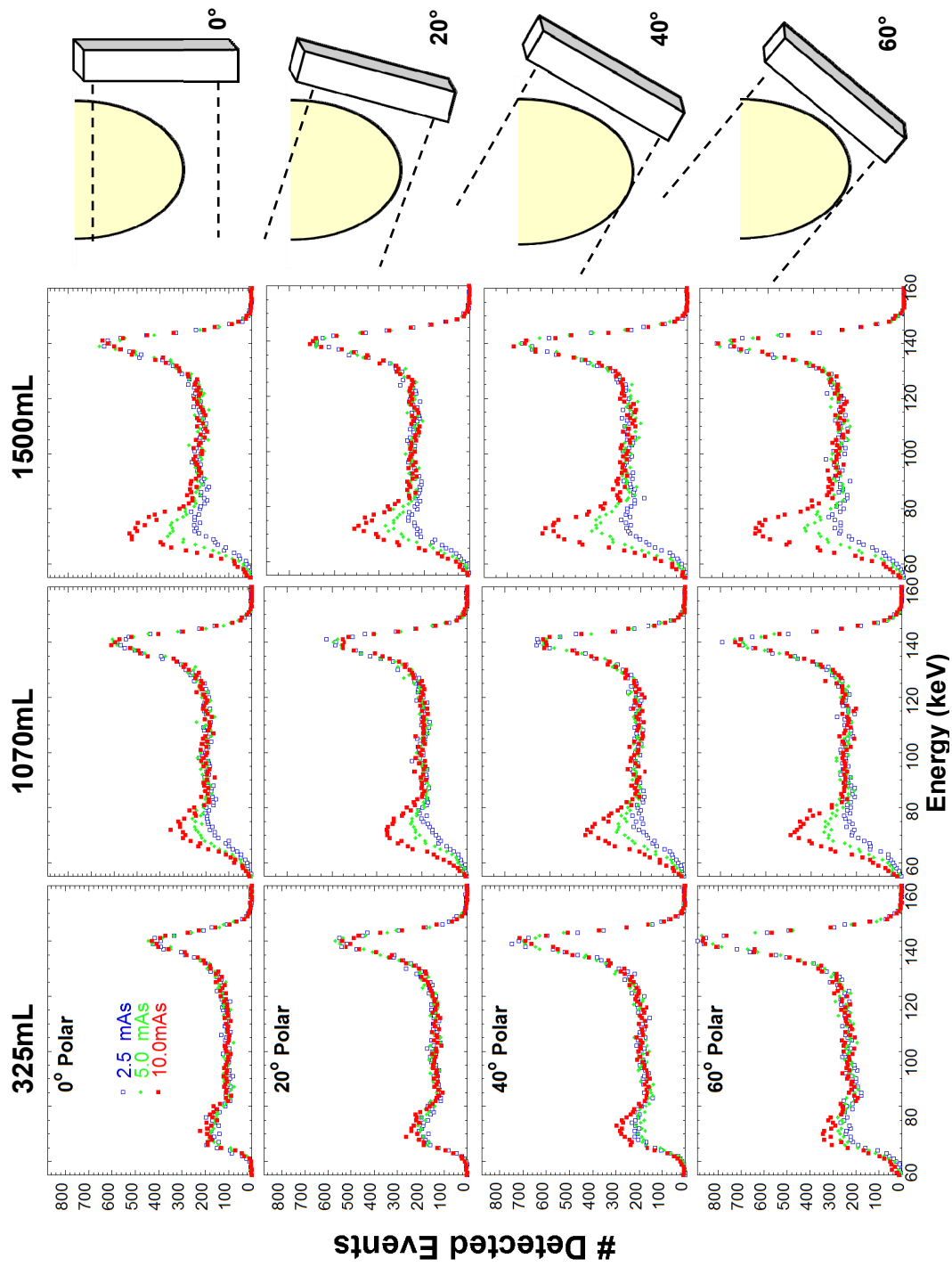
Figure 4.8: Transmission scatter-contaminated emission spectra acquired with a constant azimuthal angle of 0°relative to the central ray of the cone beam for the three indicated breast sizes. Polar tilt angle varies from (top row) 0° to (bottom row) 60°. As polar angle is increased, total detected counts in fixed 20 sec. acquisition increase, since more of the breast volume is viewed. Illustration of the orientation of the SPECT camera to the breast are shown to the right of the images.
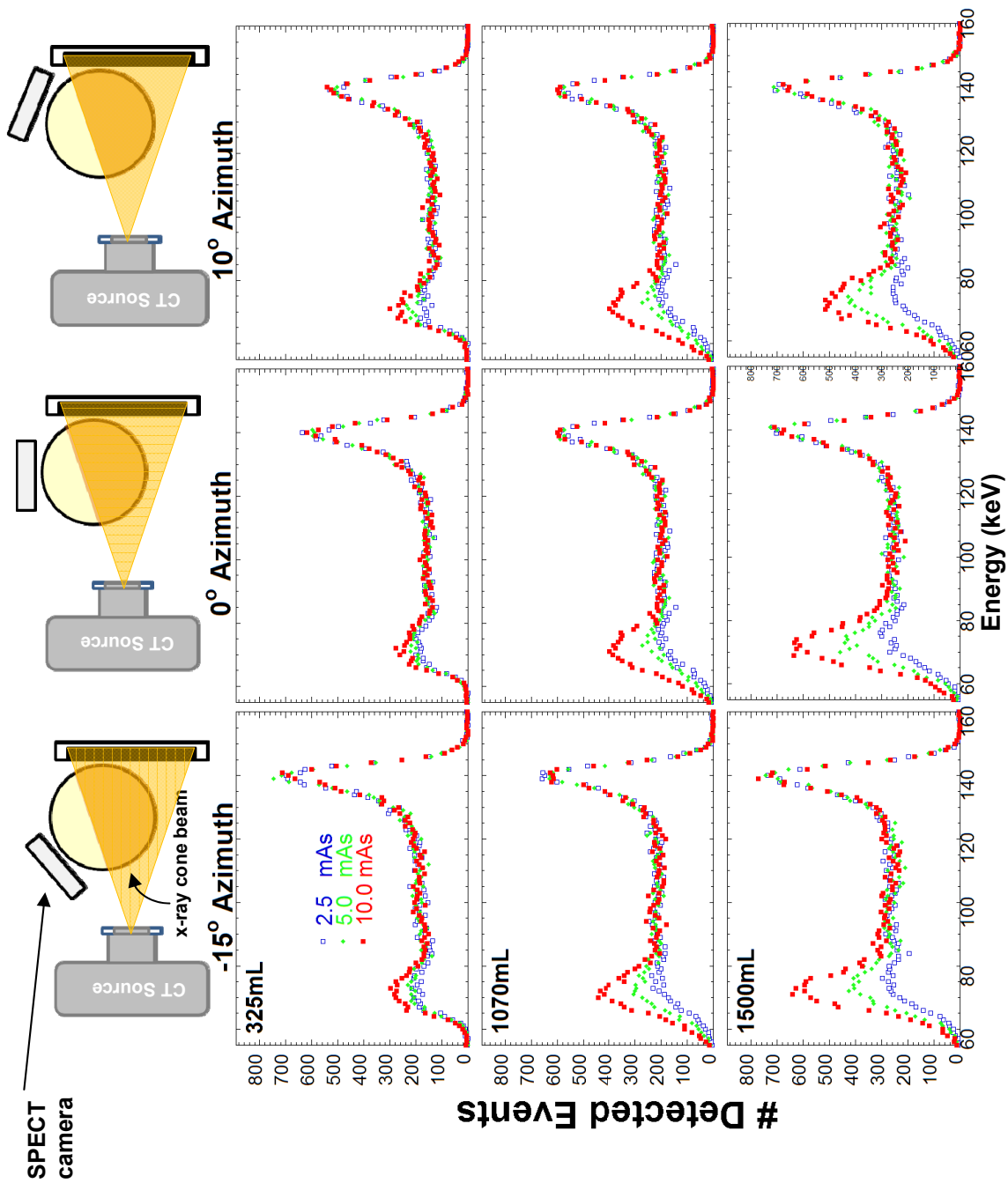
Figure 4.9: Transmission scatter-contaminated emission spectra acquired at a polar tilt angle of 40° for the three indicated breast sizes. Azimuthal angle varies from (left) -15° to (right) +10°, with illustrations at the top indicating the orientation of the SPECT camera to the x-ray source-detector.

Table 4.1 Maximum and minimum photopeak contamination for the 325 mL breast across the full range of polar angles at each azimuthal angle, and for each energy window. Photopeak contamination levels <0.1% are represented by a dash.

X-ray Exposure (mAs)	Energy Window (%)	Photopeak contamination per x-ray exposure (%)					
		-15° azimuth		0° azimuth		+10° azimuth	
		Min.	Max.	Min.[†]	Max.	Min.	Max.
2.5 mAs	Open	1.5	4.0	1.6	2.7	1.1	3.2
	±3	0.3	1.9	-	0.6	0.2	0.6
	±5	0.3	2.2	0.2	0.5	0.3	0.7
	±8	0.3	2.2	0.3	0.6	0.4	0.7
5.0 mAs	Open	1.9	3.8	1.6	3.1	1.7	3.0
	±3	0.5	1.7	0.1	0.5	0.2	0.4
	±5	0.4	1.8	0.3	0.6	0.3	0.5
	±8	0.4	1.9	0.3	0.7	0.3	0.6
10.0 mAs	Open	2.4	4.2	2.3	3.5	2.0	3.9
	±3	0.2	2.1	-	0.6	0.2	0.3
	±5	0.3	2.1	0.1	0.6	0.3	0.4
	±8	0.3	2.1	0.3	0.6	0.4	0.5

[†]   Photopeak contamination < 0.1% per x-ray exposure is represented by a - symbol

Table 4.2 Maximum and minimum photopeak contamination for the 1070 mL breast across the full range of polar angles at each azimuthal angle, and for each energy window. Photopeak contamination levels <0.1% are represented by a dash.

X-ray Exposure (mAs)	Energy Window (%)	Photopeak contamination per x-ray exposure (%)					
		-15° azimuth		0° azimuth		+10° azimuth	
		Min.	Max.	Min.	Max.	Min.	Max.
2.5 mAs	Open	1.1	1.5	1.1	1.3	1.0	1.7
	±3	0.5	0.9	0.4	0.6	0.4	0.6
	±5	0.6	1.1	0.4	0.5	0.4	0.7
	±8	0.7	1.2	0.4	0.6	0.5	0.7
5.0 mAs	Open	2.1	2.6	1.8	2.5	1.9	3.1
	±3	0.4	0.7	0.3	0.5	0.2	0.7
	±5	0.4	0.9	0.3	0.5	0.3	0.8
	±8	0.5	0.8	0.4	0.5	0.4	0.8
10.0 mAs	Open	2.8	3.7	2.8	3.6	3.2	4.5
	±3	0.3	0.8	0.4	0.7	0.3	0.9
	±5	0.4	0.7	0.3	0.5	0.3	1.1
	±8	0.4	0.8	0.4	0.6	0.5	1.2

Table 4.3 Maximum and minimum photopeak contamination for the 1500 mL breast across the full range of polar angles at each azimuthal angle, and for each energy window. Photopeak contamination levels <0.1% are represented by a dash.

X-ray Exposure (mAs)	Energy Window (%)	Photopeak contamination per x-ray exposure (%)					
		-15° azimuth		0° azimuth		+10° azimuth	
		Min.	Max.	Min.	Max.	Min.	Max.
2.5 mAs	Open	0.6	0.6	0.6	0.9	0.6	0.6
	±3	-	0.3	0.1	0.2	-	0.3
	±5	0.1	0.4	0.1	0.5	0.2	0.3
	±8	0.3	0.5	0.2	0.7	0.3	0.5
5.0 mAs	Open	0.8	1.1	1.3	2.5	0.9	1.4
	±3	-	0.3	0.1	0.3	-	0.3
	±5	0.1	0.3	0.1	0.4	0.1	0.3
	±8	0.2	0.4	0.3	0.6	0.3	0.5
10.0 mAs	Open	2.2	3.1	2.3	3.3	1.7	3.3
	±3	-	0.2	-	0.2	-	0.1
	±5	0.1	0.2	0.2	0.4	0.2	0.2
	±8	0.3	0.4	0.3	0.5	0.3	0.4

4.1.2.2.   Energy windowed emission images

A series of emission images of the 325 mL, 1070 mL and 1500 mL breast phantoms are shown in Figure 4.10. The images in Figure 4.10 (top) were acquired with an open energy window for the noted cases of added x-ray exposure (2.5, 10 mAs) in addition to the baseline emission case without added x-ray exposure (0 mAs). The images in Figure 4.10 (bottom) were acquired with a constant x-ray exposure of 2.5 mAs and illustrate the spatial distribution of scatter with and without energy windowing for various x-ray exposure levels. The images were acquired in list-mode and post-processed using energy windows as indicated (open, ±8% and ±3%) to illustrate the progressively narrower range of energies allowed as constituent contamination elements in the images.

The spatial gradient in scatter intensity (apparent from left to right) is due to the x-ray flux incident on the left side of the breast. For the open energy window, the scatter contamination increases in severity with increasing x-ray exposure. Figure 4.10 (bottom) indicates no visible scatter contamination of the image when the emission data is restricted to the ±8% or ±3% energy window about the photopeak. This is consistent with the measured energy spectral distributions previously described (Figures. 4.8, 4.9, and Tables 4.1 to 4.3).

4.2. Emission source (^{99m}Tc) contamination of the transmission (x-ray CT detector) image

4.2.1. Theoretical calculation of contamination in the transmission image

This section makes a theoretical calculation of the expected level of ^{99m}Tc contamination in an x-ray projection image. The calculation uses activity levels employed in contamination experiments described in Section 4.3. The calculation also assumes that all of the source of ^{99m}Tc activity is concentrated at a point located above the x-ray detector at the isocenter of the CT system and takes into account the:

- absolute ^{99m}Tc activity in the volume of interest – **16 mCi**

- distance of the concentrated point source of activity from the detector active edge – **22.4 cm**

- area of the detector active face relative to the surface area of the sphere of activity at that distance – **0.08**

325 mL   **1070 mL**   **1500 mL**

Open energy window

0 mAs

2.5 mAs

10.0 mAs

325 mL   **1070 mL**   **1500 mL**

2.5 mAs x-ray exposure

Open

±8%

±3%
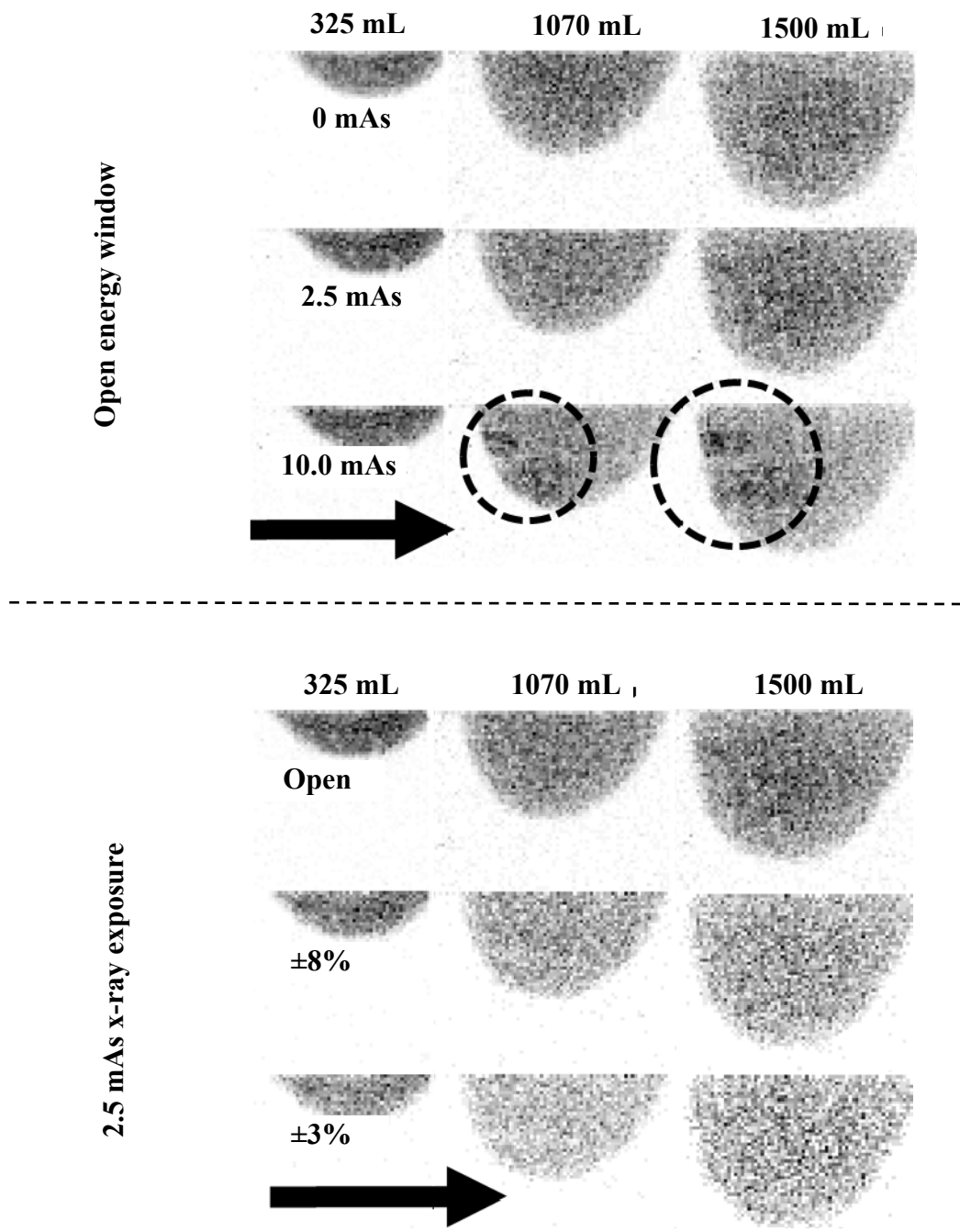
Figure 4.10: Emission images of the three breast phantoms each acquired at an azimuthal angle of 0° and a polar tilt of 20° using (top) an open energy window with varying x-ray exposures and (bottom) varying energy windows about the photopeak at a constant x-ray exposure of 2.5 mAs. Note, at left, that the highlighted image contamination increases in the open window case with both increasing x-ray exposure and breast size, but is absent at right, as the energy window tightens about the photopeak. The direction of incident x-rays is indicated with arrows.

- fill factor of each x-ray detector pixel – **57 %**

- efficiency of the x-ray detector at the energy of the incident gamma rays – (**19% for 140 keV ^{99m}Tc γ-ray photon**)

- exposure time of the x-ray detector per projection – currently we use **25 ms**.

The isocenter of the integrated CT system, with a 60 cm SID, is coincident with the vertical axis of rotation of the system, and is nominally located 21.8 cm from the detector active edge. If it is assumed that the point source of ^{99m}Tc is located along the vertical axis of rotation and 5cm vertically above the level of the active edge of the *Varian 2520* detector (approximating the location of the patient's heart), the mean distance to the middle of the detector's active area is 27.8 cm. The source of activity is closest to the top edge of the x-ray detector, a distance of 22.4 cm. Since the flux of emitted γ-ray photons reduces according to the inverse square of the distance from the source, this shortest distance of the source from the detector, 22.4 cm, will be used to calculate worst case scenario emission contamination levels.

The maximum amount of contaminating ^{99m}Tc activity added to the volume of interest (see Section 4.3) was **16 mCi** which equates to **5.92×10^8 Bq**. This is used as the upper bound on ^{99m}Tc γ-ray activity. This specific level of activity is calculated using clinically relevant activity concentrations of ^{99m}Tc during patient imaging [22].

The CT technique currently employed uses a 25 ms x-ray exposure time and this is assumed to be the time interval that the x-ray detector is active and integrating the energy of incident photons.

Assuming isotropic emission of the ^{99m}Tc γ-rays in the volume, the proportion of γ-rays emitted from the source that are incident on the x-ray detector at a distance of 22.4 cm is equal to the proportion of the surface area of an isotropic sphere at a radius of 22.4 cm that is covered by the active area (25 x 20 cm) of the x-ray detector:

$$\frac{(25 \times 20)}{4\pi \times 22.4^2} = \mathbf{0.08} \qquad (4.1)$$

This calculation assumes only primary photons are emitted from the volume of interest and means that the number of primary γ-rays impacting the entire detector active surface is:

$$5.92 \times 10^8 \times 0.08 = \mathbf{4.7 \times 10^7} \text{ } \mathbf{Bq} \qquad (4.2)$$

for a 1 second exposure. This equates to $\mathbf{1.2 \times 10^6}$ γ-rays emitted in the standard 25 ms x-ray exposure time. The fill-factor, or photosensitive area of each x-ray detector pixel is 57%, and so this reduces the effective incident γ-rays to:

$$1.2 \times 10^6 \times 0.57 = \mathbf{6.8 \times 10^5} \qquad (4.3)$$

per 25ms exposure interval across the entire active face of the detector.

This figure for ^{99m}Tc contamination assumes all the incident γ-ray photons on the active detector face are in fact detected. However, the detection efficiency of the x-ray detector is approximately 19% for 140 keV γ-rays and remains far below 100% for much of the ^{99m}Tc spectrum. Simulations of the Ce-filtered cone beam x-ray spectrum after passing through a 14 cm breast of 100% glandular (shown in Figure 4.9) indicate that the 2.5

mAs beam at 60 kVp has a cumulative photon flux of approximately **3.52x10⁵** photons **per cm²**. The beam will be most heavily attenuated by the 100% glandular breast and so this is a worse case post-breast beam flux, with other breast compositions transmitting more photons than the 100% glandular breast. After taking the fill factor into account and assuming approximately 85% detection efficiency for 36 keV photons using the Varian 2520 (see Figure 4.9), a total of approximately **85x10⁶** photons are detected across the detector active face (25x20 cm²) in a 25 msec. x-ray exposure.

This means that the ratio of primary γ-rays to primary x-rays over the entire face of the detector is approximately

$$\frac{6.8\text{x}10^5}{85\text{x}10^6}\text{ x }100 = \textbf{0.8\%} \tag{4.4}$$

Such a small level of contamination may manifest itself as one of many other sources of non-idealities in the image collection pathway, and so taking these analyses as a whole indicates that contamination of the transmission image by the emission of γ-rays from the breast volume may not be a concern.

Chronologically, this theoretical calculation was carried out after empirical experiments had been performed to quantify the level of emission contamination in the transmission image. A description of these experiments follows.

4.2.2. Quantifying emission contamination in the x-ray image in the independent CT system

To initially quantify the effects of emission source contamination of the transmission image, the same three breast phantoms that were used in the experiments quantifying transmission contamination of the emission image, 325, 1070 and 1500 mL, were each attached to an anthropomorphic torso phantom (*Radiology Support Devices*, Newport Beach, CA) that was filled with approximately 7000 mL of water (see Figure 4.11). The anthropomorphic torso phantom provided a realistic non-uniform distribution and scatter medium for the ^{99m}Tc radioactivity in the patient's chest. In the experiments, undertaken prior to the development of the shielded patient bed, a ¼" thick lead (Pb) plate was fastened to the torso to simulate the shielding anticipated by a shielded patient bed (see Chapter 5 for the shielded bed and also Figure 4.13 for the Pb shield used in this experiment, bottom row, right) . A ¼" Pb shield attenuates over 99% of photons at 140 keV. The independent breast CT system was used in the initial set of experiments with its compact 55 cm SID, and also with its 3D orbiting capabilities to allow tilting of the x-ray detector for improved sampling of the breast volume.

Single projections and reconstructed tomographic data were acquired and analyzed to observe effects on image quality due to emission source contamination. Projection data sets were acquired using each of the three breast phantoms. Images were acquired with the detector in two positions: lateral to the phantom in position A, and medial-inferior to the phantom in position B (Figure 4.11). The positions are offset approximately 90° from each other, and were used to measure differences due to orientation between the source-detector axis and the contaminating torso emission source. To equalize the signal level in the breast images, each projection image was acquired using 2.5 mAs per projection but

using three different tube exposure times: 40 ms, 100 ms and 250 ms, to investigate the effect of exposure times on any quantified contamination. The breast-torso combination was attached to a custom made support and suspended in the detector FOV. Ten successive exposures in each orientation were then acquired using each x-ray exposure time interval.

Due to the different geometrical orientation of the uncollimated x-ray detector to the torso, image contamination was expected to be maximized when the detector was located directly below the torso of the patient (position B) and minimized when located lateral to the patient (position A). Additionally, with the total x-ray flux kept constant, a longer exposure time was expected to generate increased image contamination since proportionally more emission source decays can impact the imaging detector.

Images were acquired under the conditions shown in Figure 4.12: (1) no radioactivity in the breast and torso region (cold breast, cold torso = CBCT), which simulates a patient who has not been injected with a radiotracer; (2) radioactivity in the breast but no radioactivity in the torso (hot breast, cold torso = HBCT), which represents the ideally shielded patient, or one with an ideally localizing radiotracer, for both emission and transmission scans; and, (3) radioactivity in both the breast and torso (hot breast, hot torso = HBHT), which simulates the worst case scenario of having a radiopharmaceutical injected patient without a shielded bed.
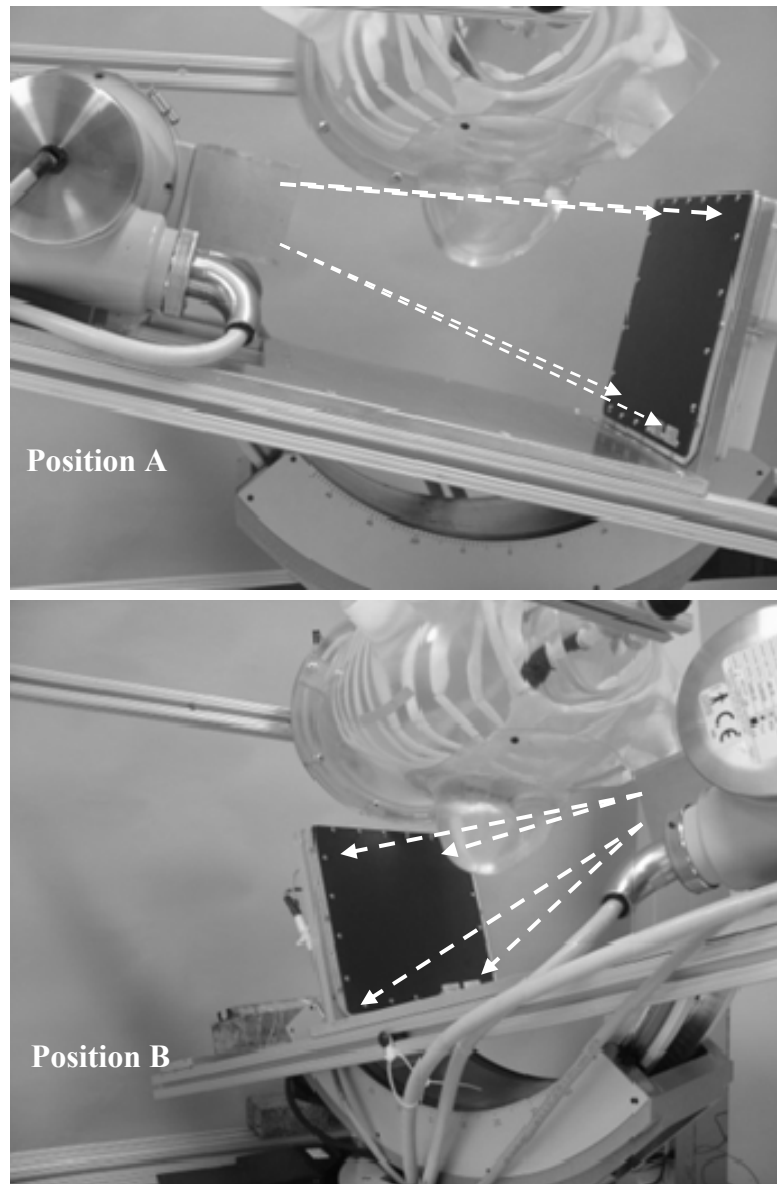
Figure 4.11: The x-ray system imaging the breast and torso phantoms in Positions A, medial-lateral to the torso, and Position B, in a superior-oblique vantage with respect to the torso, where the x-ray detector is immediately underneath the torso.

An additional condition tested with the 1070 mL breast was with tailored PB shielding attached to and covering a majority of the torso to mimic the intended bed shielding during a scan (or HBHT with Shielding = HBHTS).
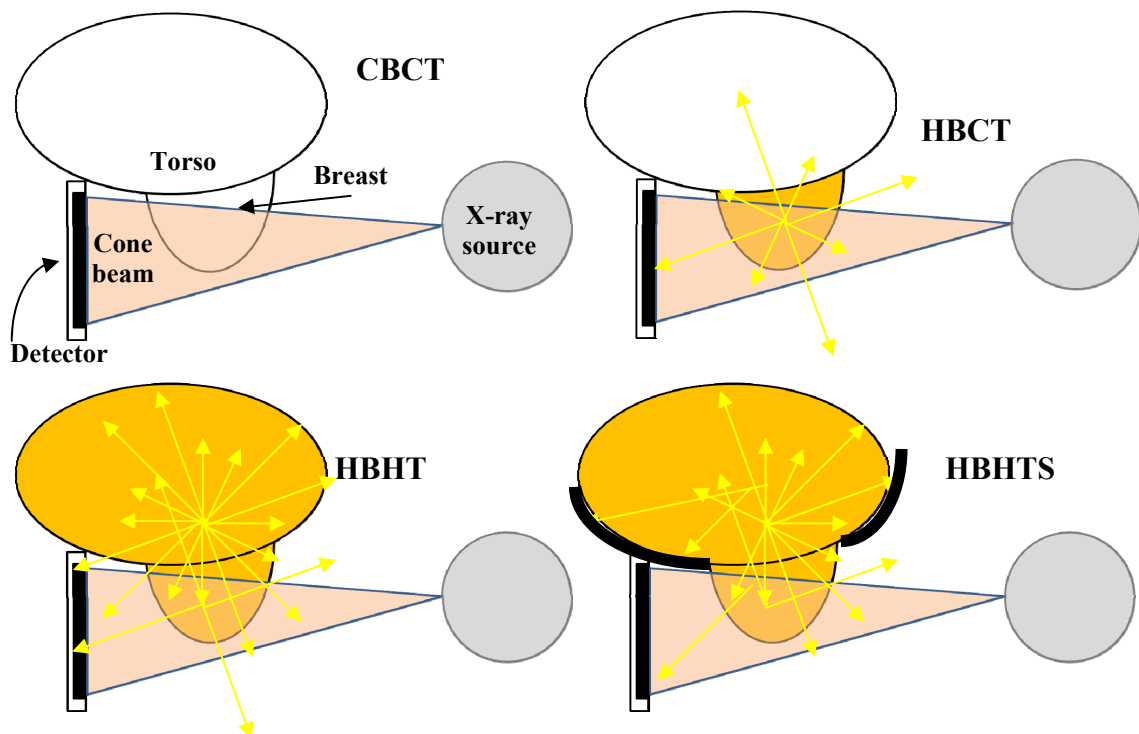
Figure 4.12: Illustrations of the torso and a single breast being irradiated by an x-ray cone beam (red) in the various conditions with and without added radioactivity described in the text. The presence of radioactivity is denoted by the orange background and the yellow arrows. The active area of the detector is shown in black. The lead shielding in the HBHTS case is denoted by the thick black curved line.

Initial CBCT images of the breast and torso phantoms were used as baseline (control) images against which emission image contamination was measured. Based on previously determined clinical uptake with ^{99m}Tc labeled radiotracers [146], an activity concentration of 0.33 µCi/mL was added to the water-filled breast via catheter, while keeping the torso phantom 'cold' to estimate contamination seen from the breast region alone. A dye (food coloring) was also added to the water to ensure adequate visual mixing of the radioactivity in the torso. The imaging setup for the three breasts attached to the torso phantom and for the 1070 mL breast with added lead shielding is shown in Figure 4.13.

Tomographic data was additionally obtained with a custom designed 3D orbit about the medium sized (1070 mL) breast only. The ½" thick Pb shield (see Figure 4.13), along with the sizeable imaging dead-zones of the x-ray tube, made it impossible to acquire tomographic data of the 325 and 1500 mL phantoms, and so it was decided to acquire tomographic data of just the 1070 mL phantom.

To acquire tomographic breast data, a custom 3D image acquisition orbit was generated with varying azimuthal and polar tilt angles that allowed close contouring and adequate sampling of the pendant 1070 mL breast volume (Figure 4.14). CT data was acquired under the three conditions of radioactivity described above, with the control data being breast and torso without added radioactivity. The collected projection data were reconstructed using the standard OSTR reconstruction algorithm with 10 iterations and 8 subsets.

To analyze the projection images for each breast size and x-ray exposure set up, four regions of interest (ROIs) were drawn (as shown in Figure 4.15 with the 1070 mL breast) and the mean and standard deviation value of each ROI obtained. Two ROIs were drawn inside the breast region (B #1, #2) and two in the background region (BG #1, #2), combined into two breast-background ROI pairs.
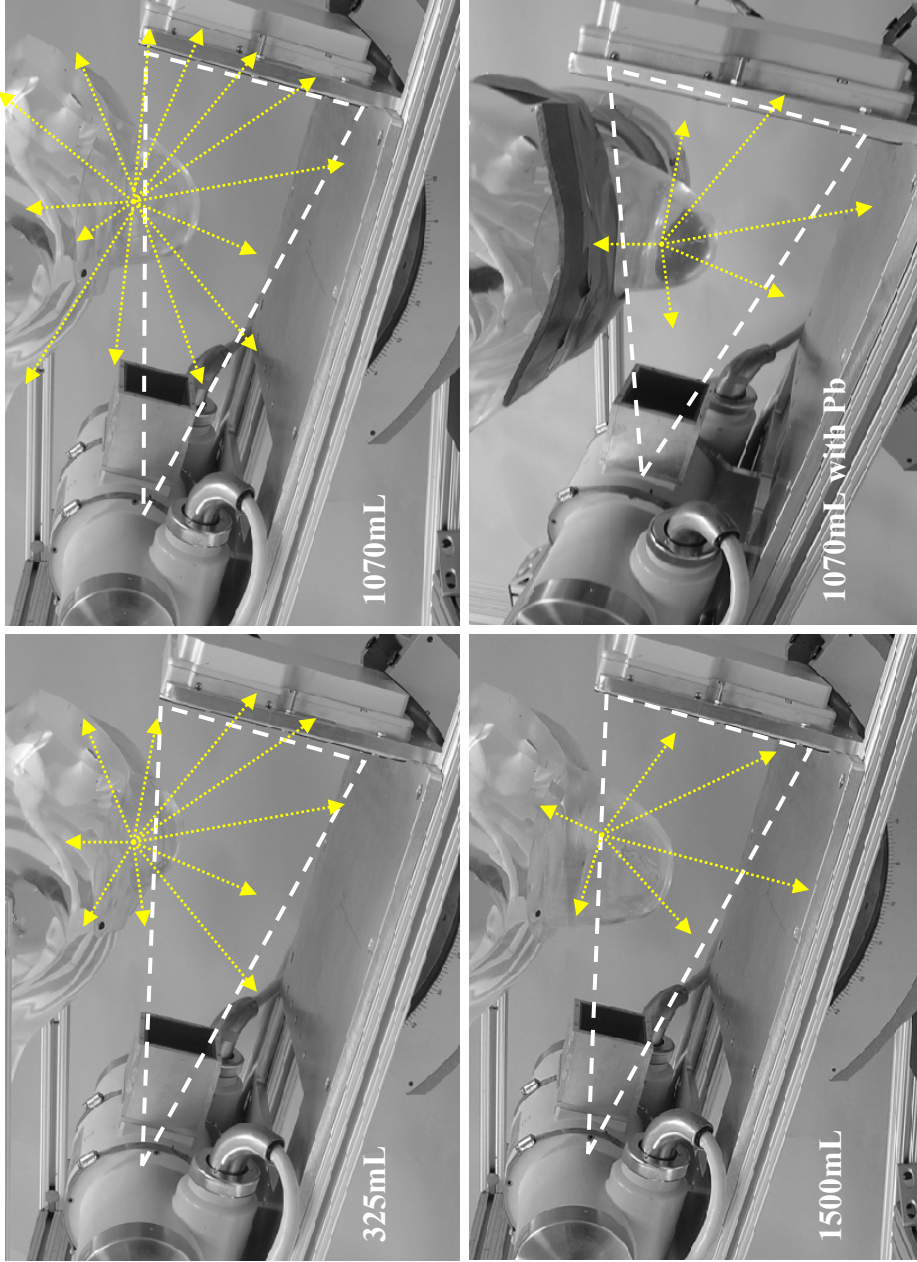
Figure 4.13 Images of the torso and various breast phantoms suspended into the independent breast CT system FOV. The approximate outline of the cone beam x-ray is also shown, as are ^{99m}Tc ray paths emanating from inside the breast volume. (Lower right) Combined Pb shield, torso and 1070 mL breast.
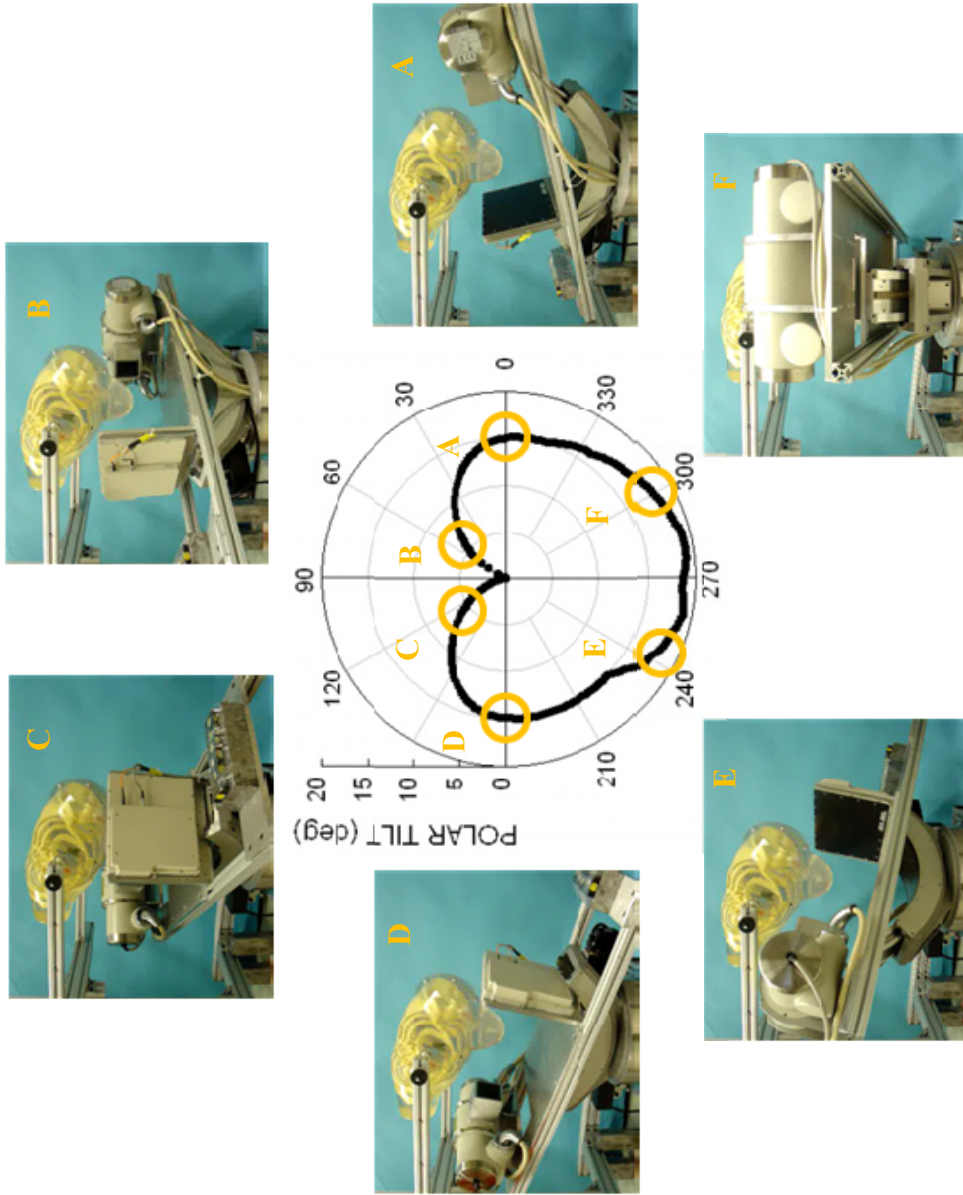
Figure 4.14: A series of photographs of the independent CT system oriented in various azimuthal and polar orientations indicated on the (center) polar plot of the same trajectory.

One ROI pair (#1) was drawn closest to the top of the detector (nearest the torso) since this region was thought to see the largest emission contamination with the detector placed below the torso region, as in position B (see Figure 4.11) .
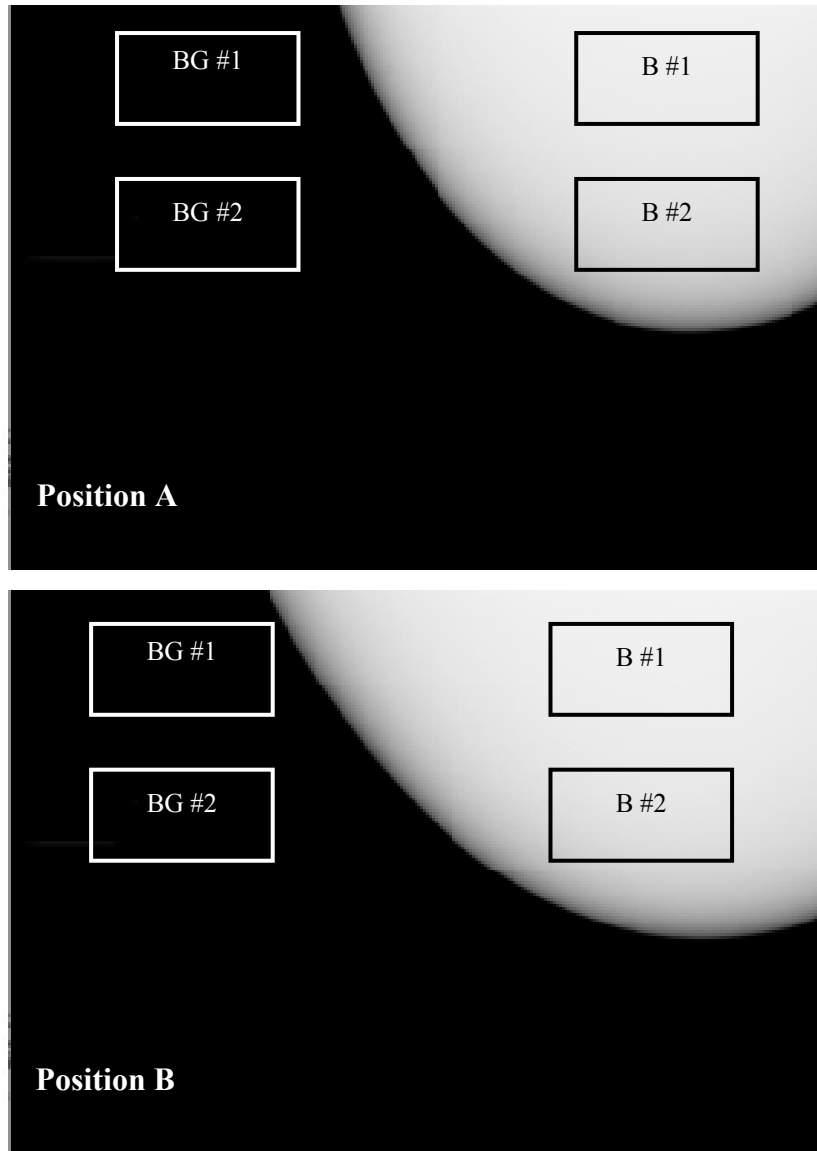
Figure 4.15: Projection images of the 1070 mL breast phantom in positions A and B (see Fig. 4.13) with the placement of the breast and background ROIs superimposed on the images. For the image gray scales, dark means high exposure (pixel value), and lighter means less exposure.

The other ROI pair (#2) investigates contamination closer to the nipple. Comparisons were made between mean and standard deviation values to identify trends in contamination with changing radioactivity levels/conditions in the breast and torso.

A standard deviation image was also generated for each breast size from the multiple projection images taken under each radioactivity condition. This image was examined for any obvious areas of contamination caused by emission contamination, since it was believed that any area of the x-ray detector contaminated more than another would have a greater associated standard deviation in pixel values.

The reconstructed breast CT data was analyzed by drawing an ROI inside each of the reconstructed breast volumes in two orthogonal view planes, coronal and transverse. A single slice of the reconstructed data was used, approximately the same distance inside each of the reconstructed volumes. An overall image SNR was calculated for each view under each of the three radioactivity conditions by taking the signal inside the ROI and dividing it by the noise within that volume.

Figure 4.16 shows single sample projection images of each breast in position A. Qualitatively, the images of the three breasts under all radioactivity conditions showed very little variation, even when the image was tightly windowed.

Standard deviation images of the 325, 1070 and 1500 mL breast phantoms in position A are also shown in Figure 4.16. As the images have a very uniform texture across the breast and background regions, it was reasonable to conclude any contamination in the

transmission image does not appear to be spatially dependent emission contamination but rather is uniformly distributed across the entire image surface.

Quantitative plots in Figures 4.17, 4.18 and 4.19 show measured mean and standard deviation values for signal and background ROIs tested in the 325, 1070 and 1500 mL breasts, respectively. Mean and standard deviation pixel values for either the breast or background ROIs for the 325 and 1500 mL breast phantoms do not indicate a clearly discernable trend in image contamination with a change in overall radioactivity of the breast. Indeed, values for the background ROIs are generally flat across the three states of radioactivity. The clear differences between mean pixel values in the breast ROIs in regions #1 (posterior breast, near chest wall) and #2 (anterior breast, near nipple) can be explained by the increased x-ray penetration nearer the nipple where the breast is thinner. ROI #1 and #2 should therefore not be compared against each other, per se, but compared across similar ROIs for the various breast radioactivity and exposure window configurations.

There is no discernable systematic trend in the mean or standard deviation in ROI values to accompany the greater than doubling of exposure times from 40 to 100 msec. While the x-ray flux is expected to be constant (equal mAs was used), it was expected that a doubling or further increase in the exposure time would result in greater emission contamination incident on the transmission detector, but no such trend is evident.
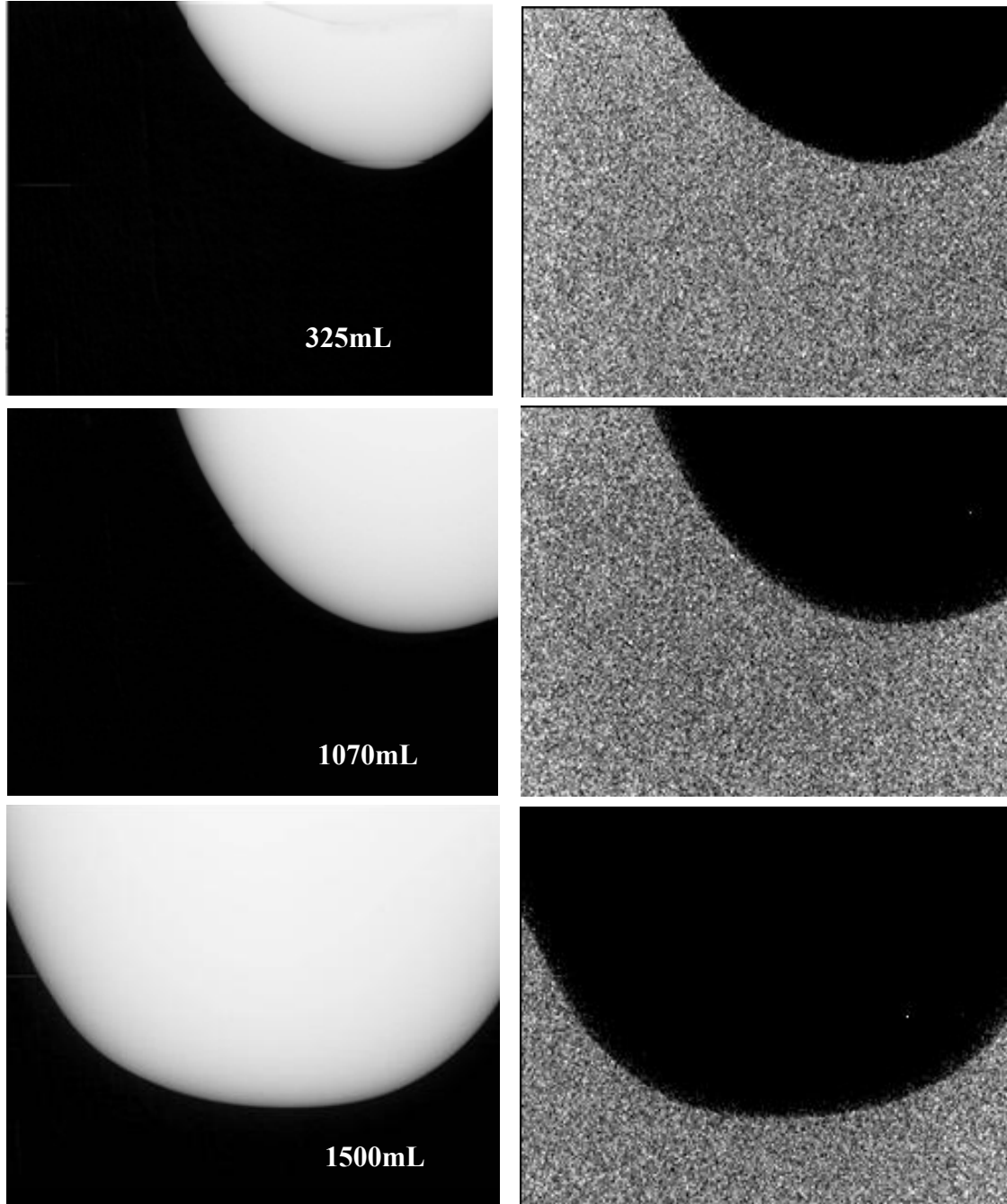
Figure 4.16: (Left) Sample projections of the three breasts acquired in position A. X-ray exposure is kept constant at 2.5 mAs. Dark areas indicate areas of high detector exposure. (Right) Standard deviation images of the three breasts exhibit no obvious spatially-dependent noise due to emission contamination. The contrast has been enhanced to highlight variations in the image. The coefficients of variation in the background regions for the standard deviation images are 10.1%, 10.89, and 11.1% for the 325, 1070, and 1500 mL breasts, respectively; the coefficients of variation in the breast regions are 8.1%, 13.2%, and 12.1% for the 325, 1070, and 1500mL breasts, respectively.
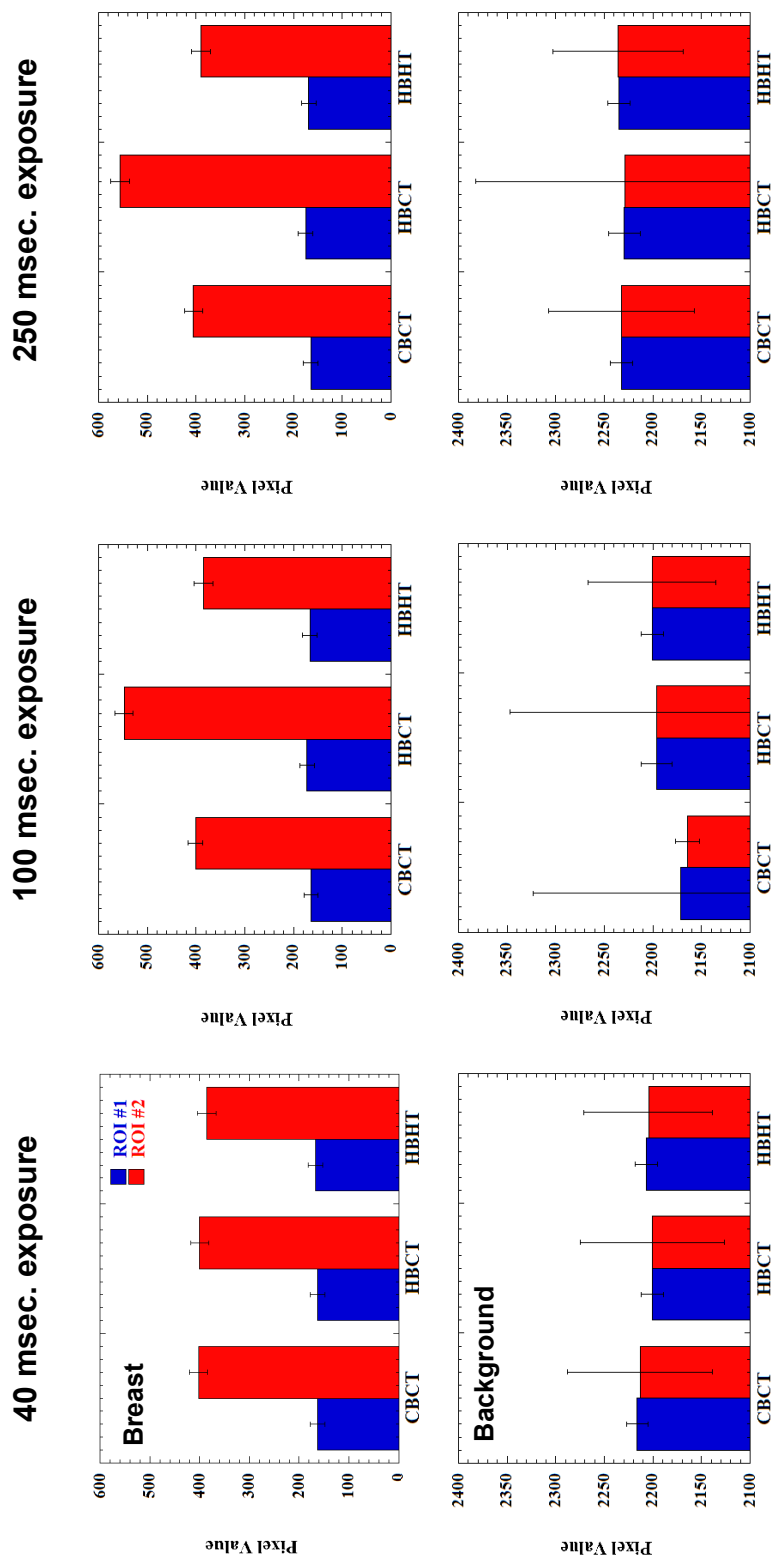
Figure 4.17: 325 mL breast in Position A showing mean and standard deviation (error bars) pixel values for the (upper row) breast and (lower row) background ROIs obtained from projection images. Note scale differences between breast and background ROI values.

174
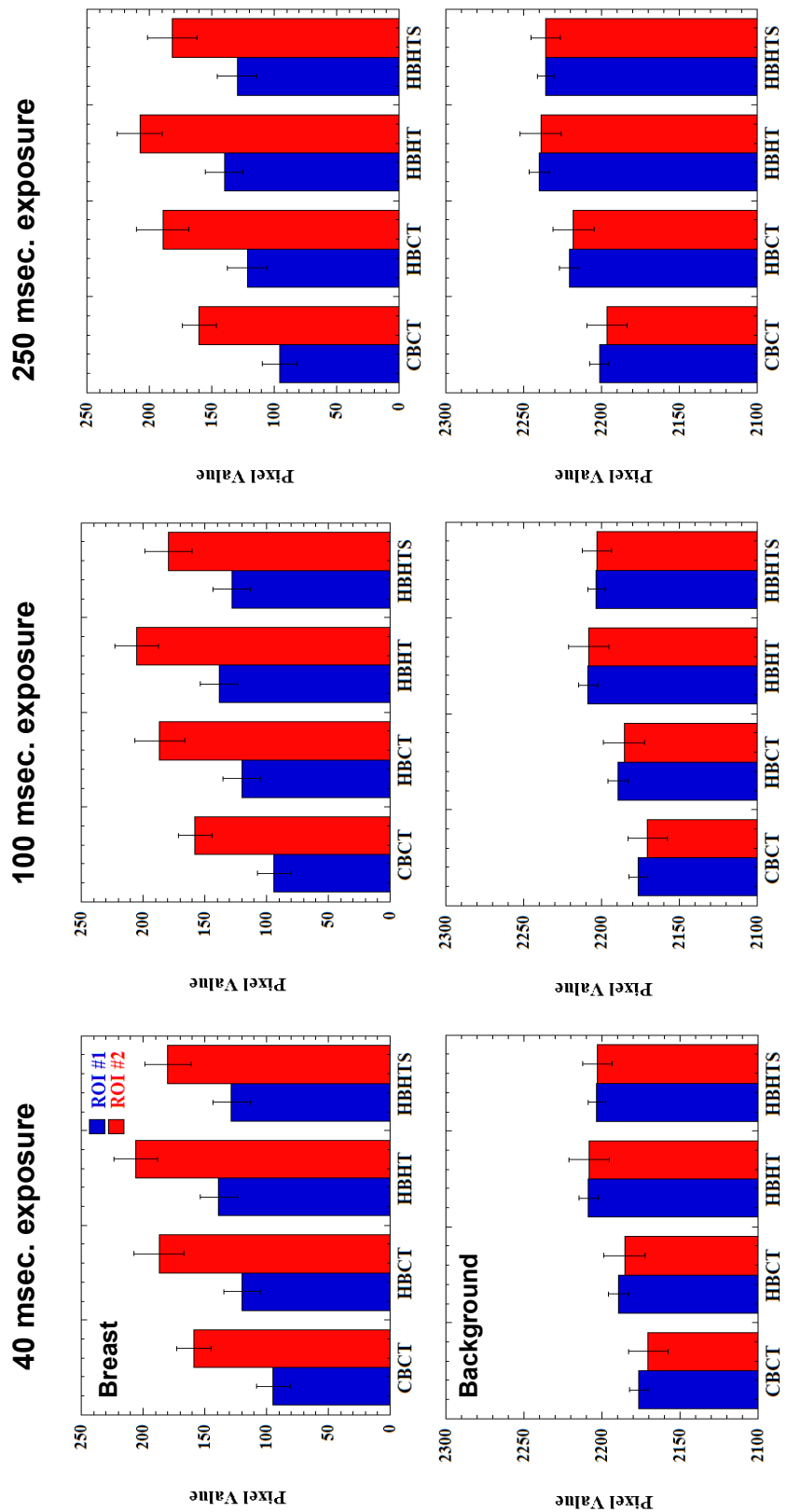
Figure 4.18: 1070 mL breast in Position A: mean and standard deviation ROI pixel values for the (upper row) breast and (lower row) background obtained from the projection images. Note scale differences between breast and background ROI values.

175
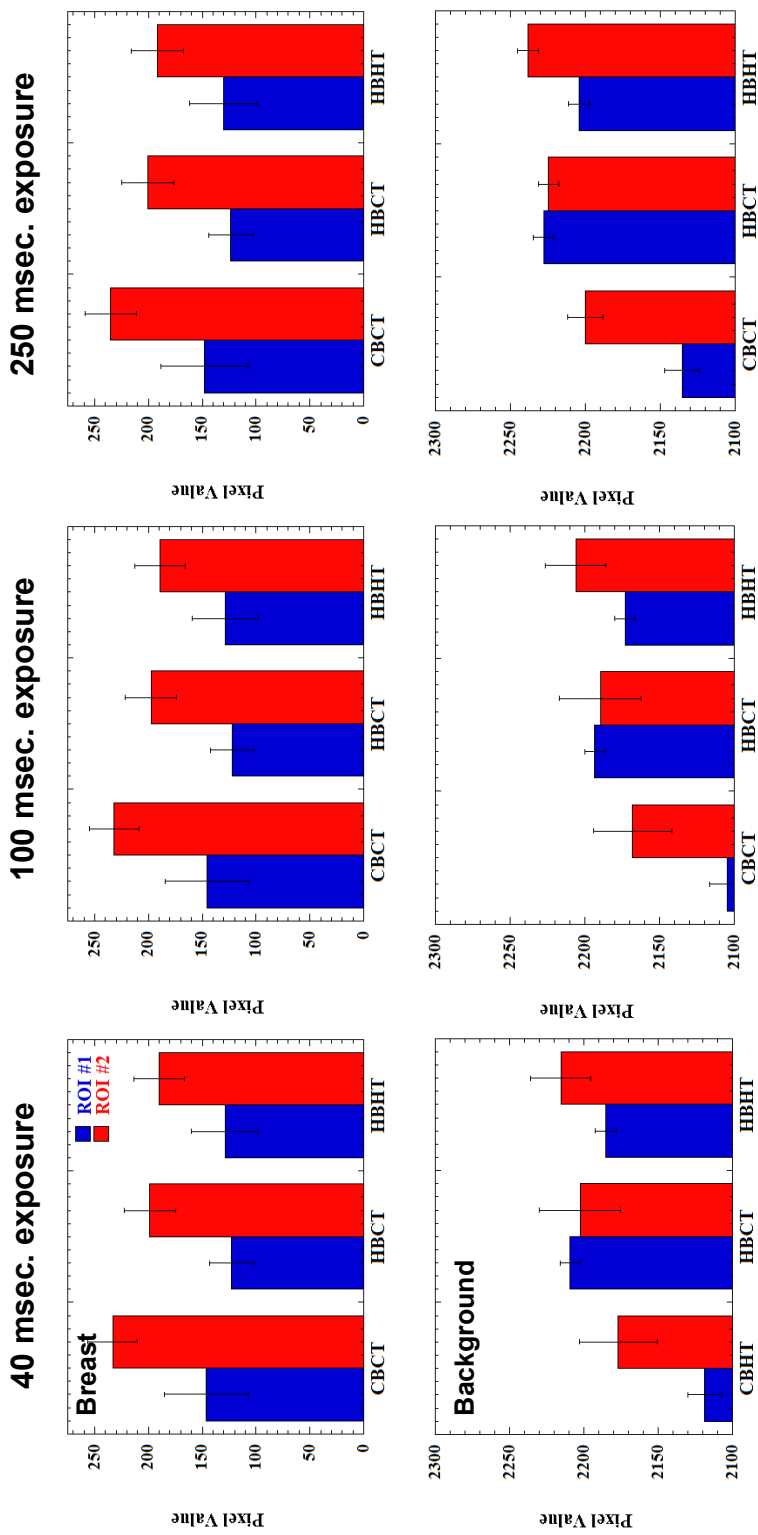
Figure 4.19: 1500 mL breast in Position A: mean and standard deviation (error bars) ROI pixel values for the breast and background obtained from the projection images. Note scale differences between breast and background ROI values.

One possible explanation for lack of systematic effects seen with the arrangement in position A was that, relative to the patient and x-ray source, the image detector was geometrically oriented in such a way as to limit the effect that emitted contamination had on the image compared to the x-ray flux. In this orientation therefore, it was possible that the effect of emission contamination is masked by that of the x-ray flux.

However, the trend in mean ROI pixel values for the 1070 mL breast pointed to increased image contamination with increasing levels of radioactivity. ROI values rise to a maximum for the unshielded HBHT case but slightly reduce when the torso is shielded, following an expected pattern of increased image contamination with increasing added activity, followed by a reduction when shielding is introduced. Background and breast ROI values follow similar trends to each other.

Mean and standard deviation ROI pixel values for the 1070 and 1500 mL breasts in position B are shown in Figures 4.20 and 4.21. In the independent CT configuration without a patient bed, it was not physically possible to position the 325 mL breast in the detector FOV in this position. In addition, it was also not possible to make adequate measurements with the lead shielding attached to the torso (HBHTS configuration) with the 1070 mL breast in this position. Results for both breasts in Position B suggest that emission contamination affects the mean detected events, and thus may play a role in tomographic transmission image formation. There is a systematic pattern of increasing mean ROI pixel value with increasing amounts and location (first in breast, then torso background regions) of radioactivity in the phantom.

The increases in ROI values were more apparent in the breast ROIs, but were also present to a lesser degree in the background ROIs. One possible explanation was that any incremental differences, e.g. those due to a uniform irradiation of the breast CT detector, would be more clearly observable when a region had a low mean value. This is indeed the case for ROIs in the breast, which otherwise attenuates the x-ray flux, compared with the shine-by regions on the detector. Moreover, that there are relatively stable differences between ROI #1 and #2 in the background region, similar to the results for Position A, indicates that there is more likely a uniform distribution of contamination events rather than a position bias, such as from the torso which is situated directly above the detector in this Position B configuration.

Transverse and coronal images of the reconstructed 1070 mL breast under various noted conditions of added radioactivity are shown in Figure 4.22. SNR figures are also tabulated in Table 4.4 with the approximate position of the ROI superimposed on the first image. Signal is calculated as the mean pixel value of the ROI, and the noise is the standard deviation of the pixel values within the ROI.

Table 4.4 Mean SNR and linear attenuation coefficients calculated in the transverse and coronal orientations for the indicated cases of added radioactivity.

		CBCT	HBCT	HBHT
Transverse	**SNR**	53.12	43.34	37.15
	Mean Attenuation (cm^{-1})	0.251	0.252	0.248
Coronal	**SNR**	48.21	38.74	37.17
	Mean Attenuation (cm^{-1})	0.256	0.251	0.248
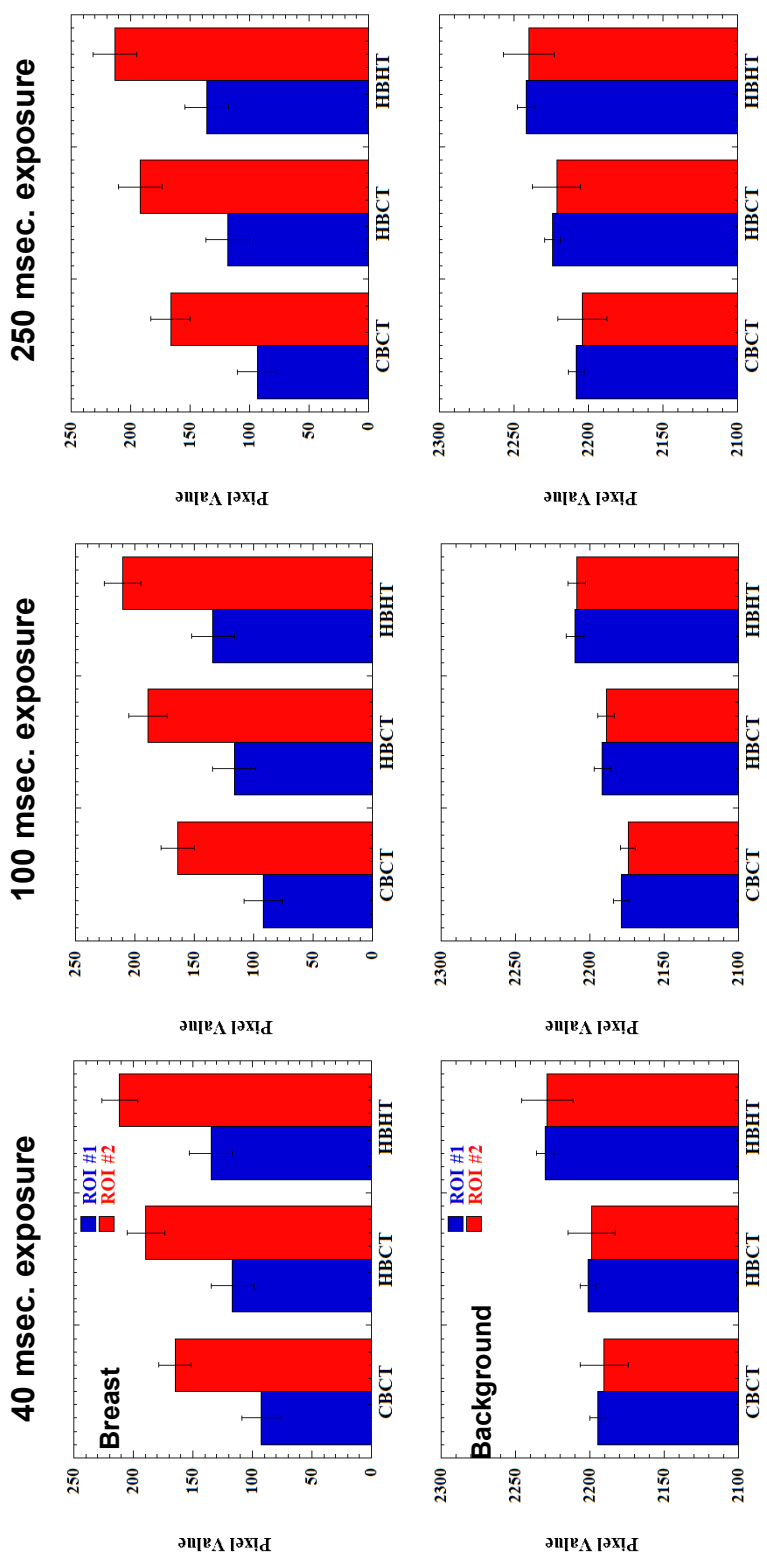
Figure 4.20: 1070 mL breast, position B. Mean and standard deviation (error bars) ROI pixel values for the breast and background obtained from the projection images. Note scale differences between breast and background ROI values.
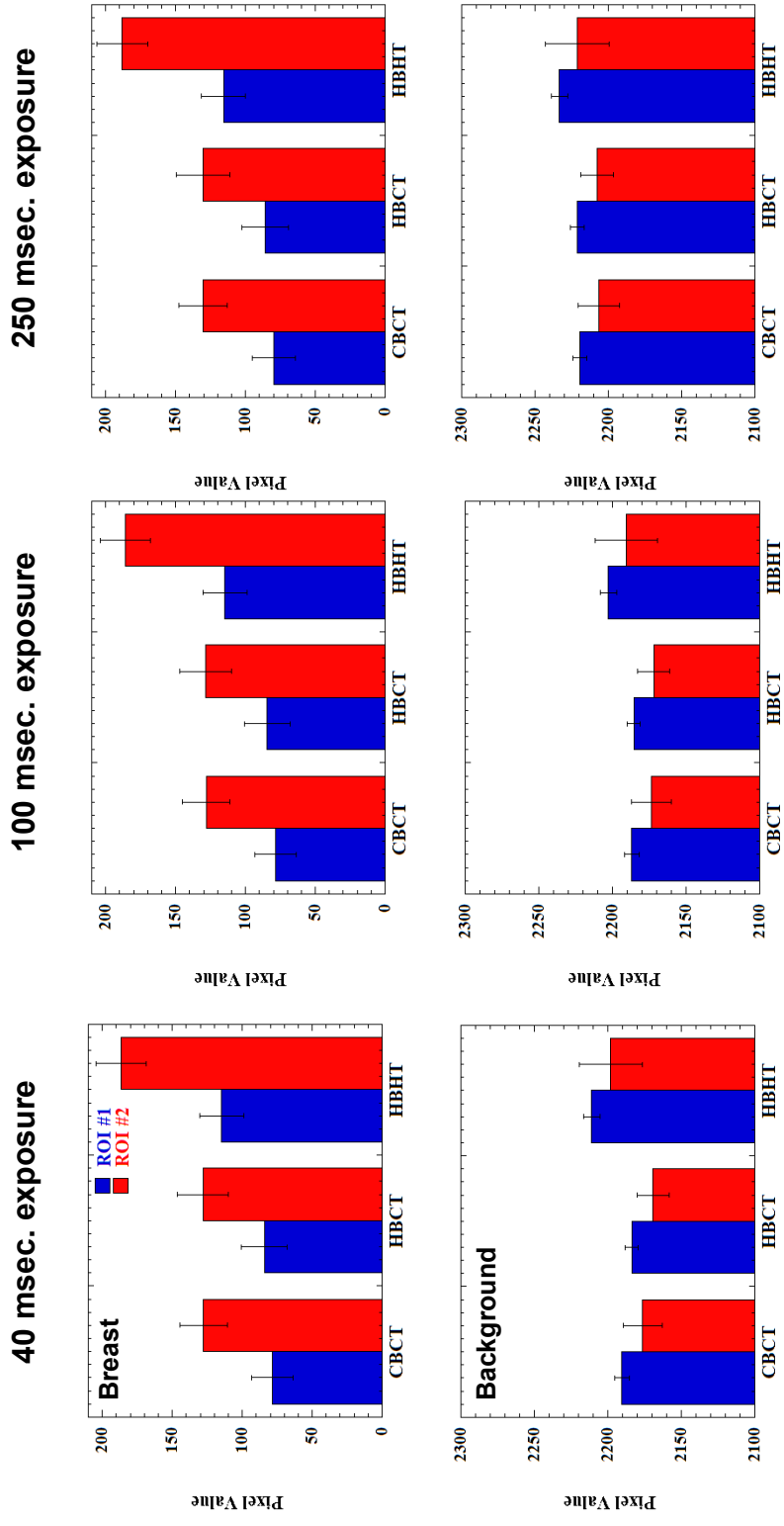
Figure 4.21: 1500 mL breast, position B. Mean and standard deviation (error bars) ROI pixel values for the breast and background obtained from the projection images. Note scale differences between breast and background ROI values.

Measured SNR values decrease with increasing radioactivity in the breast and torso region. Taking the CBCT coronal data as the true mean value, we see a 20% drop in SNR for the HBCT case and a 22% decrease in SNR values with greater emission activity in the HBHT case. Note also that there is a decrease in the effective reconstructed attenuation coefficient ("mean" value in the ROIs), also tabulated in Table 4.4, with increasing activity. The calculated absolute attenuation coefficient of water with this beam technique, measured using values from NIST at 36 keV is 0.2786 cm^{-1}. These trends are consistent with the earlier observation (from the projections in Position B and the 1070mL breast in Position A) that there are indeed events added to the projection images when increased emission activity is added to the breast and torso phantoms. That is, an increase in detected events which are uniformly added in projection space may increase the apparent noise variance in an image, and hence lower the ROI SNR. Additionally, these increased events may add to the mean detected events and yield lower effective attenuation coefficients. Despite this emission contamination and increased image noise, there were no obvious systematic reconstruction artifacts in these images. This supported the notion that emission contamination among projection images is uncorrelated. However, it remains to be seen how this measured emission contamination will affect quantification of attenuation coefficients after scatter correction is implemented for CT.
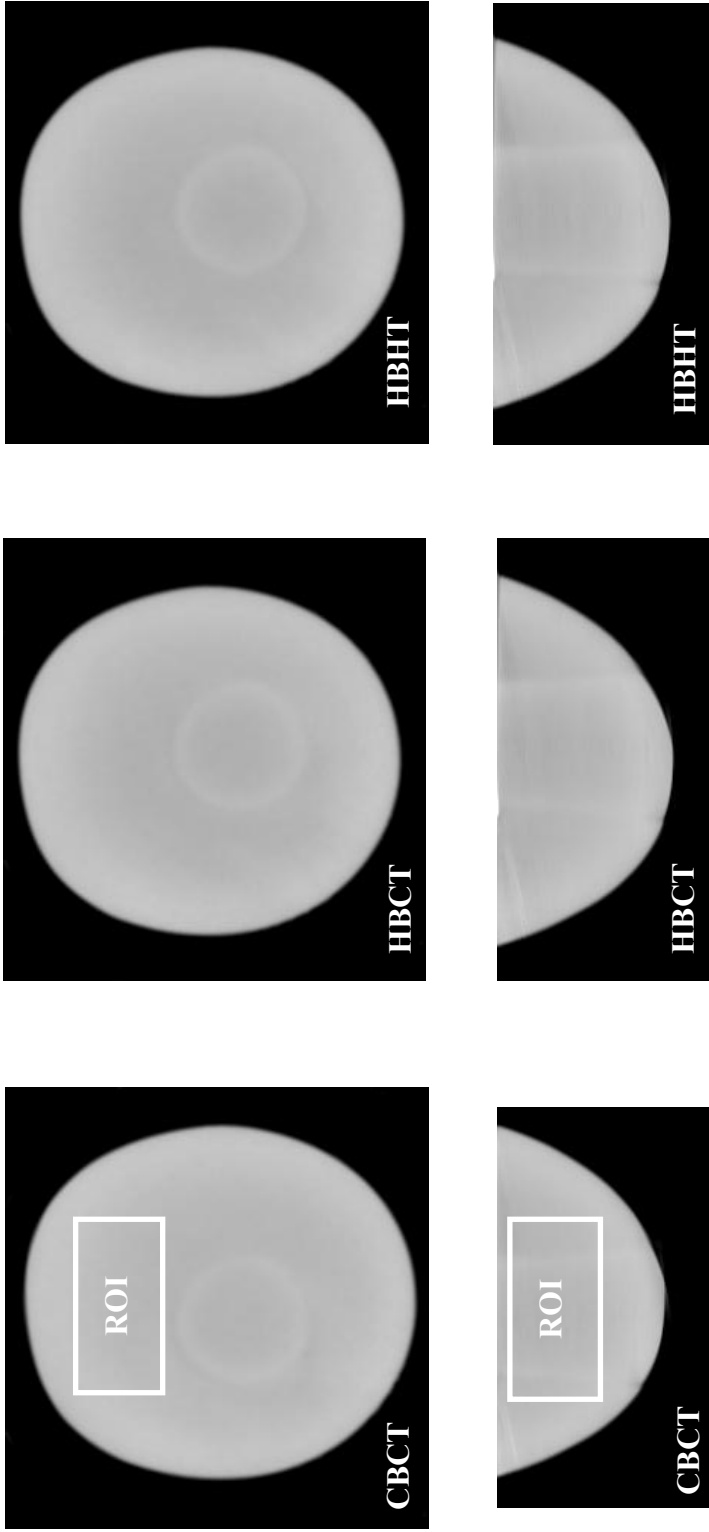
Figure 4.22: Reconstructed Breast CT data of the 1070 mL breast. (Top) Coronal and (Bottom) transverse slices are shown with some breast ROIs. Artifacts caused by the use of an offset CT geometry are visible in the coronal and transverse slices. These artifacts disappeared when a centered system geometry was placed in the coronal viewpoint was placed in an artifact free zone. The ROI used to measure SNR in the integrated SPECT-CT system. The ROI used to measure SNR in the coronal viewpoint was placed in an artifact free zone.

4.3. Integrated CT system: Emission Source Contamination Revisited

Due to the potential adverse effects that a 20% drop in SNR may have on the visibility of objects in a reconstructed image, especially small objects in a low-contrast environment, the effect of emission contamination was reinvestigated in the integrated CT system (for images of the integrated system, see ahead to Chapter 5). This was done by examining the effect of emission source contamination on the visibility of small 5mm acrylic spheres in reconstructed CT images in a uniform background of water. The inherent contrast in CT images between acrylic and water at 36 keV is less than 1% [123] and so it was proposed that, if image contamination was indeed an issue, this difficult imaging task should be made even more difficult by the introduction of contaminating photons into the x-ray projection images. Thus, observers should find it increasingly difficult to visualize the spheres as the levels of added emission contamination increase.

The phantom used in these experiments consisted of 2 concentric rings of 4 acrylic spheres, each 5mm in diameter, secured with adhesive (*Krazy Glue*, Columbus OH) onto a plastic sheet of overhead projector transparency (typically made of cellulose acetate) located at radii of 20 and 40mm from the center of a thin-walled (3mm) cylindrical disk made of acrylic. The disk, secured to the bottom of a 14cm cylinder filled with 1000 mL of water, was placed in the FOV of the CT system and imaged using the standard tomographic protocol. To simulate the contaminating effect of the patient's torso i.e. a large source of emission activity outside the breast volume of interest and above the x-ray detector, a plastic container was filled with 200 mL of an aqueous-^{99m}Tc solution. While the anthropomorphic torso phantom used in previous experiments more faithfully

simulates the scatter properties of a real patient torso, I decided that using a small container would simulate a highly concentrated source of ^{99m}Tc activity from the heart above the detector (cf. Position B in Figure 4.13), and would generate a worst-case contaminating effect. Although it is understood that the uptake of ^{99m}Tc is greater in the heart and liver than in the background, and that there may be a spatially dependent contaminating effect, having a highly concentrated source of emission activity directly above the imaging FOV to expose potential contamination effects was more important than having similar, but spatially more diffuse, activity in an anthropomorphic phantom.

The activity concentration levels added to the breast phantom and the torso container were based on activity concentrations used regularly in nuclear imaging experiments performed in the lab [146]. See Table 4.5 for further details of the cumulative amounts of radioactivity in the breast and torso volumes. To observe an upper bound in x-ray image contamination, ^{99m}Tc activity was added to a cumulative level twice that of the levels reported clinically in the breast and in various organs in the torso [146]. Based on the literature, 16 mCi of ^{99m}Tc was calculated to be twice the reported level of absolute activity in the 'torso' container. Approximately 1.25 mCi of ^{99m}Tc activity was added to the water in the breast phantom to simulate twice the clinically observed breast background activity concentration levels (2 x 0.33 μCi/mL).

Similar to the previous contamination study, the breast phantom was initially imaged without added radioactivity in the breast cylinder or in the torso container – this cold breast, cold torso (CBCT) setup was taken as the control case against which results from all other setups were compared. Next, ^{99m}Tc activity was added to the breast phantom

only, i.e. a hot breast, cold torso (HBCT) setup, to mimic perfect shielding using the lead sheet. At first, the same absolute amount of [99mTc] activity was added to the pendant breast phantom at the same concentration reported in the literature (HBCT 1X). Subsequently, this activity level in the breast was doubled (HBCT 2X). Activity was modified in the container and the cylinder, first at the same activity concentrations as are reported in the literature (HBHT 1X or 8 mCi in total), and then at twice the reported level (HBHT 2X or 16 mCi in total). At each setup, three separate complete tomographic scans were acquired using the standard technique (60 kVp tube potential, 2.5 mAs per projection, 240 projections evenly spaced over 360°). The raw projection data was binned to 0.5mm pixels and reconstructed to an image gridsize of 350x350x384 using 16 subsets for 10 iterations, since this number of iterations was previously shown to be optimal for a lesion like sphere approximating this 5 mm diameter [123].

Sample reconstructed coronal slice images for each tested scenario are shown in Figure 4.23. The images qualitatively look similar across all states of added radioactivity. The mean and standard deviation SdNR and contrast metrics for the inner and outer rings of spheres is tabulated in Table 4.5 and plotted in Figure 4.24. SdNR is defined as the difference between the signal in the sphere and in an equivalent sized ROI in the background, divided by the noise in the background. There is a definite variation in the measured SdNR levels in the spheres, but the trend in results is not consistent with increasing levels of [99mTc] contamination.
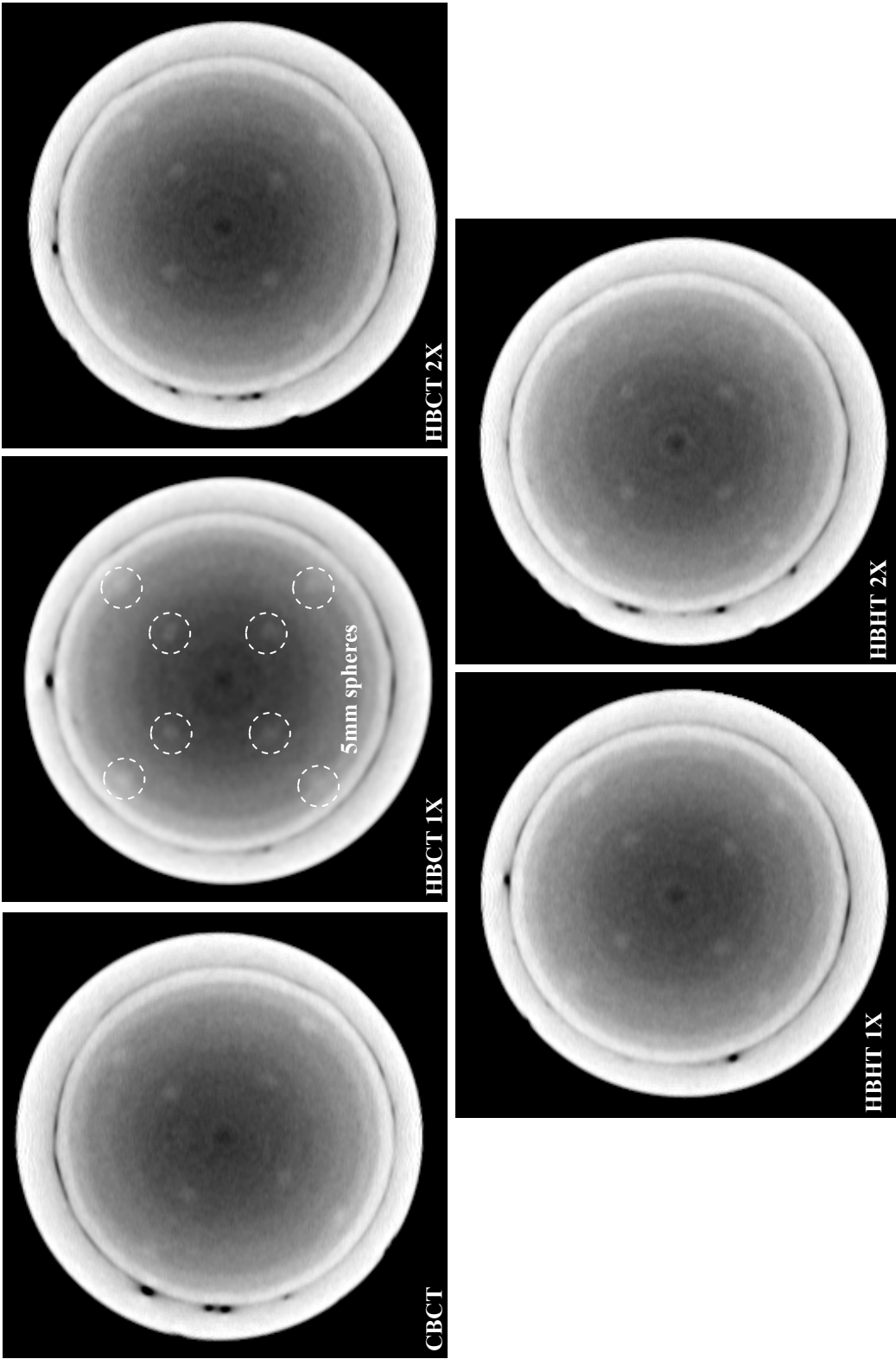
Figure 4.23: Sample slice images in the coronal view of the disk of spheres under each state of added radioactivity in the breast phantom. The locations of the eight 5mm spheres on the disc are indicated by the dashed circles. The darkening toward the center is due to the uncorrected effects of scatter on the projection images.

In fact, the SdNR and contrast of the HBHT2X case, i.e. the most contaminated case, is apparently better than that of the CBCT setup, the control case. A t-test was performed on the SdNR data for the various contaminated conditions versus the control case, CBCT, using a significance level of $p<0.05$. The data shows that the differences in SdNR are significant only in the case of the two lowest levels of added contamination in the breast, but are not significant when 16mCi of activity is added to the breast and torso.

Table 4.5 SdNR and contrast values for the 5mm spheres in the inner and outer rings for each state of added radioactivity.

| Setup | ^{99m}Tc breast & torso activity (mCi) | Inner Ring | | | Outer Ring | | |
		SdNR	p-value vs. CBCT	Contrast (%)	SdNR	p-value vs. CBCT	Contrast (%)
CBCT	0	8.0 ± 4.4	-	2.2 ± 0.6	7.9 ± 2.9	-	2.6 ± 0.9
HBCT 1X	0.65	4.6 ± 1.6	0.06	1.5 ± 0.4	2.9 ± 1.8	<0.01	1.4 ± 0.3
HBCT 2X	1.30	6.1 ± 1.6	0.27	1.6 ± 0.3	3.4 ± 2.3	<0.01	1.6 ± 0.6
HBHT 1X	8.0	4.5 ± 2.3	0.07	1.3 ± 0.6	5.4 ± 3.2	0.12	2.1 ± 0.9
HBHT 2X	16.0	7.6 ± 2.9	0.83	2.1 ± 0.7	8.5 ± 3.0	0.69	3.1 ± 1.0

In addition to performing semi-quantative analysis by image metrics, a mini-observer study was performed to quantify the ability of observers to visualize the low-contrast acrylic spheres under different conditions of added contamination radioactivity. To prepare the reconstructed image data for the observation study, a stack of images in the coronal perspective (reduced from the original stack of 384 slices to 30) were first re-sliced into the transverse direction using image processing software (ImageJ) smoothed using a 2 point Gaussian smoothing filter and re-sliced into the coronal orientation.
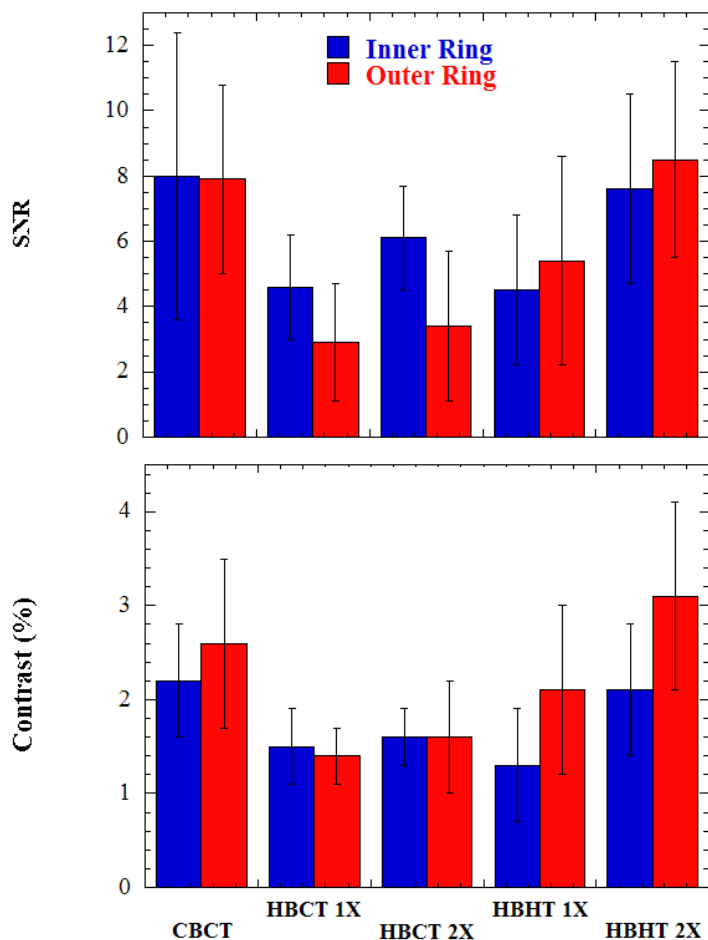
Figure 4.24: Plots illustrating (top) SdNR and (bottom) contrast of the inner and outer ring of spheres in Figure 4.25.

To avoid biasing the observers' results, three 20-slice sub-selections of the same 30-slice image stack were processed to ensure that the specific slices that contained the 5 mm acrylic spheres were in different positions in the image stack: one towards the front of the stack, one in the middle and one towards the end of the 20-image stack. The brightness and contrast of each of the image stacks were equalized across each of the experimental set ups. The image stacks were then numbered and randomized in the order in which the image stacks were to be shown to each observer. Sample successive image slices of the HBHT 2X stack are shown in Figure 4.25 to illustrate the images that seen by observers.
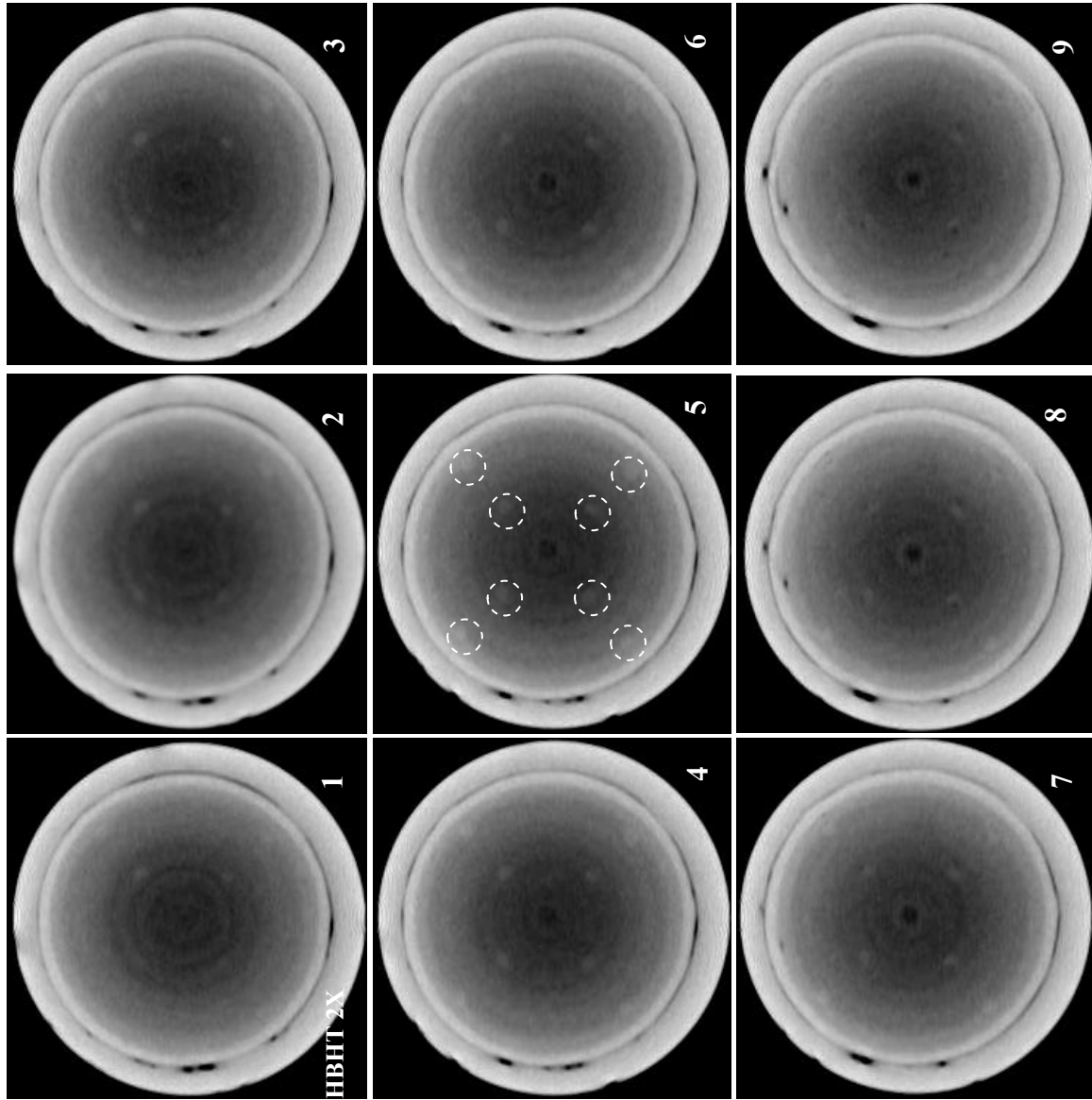
Figure 4.25: Sample stack of images that observers viewed in the study. This stack is from the HBHT2X image data set. The stack of images is sequenced beginning above the disk of 5 mm spheres (posterior breast) moving towards the nipple (anterior breast). Dashed circles indicate the locations of the eight 5 mm spheres.

189

Observers were trained on a sample stack of reconstructed data similar to the real and were subsequently shown 42 separate stacks of images of the spheres in water under various radioactivity conditions. For each stack, observers were asked to note the number of spheres visible on the outer and inner circles of spheres. The observer study was stopped after 2 observers had completed the study since it quickly became apparent that, regardless of whether activity was added or not and regardless of the absolute level of additional activity, the 8 spheres (4 on the inner ring and 4 on the outer) were visible under all conditions.

4.4. Discussion

The chapter quantified the effects of image cross-contamination in the SPECT-CT imaging system. The first set of experiments examined contamination of the SPECT (emission) image by photons from the x-ray (transmission) source, while the second set of experiments investigated the complementary issue of contamination of the reconstructed transmission image by the emission source.

To investigate transmission contamination of the emission image, three breast volumes were tested with the SPECT camera positioned at different azimuthal and polar tilt orientations relative to the central-ray of the x-ray cone-beam. Cumulative low energy contamination increases with an increase in x-ray exposure, with a large increase apparent at energies between 60-80 keV (would likely go lower, though, and is limited by the SPECT lower hardware threshold). However, observed photopeak scatter contributions per single x-ray exposure were consistently <1% for any energy window

other than an open window, across all camera orientations. SPECT images of the x-ray exposed breast also indicated a contaminating effect that was eliminated with tighter energy windowing. With such consistently low contamination levels, overall results indicated that the optimal choice of SPECT gamma camera positioning relative to the x-ray source-detector axis in the integrated system design was to be constrained more by physical space limits rather than by contamination of the emission image. The process of designing the initial integrated SPECT-CT imaging system will be described in Chapter 5.

There were caveats to these sets of experiments. The low scatter measurements in the gamma camera are only valid for the parallel collimator used in the SPECT system, and the percentage contamination would likely change with a change in collimator geometry and consequent sensitivity, although this phenomenon was not investigated in this set of experiments since there are currently no plans to change the type of collimator used in the SPECT system. Additionally, the offset CT geometry setup used in this experiment (Figure 4.5) may reduce measured emission contamination by allowing the remaining unexposed breast volume to self-attenuate some of the scattered x-ray photons before reaching the gamma camera's active area. Different degrees of this offset may yield decreased or increased contamination. However, it is assumed that such low measured results (<2%) indicate that contamination of the emission image at x-ray exposure levels clinically relevant for CT projections are likely to remain low with or without offset geometry. Indeed, due to some uniformity issues in the CT reconstruction, it was subsequently decided to use a centered CT system when the systems were integrated,

since contamination was not anticipated to be an issue.

It has not yet been decided whether the final dual-modality breast imaging system will scan a patient's breast using a simultaneous acquisition protocol, an interleaved emission-transmission projection sequence or sequential scans using each modality separately (see the Introduction section to this chapter). When using an interleaved or sequential imaging protocol contamination of the emission image can be completely eliminated by simply turning the SPECT acquisition off during x-ray exposure of the breast [49]. Another method to employ may be to physically use a blocking filter. However, for faster patient throughput and improved image registration, a true simultaneous image acquisition protocol may be preferred. In any case, the quantitative results of this study indicate that a simultaneous SPECT-CT breast imaging protocol should be possible without unduly compromising SPECT image data.

The rate-limiting step in dual-modality SPECT-CT data acquisition is the time required to acquire SPECT (~15 minutes) and not CT data (< 1minute is planned in the future). To protect against inducing motion artifacts in reconstructed CT images, it is possible that a sequential data acquisition protocol will be followed (i.e. an entire dataset of CT first, followed by SPECT data acquisition) which will eliminate the possibility of x-ray contamination of the SPECT image (in addition to possibly providing attenuation correction data for the SPECT system and reducing motion artifacts in the CT image).

For emission source contamination of the transmission image, theoretical calculations using large amounts of ^{99m}Tc activity, and also using cone beam x-ray spectrum data

indicate that that the cumulative flux from the heavily filtered x-ray beam is orders of magnitude higher than that of any emission source contaminating activity that is incident on the detector face. Despite these theoretical calculations, some results from early stage experiments using both planar and tomographic x-ray techniques with realistic anthropomorphic phantoms indicated a trend in increased image contamination consistent with a rise in ^{99m}Tc activity in the vicinity of the x-ray detector. Further studies were then performed using the integrated SPECT-CT system to evaluate the effect of increased ^{99m}Tc activity on the ability of observers to visualize small 5 mm in a low contrast environment in the presence of large quantities of ^{99m}Tc activity. No discernable trend in results occurred, with the SNR of the spheres in the worst-case contamination scenario being actually higher than that of the best case scenario without additional activity.

When the results reported here are considered with the fact that the cumulative actual total of ^{99m}Tc activity in the breast and torso of the patient is more likely to be closer to 8mCi rather than 16 mCi, and that the bed is lined with Pb specifically to reduce contamination of the transmission image, it can be assumed that x-ray scatter from inside the breast volume is of greater concern than any contamination of the x-ray image from the ^{99m}Tc source.

Overall, results from the contamination studies performed in this section of thesis research indicate that measured levels of image signal cross contamination in the current iteration of the common FOV integrated imaging system is not of great concern for the design of the integrated system.

Chapter 5

5. Integrated SPECT-CT System and Patient Bed Design

This chapter has a two-fold purpose: it initially describes the design and implementation of the prototype integrated SPECT-CT dual-modality imaging system; the chapter then describes the design, manufacture, integration, and performance of a novel custom-designed patient bed that enables the prototype integrated SPECT-CT imaging system acquire tomographic data of the pendant breast of a patient lying prone on its surface.

The design of this integrated system is a collaborative effort between colleagues in the lab, and therefore there is quite a bit of crossover between colleagues and their projects. I have indicated in this chapter where other colleagues have completed sections of the system development. The design of the patient bed was presented at the *Nuclear Radiology of Breast Cancer Symposium* in San Diego in 2006 and with additional information presented at the *SPIE Medical Imaging Conference* in San Diego in 2007. The research was published in the 2006 *IEEE Nuclear Science Symposium and Medical Imaging Conference Proceedings* and also in the *Proceedings of the SPIE, Medical Imaging Conference* in 2007. Work on the first results from the integrated imaging system was shown at the 2008 *Duke Comprehensive Cancer Center Annual Meeting,* and the patient bed design has been included in numerous presentations and posters since 2006.

5.1. Designing the Initial Prototype Integrated SPECT-CT Imaging System

To develop the initial prototype integrated SPECT-CT imaging system, the constituent components of the independent CT and SPECT imaging systems were first modeled in 3D using accurate computer aided design (CAD) software (Autodesk Inventor Professional R10, *Autodesk Inc.*, CA). Each of the system components, shown in Figures 5.1 and 5.2, was modeled either by downloading 3D CAD models directly from manufacturers websites, by consulting with published datasheets for dimensions of the various components or by manually measuring dimensions on the surface of the various system components in the MMI lab.

Based on these models, a base plate was designed by a lab colleague to integrate the SPECT and CT systems onto the same rotating gantry. The base plate, shown in Figure 5.1 (middle column), was designed to support the weight of both the SPECT and CT systems on the common gantry and allowed flexible positioning of the integrated CT system in terms of system SID and SOD.

The separate systems were then integrated onto the common gantry as shown in Figure 5.2. Based on the results of the investigation into contamination of the emission image by the transmission source, described in Section 4.1, the initial prototype of the integrated imaging system was designed with the SPECT system positioned orthogonally to the central x-ray axis of the integrated CT system.

The base plate, reinforced with several 1.5"x1.5" metal bars to negate bowing from the weight of the individual SPECT and CT components, is mounted on a high-load rotation

stage (RV350CCHL, Newport Corp., Irvine CA) capable of supporting the asymmetric load without undue torque issues, and maintaining a maximum rotational speed of 16°/sec. The integrated SPECT system was mounted so that its center of rotation (COR) coincided with the center of rotation of the rotation stage while the integrated CT system was initially mounted with its COR offset by 5 cm. This offset geometry is used accommodate larger breast sizes, although this was later changed so that the centers of rotation of both systems coincided with that of the rotation stage. While the integrated SPECT system retained its full 3D positioning capability, the integrated CT system was constrained to simple circular orbits about the common system vertical axis of rotation at a fixed height above the ground.

A CAD drawing and photograph of the initial integrated SPECT-CT system is shown in Figure 5.3.
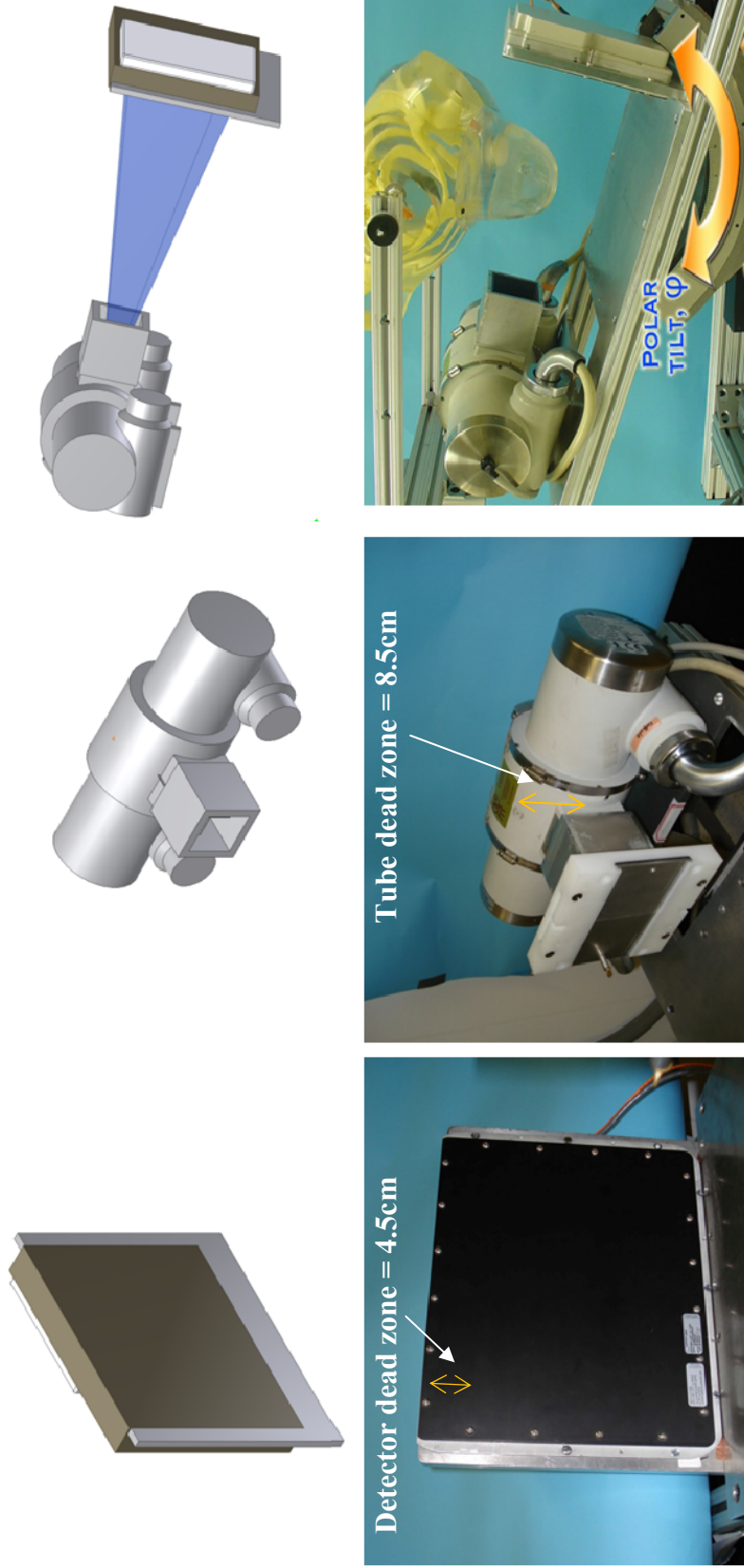
Figure 5.1 (Top row) CAD images of (left) *Varian 2520* x-ray detector, (middle) *Varian Sapphire* x-ray tube housing without the collimator jaw housing, and (right) the independent CT system with the cone beam indicated in blue. (Bottom row, left and middle) Photographs of the same system components showing the similarity between modeled and actual system components and (bottom row, right) photograph of the tilted CT system imaging a suspended anthropomorphic torso and breast phantom. Device dead zones for the tube and detector are also indicated on the photographs.

197
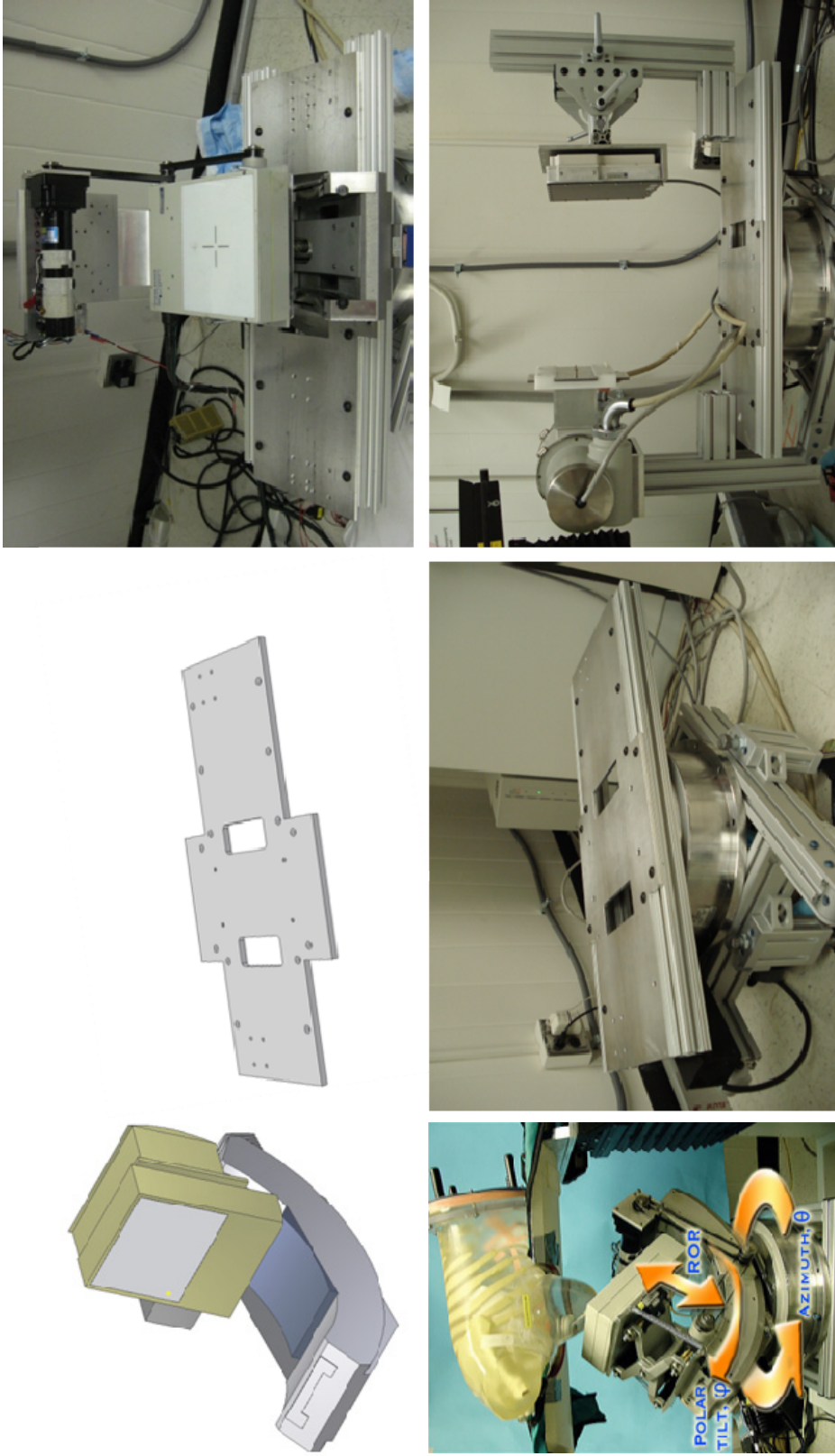
Figure 5.2: (Top, left) CAD image of the SPECT system with attached goniometer that models the (lower, left) actual SPECT system shown acquiring data below an anthropomorphic breast and torso phantom. (Top, middle) CAD image of the (lower, middle) actual baseplate design, reinforced with 1.5x1.5" metal bars, on the azimuthal motor stage with accompanying holes for attaching the integrated (top, right) SPECT and (lower right) CT systems.
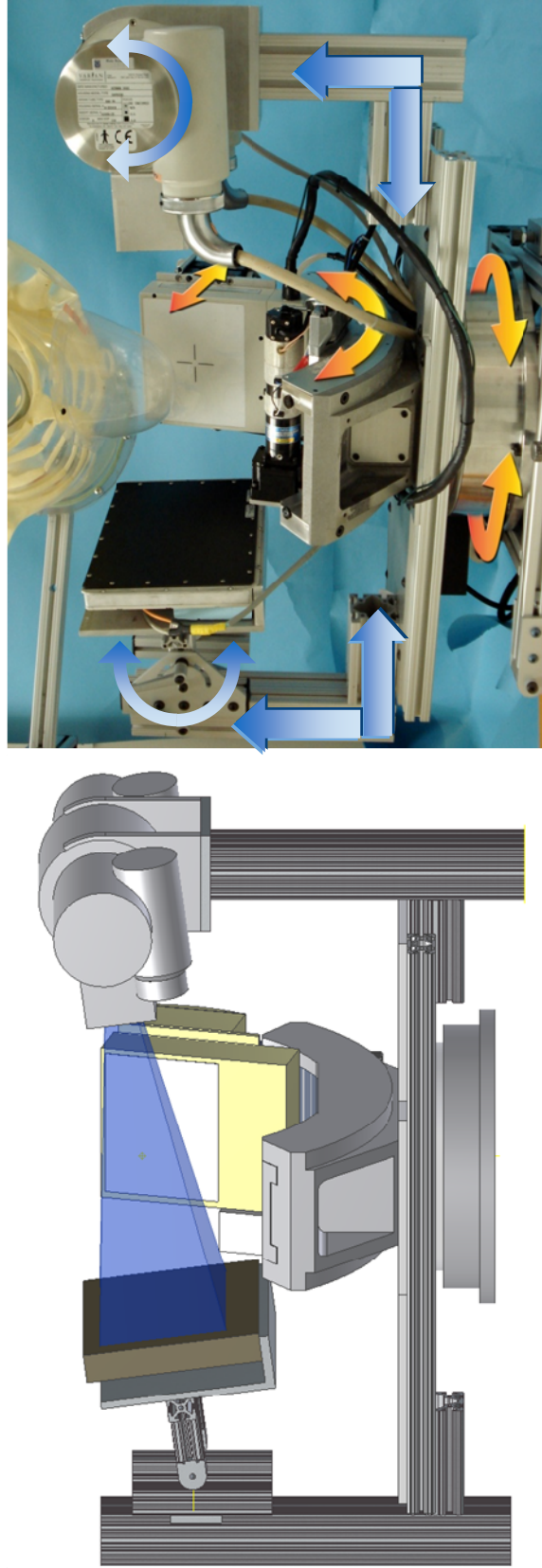
Figure 5.3: (Left) CAD image of the integrated SPECT-CT imaging system with superimposed x-ray cone beam (blue) and (right) photograph of the integrated system imaging a pendant anthropomorphic torso and breast phantom. The orange arrows indicate the degrees of controlled freedom of the integrated SPECT system. The SPECT system retains full 3D positioning capability while the CT system can rotate $360°$ in the azimuthal direction but cannot tilt in the polar direction. The blue arrows superimposed on the integrated CT system indicate further degrees of freedom available to the integrated CT system. However, in contrast to the SPECT system, these degrees of freedom on the integrated CT system are not controllable during data acquisition, but were used to test different system source to image distances and x-ray source-detector tilts when the patient bed was being integrated, (cf. Sections 5.4.6 and 5.6.1).

5.2. Introduction to Bed Design for Prone Patient Breast Imaging

To understand why it was necessary to custom design a bed for prone patient breast imaging, it is instructive to model the practical challenges of prone patient breast imaging. Figure 5.4 (top left) illustrates a situation where a point source of cone beam x-rays (blue) irradiates an isolated pendant breast (red) hanging in free space. The chest wall is assumed to begin directly above the uppermost surface of the isolated breast. In this case, the cone beam images the maximum volume of breast tissue. To mimic a practical clinical imaging scenario (Figure 5.4, top right) , we need to first include the housing for the x-ray source and detector, and then further include the effect of the bed on which the patient lies (Figure 5.4, bottom row). In the breast CT imaging protocol, the patient lies prone on a bed that is manufactured with a certain thickness of high strength material to support the weight of the patient (see Figure 5.5). This bed thickness has the effect of separating the top plane of the cone beam from the patient's posterior breast volume. The top plane of the x-ray cone beam is also further separated from the posterior breast volume due to the finite dimensions of the source and detector 'dead zones'. A dead zone is defined here for the x-ray source as the distance between the focal spot of the x-ray source and the top of the tube housing; for the x-ray detector it is defined as the distance between the top of the active edge of the detector and the top of the detector housing.

The cumulative effect of the physical dimensions of the bed and the dead zones of the imaging components is to separate the top plane of the cone beam from the patient's
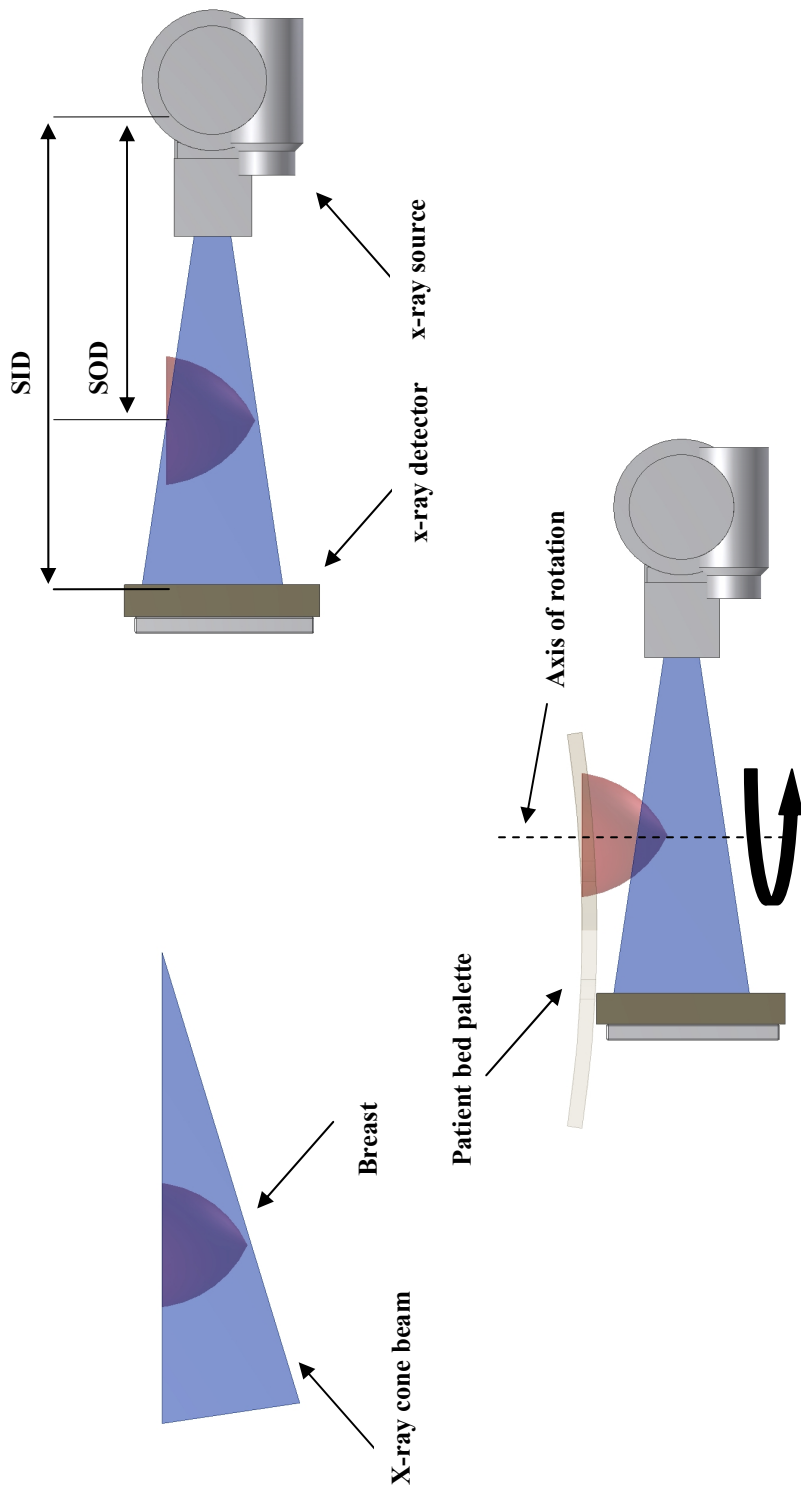
Figure 5.4: CAD images of (top left) an isolated breast (red) being irradiated by an x-ray cone beam (blue) in space. (Top right) The modeled x-ray source and detector used in the MMI lab are included, showing how the beam intersects the breast volume. The SOD and SID are modeled for our existing CT imaging system. (Bottom) When the curved patient bed is now included (0.75" thick and modeled on the very first bed palette used in experiments in the lab, see Figure 5.2 and 5.5) the top plane of the cone beam is separated from the chest wall by the combined bed thickness, dead zones of the x-ray system components, and the divergent nature of the beam.

201

breast volume. The patient bed must therefore be specifically designed to overcome these physical impediments in order to maximize the imaged breast volume.

To develop a patient bed for routine dual-modality imaging in a clinical setting, the bed design should prevent a collision between the patient and imaging system in addition to maximizing comfort for the patient during the scan, all while concurrently enabling dual-modality imaging of the patient. With the current imaging system, however, these last two factors, ergonomic design for comfort and the technical requirements for image quality, are in competition with each other. Therefore, the challenge in designing this patient bed was to find the optimal operational range where patient comfort was adequate while providing sufficient breast volume and chest wall sampling. Such were the aims of the patient bed design described in this chapter.

5.3. Early Bed Design for Dedicated SPECT Imaging

The first volunteer subject imaged in the MMI lab was a 55 year-old, 59kg post-menopausal woman with biopsy confirmed adenocarcinoma in her left breast.

The bed palette used to support the subject during the scan, (~1" thick standard nuclear imaging palette), was designed for supine, not prone patient imaging, and so several modifications were made to the bed to prepare it for prone patient breast imaging. A section of the bed was removed around the torso area of the patient to allow the left breast of the patient to hang pendant in the FOV of the SPECT system, noted in Figure 5.5. The bed was lined with a thin sheet of Pb to reduce out-of-breast activity, such as activity taken up in the heart and liver of the patient, from contaminating
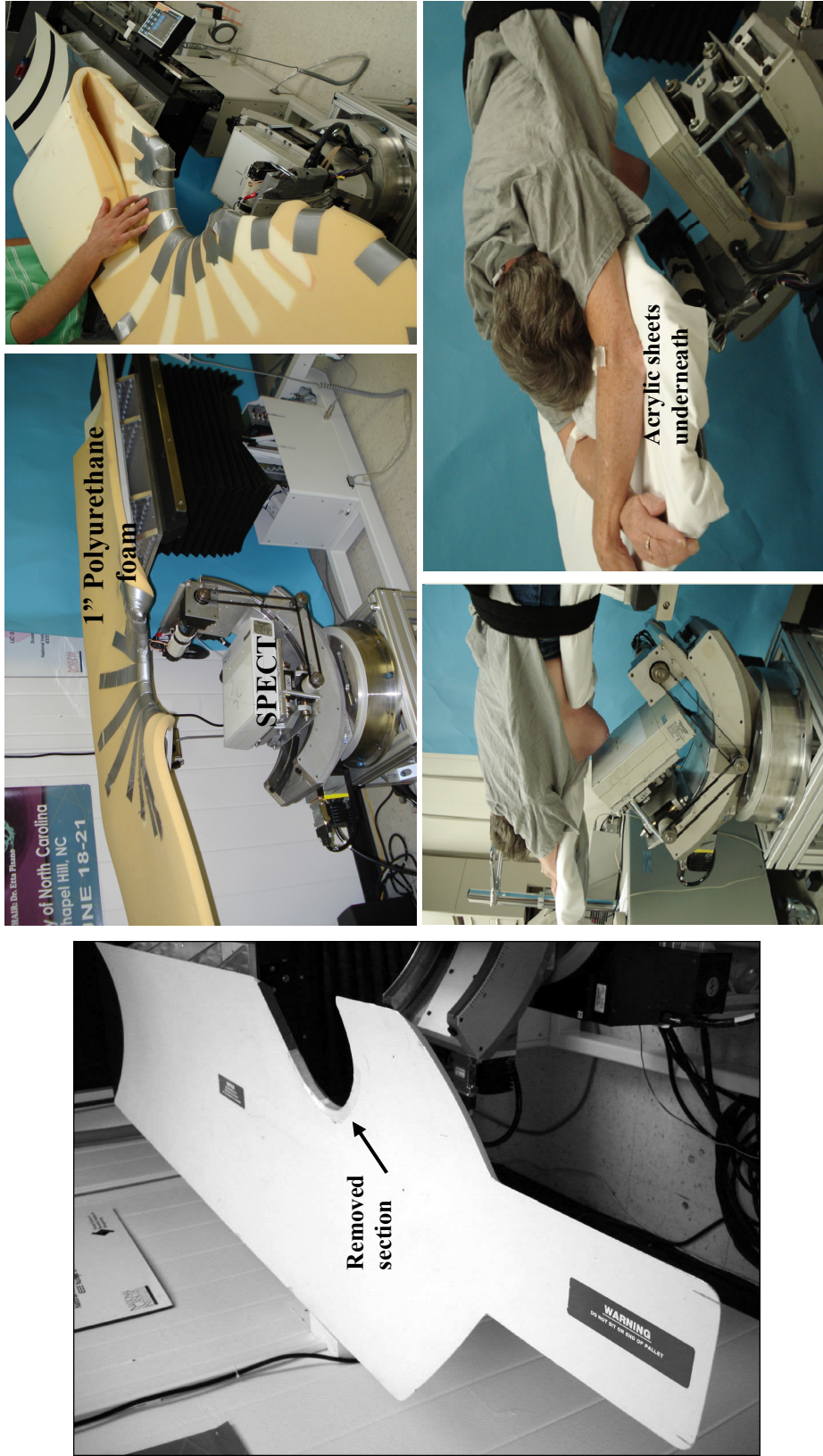
Figure 5.5: (Left) A photograph of the nuclear medicine bed palette prior to adding layers for the prone patient. The section removed from the side of the bed for imaging is shown. (Upper right) The lead-lined bed (the lead lining is not visible under the foam) is then shown with the layer of foam on the upper surface. (Lower right) The first patient volunteer lies prone on the bed while the SPECT system acquires data underneath her breast.

203

the SPECT image. To improve comfort for the patient during the ~15 minute scan, the bed was lined with a 1" layer of polyurethane foam strapped to the palette using adhesive tape. To further provide comfort for the patient, thin sheets of acrylic were attached to the head section of the bed to allow the patient to stretch her arms out in front and maintain a comfortable posture for the duration of the SPECT scan. These curved sheets of acrylic were also covered with foam, though they and are not visible in Figure 5.5.

At this stage of the system development, the SPECT and CT systems still operated independently on separate gantries. The powerful 3D positioning flexibility of the SPECT system made the design of the modified bed adequate for dedicated SPECT imaging of the pendant breast. To contour the patient's breast, data acquisition orbits were generated using a previously developed semi-automatic orbit generator [146] that takes unique operator-generated inputs of the radius of rotation of the gamma camera at several pre-determined azimuthal and polar tilt angles unique to each type of orbit. Depending on the type of SPECT acquisition trajectory required, the orbit generator uses the input from these several points to interpolate around the full 360° and generate a data acquisition trajectory for the gamma camera that incorporates complex 3D trajectories.

Reconstructed images in three orthogonal planes shown in Figure 5.6 indicate an obvious volume of increased ^{99m}Tc radiotracer uptake (~2cm diameter). The location of the area of increased activity corresponded to that seen in a contrast enhanced MRI scan (as reported by Dr. Terry Wong) performed on the patient earlier on the day of the SPECT scan. Regions of enhanced out-of-breast signal are evident in the lower left coronal view and upper left transverse views. These areas of activity were presumed to be due to the

uptake of the radiotracer in the heart and/or liver of the patient. The artifacts re-emphasized to us the necessity of incorporating lead shielding on the bed surface around the torso region of the patient in order to reduce the level of out-of-breast contamination.

Other methods to reduce this out of volume activity include incorporating novel 3D trajectories that specifically reduce the number of angles where the heart and liver are viewed by gamma camera. Such methods are currently being investigated in the lab [192-193].
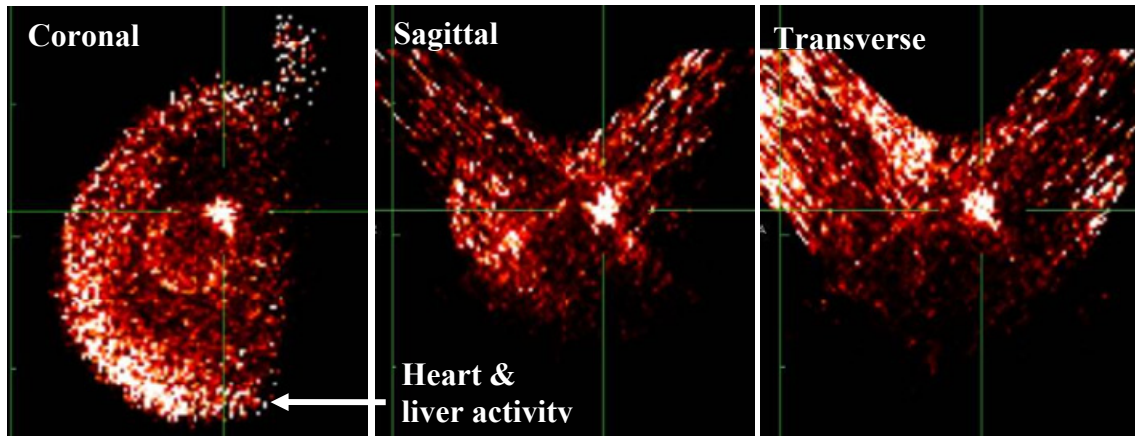
Figure 5.6: (Left) Coronal, (middle) sagittal and (right) transverse slices of the reconstructed breast. Note the clearly enhanced area of uptake that corresponded with a similar sized area seen on an accompanying MRI scan. Distortion in the breast shape, most readily apparent in the sagittal image, arises from using the tilted parallel beam orbit. The noted streak artifacts, due to uptake in the heart and liver are most readily apparent in the coronal and upper left transverse viewpoint, and indicate the requirement for shielding of the patient bed, as well as application of trajectories that minimize out-of-breast activity.

Due to physical size restrictions, the independent CT system was not capable of acquiring breast data of the patient using this early patient bed.

This limitation then drove the requirement to design a customized patient bed that would allow an integrated SPECT-CT system to perform dual-modality imaging of a pendant breast under the prone patient.

5.4. Patient Bed d Design for the Integrated SPECT-CT System

The design of the patient bed fits into a larger chain of system components, each of which must be optimized to enable close proximity imaging of the patient's chest wall. In light of the fact that the x-ray source and detector were fixed components at the time, the large imaging dead zones on both the x-ray tube, ~8.5cm, and detector ,~4.5cm, (see Figure 5.1) comprised the major limiting factors in the design of the bed.

The design process can be roughly divided into six separate stages, as shown in the design flowchart in Figure 5.7.
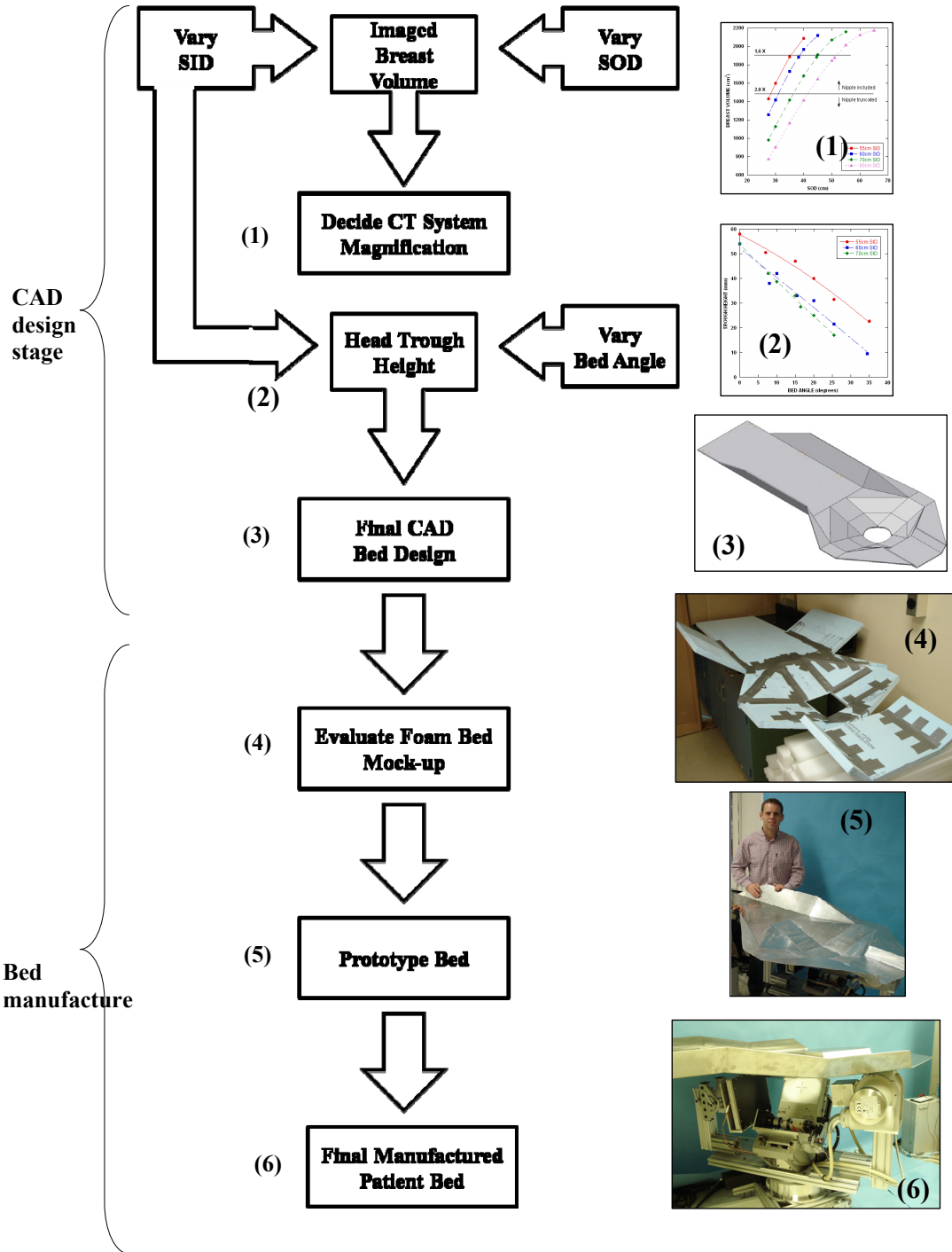
Figure 5.7: Flowchart of the bed design from design parameter generation (1) & (2) to CAD design of the concept bed (3), foam bed mock up (4), prototype steel bed (5), and modified bed design and integration with the prototype integrated SPECT-CT system (6).

207

5.4.1. Selecting System Magnification Parameters

In the initial stage of the bed design process, the x-ray tube and detector currently used in the CT system were accurately modeled using CAD software. A 2200mL breast was also modeled using a simple hemispherical shape. Different source to image distances (SIDs) of the x-ray source to the detector (55-80cm) were used, while the 2200mL hemispherical breast was placed at various points in between the source and detector to model imaging an uncompressed breast at various source to object distances (SODs) (see Figure 5.8). Each of these various SID-SOD combinations then modeled the task of imaging an uncompressed breast in the FOV with a different image magnification, i.e. the ratio of SID to SOD. The x-ray cone beam that resulted from each SID-SOD combination was also modeled, with the cone beam beginning as a point source of x-rays at the x-ray tube focal spot and diverging in the shape of a four-sided pyramid to impinge the modeled active face of the x-ray detector at the required SID (see Figure 5.3 for an example of a modeled cone beam shape).

For each of the various combinations, some of which are shown in Figure 5.8, the total breast volume irradiated by the cone beam for each setup was then generated by calculating the intersection of the modeled x-ray cone beam with the breast. This intersection volume information was automatically generated using a built-in procedure in Autodesk Inventor. Nipple truncation in the FOV was additionally noted although no setups with nipple truncation are shown in Figure 5.8.
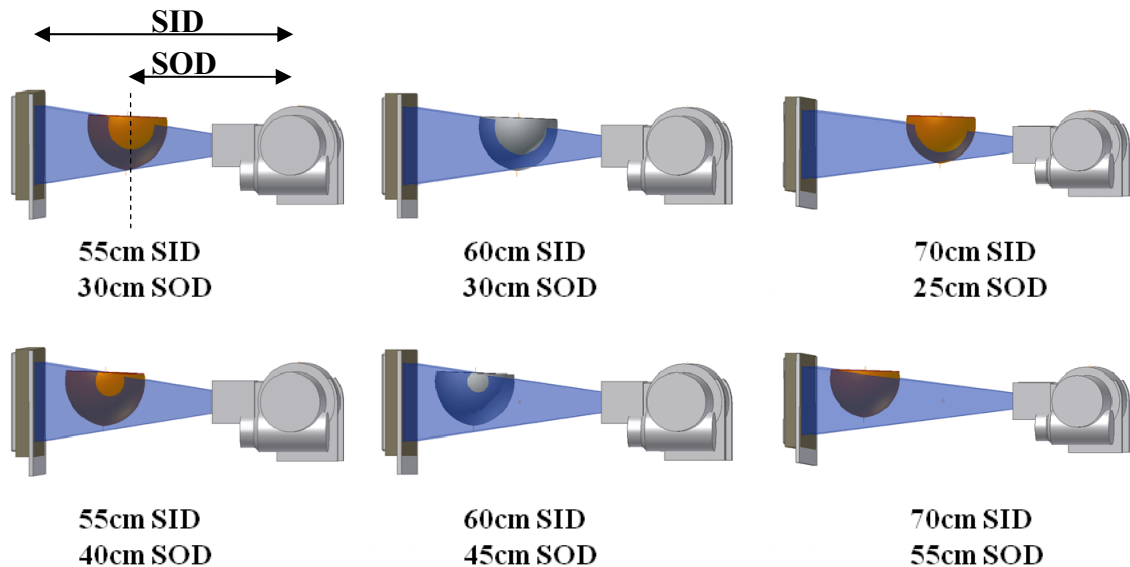
Figure 5.8: CAD images of the CT source-detector system with cone beam (blue) imaging pendant hemispherical breasts at various SID and SODs. Note the change in imaged breast volume, calculated as the intersection of the modeled x-ray cone beam with the breast volume, as SOD changes for each SID.

Figure 5.9 shows data generated from the CAD models employed in Figure 5.8. Magnifications larger than 2X involve nipple truncation, decrease the imaged breast volume for the *Varian 2520* detector, and have additionally been shown to increase focal spot blur [194]. Increased x-ray scatter is associated with smaller magnifications as the breast is positioned closer to the x-ray detector [97, 195].

The overall results of this stage of the design process suggested using an image magnification similar to the magnification of the independent system (i.e. ~1.6). Additionally, an 80cm SID was considered too large for routine use with the heavily filtered x-ray beam since this large SID would have increased the power required to routinely generate adequate flux of the heavily filtered beam to pass through the breast.
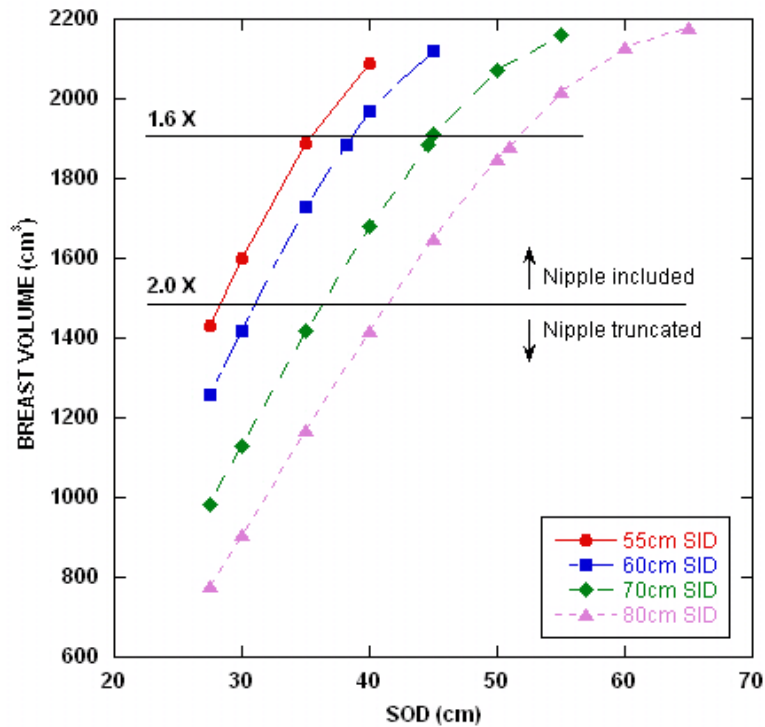
Figure 5.9: Imaged breast volume with accompanying nipple truncation as a function of CT system SOD at various SIDs. Lines at 1.6x and 2.0x indicate the relative object magnification from isocenter.

5.4.2. Determine the 'Trough Height'

A subset of these SIDs, (55-70cm) was then used to generate outlines of potential patient bed designs. A sample skeleton bed design for a 60cm SID with the relevant bed design parameters noted on the image is shown in Figure 5.10. In these images, the chest wall of the patient is assumed to contact and rest on the upper surface of the thin bed. The appropriate 'trough height' at the head section of each bed design was determined in the second stage of the process by varying the angle of the bed at the patient's waist across the tested SIDs. The approximate placement of the head and waist of the patient is noted on Figure 5.10.

210

The trough height is also indicated on Figure 5.10 and is defined as the distance between the plane where the head of the patient is resting and the surface of the patient bed over the axis of rotation of the x-ray system. It was thought that a larger trough height is associated primarily with increased strain on the neck of the patient, since the patient's torso curves more into a deeper torso section when the patient is lying prone.
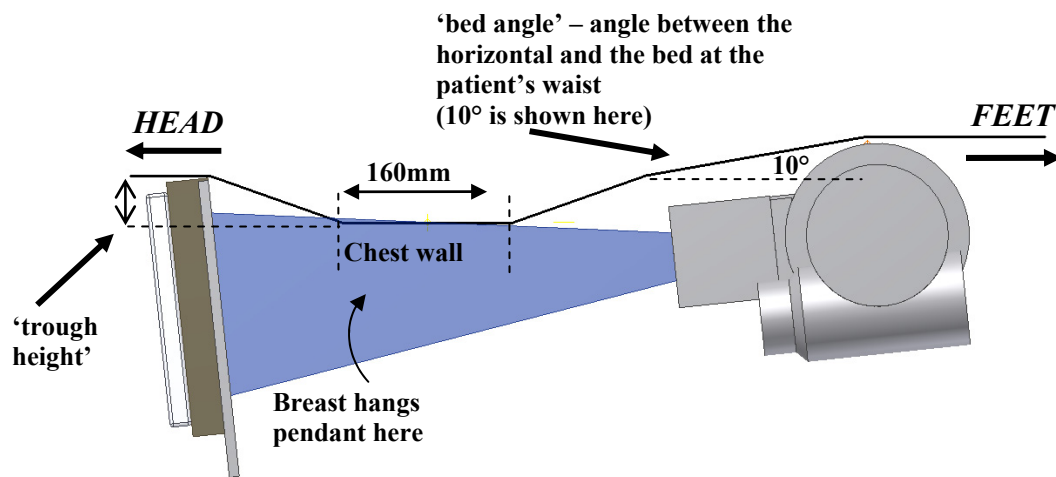
Figure 5.10: Schematic of the CT system at 60cm SID and 10° bed angle with an outline of one potential patient bed design superimposed on the sketches. The designed clearance between the underside of the bed and the top of the detector and source housing is 5mm.

Trough height and bed angle are co-dependent design parameters. In general, when trough height is increased, bed angle reduces and *vice versa*. To reduce trough height at the head section of the bed and consequently reduce neck strain, it was proposed to increase the angle of the bed at the waist in order to encourage the patient's torso and chest wall to naturally extend down and into the FOV of the cone beam.

70cm

60cm

Axis of rotation of the CT system

SID = 55cm

0°

10°

20°

212
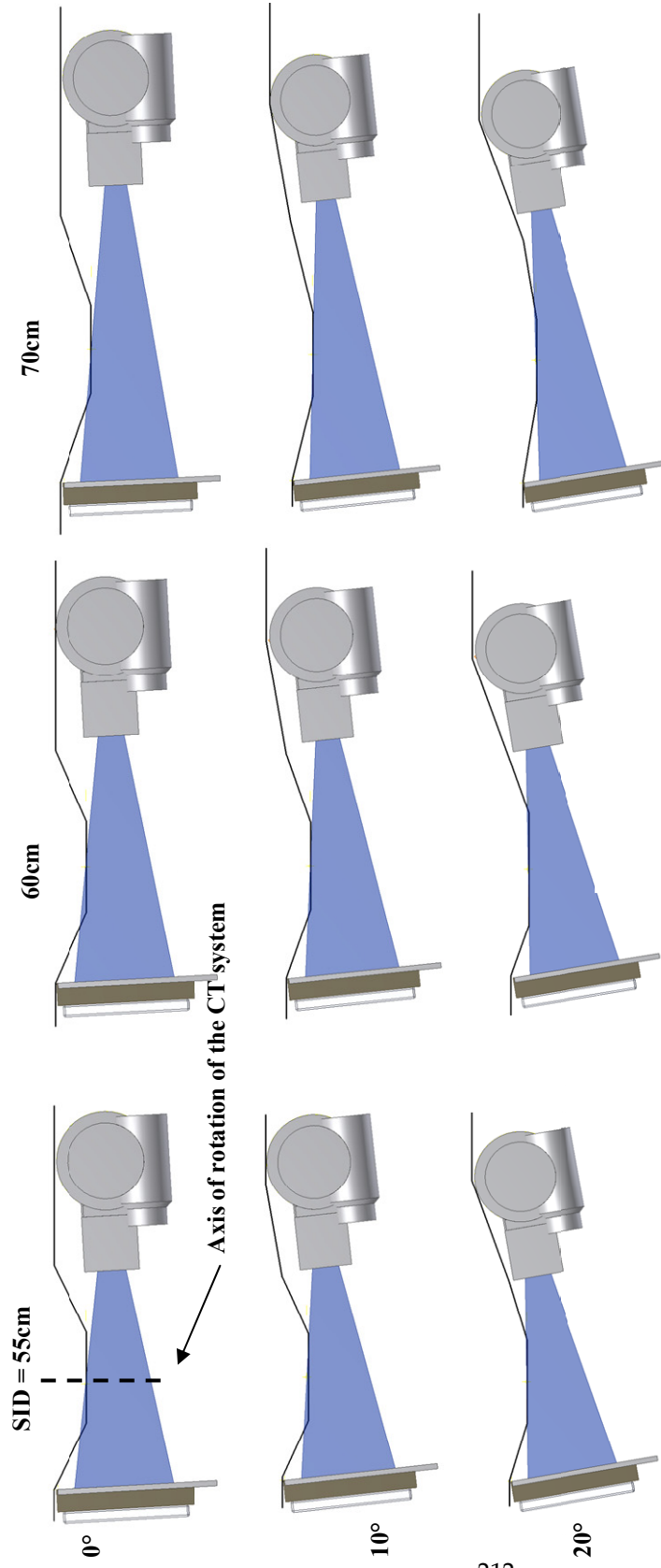
Figure 5.11: A series of CAD images showing the skeleton outline bed designs superimposed on CT systems with a variety of SIDs noted above the images, and at various bed angles noted to the side of the images. Note the reduction in trough height as the bed angle decreases. The vertical axis of rotation for the CT system is indicated in the top left hand corner image.
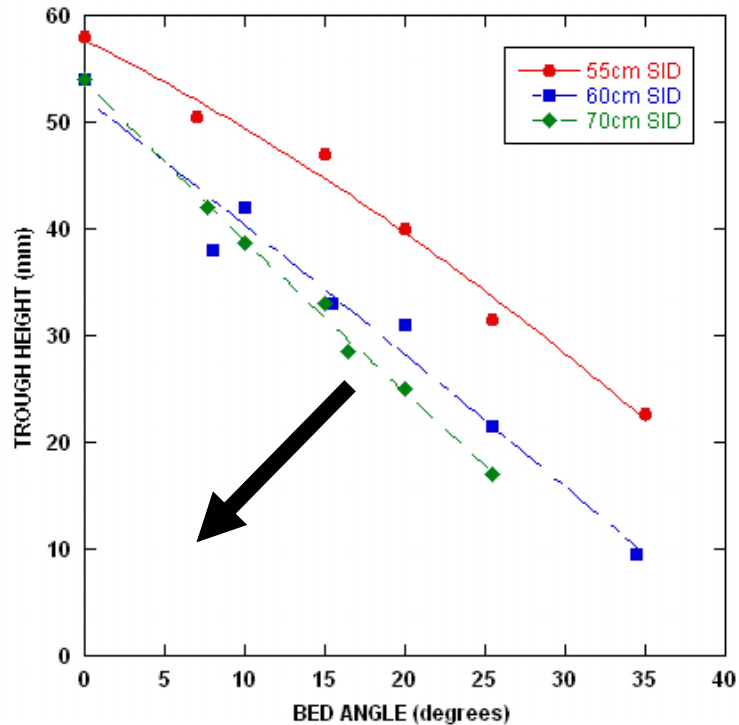
Figure 5.12: Plot of trough height as a function of bed angle for various SIDs. Note the reduction in trough height as SID and bed angle both increase. The presumed ideal bed characteristics for patient comfort of zero trough height and bed angle are indicated by the arrow.

While this action may make it easier to extend the patient's chest into the FOV, the patient still needs to be able to manipulate her head and neck out of the torso section and onto the head section of the bed. This action becomes increasingly difficult as the bed angle increases and it was recognized that too high a bed angle would also create discomfort, although the angle at which this would affect the patient was a subjective decision (indeed it would likely vary from patient to patient).

Outlines of potential bed designs with varying bed angles for various SIDs are shown in Figure 5.11. Note that the indicated trough height decreases with increasing bed angle.

213

This is confirmed by the results of measured trough height versus bed angle shown in Figure 5.12. The superimposed arrow points towards a comfortable patient bed design i.e. that of zero trough height (a flat bed) and zero bed angle which still allows the CT system to rotate about the breast.

5.4.3. Design the Bed in CAD software

Using the CAD models and the imaged breast volume data, a bed design was chosen that was judged to give the best compromise between the ability to image breast volumes closer to the chest wall of the patient, while possessing an acceptably small bed angle and trough height. This final choice was for a bed designed for a 60 cm SID that possessed a bed angle of 7.5°, and a trough height at the head of 41mm.

The CAD bed design is shown in various orientations in Figure 5.13 with the dimensions superimposed. A tiered bed design is the only practicable solution to accommodate the large dead zones of the source and detector while also allowing comfortable patient imaging close to the chest wall. The torso section of the bed was octagonally shaped to increase the strength of the bed and to also provide symmetry for either left or right breast imaging. Side panels (wings) added to the bed provide additional protection for the patient/detectors from scatter/emission contamination as the system rotates below, and increase strength along the bed axis.

Figure 5.14 illustrates the bed overlying the integrated SPECT-CT system with the simulated x-ray cone beam and SPECT camera FOV superimposed.   This figure

illustrates that the bed was designed to allow the x-ray cone beam penetrate through the undersurface of the bed.
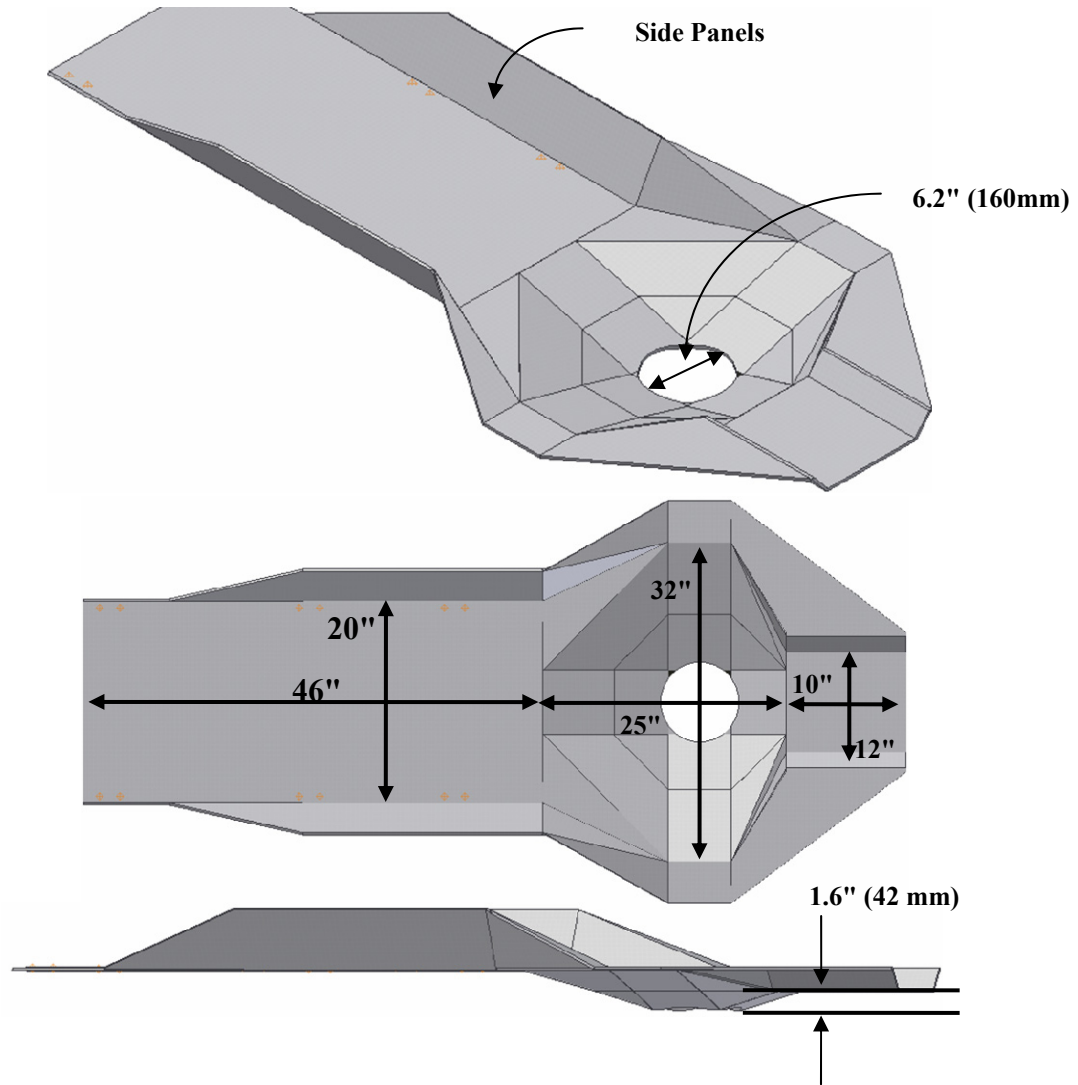
Figure 5.13: CAD images of the prototype bed design sent for initial manufacture shown in various orientations to demonstrate the angled and asymmetrically tiered design. Although this was not the final implemented bed design, the area of eth bed directly involved in imaging the patient, i.e. the tiered octagonal torso area was the same between this prototype and the final bed design. The dimensions of some important sections of the bed are superimposed.

Anterior View

Anterior-oblique View
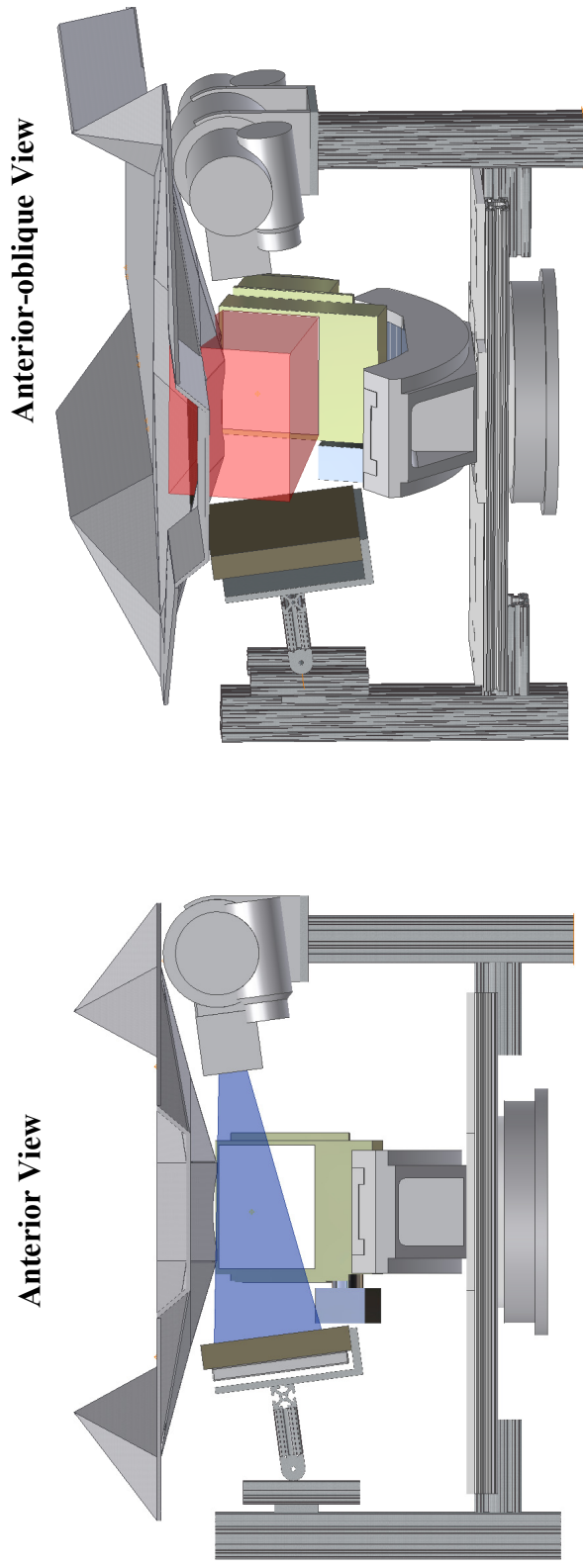
Figure 5.14: CAD model images of the prototype bed with superimposed (left) x-ray cone beam in blue and (right) SPECT gamma camera FOV in red. The cone beam intersects the bottom of the bed and therefore the chest wall. The SPECT FOV intersects the torso region of the patient but photons emanating from outside the breast volume of interest (except that volume directly above the hole) should be removed by additional 1/16"lead sheet lining the bed (not shown).

5.4.4. Foam Mock-up of the Bed

The next stage of the process consisted of assembling a polyurethane foam-based prototype of the designed bed in the lab (Figure 5.15). The sections of 1" dense foam were manually cut using the dimensions of the CAD design and attached to each other using both glue-based adhesive (*Gorilla Glue Inc*., Cincinnati, OH) and strong duct tape; all three components were sourced at a local hardware store. A protractor was used to manually measure the angles of the side panels that were used in this prototype design. Due to the complex and complementary angled sides, assembling the octagonal torso section was particularly difficult but general accuracy was maintained, enough for the purposes of this early stage prototype.

Upon assembly the bed was lined with 1" thick polyurethane foam to mimic the intended set up while imaging volunteer subjects. The bed was then tested by several volunteers and the design was found to be adequate in terms of its comfort and its ability to accommodate people of different sizes. The decision was made to proceed with the next stage of the process, manufacturing a metal-based prototype patient bed.

Figure 5.15: Photographs of the foam-based mock up of the bed used to initially test the CAD design.

5.4.5. Manufacture of a Prototype Bed

Designs for the manufacture of a 1/16" galvanized steel prototype bed were submitted to a local design and manufacturing company (*Barnes MetalCrafters Inc.*, Wilson, NC) that possessed the necessary software and hardware skills to accept the CAD designs and accurately build the patient bed.

Upon manufacture and delivery, the 1/16" thin prototype patient bed was integrated with the other components of the hybrid imaging system (Figure 5.16) and the dimensions of the design checked to determine if late stage modifications to the design were required before the final bed design was submitted for manufacture. The newly integrated prototype imaging system, complete with patient bed, was successfully tested by mechanically operating it in a manner similar to the planned imaging protocol. It was decided to extend the side panels for the extra comfort and safety of the patient, especially at the side of the torso and head sections. Once these modifications were completed in CAD (Figure 5.17) the final bed design was approved and submitted for manufacture. The final designed bed had the exact same dimensions as the bed design in Figure 5.13, and differed only in the presence of extra protection at the extreme sides to protect the patient.

220
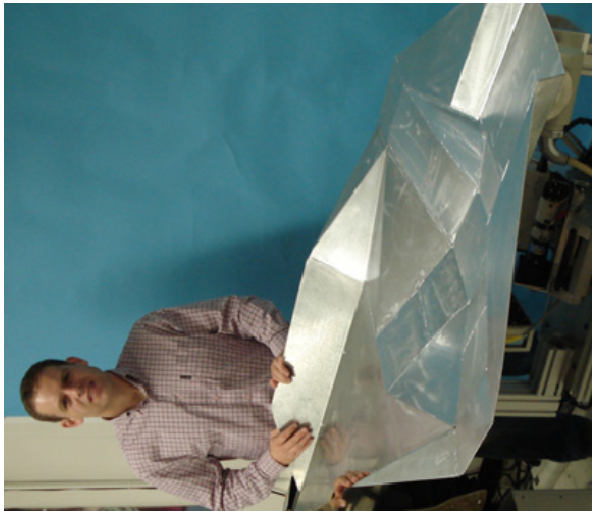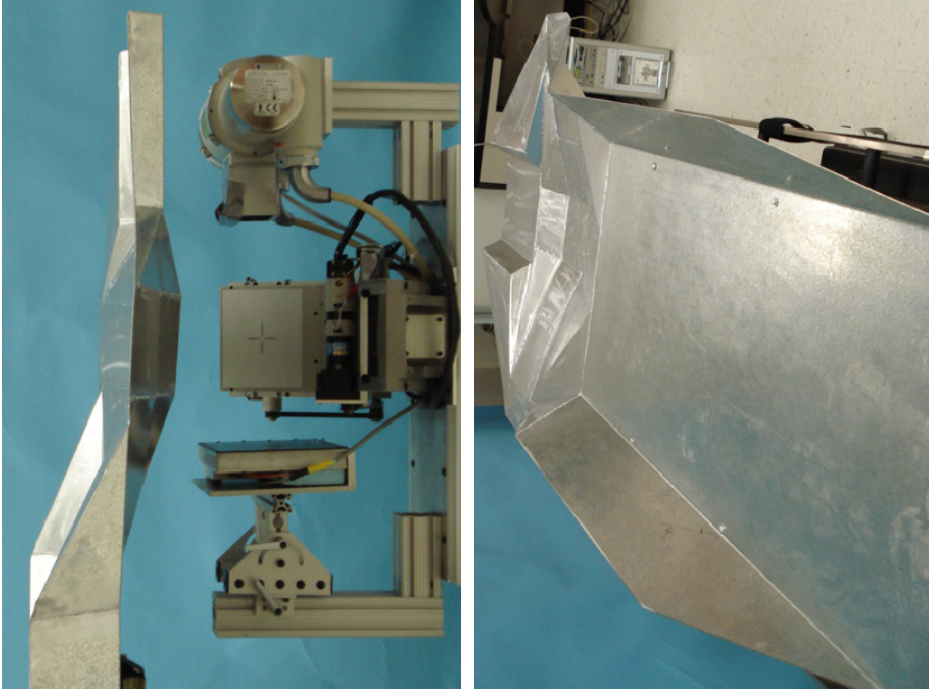
Figure 5.16: Photographs of the thin 1/16" galvanized patient bed (note the lack of a hole built into the torso section of the bed) integrated with the hybrid imaging system.

Removable torso section

10"
12"
32"
25"
50"
50"
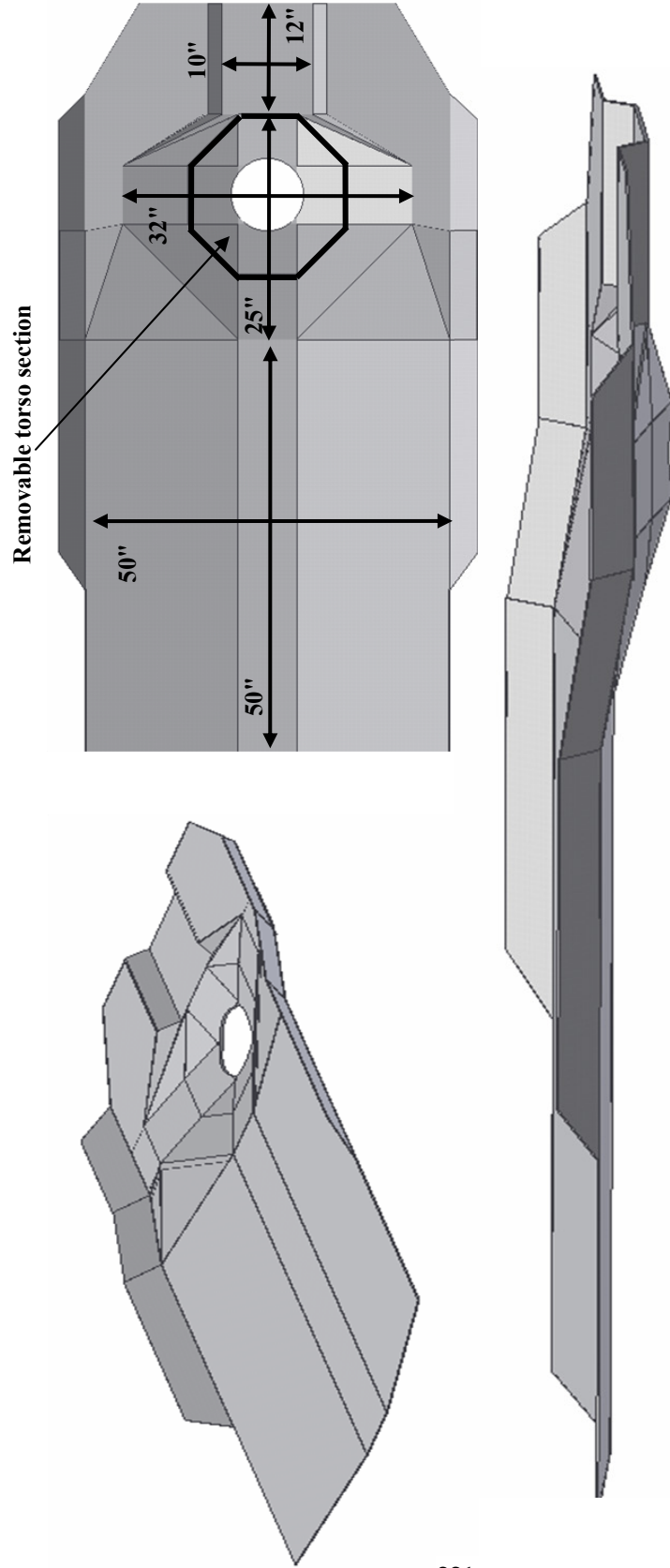
Figure 5.17: CAD sketch of the final bed design sent for manufacture. The dimensions of the bed are nearly exactly the same as those of the bed shown in Figure 5.13, except that there are extra side panels for patient protection, and the bed is now angled along the bed axis for extra strength. This bed, in contrast to the prototype galvanized stainless steel bed, includes the removable torso section that could be replaced by radiolucent materials, or be removed completely. The outline of the removable torso section is indicated by the superimposed black lines.

221

5.4.6. Manufacture and Integrate the Final Patient Bed Design

The final bed was manufactured from ⅛" thick stainless steel and is shown from different orientations in Figure 5.18. A unique feature in the bed design was to allow the lower half of the stainless steel octagonal torso section to be removed so that it can be replaced by a radiolucent material. The reasoning behind this was that the flexible bed design could then accommodate future CT system components with smaller dead zones to enable imaging closer to the posterior breast and chest wall of the prone patient.

As shown in Figure 5.18, the new customized bed design was integrated with the Biodex bed system before the initial dual-modality patient scan was performed. The Biodex positioning system (model 830-058, *Biodex Medical Systems*, Shirley, NY) has five degrees of movement: an adjustable vertical range of 25.4cm, 25.4cm lateral travel and axial travel range of 50.8cm, trendelenburg of 60°, lateral role of ±20°, and can hold up to 500kg. The strength of the positioning system and the five degrees of controlled movement aid in extending maximal patient breast volume into the FOV and can also be used to negate bowing in the bed due to the weight of the patient [146].
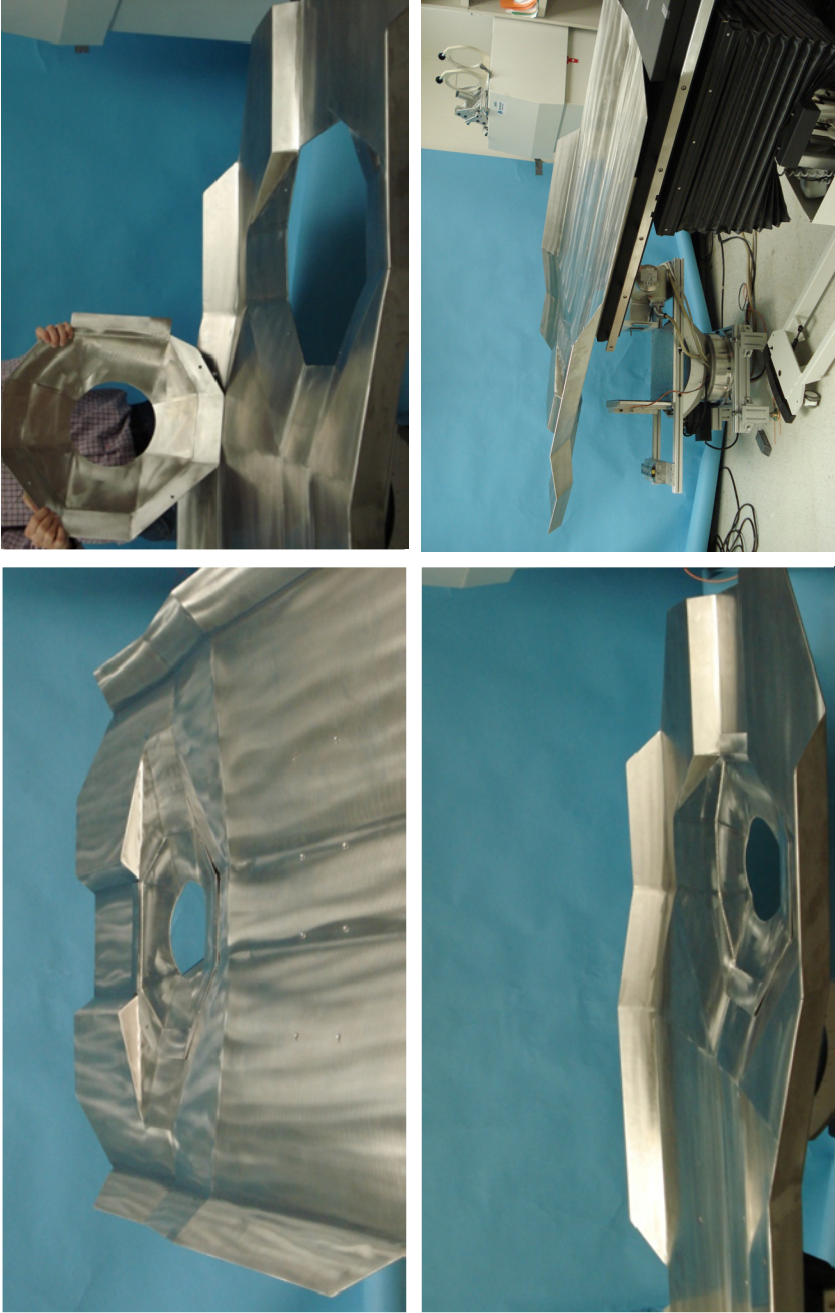
Figure 5.18: Photographs of the manufactured custom designed patient bed in different orientations. Note the torso section of the bed (top right) that can be removed to increase access to the patient breast and chest wall. (Bottom right) The new bed integrated with the Biodex positioning system and positioned over the original independent CT system.

5.5. Modifications to the Bed to Prepare for Volunteer Imaging

A number of modifications were made to the bed to prepare it to be involved in planned human volunteer subject imaging trials. The first modification to the patient bed was to line the upper surface with lead sheeting to protect the prone patient from x-ray backscatter, to protect the x-ray detector from primary and scattered ^{99m}Tc γ-rays, and to also limit out-of-volume activity from impinging on the gamma camera when tilted in the polar direction. The initial lead sheeting was in the form of modified lead aprons normally used by radiology technologists in imaging clinics. Two such aprons were laid on the bed, with a circular opening cut into one of the aprons to enable the pendant breast to protrude into the imaging FOV. The upper surface of the stainless steel bed was then additionally lined with a thin (1/16") sheet of lead (Figure 5.19), a thickness of lead that blocks over 99% of 140 keV ^{99m}Tc γ-ray photons.
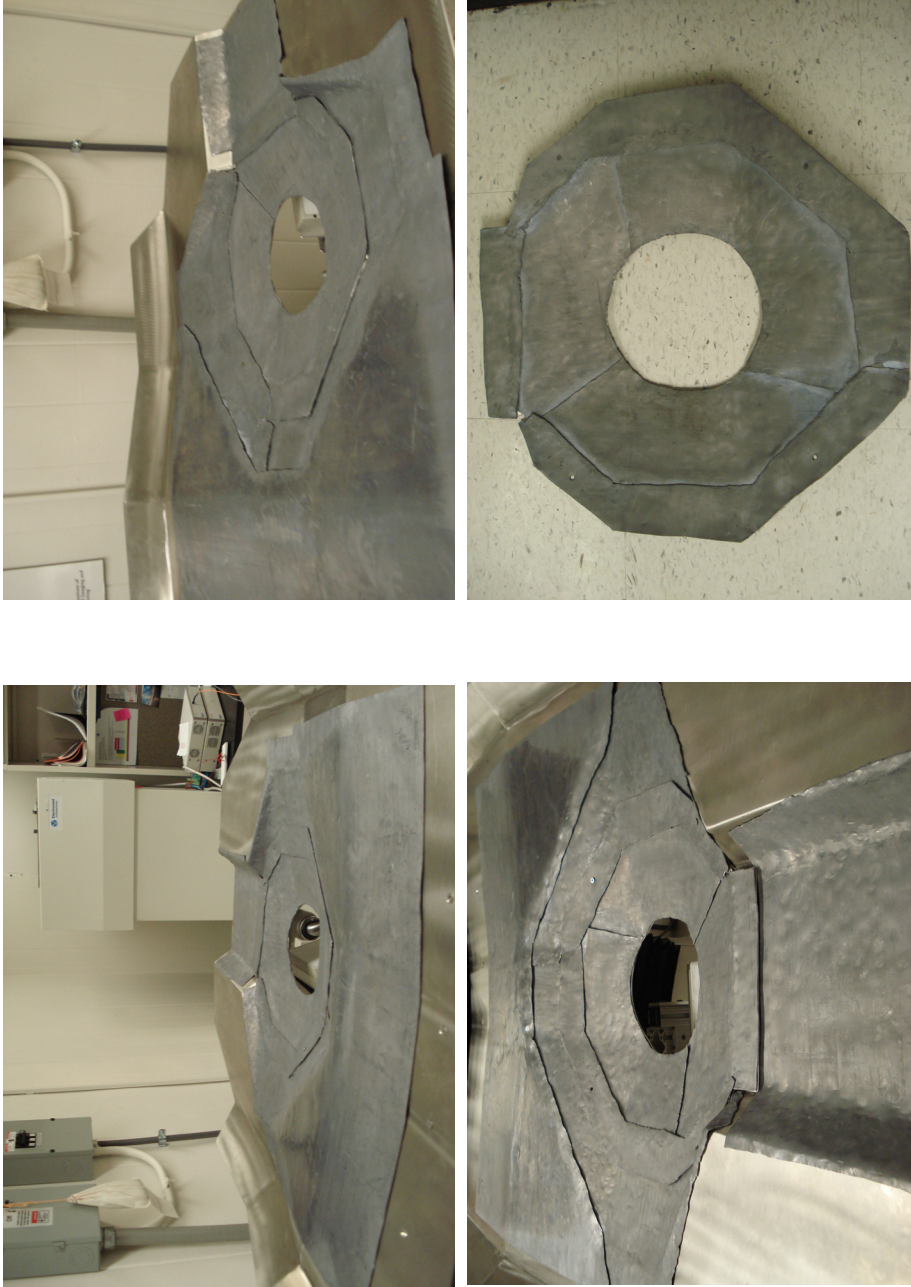
Figure 5.19: Photographs of the patient bed lined with the 1/16" sheets of lead that are molded to contour the upper surface of the 1/8" thick patient bed. (Bottom, right) The lead lined octagonal torso section is also shown removed from the bed.

225
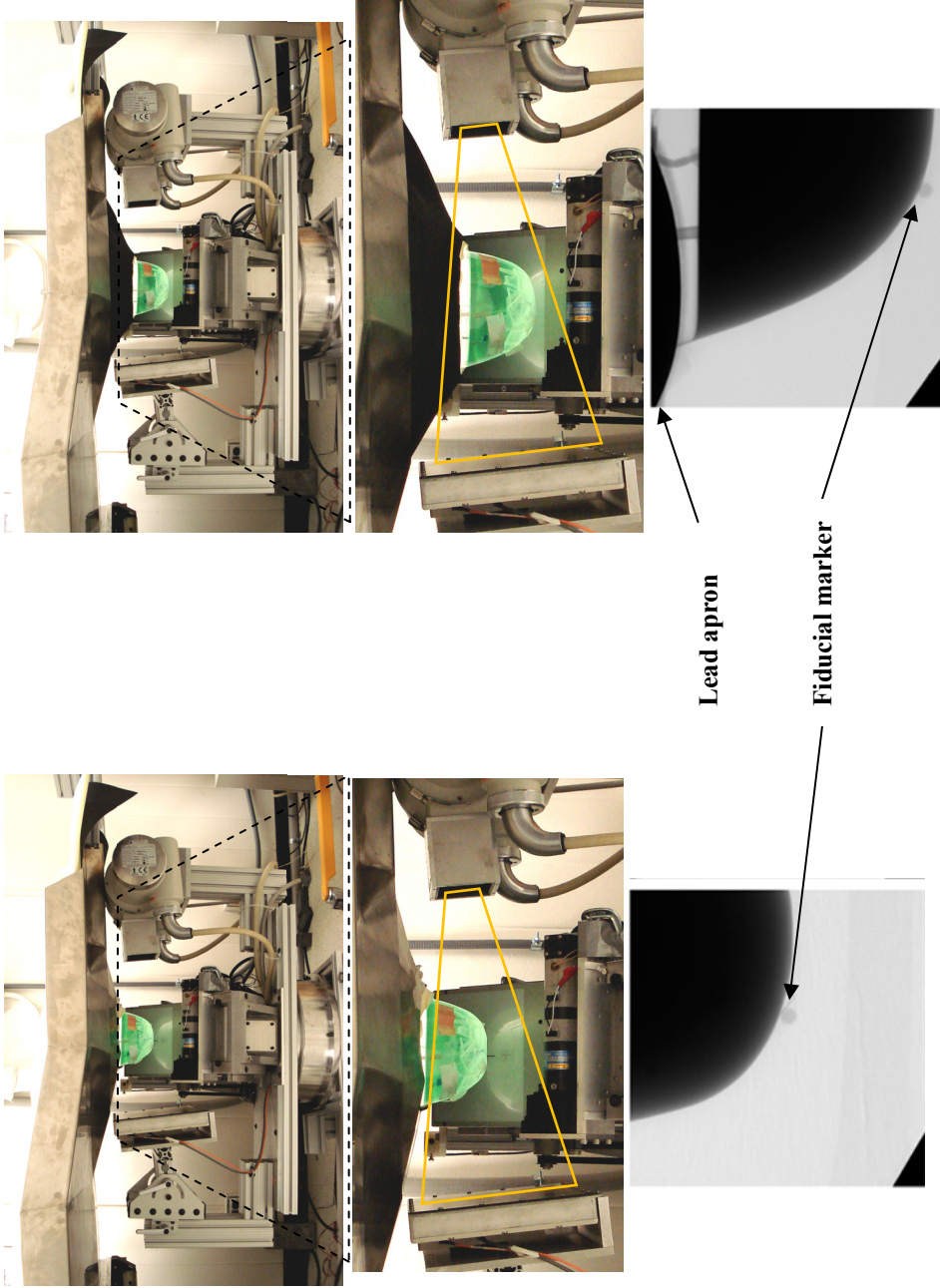
Figure 5.20: The volume of breast imaged with (left column) the rigid torso section in place, which is increased by (right column) replacing the rigid section with flexible neoprene to allow the breast phantom to sag more into the cone beam FOV. This increased volume in projection images viewed by the cone beam (orange overlay) can be appreciated by comparing the location of the same fiducial marker in both cases as well as the increase in breast volume at right. (Photos and images courtesy of Spencer Cutler M.S.).

It was also thought that when integrating the bed with the CT system the imaged breast volume would be increased greatly by removing the rigid steel octagonal torso section (see Figures 5.18 and 5.20). The original bed design had a removable torso section, and so this possible breast volume increase could be evaluated. Figure 5.20 shows the results of an experiment carried out by a lab colleague that indicates the increase in imaged volume of a geometric breast phantom when the inner torso section is removed [87]. The flexible neoprene sheet attached to the surface of the bed sags under the weight of the object that lies on top, and so introduces the object volume more into the FOV of the system. In the same way, it was expected that the layers of neoprene and thin lead sheeting would give support to patients, but also allow them the flexibility to comfortably and securely suspend their chest farther into the common system FOV rather than if the rigid torso section was in place.

5.6. Performance of the Patient Bed during the Patient Imaging Trials

5.6.1. Chest Wall Imaging

The original patient bed was designed to enable pendant breast imaging through the chest wall with the realization that the integrated CT system, restricted to azimuthal rotation about a vertical axis of rotation at a fixed height above the ground would impact the head section of the bed before it was able to rotate fully through 360°. However, the powerful *Biodex* positioning system allowed more variety in bed orientations than were tested during the original bed design process using CAD software. After a process of trial and error, it was found that by using the trendelenberg feature of the *Biodex* system, the

patient bed could be tilted in such a way as to enable the CT system to rotate a full 360°
around the vertical axis of rotation and acquire a full set of projection data while
maintaining imaging relatively close to the chest wall of the patient. To enable this
change from increase configuration, the CT system was tilted at a 6.25° tilt to the
horizontal. This is the patient imaging system setup that was used during the human
volunteer patient imaging trials.

In addition to the initial SPECT-only patient imaging trial described earlier, four
subsequent volunteer subjects were imaged using the CT and/or SPECT systems [165].
A photograph of one of the subjects undergoing imaging is shown in Figure 5.21, and the
zoomed in photograph shows a red laser line used in the volunteer imaging process. This
laser line was used in initial positioning of the subject and was designed to indicate the
approximate height of the top plane of the cone beam relative to the posterior portion of
the patient's breast.

The rationale for including the image of the patient and the laser line is to highlight the
fact that the chest wall was not seen on either of the CT images reconstructed from data
acquired using the new patient bed. Although the powerful 3D positioning of the SPECT
system allows viewing deep into the torso of the patient (note the signals from out of
volume views of the heart and liver in Figure 5.6), the integrated CT system was never
able view the chest wall in any of the patient trials.

Figure 5.21: (Left) Photograph of a volunteer subject lying prone on the bed and being imaged by the integrated system. (Right) Zoomed in photograph of her pendant breast in the common field of view of the SPECT-CT system. The breast has a laser line superimposed that is approximately 1 cm below the top plane of the x-ray cone beam. As can be deduced from the image, the top plane of the cone beam did not intersect the chest wall (not visible in the photograph) of the volunteer.

There are several potential reasons why the CT system was unable to image the chest wall of the patient. As described earlier, CAD models indicated that the ability of the divergent cone beam to penetrate the chest wall using this patient bed was contingent on the CT system performing limited angle tomography (<360°) of the breast. Limited angle tomography will be investigated more fully in Chapter 6 but, briefly, the advantage of the method is that it potentially allows for imaging deeper into the chest wall, while accepting a reduction in angular sampling.

Limited angle tomography was not performed on any of the human patients. During the patient scans the bed was always positioned in such a way to allow a full 360° rotation of the integrated CT imaging system. This arrangement increased angular sampling but at a cost of imaging closer to the chest wall. The reason for a reduction in imaged breast volume is that, in order to allow the x-ray source to rotate 360° under the bed, the bed must be raised to accommodate the rotating x-ray source. However, we have already seen that the x-ray source possesses an 8.5 cm imaging dead zone (see Figure 5.1). Simply raising the bed then also increased the separation of the top plane of the cone beam from the patient's chest wall, with the effect of ensuring that the chest wall of each patient lay outside the field of view of the cone beam. It was hoped that the multi-axis positioning capability of the bed positioning system could compensate for this increased separation and be used to position the breast and chest wall into the FOV. In addition, it was hoped that the flexibility of the neoprene center would partially compensate for the separation by enabling the patient's breast to sag further into the field of view, but neither the effect of the neoprene, nor of the bed positioning system was enough to accomplish this.

One other factor in the practical implementation of the bed during patient imaging is the extra layers of material adjacent to the upper surface of the bed to increase the comfort and protection of the prone patient. A list of such extra material includes the 1/16" lead sheet, the layer of flexible neoprene, the additional layer of the more mobile lead aprons for extra protection, the 1" thick compressible polyurethane foam, and finally pillows to comfort the head of the patient. While the effect of each of the layers in prone patient imaging is individually small, the cumulative effect of all these extra layers is to further separate the chest wall from the top plane of the cone beam. The addition of extra layers on the upper surface of the bed must be addressed in any future bed design.

By analyzing photographs of the pendant breasts hanging in the system FOV taken during imaging trials and by comparing the known dimensions of imaging components to the apparent dimensions of the breasts, we can estimate the depth of breast coverage missed. For the volunteer whose breast is being imaged in Figure 5.22, it can be estimated that an approximate 4cm difference exists between the top place of the cone beam and the approximate border of the chest wall (indicated by the superimposed dashed white line) for this subject. This was an inexact method but indicates the level of separation that must be overcome in any new bed design.
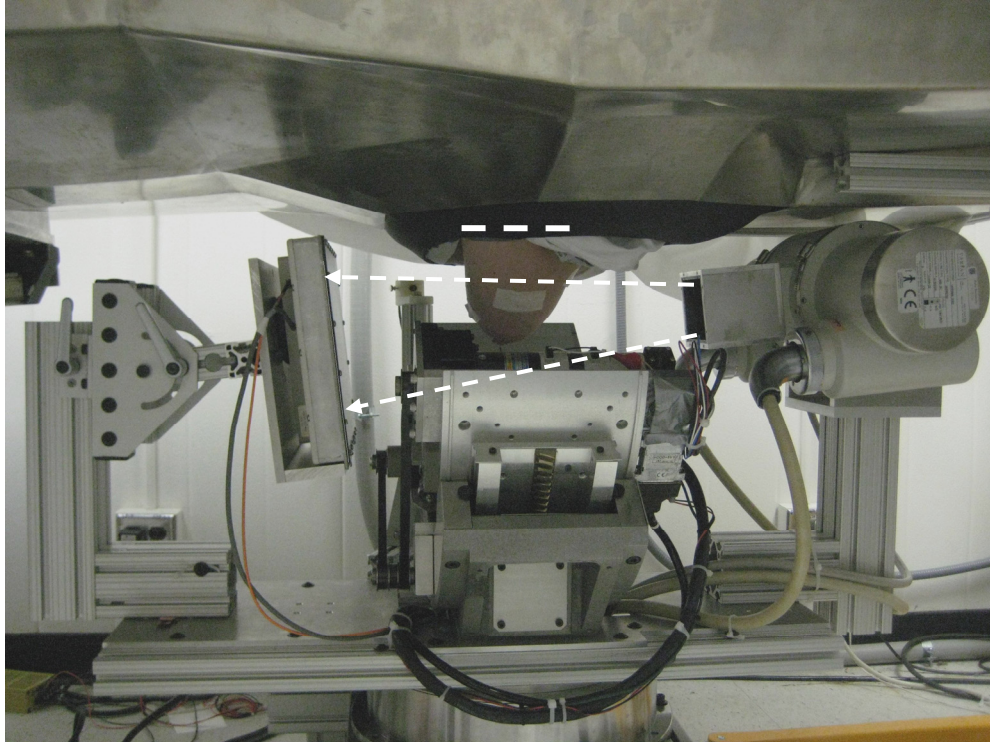
Figure 5.22: Photograph of a volunteer's pendant breast undergoing imaging, with the bed raised to allow the system to traverse under the head section at right. The top plane of the cone beam (whose limits are approximated by the dashed arrows) is separated an estimated 4cm from the presumed chest wall (approximated by the dashed white line).

5.6.2. Patient Comfort

Volunteers freely offered anecdotal evidence during and after each imaging session about their perception of comfort and pain while lying on the bed. In general, most volunteers found the bed to be comfortable during the course of the scans, but some patients complained of pain in their neck and shoulder regions after an extended period (~15minutes) of lying prone on the bed. The tiered and angled design of the patient bed, especially near the head section, likely contributes to the perceived level of pain, and it is vital that this issue be addressed in future iterations of the bed design.

5.7. 2nd Iteration of the Integrated System Design

Accurate CT reconstruction of objects in 3D space demands great accuracy in the relative positioning of the x-ray source and detector components as it acquires tomographic images around the object. The components in the original independent CT system were securely attached together to a common baseplate using custom designed holders for both the detector and x-ray tube.

In contrast to the independent system, the metal parts connecting the components of the initial prototype integrated CT system were not custom designed to securely fit the detector and x-ray tube (Figure 5.2). Instead, they were specifically designed to be flexible in terms of their ability to modify SID, SOD, and the source-and-detector pair polar tilt if the need arose, as it did when the patient bed was initially integrated with the positioning system (Sec.t. 5.3). However, this flexibility meant that there were too many degrees of freedom, which resulted in decreased positioning precision.

In the initial integrated CT system, the attachment points for the x-ray tube and detector tended to shift when contact was made with them. Over the span of a 60cm SID, a deviation of even 1° in the x-ray detector tilt angle shifts the central x-ray over 10mm (or approximately 80 un-binned detector pixels) from the center of the detector. Therefore the high level of precision required for accurate 3D reconstruction was not present in the initial prototype integrated configuration.

In order to ensure that the relative orientations of the components remained fixed in 3D space, it was decided to implement a more robust U-shaped arm that, similar to the

independent CT system, physically connected the x-ray source to the x-ray detector on a single piece of material. The thick U-shaped-arm, along with stiff connectors, including a new U-shaped holder designed to fit securely around the x-ray detector, increased the ability of the system to withstand small impacts without changing orientation. This was an important advance over the previous integrated system design.

Images of the CAD designs for the c-arm based system components are shown in Figure 5.23 and located in place in Figure 5.24. The new designed parts included the source-detector U-shaped connector, a new thicker U-shaped x-ray detector holder, and angled wedges to enable a fixed and stable x-ray source-detector tilt. The c-arm is designed for a 60cm SID but the design can accommodate slightly longer SIDs (~5-10cm) by moving either the source or detector farther away from the center of rotation.

The tilt angle of the x-ray source-detector combination can also be changed by adding wedges machined at desired angles. These wedges are designed to be attached to standard 3x3" metal bars cut to the desired height (this will change with a change in wedge angle) above the common baseplate. This arrangement adds flexibility to the overall system design in terms of the tilt capability of the integrated CT system [141]. Using this flexibility, the x-ray source and detector are tilted now at 3.11°, which ensures that the upper surface of the x-ray source and the upper surface of the x-ray detector are at the same height. The wedges were designed to be tilted at an angle of 3.11° to accommodate this new angle.

60 cm SID
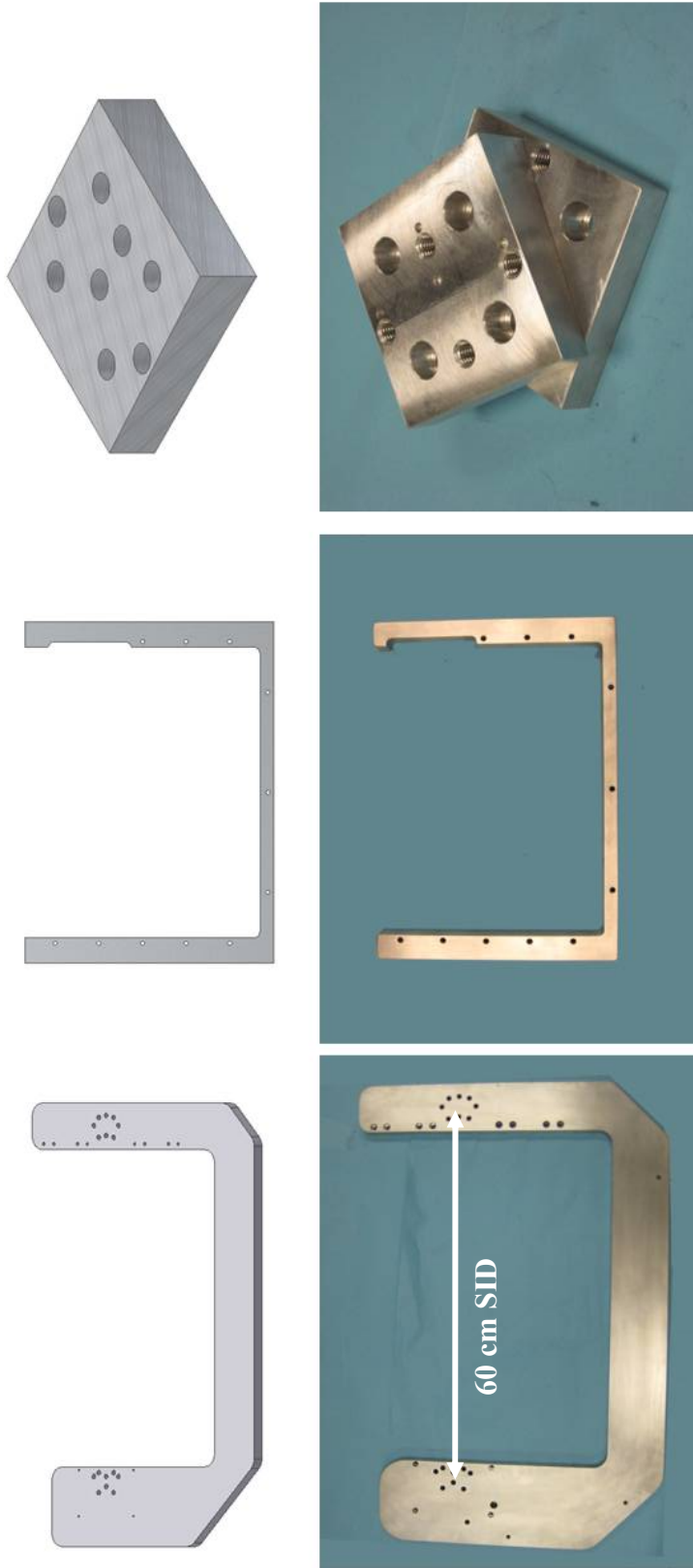
Figure 5.23: CAD images of the (top left) modeled U-arm (top row, middle) U-shaped detector holder and (top row, right) 3.11° angled wedge for the source and detector to modify the relative tilt of the CT system. The equivalent photographs of the manufactured aluminum pieces are shown in the bottom row.

235
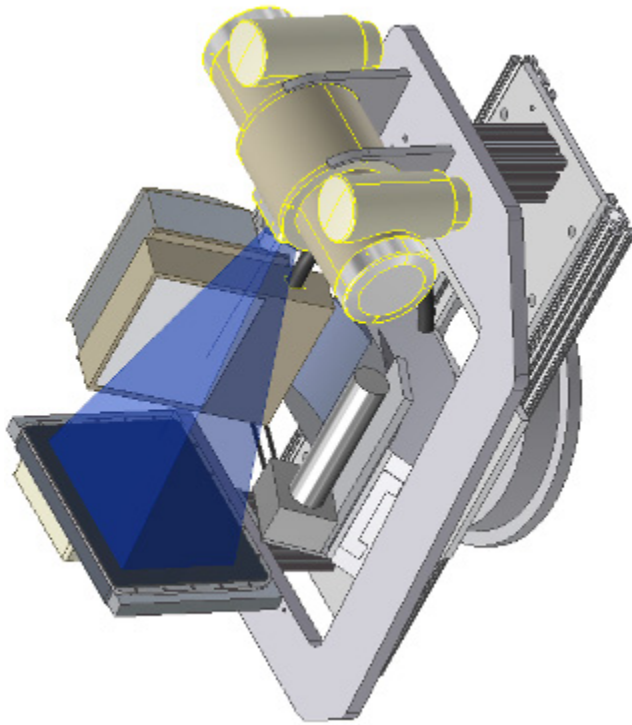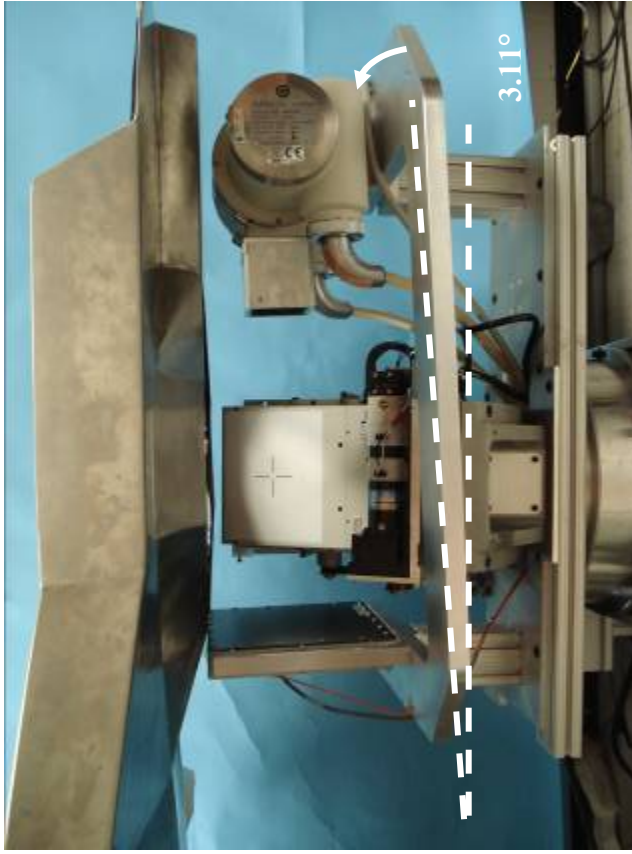
Figure 5.24: (Left) CAD image of the u-arm based CT system and (right) photograph of the new integrated CT system design tilted at 3.11° such that the tops of the x-ray source and detector are co-planar. The modeled x-ray source (left) is a CAD model obtained directly from Varian and so the vertical orientation of the anode and cathode terminals in the modeled x-ray tube are fixed and different from the orientation of the anode and cathode shown in (right) the implemented integrated SPECT-CT system.

This new relative tilt means that both the source and detector can practically rotate 360° under the bed, assuming one component can already do so. But there is a tradeoff in this new arrangement: reducing the x-ray source-detector tilt angle means that the top plane of the divergent cone beam at the isocenter now penetrates through the breast farther from the patient's chest wall. This system has yet to be used to image human volunteer subjects.

5.8. Discussion

The chapter described the concept, development, and hardware implementation of a patient bed, custom designed to enable comfortable dual-modality SPECT-CT imaging of a prone patients' pendant breast using the prototype integrated breast imaging system. Initial patient imaging trials were conducted using the integrated imaging system with the patient bed and the results of these imaging studies were analyzed from the point of view of the design of the patient bed.

The requirements for effective prone patient imaging are challenging and it is clear from the results of the first patient imaging trials the current system designs are sub-optimal from the perspective of maximizing the imaged breast volume, chest wall and axilla. However, the current designs are recognized as successful waypoints on the road to effective and comfortable, fully 3D SPECT and CT patient imaging.

The ability to image the chest wall and axilla of a prone patient is a vital issue for dedicated breast imaging and is dependent on a variety of factors from effective initial

patient positioning to the ability to mechanically position the imaging system so that it can access and sample the chest wall.

It must be emphasized that the design of this patient bed is unique to the current x-ray system design, based upon the currently available x-ray source and detector. If different x-ray imaging components, such as a unipolar x-ray tube and a detector with smaller dead zones are implemented in the system, the design of the patient bed will change accordingly, and possibly dramatically. In addition, re-establishing the ability of the CT system to tilt in polar direction will likely further change the bed design to accommodate this added positioning flexibility. The ultimate drivers of a more effective bed design for breast CT imaging are therefore going to be the selection of imaging components that have small dead zones, thus enabling chest wall proximity imaging and a flatter bed design without the need for a highly-angled bed design that accommodates the component dead zones.

The last part of this thesis describes the use of novel trajectories to overcome positioning limitations of the integrated CT system that were described in this chapter.

Chapter 6

6. Limited Angle Acquisitions and Vertical System Shifting

This chapter investigates x-ray source detector trajectories that are specifically designed to increase the imaged volume of breast tissue near the posterior portion of the patient's breast and chest wall.

In Chapter 5, initial patient volunteer scans using the integrated breast CT system showed that a combination of challenges in effective patient positioning and dead zones in the CT components resulted in the top plane of the CT cone beam invariably being separated from the patient's chest wall when a 360° circular data acquisition orbit was employed (Figure 6.1) [196]. The objective of the studies completed here was to assess the feasibility of using unique x-ray source-detector trajectories designed to overcome these limitations, and in the process increasing the imaged volume of the patient's breast and chest wall.

Two potential solutions are investigated: (1) limited angle tomography, i.e. using incomplete (< 360°) breast CT trajectories to acquire data projections, and (2) vertically shifting the entire CT imaging system mid-acquisition for a portion of the 360° azimuthal rotation. Reconstructed images of geometric phantoms in a variety of contrast backgrounds are analyzed qualitatively and quantitatively, including observer studies, to evaluate the effect of both these types of trajectories on improving the visibility of lesion-like spheres in the posterior breast and anterior chest wall. The effect of limited angle

techniques on human breast tissue is also investigated using previously acquired patient breast CT data.

Although initially designed to be used for limited angle (<360°) tomographic data acquisition trajectories, in practice the patient bed was positioned just above the uppermost surface of the imaging system for volunteer imaging studies (Figure 6.1 and Figure 6.2, top left). This positioning enabled the CT imaging system to rotate unrestricted for a full 360° about a vertical axis of rotation beneath the prone patient while acquiring projection data, in the process improving angular sampling of the pendant breast. However, raising the height of the bed also results in increasing the separation of the top plane of the cone beam from the posterior breast of the patient.

The patient bed design is currently fixed, custom designed for this iteration of the integrated CT system design, and so two novel types of trajectories are described in this Chapter with a view to increasing the imaged volume of breast in the CT field of view (FOV) while also adequately sampling the pendant breast volume in the azimuthal direction. These sets of experiments established the feasibility of using these novel trajectories in future CT system design iterations.

Limited angle imaging techniques implemented here for dedicated breast CT involve intentionally lowering the patient bed below the uppermost surface of the CT system components. Consequently, while the CT system is limited to rotations <360° before it makes physical contact with the patient bed, the patient's breast and chest wall are positioned further into the imaging FOV. The tradeoff in employing limited angle

techniques is to increase the imaged volume of breast and chest wall but with a loss of angular sampling. Iterative reconstruction techniques employed in this system may be able to compensate for the effects of the lost projection data and minimize any resulting object distortion [101].
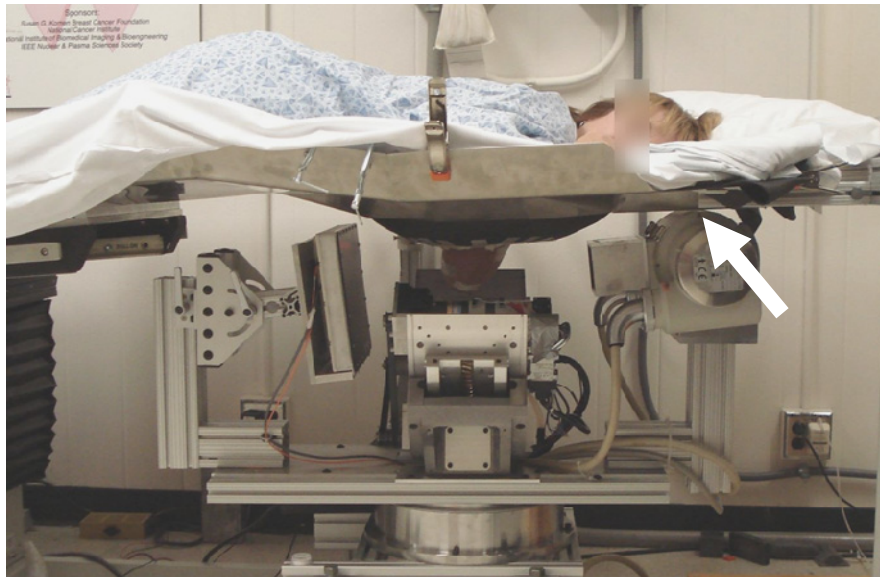
Figure 6.1: Image of the prototype integrated 1st iteration SPECT-CT imaging system with the tilted CT system visible while imaging a prone patient. In this photo, the bed is tilted slightly and raised (arrow) to allow the CT system to pass underneath the head section of the bed, thus separating the top plane of the cone beam farther from the chest wall.

We also evaluated using a vertical shift of the entire CT imaging system in mid-acquisition as another proposed novel trajectory to increase the imaged posterior breast volume near the chest wall. Given appropriate design of the patient bed and CT imaging system components, it may be possible to implement vertical shifting of the system, especially when the x-ray source-detector pair is aligned perpendicular to the longitudinal axis of the patient and there is sufficient clearance to shift the CT system. In practice, it is proposed to vertically raise and lower the CT imaging system while keeping the patient bed stationary. However, due to the inability of the current integrated CT system to shift

vertically, we instead vertically shifted the patient bed system using the *Biodex* bed system while restricting the CT system to a single height as it rotated around the vertical axis. There is active investigation of other various acquisition trajectories to try to improve data sampling of pendant breasts in dedicated breast CT systems currently being developed [122, 137, 142, 189]. In contrast to those other studies, this research was completed not to improve data sampling of an existing breast volume but the studies were specifically designed to increase the imaged volume of breast in order to visualize lesions near the chest wall.

Limited angle methods and their effect on reconstructed data were initially presented at the *2006 Workshop on Nuclear Radiology of Breast Cancer* in San Diego as part of the *IEEE Nuclear Science Symposium and Medical Imaging Conference,* and at the *2007 SPIE Medical Imaging Conference* in San Diego, California. More extensive limited angle data, in addition to newly acquired vertical shifting methods, were presented at the *2008 International Workshop on the Molecular Radiology of Breast Cancer* in Dresden, Germany as part of the *IEEE Nuclear Science Symposium and Medical Imaging Conference* and at the *2009 SPIE Medical Imaging Conference* in Orlando, Florida.

6.1. Limited Angle Acquisitions

6.1.1. CAD Simulation of the Benefits of Limited Angle Techniques

The question of just how much breast volume sampling is gained by employing limited angle tomography was initially estimated using CAD simulation of the integrated breast CT and patient bed system. The pendant breast in the combined system's FOV was

modeled as an approximate 1000 mL semi-ellipsoid with a 12cm chest to nipple distance. The chest wall of the breast was assumed to begin directly above the uppermost/posterior edge of the modeled breast. The CAD software enables dynamic mechanical modeling of the system components during a simulated tomographic scan.

Using this functionality, a full tomographic acquisition was initially simulated by raising the modeled bed just enough to allow for a 360° rotation of the integrated imaging system, including underneath the head section (Figure 6.2, top left). For this set up, the distance between the top plane of the modeled cone beam and the posterior edge of the breast was measured along the system's modeled axis of rotation.

Two limited angle trajectories were then simulated to compare the effects of limited angle tomography with the full 360° rotation. Using the dynamic simulation functionality of the CAD software, the proposed limited angle x-ray source-detector trajectories were simulated by lowering the modeled bed during rotation of the CT system about the vertical axis of rotation, until the x-ray tube housing made contact with the bed. By superimposing the 3D profile of the x-ray cone beam on the modeled breast, the software allowed assessment of changes in breast coverage using these trajectories.

The first limited angle trajectory modeled the bed (and the breast) being lowered into the FOV to the point where the tomographic imaging system could rotate until it made contact with the inner circular edge of the wide body RAD-94 x-ray tube (300° rotation indicated in Figure 6.2).
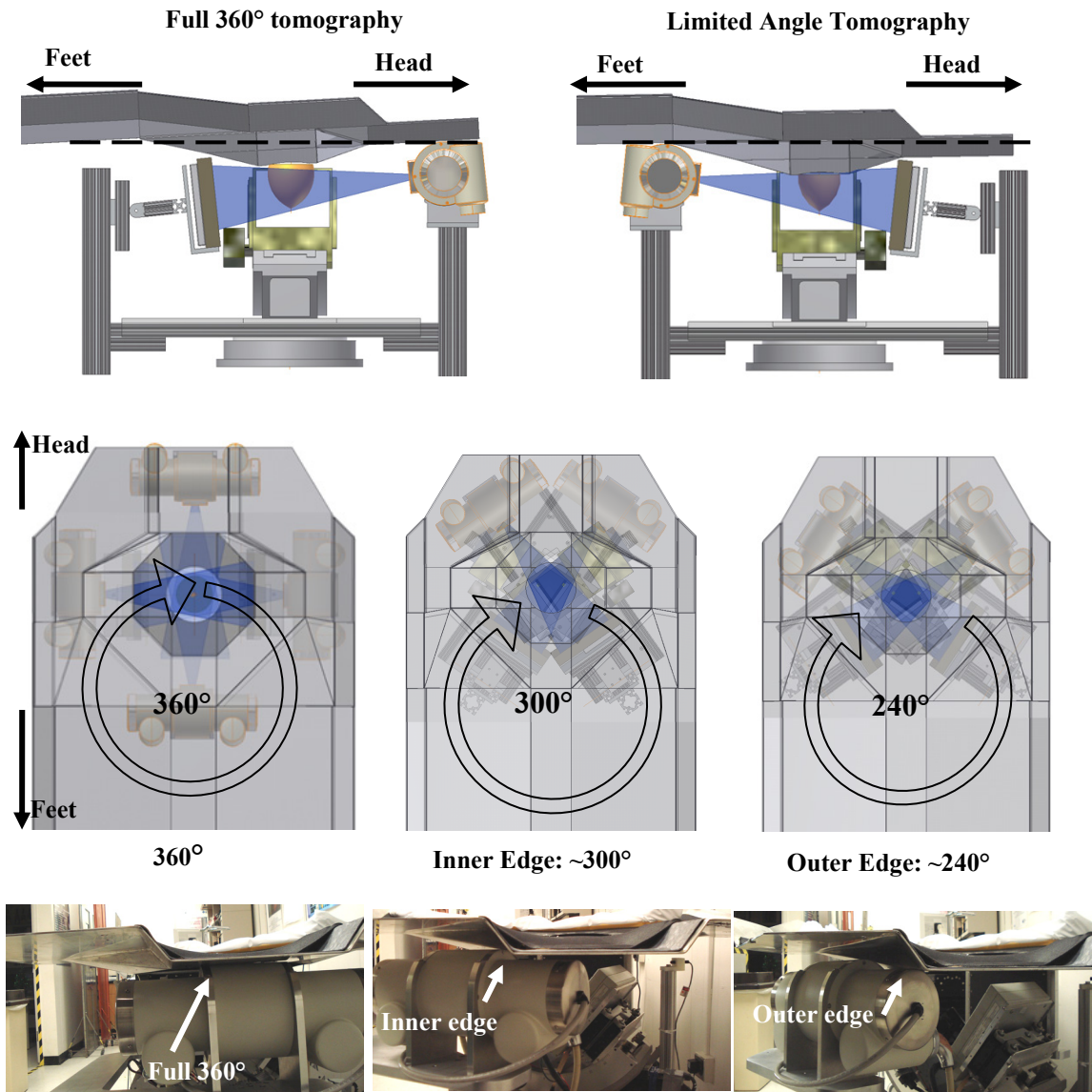
Figure 6.2: CAD images from a side perspective of the integrated SPECT-CT system performing (top, left) a full 360° azimuthal rotation with the bed tilted and raised, and (top, right) limited angle trajectory with the bed lowered and flattened. Note the increase in imaged breast volume when the bed is lowered/system is raised. (Middle, left) Top-down view of the CT system rotating the full 360° underneath the patient bed, and (middle, right) top-down views of the SPECT-CT system performing limited angle tomography up to the inner (300°) and outer (240°) edges of the tube. (Bottom row) Photographs of the CT tube (left) passing unrestricted under the head section of the bed, (middle) impacting the bed at the inner edge for 300° rotation and (right) impacting the bed at the outer edge of the tube for 240° rotation.

The second limited angle trajectory modeled lowering the bed further into the FOV, and allowing the tomographic imaging system to rotate until it made contact with the outer circular edge of the x-ray tube housing for a 240° total rotation, i.e. a larger reduction in projection angles compared to the first iteration. Thus, the two limited angle trajectories trade increased breast volume imaging for a loss in angular sampling. For limited angle trajectories, the total rotation angle of the imaging system and the vertical distance between the chest wall and the top plane of the cone beam at system isocenter were measured.

Table 6.1 lists the results from the CAD simulation quantifying the tradeoffs in employing limited angle tomography trajectories in order to increase the imaged volume of breast and chest wall to the simulated chest wall, i.e. the chest wall is not sampled, while a positive number indicates that the top plane of the cone beam images into and through the chest wall. While mindful of not truncating the nipple region from the distal side of the cone beam, the more optimal result would be to arbitrarily image as much chest wall as possible, and so making this positive number as large as possible.

If a 120° reduction in azimuthal sampling is accepted (arising from the difference between employing a limited angle trajectory of 240° versus the full 360°), CAD simulation results indicate that there is a greater than 19 mm (a change from -10 mm to + 9.3 mm from 360° to 240°) increase in visualization of the breast in the vertical direction towards the chest wall. A proportionally increased breast volume will result from this increased visualization. However, the exact volume increase will depend on the dimensions of the breast being scanned. By using average dimensions of breasts in the

superior-inferior and medial-lateral directions, 10.5 and 14.1 cm, respectively, taken

from a study performed by a colleague [168], and by modeling the cross section of the

breast as an ellipse, the increase in imaged breast volume by using limited angle

tomographic trajectories may be of the order of 225 mL.

Table 6.1 Simulated effect on the ability of limited angle trajectories to increase the volume of breast imaged near the anterior chest wall.

Total azimuthal projection range	Setup description	Distance between anterior chest wall and cone beam (mm)*
360°	Tube passes below head section of the bed	-10
300°	Tube housing inner circular edge contacts the bed	-2.9
240°	Tube housing outer circular edge contacts the bed	+9.3

＊ Negative values indicate the top plane of the cone beam is anterior to the chest wall, positive values mean the beam penetrates the chest wall.

This result demonstrated the potential advantages for using limited angle tomography to

view more of the breast tissue. Although less than that of the 240° trajectory, the

increase in amount of breast gained by employing a 300° trajectory is still over 7 mm

more (the difference between -10 mm and -2.9 mm) or ~82 mL.

Neither do these simulation results indicate the resulting quality of images reconstructed

from employing these limited angle trajectories. This is the subject of the next section of

the study.

6.1.2. Effects of Limited Angle Trajectories on SPECT Data

The integrated SPECT system, in contrast to the integrated CT system, retains the full 3D

positioning capability that it possessed in the independent system. However, if a

simultaneous dual-modality acquisition imaging protocol is used, and the bed is additionally lowered below the upper surface of the CT components to maximize the imaged volume of breast tissue, the SPECT system, with its movements coupled to the integrated CT system in the simultaneous acquisition protocol, will also be restricted to limited angle trajectories. A study was therefore undertaken to evaluate the effect of limited angle tomography on reconstructed data using the integrated SPECT-CT system.

Figure 6.3 shows the dual disc phantom used in the dual-modality SPECT-CT experiments. Each phantom consists of 4 thin walled balloon 'lesions': 2600, 500, 140 and 70 μL (*Harvard Appartus Inc*., Holliston, MA), arranged on the same radius circle at 90° intervals. Attached to an acrylic ring, two such discs were stacked, vertically separated by ~1.5", placed in a water-filled cylinder (to mimic dense breast tissue) and suspended in the common FOV of the imaging system. The upper disc of the phantom represents tissue closer to the posterior portion of the breast, or the chest wall, while the lower disc mimics tissue closer to the anterior portion of the breast, or the nipple.

For dual mode scanning, the lesions were filled with a mixture of CT contrast (1:60 Iodine:water concentration) and activity-filled water (40 μCi/mL ^{99m}Tc). For CT, this contrast filled balloon in a water background may replicate the appearance of a lesion in a predominantly fatty background, such as is present in older patients.
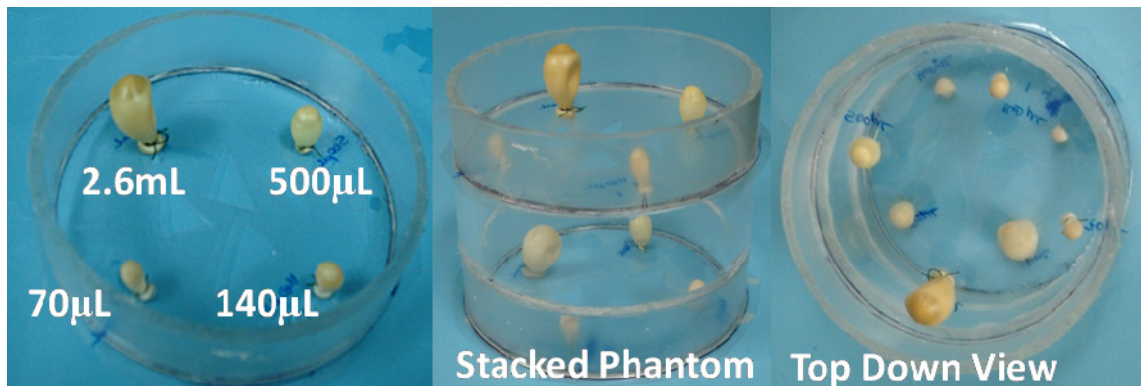
Figure 6.3: Photographs of the stacked balloon phantom used in the dual-modality experiment with the volumes of the balloons indicated on the images.

For SPECT imaging, three lesion:background concentrations were employed: inifinity:1, 10:1 and 3:1 with the ratio modified by adding activity to the water background. A three lobed projsine was used as the trajectory for contoured SPECT imaging [148, 192, 197], with 128 projections acquired, equally spaced over 360°. Each projection was acquired over the course of 20 seconds.

Depending on the final choice of patient imaging protocol, limited angle tomography for the SPECT system may not be needed. In fact, one potential imaging protocol for the final system design is for the CT system to initially acquire projection data which is used to model attenuation information for the subsequent SPECT acquisition.

By effectively decoupling the movement of the SPECT system from the CT system, this potential imaging protocol will obviate the need for using limited angle tomography for the SPECT system. However, it is instructive to know the effects of limited angle
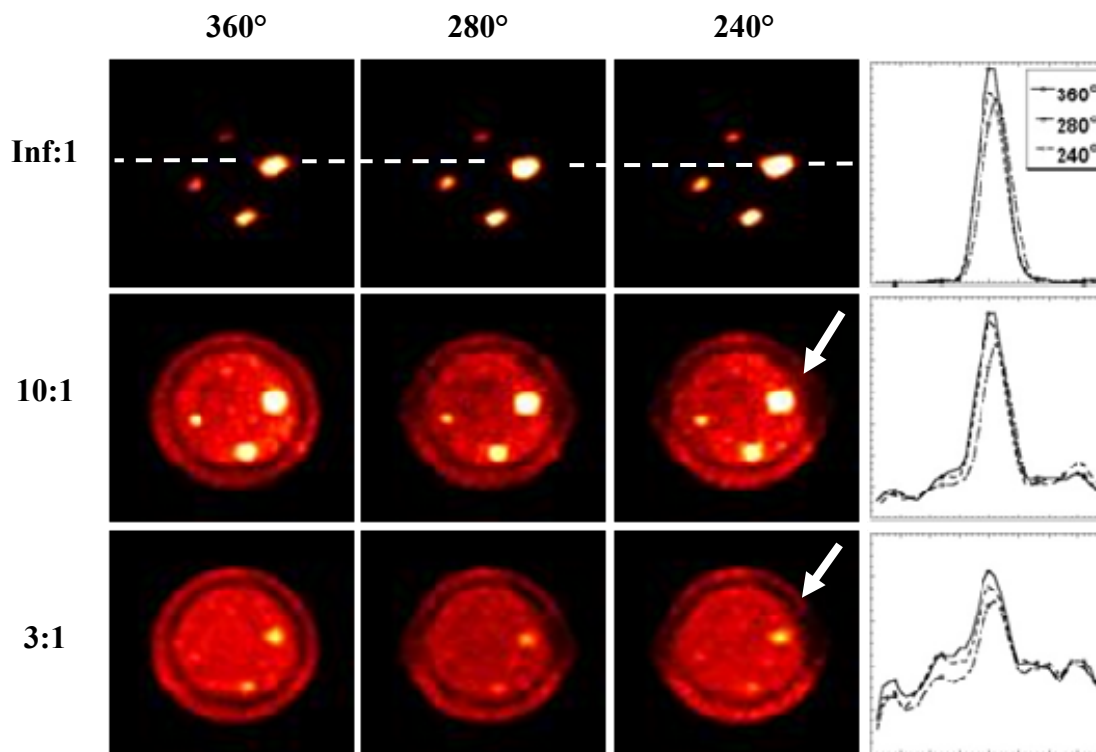
Figure 6.4: Coronal images of the upper plane of lesions for different activity ratios. Images are divided into 360° data set (left col.), 280° (middle col.) and 240° (right col.). Horizontal profiles through the largest lesion are also shown (far right). Note, white arrows, the distortion towards the edges of the reconstructed cylinder images as the number of angular views is reduced.

tomography on SPECT data if the need arises.

OSEM reconstructed images in the coronal orientation of the upper disc of balloons from the SPECT study using the projsine trajectory are shown in Figure 6.4, using the full 360° data set and the 280° and 240° data sets. The missing 80° and 120° sets of projection data were removed from single contiguous sections of projection data. Image quality degrades as the activity ratio and the angular range of projections is reduced, with distortion visible closer to the edge of the cylinder for 280° and 240° of views especially for the 3:1 data set. Lesion visualization degrades more with decreased uptake than with reduced angular sampling. However, profiles of the 2600µL lesion indicate that lesions remain discernable despite a reduction in angular sampling, reinforcing conclusions

found in prior studies concerning limited angle tomography using the SPECT system that removing 75° of SPECT azimuthal data does not significantly reduce image quality [87].

6.1.3. Quantative Effects of Limited Angle Trajectories on CT Data

To quantatively investigate the effect of limited angle tomography on reconstructed CT images. Data were acquired of the stacked disk phantom (Figure 6.3) at a tube voltage of 60 kVp, for 360 projections at 2.5 mAs per projection and 1° intervals. The CT data set was post-processed to mimic limited angle data sets by removing projections in contiguous sectors from desired positions around the projection data set, shown in Figure 6.5. Figure 6.6 shows coronal images of the upper disc balloons reconstructed using limited angle acquisition methods. The range of projections included in reconstructions for limited angle tomography is noted on each image. For example, '280°' means that 280° of projection data was included in the reconstruction with the other 80° missing. The full 360° projection data set is also reconstructed (16 subsets, 8 iterations), and is taken as the standard against which the quality of images reconstructed using limited angle methods are compared.

Qualitatively, noticeable distortion of the balloons is evident in images reconstructed using 240° or less of the original projection data while balloons in data sets reconstructed using >280° of projection data are apparently minimally distorted. Vertical profiles across the different balloons are shown in Figure 6.7 and reinforce this trend in increased distortion with reduced projection angles. Distortion is most evident for the four balloons as the number of projection angles used reduces below 280°. Horizontal profiles,

illustrated in Figure 6.8, indicate that the shape of the balloons is maintained in profiles generated in orientations not in the direction of the missing projections. SNR and contrast metrics for an ROI centered in each of the balloons are indicated in Table 6.2. SdNR was calculated using the difference in signal between the ROIs in the various balloons and the background signal, divided by the standard deviation in the background. The trend in results indicates generally improved image quality metrics for balloons reconstructed with progressively more projections, as expected. Despite these reduced figures of merit, all the contrast-filled balloons are visible even with 160° of missing data.
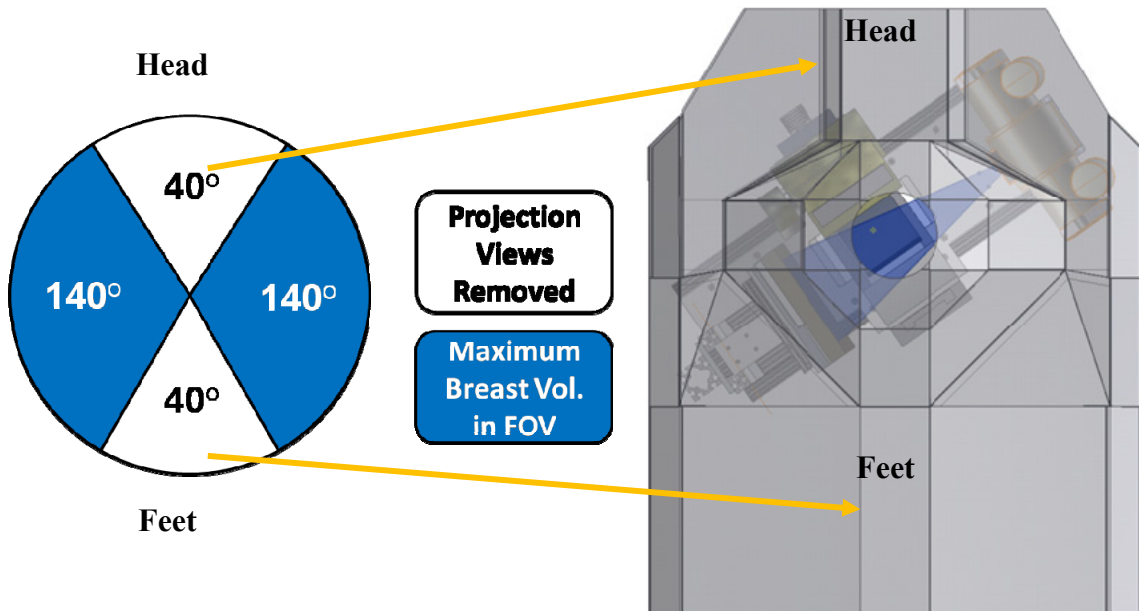
Figure 6.5: Sketch of the method of limited angle tomography used in the study with iodine filled balloons. Projections were removed from both the head and the feet sections of the trajectories. Illustrated on the left is the 280° trajectory, with the 80° of missing projection data divided equally between the head and feet sections. Other limited angle trajectories were similarly generated for this study.
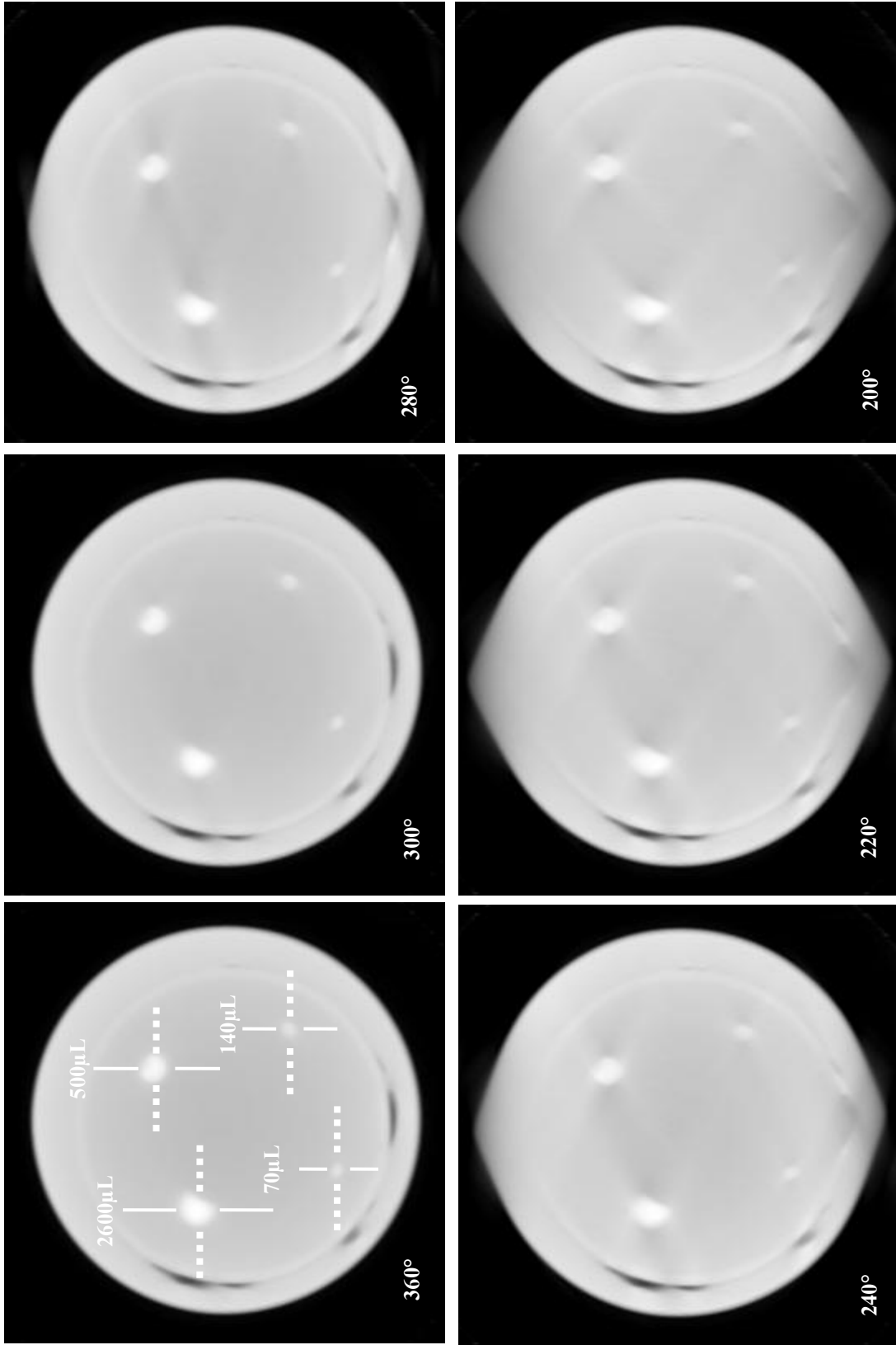
Figure 6.6: Coronal images of the contrast filled balloons in the upper disc of spheres reconstructed under different conditions of full or limited angle tomography. The location of vertical and horizontal profiles are indicated by the solid and dashed white lines, respectively. Increased distortion is clearly apparent with a reduction in the number of angles removed from the data set. The location of vertical and horizontal profiles, show in Figures 6.7 and 6.8, are also indicated.
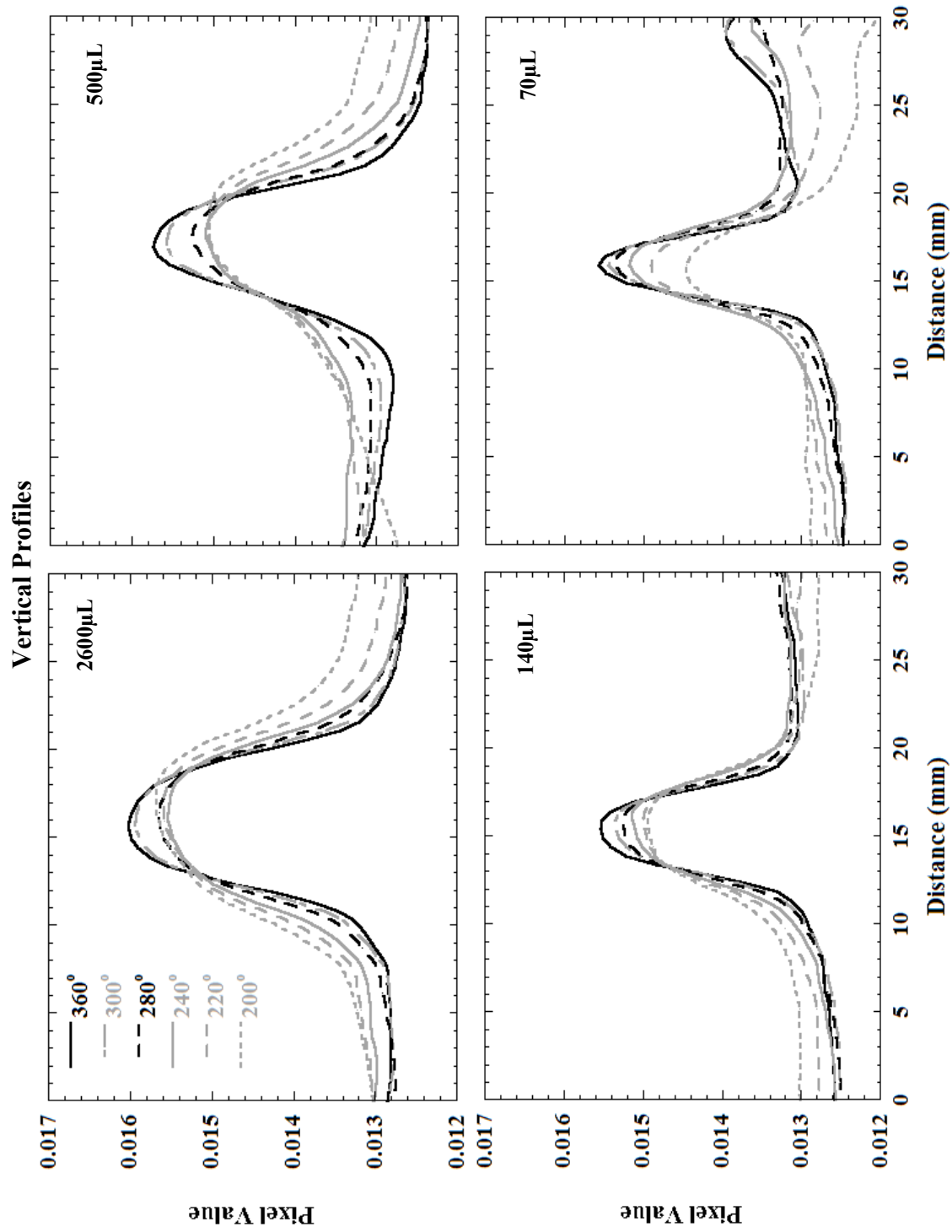
Figure 6.7: Vertical profiles across the reconstructed balloons (locations indicated by solid white lines in Figure 6.6). Shape distortion is increasingly evident as more projection angles are removed.
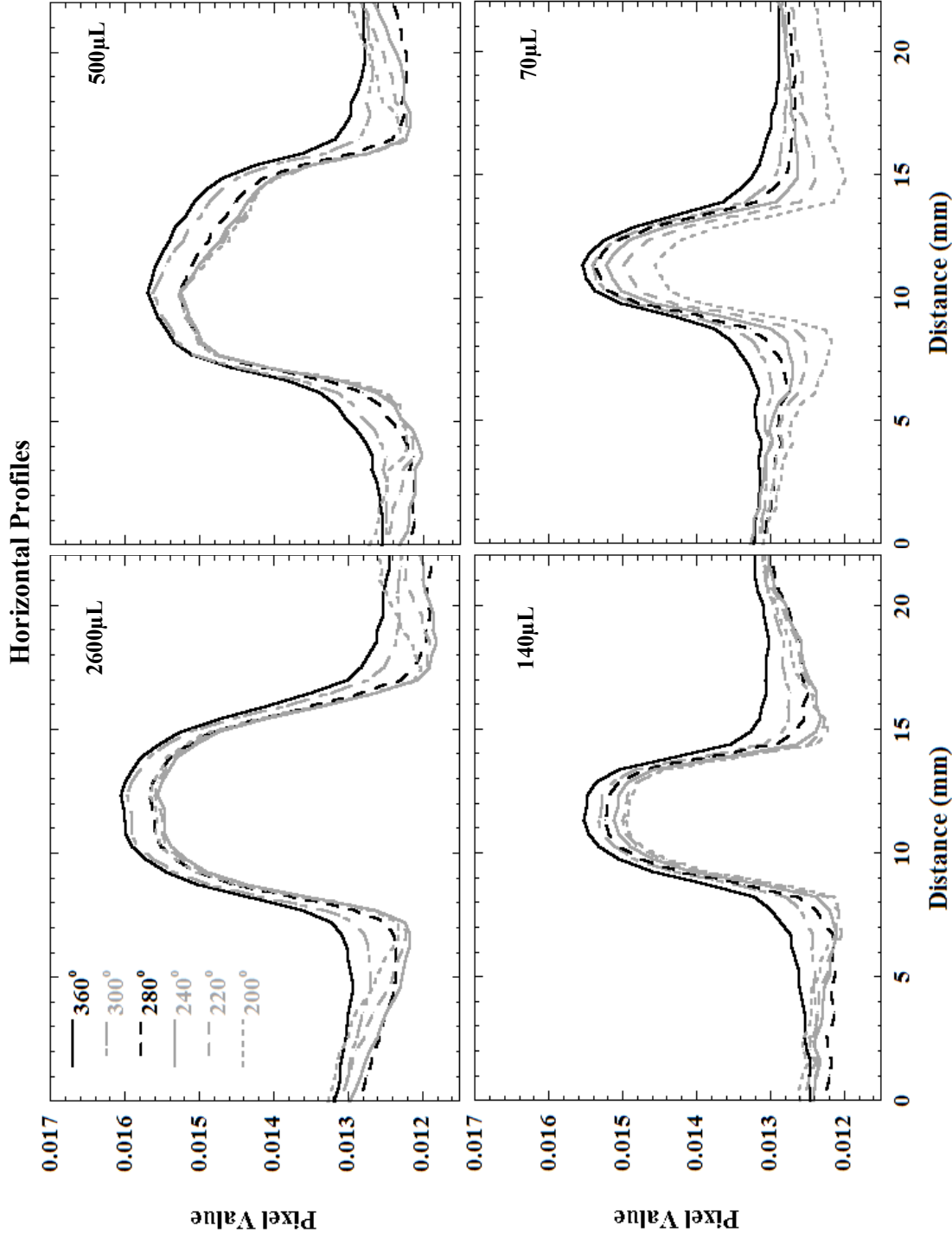
Figure 6.8 Horizontal profiles across the reconstructed balloons (locations indicated by dashed white lines in Figure 6.6). The shape of the balloons is generally maintained better in the horizontal direction rather than the vertical, indicating that distortion depends on the orientation of the balloons relative to the location of the missing projections.

254

Table 6.2 SdNR and contrast image quality metrics for the various balloons on the upper disc of the phantom.

Metric	Volume (µL)	Projection angle range					
		360°	300°	280°	240°	220°	200°
SdNR	2600	38.00	37.00	16.50	14.50	13.50	11.5
	500	33.00	31.00	14.00	12.50	11.00	9.00
	140	26.00	24.00	11.50	10.00	9.00	7.50
	70	26.00	26.00	11.50	10.00	8.50	7.00
Contrast	2600	0.30	0.30	0.26	0.22	0.20	0.17
	500	0.27	0.25	0.22	0.19	0.17	0.13
	140	0.20	0.19	0.18	0.15	0.14	0.11
	70	0.20	0.20	0.18	0.14	0.13	0.10

6.1.4.   Observer Study into the Effects of Limited Angle Tomography
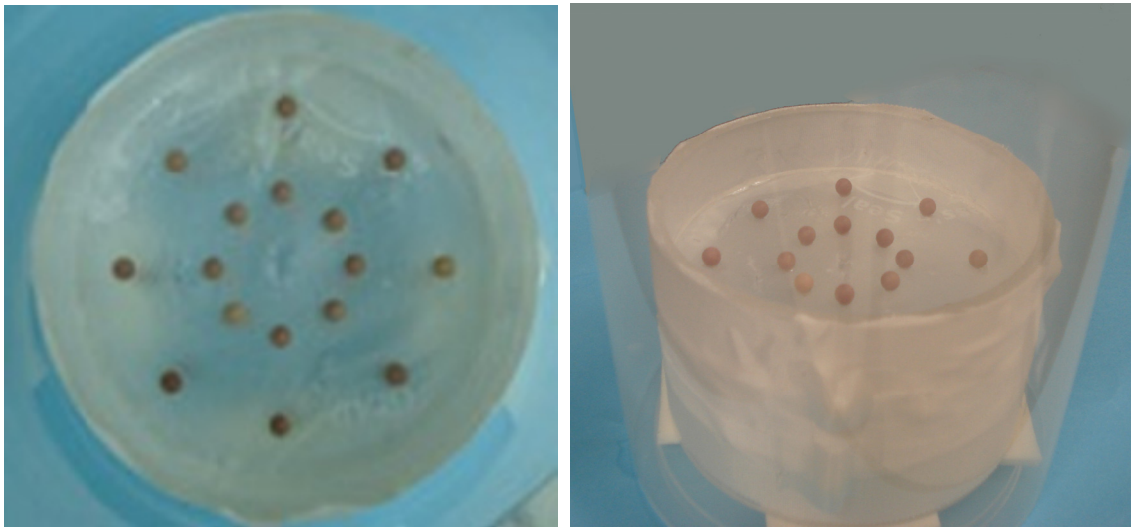
Figure 6.9: Photographs of the (left) disc phantom designed for the observer study and (right) two such discs stacked together and placed in the cylinder (with a spacer disc in between) prior to imaging. The upper disc represents signals closer to the posterior breast and chest wall, and the lower disk represents signals closer to the anterior portion of the breast.

An imaging phantom was developed that consisted of concentric circles of 5 mm acrylic spheres spaced at regular 45° intervals about the compass on a thin plastic disc-shaped sheet (Figure 6.9). Two such disc phantoms were stacked inside a 14 cm diameter plastic

cylinder and placed in water to mimic a very low contrast (~1%) imaging task in a fluid that approximates dense, homogenous glandular tissue. A full 360° of projection data was initially collected using this phantom at 1° intervals, at 2.5 mAs per projection and a tube potential of 60 kVp. In addition to reconstructing the full 360° of data, contiguous angular sets of projections were also removed from the full projection data set to mimic 240° and 300° limited angle tomographic scans. Projections were removed from around the head section of the projection data set, to mimic the intended protocol in the clinic. The trajectories are illustrated in Figure 6.2, and are different from the trajectories used in the study with the iodine filled balloons. It should be noted that by removing contiguous sectors from a single dataset of projections the modified tomographic data sets represent data acquired at reduced overall dose, i.e. the 240° dataset is acquired at only 2/3^{rds} the dose of the 360° dataset. Therefore the noise quality of these reconstructed images is likely to degrade, potentially biasing the results towards the fully reconstructed data set.

The 5 observers (4 biomedical engineers and a medical physicist) were presented with images of the upper and lower discs reconstructed under conditions of full or limited angle tomography, shown in Figure 6.10. The observers were presented with stacks of images prepared in image processing software (*imageJ* – http://rsb.info.nih.gov/ij/) using a previously derived method [123]. Due to the effects of scatter on reconstructed images and an inability to see the inner spheres, observers were only queried on the outer ring of 8 spheres. When presented with stacks that contained the upper and lower discs observers were asked two questions: (1) How many spheres do you see? (2) How do you rate the overall quality of the reconstructed spheres?

	Upper Disc	**Lower Disc**
240°		
300°		
360°		
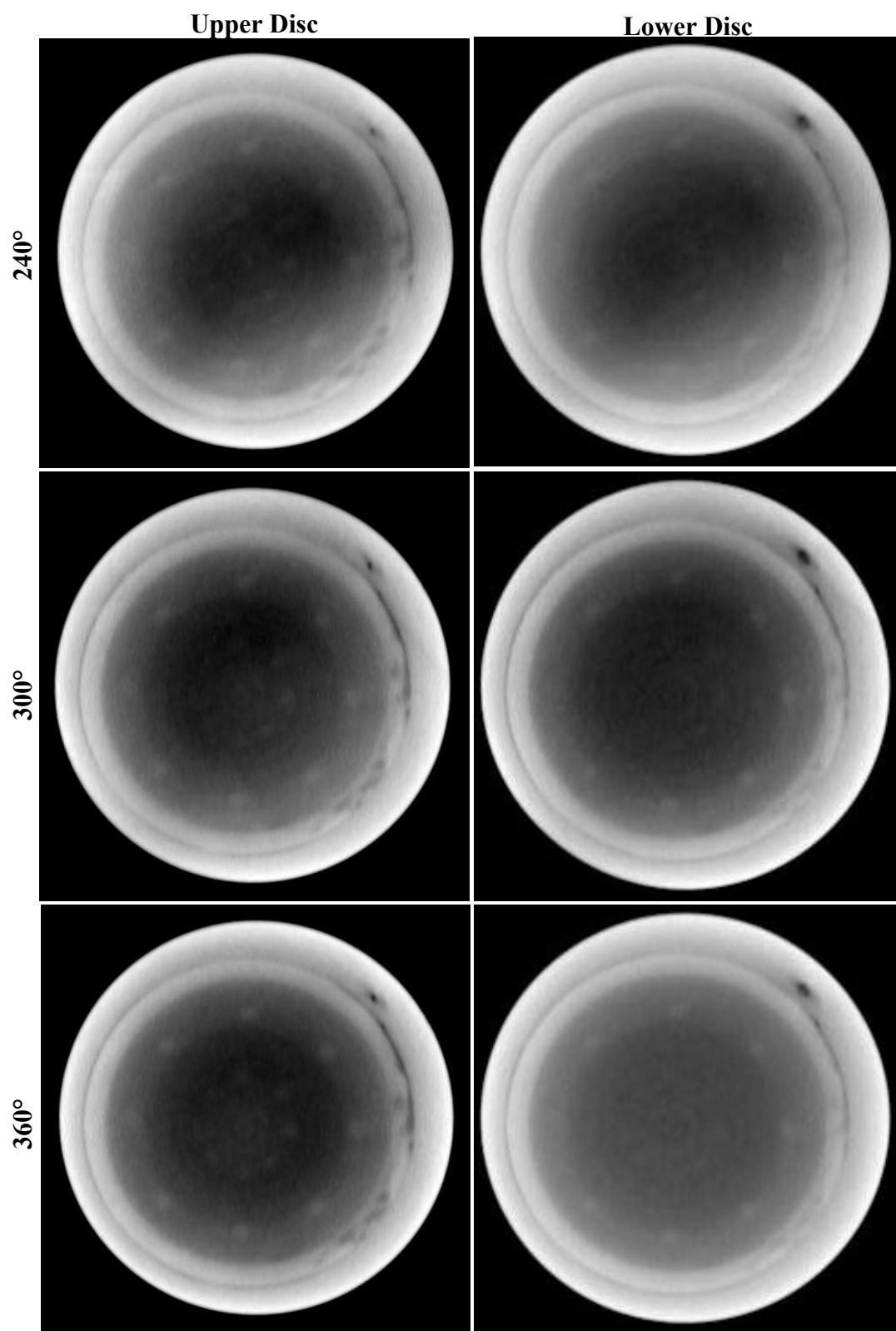
Figure 6.10: Reconstructed coronal images of the (top) upper and (bottom) lower disc of the stacked phantom containing 5mm acrylic spheres, and reconstructed using the indicated limited angle tomography methods.

257

The ratings were made on a scale of 1-10 with 10 being the best. Observers were trained with a sample so that the relative range of observations would be known beforehand and so that the entire measurement range could be used consistently. The results of these questions are listed in Tables 6.3 and 6.4, respectively.

Table 6.3 Results from the observer test to determine how many 5mm spheres the observers saw under conditions of full or limited angle tomography

Disc location	Range of Projections	Mean # spheres	σ	p-value vs. 360°
	360°	8.0	0	-
Upper	300°	7.8	0.5	0.24
	240°	7.8	0.5	0.24
	360°	8.0	0	-
Lower	300°	8.0	0	-
	240°	7.8	0.5	0.24

Table 6.4 Results from observer test to rate the quality of the reconstructed 5mm spheres under conditions of full or limited angle tomography. A score of 10 was rated best quality.

Disc	Range of Projections	Mean quality score (1-10)	σ	p-value vs. 360°
	360°	8.4	1.1	-
Upper	300°	7.0	2.0	0.13
	240°	6.0	1.6	0.01
	360°	8.4	1.1	-
Lower	300°	7.4	2.1	0.23
	240°	5.8	1.6	0.01

Using a 2-sided student's t-test with a significance level of $p<0.05$, results for question (1) indicated that there was a very slight decrease in the average number of visible spheres (i.e. from 8.0 to 7.8) in both the upper and lower discs when going from a 360° to the 300° and 240° scans, but the differences were not statistically significant (p=0.24).

When asked about the quality of the reconstructed spheres, observers indicated that the images reconstructed using 240° of data were degraded significantly compared to the 360° data for both upper and lower discs (p=0.01 for both the upper and lower discs), but that the difference was not significant when viewing spheres reconstructed using 360° of data compared to the 300° data (p=0.13 and 0.23 for the upper and lower discs, respectively).
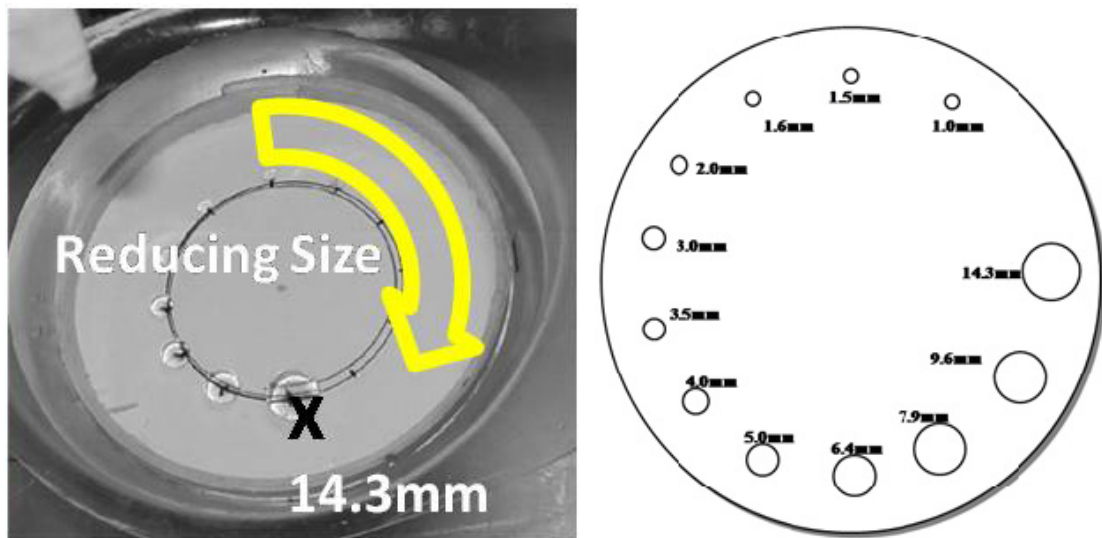
Figure 6.11: (Left) Photo of the previously developed phantom with decreasing–sized acrylic spheres, and (Right) a drawing of the different diameters of spheres present in the phantom. The location of the 14.3mm acrylic sphere is indicated with an X.

To examine the effect of removing projections for spheres of different sizes, data was acquired using another phantom made by arranging acrylic spheres with diameters ranging from 1.0-14.3mm on a single circular radius (Figure 6.11). This full set of projection data had been previously acquired for another study [123].

The full projection data set was subsequently post-processed to remove angles from different angular sections to mimic limited angle tomographic techniques. Given the

different sized spheres present in the phantom, equivalent angular sectors from around

the phantom were removed to test the effect on sphere visibility as a function of angular

location. Therefore a 60° angular range was removed from 6 different sectors around the

scan (0°-60°, 60°-120°, etc). For the 240° scans, 3 contiguous sectors of 120° were

removed in 3 different acquisitions (0°-120°, 120°-240°, 240°-360°).

Table 6.5 Summary of the results to determine how many spheres of decreasing size were seen by observers under the various conditions of full or limited angle tomography

Angular range of projections	Missing projection range	Mean # seen	σ	p-value vs. 360°
360°	N/A	7.2	0.4	-
300°	0-60°	6.8	0.4	0.11
	60-120°	7.0	0.7	0.53
	120-180°	7.0	0.7	0.53
	180-240°	7.0	0.7	0.53
	240-300°	7.0	-	0.24
	300-360°	7.0	0.4	1
240°	0-120°	6.6	0.5	0.04
	120-240°	6.8	0.8	0.28
	240-360°	7	0.7	0.53

Reconstructed images of the plane of spheres acquired under various conditions are

shown in Figure 6.11 and summarized in Table 6.5. Observers indicated that the effect of

limited angle acquisition methods on visualization of spheres of differing sizes was

minimal. When presented with images of the different sized spheres, with 60° removed,

there was no significant difference between any of the sectors and the full 360° scan in

terms of the number of detectable spheres, regardless of the segment missing 60° of data.
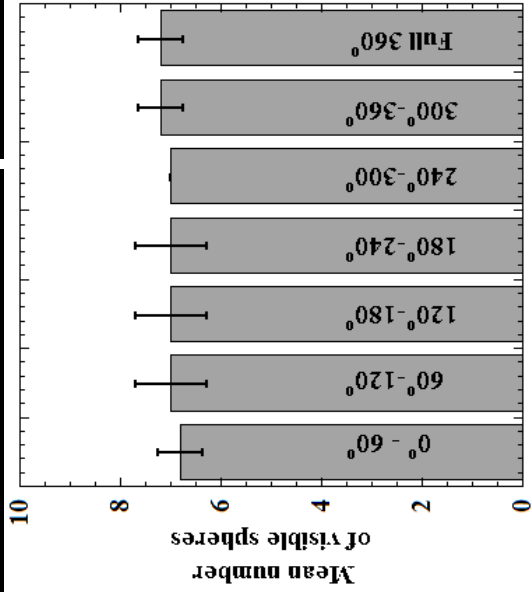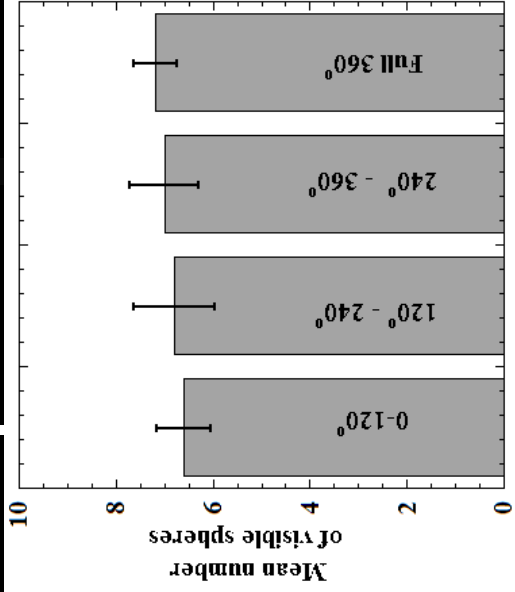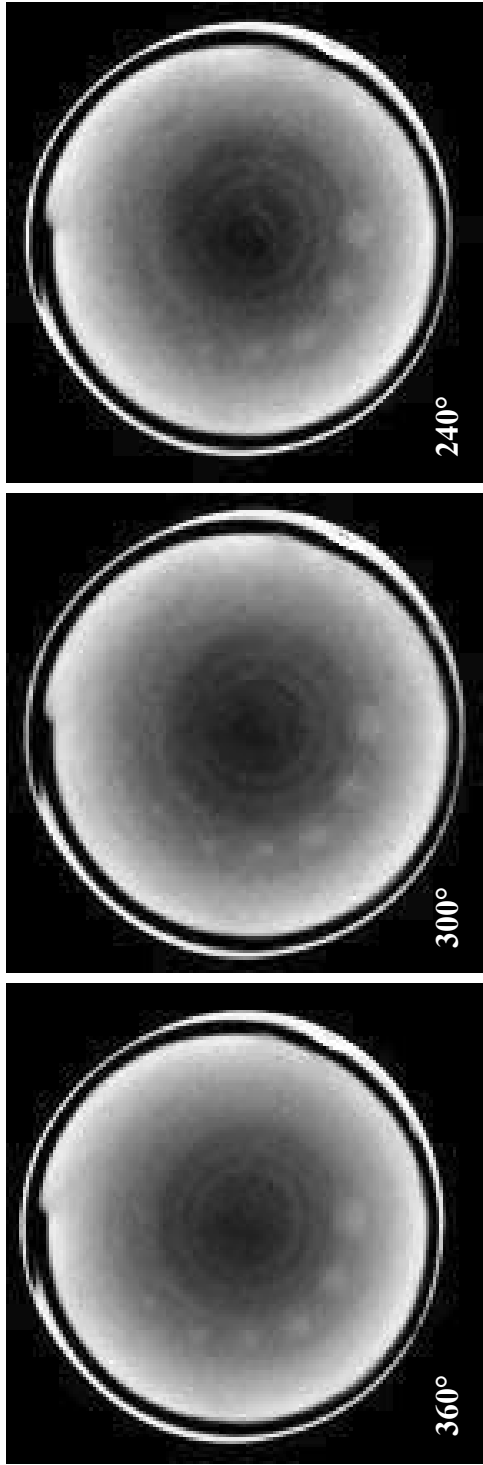
Figure 6.12: (Top) Images of the disc of decreasing sized spheres reconstructed under full or limited angle tomography conditions. (Bottom Row) Plots of the results of the observer study into the number of observable spheres with contiguous 60° (left) and 120° (right) sectors of projections removed, indicated on the plot. There were 12 total spheres in the phantom, (cf. Figure 6.10).

261

However, there was a significant difference in one instance between the number of observed spheres in the scan missing projection data from 0-120°, data that spans the locations of the smallest spheres.

6.1.5. Limited angle reconstruction of breast tissue

All the projection data of patient volunteers was acquired using a full 360° of data spread throughout 240 projections, 2.5 mAs per projection at a tube voltage of 60 kVp. To examine the effect of limited angle techniques on breast tissue, rather than geometric phantoms, a projection data set previously acquired from one of the volunteer subjects was post-processed to mimic limited angle techniques. This was done by initially removing 60°and subsequently 120° of projection data about the head from the full data set as in Figure 6.2, and reconstructing the breast volume. Figure 6.13 shows images of the reconstructed patient breast volume using a full 360° tomographic data set and the 300° and 240° limited angle data sets. Figure 6.13 also shows a difference image between the 360° and the 240° data set. Profiles are also shown for each setup across a section of tissue in the breast volume that contained a suspected lesion (the location of the profile is indicated on the image).

Table 6.6 SdNR and contrast metrics for the area of interest in the coronal plane image in Figure 6.12

Total azimuthal projection range	SdNR	Contrast (%)
360°	28.1	0.28
300°	26.1	0.21
240°	27.1	0.27

Although there is some apparent difference in the shape of the suspected reconstructed lesion, the various data sets appear to possess similar image quality despite the fact that the 240° data set contains just 160 projections (i.e. higher noise and poorer sampling). The illustrated profiles indicate good similarity in reconstructed image quality for each of the various full and limited angle projection data sets.

Table 6.6 includes the SdNR and contrast for the area of interest against the background tissue (mostly adipose/fat) and indicates that, counter-intuitively, the 240° data set possesses an improved SdNR and contrast figure for the area of interest with an adipose background. It should be re-iterated that the limited angle data sets theoretically possess worse noise quality than the full data set, although no degradation in image quality is readily apparent. One potential reason for this counter-intuitive quantative result is that the SdNR and contrast metrics are sensitive to the exact placement of the ROI. Another potential reason is that the undersampled 240° data set tends to smooth out higher frequencies and so the background (lower frequencies) may quantitatively show less variability than the better sampled data.

Nevertheless, the overall result of the reconstruction of these re-processed data sets of human volunteer breast volumes point to the fact that limited angle tomography may be considered as a feasible alternative, especially when using statistical iterative reconstruction techniques, to enable an increase in imaged breast volume.
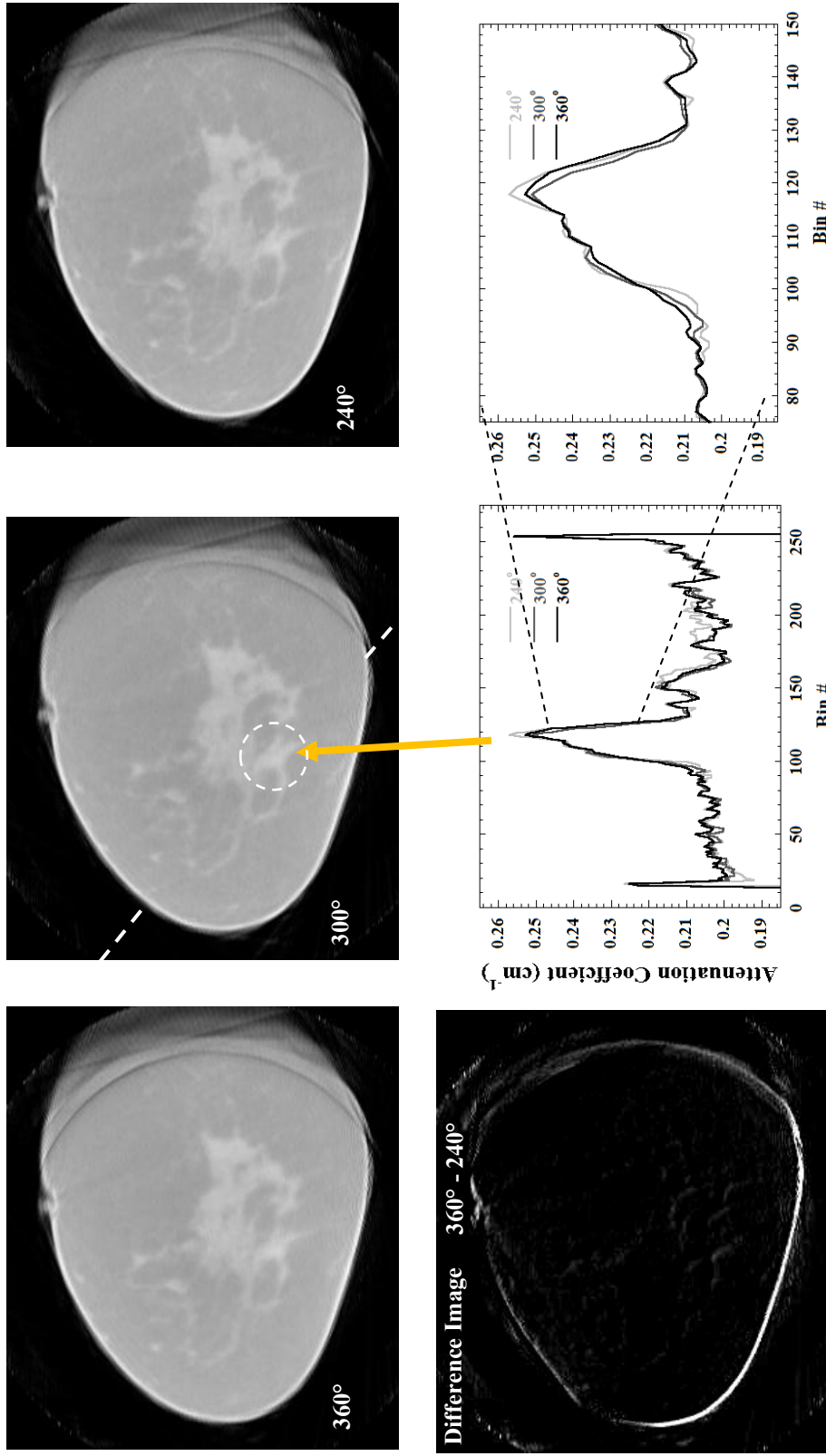
Figure 6.13: (Top) Reconstructed images of single coronal slice of a subject's breast volume at a level of interest. (Bottom middle, right) Profiles through the area of interest for each of the data sets reconstructed under the noted full and limited angle. (Bottom, left) Difference image between the 360° and the 240° acquisition shows very little variation between the two (areas of increased difference are indicated in lighter colors). (Bottom middle, right) Profiles of the area of interest showing minimal change in reconstructed attenuation coefficient for the area of interest, despite a, at most, 120° reduction in projection degrees used to reconstruct the data.

6.2. Vertical System Shifting Techniques

Using the ability of the iterative reconstruction algorithm to model the geometry of the CT system (the system matrix), the following sets of experiments investigated the feasibility of employing vertical shifting techniques using the integrated CT system.

Figure 6.14 is an illustration of vertical shifting techniques employed using the integrated CT system. With the current capabilities of the integrated CT system, it is not possible to vertically shift the CT system when the x-ray source-detector axis is aligned with the long axis of the prone patient, i.e. when the CT source-detector axis is directly under the bed. However, it may be possible in future system designs, especially using a more V-shaped bed design and components with smaller profiles, like a unipolar x-ray tube, to implement vertical shifting when the x-ray source detector axis is orthogonal to the patient's long axis, i.e. when the system rotates around the sides of the bed.

6.2.1. Quantative effects of vertical shifting on CT data

To initially investigate vertical shifting techniques using contrast filled objects for a relatively easy imaging task, the iodine-filled balloon 'lesions' used for investigating limited angle tomography in the system (see Figure 6.3) were also used to investigate the effect of vertically raising the system in mid acquisition.
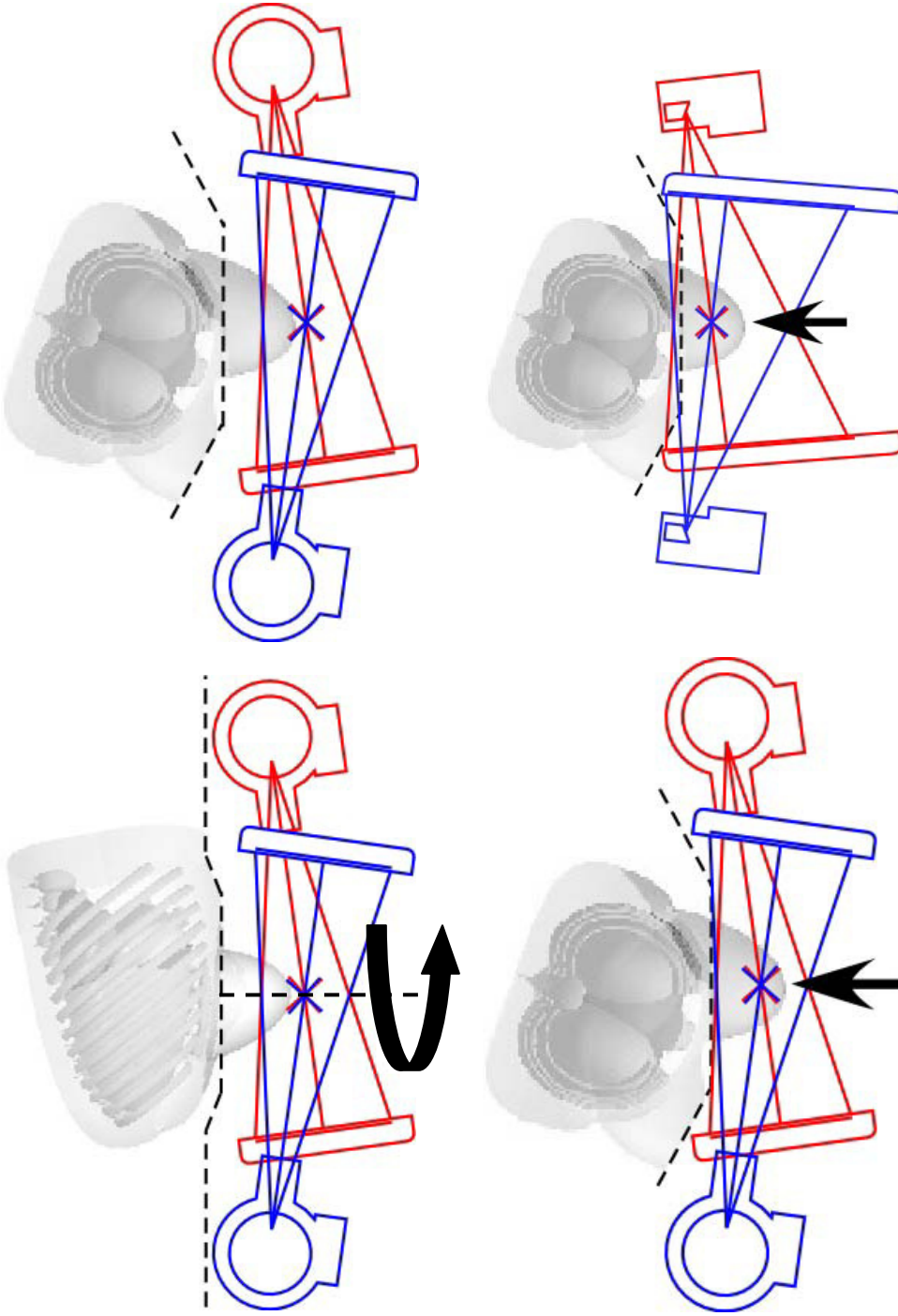
Figure 6.14: Illustrations of the concept of vertically shifting the CT system. (Top left) The CT system is aligned with the long axis of the bed where it is not possible to vertically shift the system. The axis of rotation of the system is included, as is the direction of rotation. It is clear from the illustration that the dead zones of the current CT system act to separate the top plane of the cone beam and the center of rotation from the majority of the breast volume. (Top right) The CT system is aligned orthogonal to the long axis of the bed and patient. In this orientation, there is available space to effectively (Bottom left) raise the CT system and the top plane of the cone beam to image more of the breast volume. (Bottom right) Using components with smaller dead zones, it may even be possible to raise the tube and detector enough to penetrate the chest wall of the patient in this orientation. (Illustrations courtesy of Dr. Martin Tornai)

1st data set - 1 disc in the FOV

2600μL

500μL

2nd data set - 2 discs in the FOV

500μL

2600μL

2600μL

500μL

Phantom in
cone beam FOV

X-ray source

X-ray detector
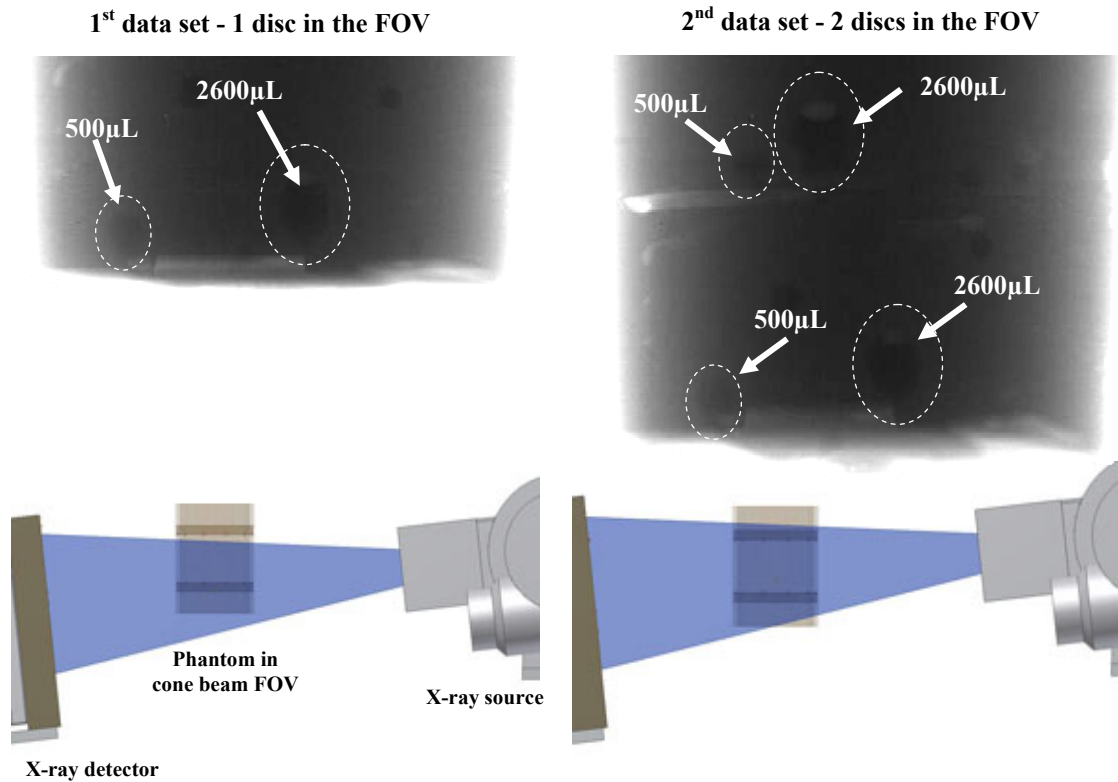
Figure 6.15: (Top row) Projections of the disc phantom with (left) 1 disc in the FOV and (right) 2 discs in the FOV to mimic vertically raising the system mid-acquisition. The contrast of the image has been modified to enable viewing of the two noted iodine-filled balloons, the only balloons visible in these projections. (Bottom row) CAD images of the same acquisition showing the concept behind vertical shifting techniques.

Two separate and complete tomographic data sets were acquired as illustrated in Figure 6.15. The first scan acquired 360 projections at 1° intervals with only one (the lower) disc of balloons in the CT system's field of view (60 kVp, 100mA, 2.5 mAs per projection). This trajectory represented having just the lower breast volume, towards the anterior breast volume and nipple, in the field of view. A second full 360° projection data set was then acquired with both discs of balloons in the field of view. This second acquisition represented having all of the 'breast' volume (nipple, anterior and posterior breast and the patient's chest wall) in the field of view of the system. The lower

schematics in Figure 6.15 illustrate the methodology used in the experiments. For this second data acquisition, since it was not physically possible to raise the integrated CT system in the lab, the phantom was lowered by approximately 3 cm using the *Biodex* bed system.

By concatenating projections in specific sectors from the first data set containing the one disc with projections from the second data set where both discs were viewed, separate tomographic data sets were post-processed to mimic vertically shifted data sets. Reconstructed images in the coronal orientation of the upper disc of balloons reconstructed using a full 360° of data and under various vertical shifting conditions are shown in Figure 6.16. The images are made from planes summed to enable viewing of all four balloons in the same image. The 360° data was acquired with both discs in the field of view for all angles. The angular range of where projections are vertically shifted is noted on each image. For example, 'Shifted 280°' means that both discs of balloons were in the field of view for 280° of projections, with the other 80° containing only the lower disc of balloons. The upper disc of balloons is shown since the lower disc of balloons is fully present in all the acquired projections, regardless of the amount of shifting involved (see Figure 6.14). Common to all images of shifted data in Figure 6.16 are streak and distortion artifacts presumably caused by a lack of tomographic sampling in those shifted data sets. This shape distortion of all four reconstructed balloons is further emphasized in vertical profiles drawn across the reconstructed balloons in the coronal orientation, and illustrated in Figure 6.17. Horizontal profiles in Figure 6.18 indicate far lower levels
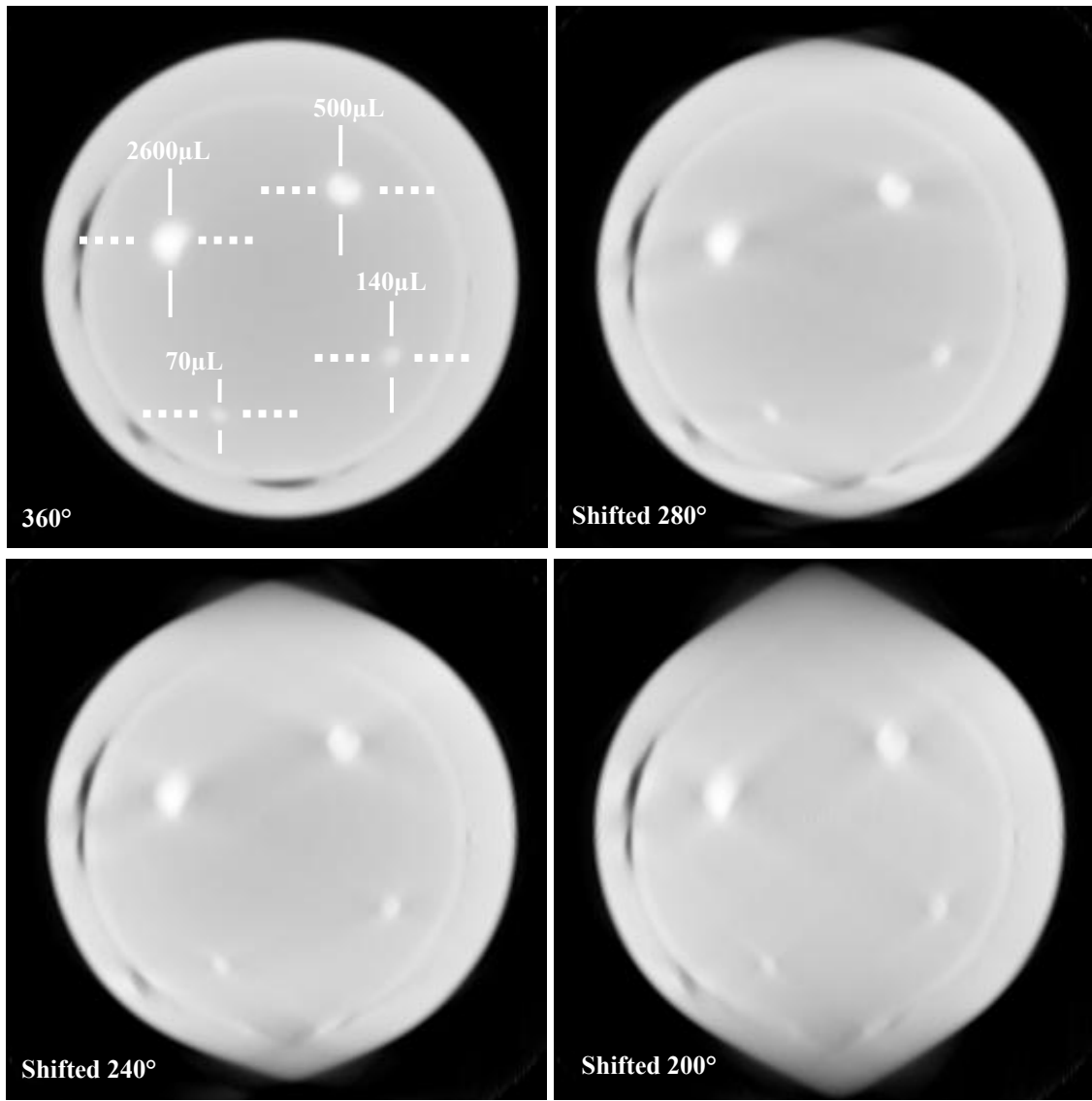
Figure 6.16: Coronal images of the upper disc of the balloon phantom with the balloon sizes indicated on the image. The different acquisition strategies employed are indicated on the images as explained in the text. Location of vertical and horizontal profiles across the balloons, shown in Figure 6.17 and Figure 6.18, are also indicated.

of shape distortion, and emphasize that the apparent shape distortion depends on the orientation of the objects in question relative to the angular location of the removed projections, in addition to the absolute number of projections removed.
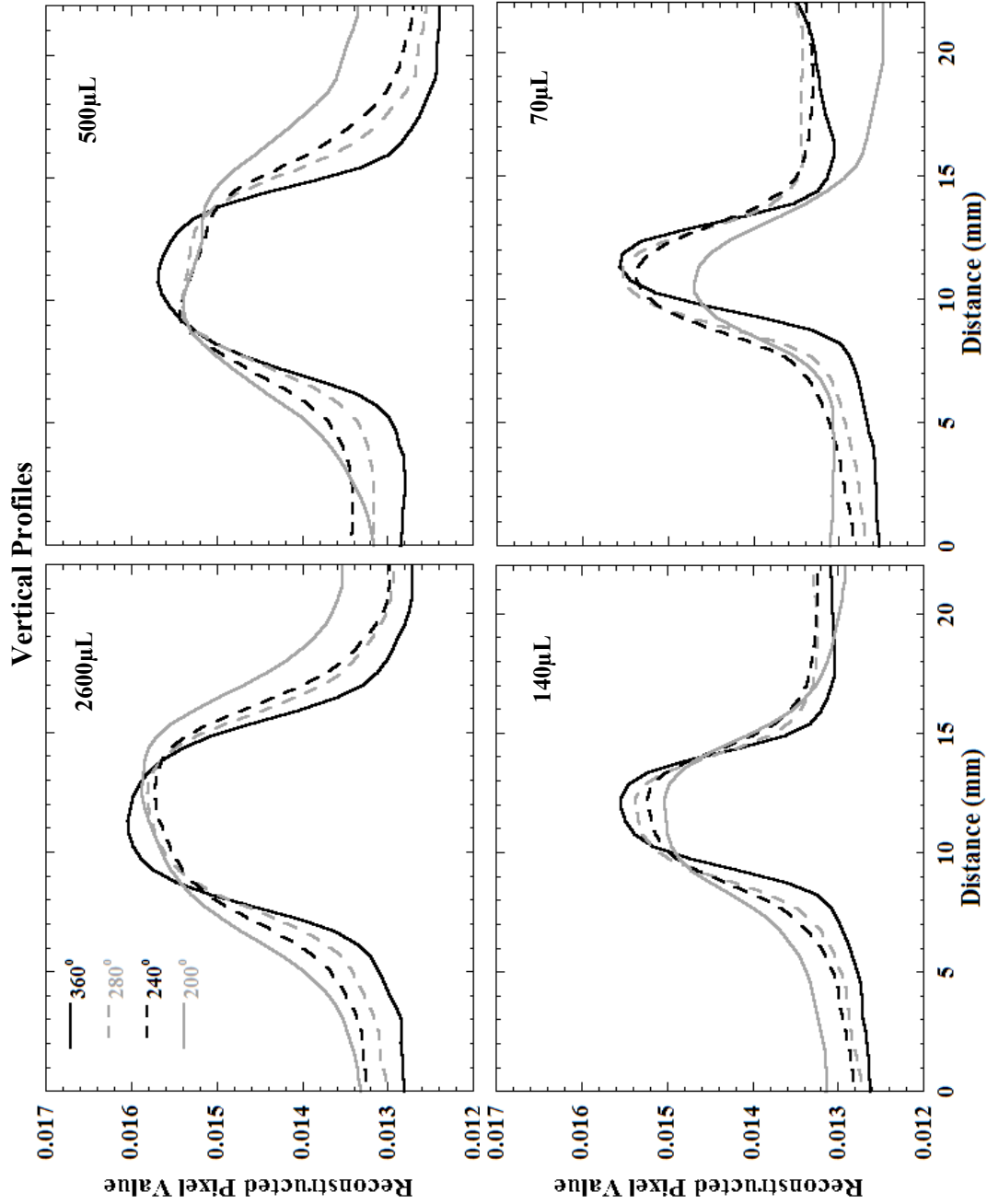
Figure 6.17: Vertical profiles drawn across the four contrast filled balloons in the upper disc reconstructed using vertical shifting techniques. The locations of the profiles are indicated by the solid vertical lines in Figure 6.15. The profiles indicate increased distortion in the balloon shape with an increasing degree of missed projections due to the effects of vertical shifting when the upper disc is out of the cone beam FOV.
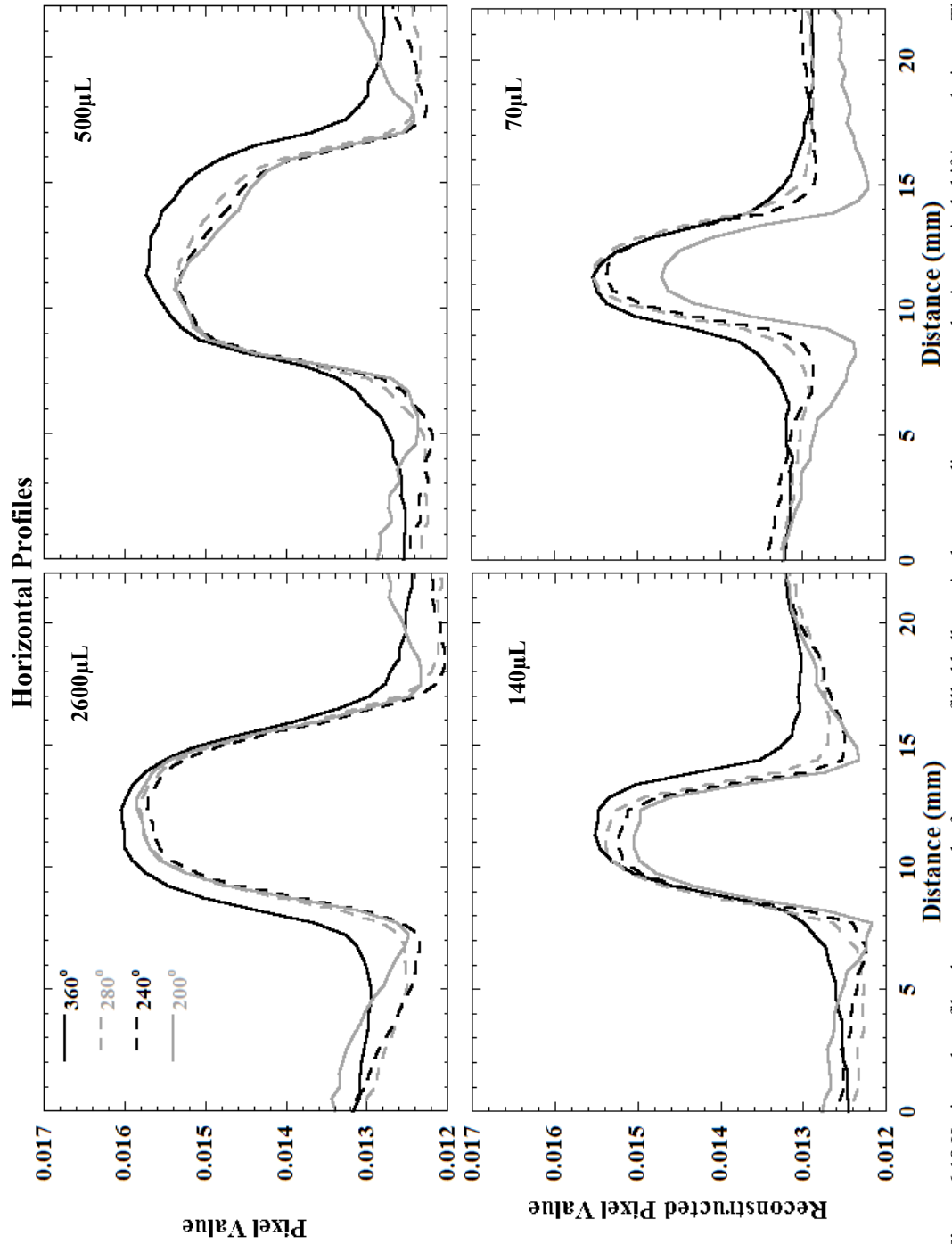
Figure 6.18 Horizontal profiles drawn across the four contrast filled balloons in the upper disc reconstructed using vertical shifting techniques. The locations of the profiles are indicated by the dashed lines in Figure 6.15. In contrast to the objects in Figure 6.16, overall shape of the balloons is well maintained, despite a the increase in missing projections of the upper disc , indicating that the amount of shape distortion is a function of both the number of shifted projections and also the orientation of the object relative to the location of the vertical shifting.

271

Table 6.7 SdNR and contrast image quality metrics for the various balloons on the upper disc of the balloon phantom, reconstructed using system shifting methods

Metric	Volume (µL)	Angular range for which 2 discs are in the FOV			
		360°	280°	240°	200°
SdNR	2600	38.00	34.00	31.00	24.00
	500	33.00	30.00	27.00	18.00
	140	26.00	24.00	22.00	17.00
	70	26.00	25.00	22.00	14.00
Contrast	2600	0.30	0.27	0.23	0.18
	500	0.27	0.24	0.21	0.13
	140	0.20	0.19	0.17	0.13
	70	0.20	0.19	0.17	0.11

SdNR and contrast of the balloons generally degrades with increasing vertical shifting, as evidenced by SdNR and contrast values reported in Table 6.7. SdNR is defined in the same manner as described in Sect. The trend in values is similar to the trends for the same balloons reconstructed using limited angle tomography (see Table 6.6).

Figure 6.19 shows images in the transverse orientation of both discs under the same conditions of full or shifted tomography, showing a loss of information in the reconstructed border of the container near the upper disc. The loss of information degrades with an increase in the number of missing projections of the upper disc. Nevertheless, all the contrast filled balloons are still visible on all images. Profiles drawn across the upper large balloon are also shown in Figure 6.19. The increased distortion in the large balloon is very apparent, especially towards the edges of the acrylic phantom holder. Nevertheless, the maximum value in the balloon is well maintained, even in the Shifted 200° data set, despite missing close to half the total number of projections.
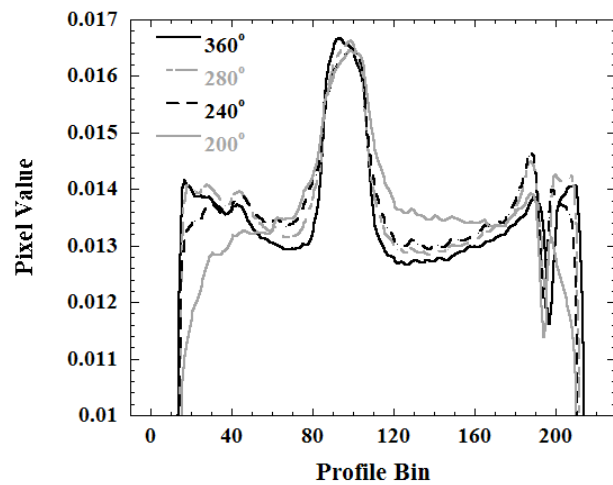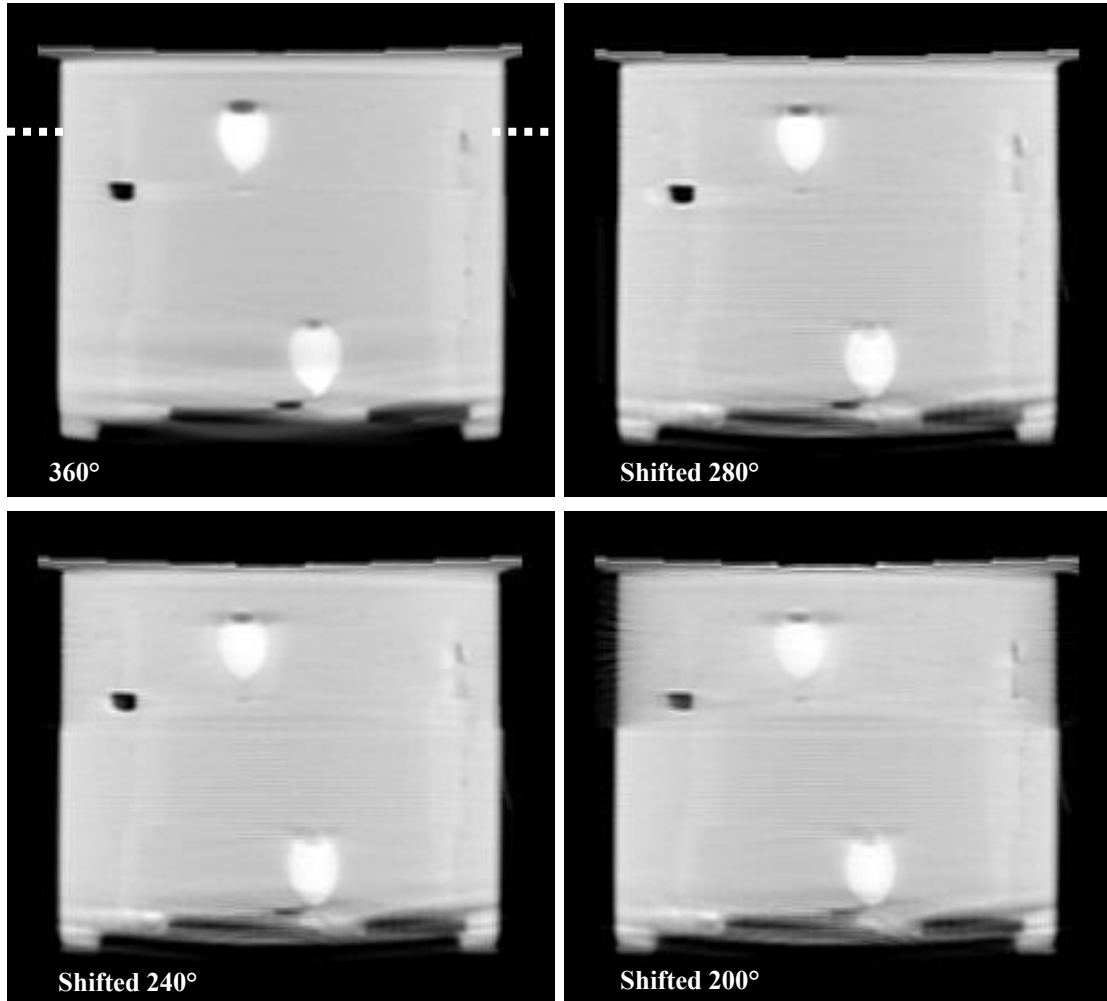
Figure 6.19: Transverse images of the balloon disc phantom under conditions of full 360° tomography and vertical shifting trajectories noted on the images. The images were generated by summing slices that showed the largest balloons in each disc. Profile across the indicated dashed line on the upper level emphasizes the increased distortion evident, especially around the edges, as projections are dropped in vertically shifted data sets.

6.2.2. Observer study into the effects of vertical shifting

Having observed the effect of vertical shifting techniques on high contrast data, the next step in investigating the feasibility of using vertical shifting techniques was to perform a small observer study in order to investigate the ability of observers to maintain visibility of low contrast objects under vertical shifting conditions.

The effects of vertical system shifting on reconstructed images of low contrast objects were investigated by acquiring two separate full projection data sets of the previously described stacked disk phantom (see Figure 6.9). The first acquired data set had only the lower disc in the FOV, mimicking imaging only the anterior portion of breast volume, and the second data set (with the phantom lowered by 2.9 cm) had both discs in the cone beam field of view, mimicking imaging the full volume of breast and chest wall. This setup was similar to the method used previously in experiments using the contrast filled balloon lesions (Section 6.2.1). Each data set was acquired using 360 projections, equally spaced by 1°, at 2.5 mAs per projection and using a 60 kVp tube potential. The data sets were then concatenated to mimic complete sets acquired using vertical shifting.

Two separate vertical shifting trajectories were investigated in the observer study and for ease of reference they are described separately. In vertical shifting technique #1 (VS #1) (Figure 6.20) the CT system is raised to maximize the imaged volume of breast tissue only when passing around both sides of the patient, i.e. approximately orthogonal to the long axis of the bed and patient (see Figure 6.14). The CT system is lowered when passing under both the head and feet of the patient bed. This vertical shifting trajectory

enables the CT system to capture as much of the breast and chest wall in the cone beam field of view as is feasible using the geometric limits of the CT system components (see Figure 6.14). In this observer study, VS #1 was performed for azimuthal spans of 60° and 120° at both sides of the bed since the wide body design of the current x-ray tube may necessitate a 120° span to fully rotate under the head and feet section, while a tube that possesses a narrower profile necessitate only a 60° span.

Vertical Shifting Technique #1   **Vertical Shifting Technique #2**
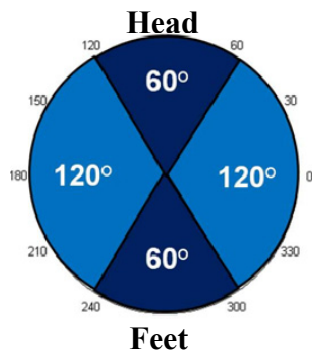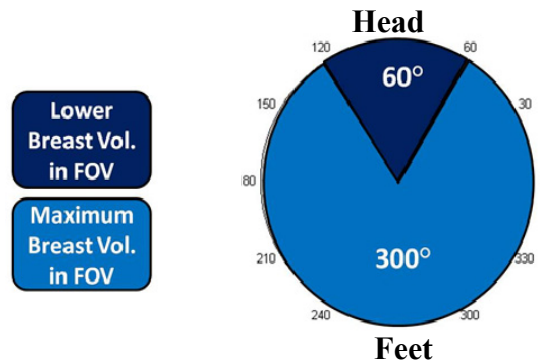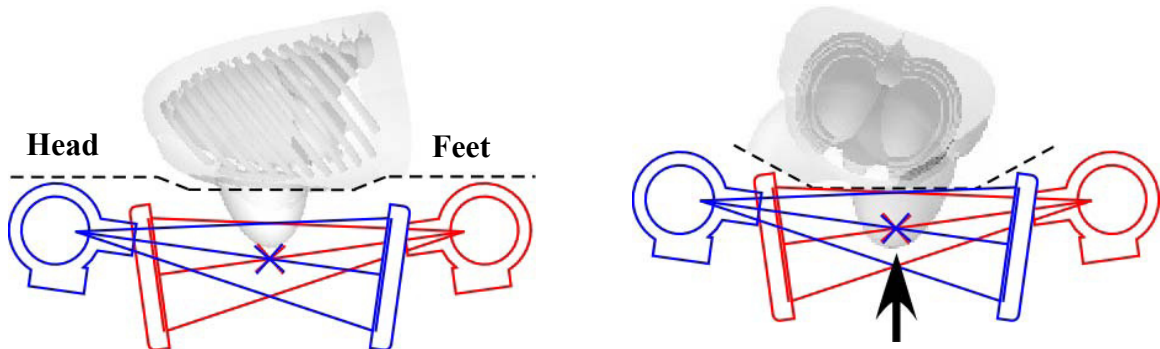
Figure 6.20: This set of images illustrates where in the 360° trajectory the CT system is raised or lowered in each tested vertical shifting technique. (Top Left) The illustration of vertical shifting technique #1 (shown here for VS#1 60°) indicates that the CT system is raised when passing around the sides of the patient bed (light blue areas), and lowered when passing under the head and feet (dark blue). Illustration of vertical shifting technique #2 (shown here for VS#2 60°) indicates that the CT system is lowered only when passing under the head (or feet section, but not both), and then raised to image more of the breast and chest wall for all other angles in the trajectory. (Illustrations courtesy of Dr Martin Tornai)

In vertical shifting technique #2 (VS #2), the CT system is raised for most of the 360° trajectory to maximize the imaged volume of breast tissue. However, the CT system is vertically shifted lower only to allow the x-ray source to pass either under the patient's head or the patient's feet section, but not both. The underlying reason for testing this trajectory is that in the initial integrated prototype system, the x-ray source, positioned higher than the x-ray detector (see Figure 6.2), comes into contact with the bed while attempting to traverse under the head section, while x-ray detector is able to clear both the head and feet of the bed without needing to adjust the height of the system. Therefore, a vertical shift is necessary during only one section of the trajectory to allow the bilateral CT system to rotate for a full 360°. This trajectory was investigated for both 60° and 120° of raised azimuthal rotation at the head since 120° is necessary with the currently implemented x-ray tube, while only 60° may be possible with an x-ray tube that possesses a narrower profile.

VS#1 is more applicable to symmetrical bed designs for prone patient imaging where the head and feet sections of the bed are designed to be at the same height. VS#2 is more applicable to the current tiered bed design, with the head and feet sections positioned at different heights. Table 6.8 summarizes the setup for both VS techniques.

For each of the study setups, observers were separately shown reconstructed images of the lower disc of 5mm acrylic spheres (which is in the FOV for a full 360°) or of the upper disc (which is in the FOV for only a subset of projections when the CT system is vertically shifted). For each presented image, observers were asked to note how many spheres were visible, and to rate the quality of the reconstructed spheres on a scale of 1-

10. Observers were then shown images reconstructed using the full 360° of data or alternatively reconstructed from data acquired using one of the vertical shifting techniques, and asked to rate the quality of the reconstructed images and to also note how many of the reconstructed spheres appeared noticeably distorted.

Table 6.8 Table explaining the various trajectories tested for vertical shifting

Vertical Shifting Technique #	Angular	CT system vertically shifted	Angular range where 2 discs are in the FOV	Angular range where upper disc is in the FOV
1	120°	Head & Feet	120°	240°
	60°	Head & Feet	240°	120°
2	120°	Head only	240°	120°
	60°	Head only	300°	60°

Images of the upper disc of spheres reconstructed using vertical shifting techniques under the tested vertical shifting cases are shown in Figure 6.21.   Readily apparent in the images is the artifacts at the border of the cylinder for both VS#1, 60° and 120° (where the system is shifted at both the head and the feet for the indicated angles).

The results of the first observer question are summarized in Table 6.9. For vertical shifting within the 60° span, observers noted no significant difference in number of visible spheres, despite the fact that there were a slightly lower number of spheres seen on average for VS #2 vs. VS #1 (7.8 vs. 8). For the lower disk of spheres, there were similarly no significant differences in number of spheres seen with a 60° span under both trajectories. This result for the lower disc of spheres is to be expected since it is in the cone beam FOV for the entire 360°, regardless of vertical shifting technique. The story

was significantly different for VS#1 120° however, with the large distortion apparent in Figure 6.21 impacting the visibility of spheres.
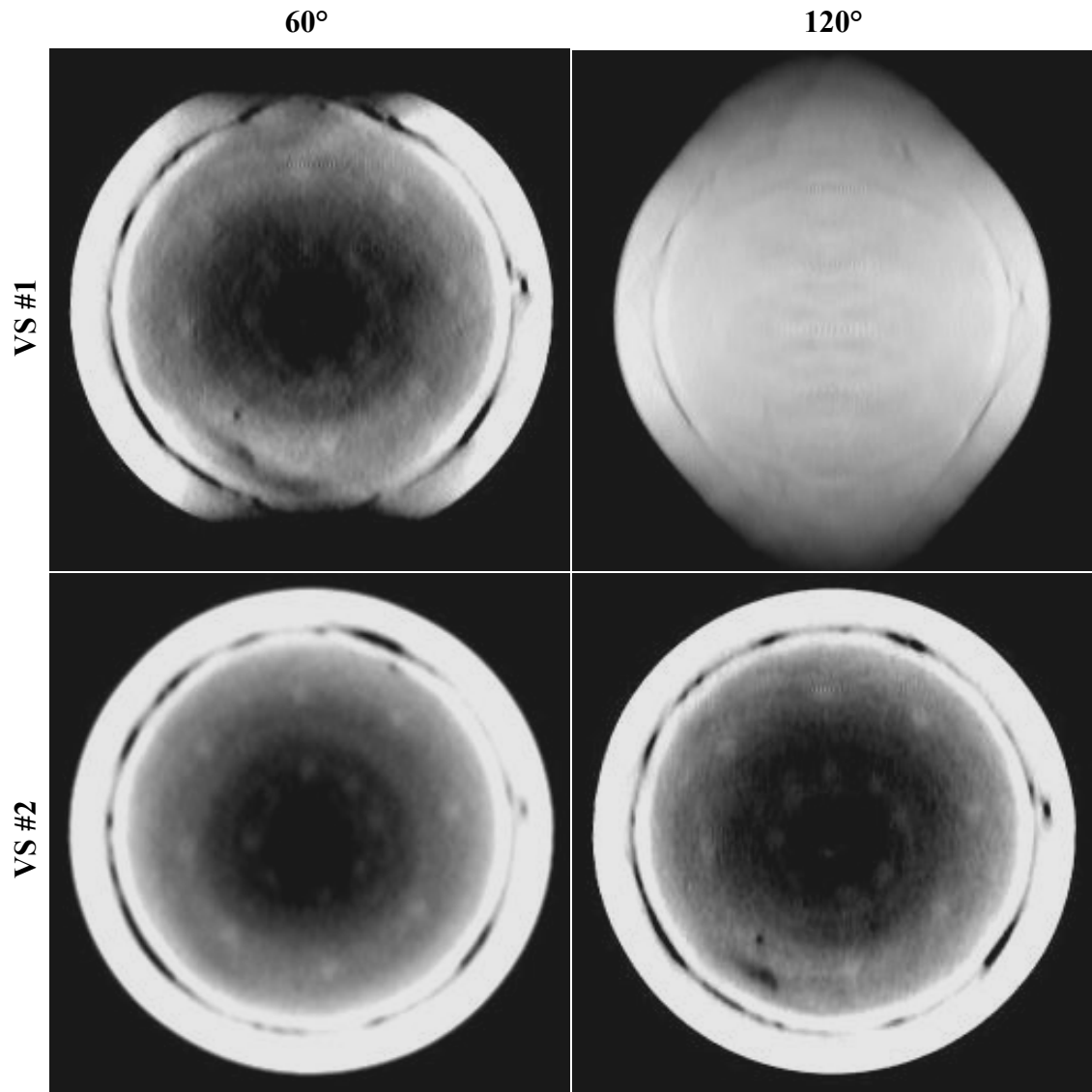
Figure 6.21: Images of the upper disc of very low contrast 5mm acrylic spheres reconstructed using the indicated vertical shifting techniques. (Top row) Although the 5mm spheres are still visible for the VS#1 60° case, distortion artifacts are apparent near the border of the cylinder container. Distortion makes it impossible for the spheres to be seen in the VS#1 120° trajectory. (Bottom row) Visibility of spheres in the upper disc is apparently well preserved for both VS#2 60° and VS#2 120° scenarios, although distortion appears to worsen in the case of VS#2 120°.

Table 6.9 Results of the observer study into the number of visible spheres under various conditions of vertical shifting

Disc	Vertical Shift #	Technique Variation	Mean	σ	p-value vs. seeing 8 spheres
Upper	1	60°	7.8	0.4	0.46
		120°	1.0	1.4	<0.01
	2	60°	8.0	0	0.38
		120°	5.0	1.4	0.31
Lower	1	60°	8.0	0	0.38
		120°	8.0	0	0.38
	2	60°	8.0	0	0.38
		120°	8.0	0	0.38

In terms of quality assessment on a scale of 1 (worst) to 10 (best), the results in Figure 6.22 indicate that, despite obvious image artifacts at the truncated edges of the phantom, especially for VS#1 60°, and a definitive trend in decreased quality rating, there was no statistically significant difference in the overall quality assessed by observers for a span of 60°. The upper disk for VS#2, 60° (where the system is shifted only for one section of projections at the head or feet) was even slightly preferred to the lower disk, further indicating that this span of shifting did not significantly affect the ability to distinguish small low contrast objects in the 60° iteration. Vertically raising the system at the head and feet for 120° each does not appear to be a viable method of reconstruction.
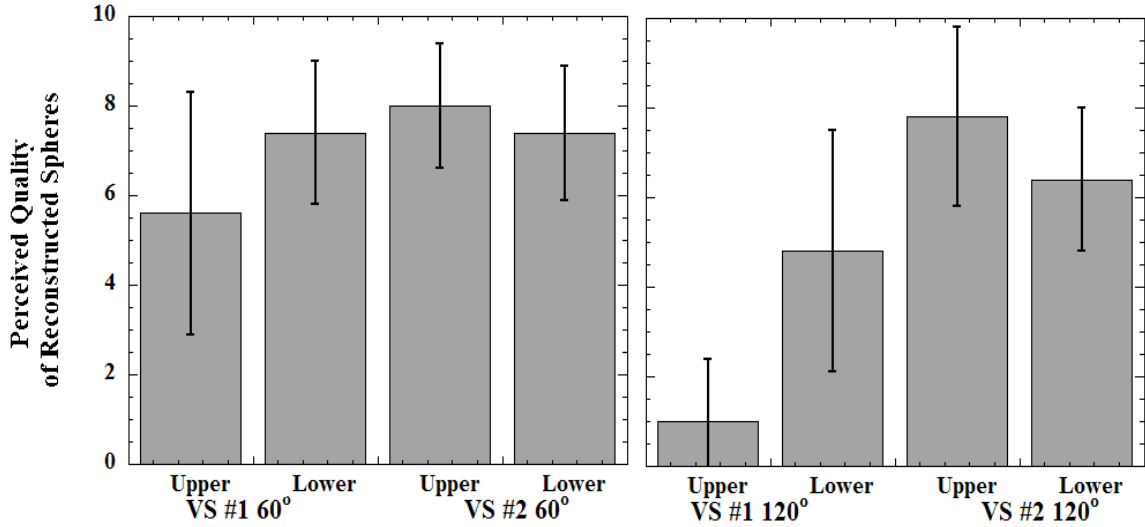
Figure 6.22: Plots illustrating the results of the observer study into the perceived quality (10 = best quality) of the 5mm spheres reconstructed under different conditions of vertical shifting.

For VS #1 with 60° removed, 3.4±2.3 spheres were considered distorted, while for the lower spheres, 1.2±1.6 were considered distorted. Distortion was more evident with observers for vertical shifting with 120° of data as indicated in Table 6.10. The data indicates that the upper disc of spheres (with a lower number of sampled angles) had additional distortion not found in the lower spheres of the same setup. It is unclear whether more realistic, irregularly shaped lesions with fuzzy borders would show any noticeable observer difference. It is also noted that this is a signal-known-exactly case and so results may be biased for that reason. Importantly, the visibility of lesions reconstructed from images acquired with two different system heights is well maintained with 60° shift spans.

Table 6.10 Results of the observer study regarding the number of distorted spheres under various conditions of vertical shifting

Disc	Vertical Shift #	Technique Variation	Mean	σ	p-value of 120° vs. 60°
Upper	1	60°	3.4	2.3	<0.01
		120°	7.8	0.4	
	2	60°	1.2	1.6	0.47
		120°	1.8	1.8	
Lower	1	60°	1.2	1.6	0.02
		120°	3.6	1.82	
	2	60°	1.8	1.3	0.14
		120°	3.0	1.6	

6.3. Discussion

A vital and ongoing challenge associated with dedicated breast computed tomographic imaging is the ability of the system to image the patient's breast up to and including the anterior chest wall. In this chapter, the use of limited angle trajectories or trajectories that involve vertically shifting the relative position of the CT system or bed in mid acquisition were investigated to determine if, by using these novel trajectories, there could be an increase in the volume of breast tissue imaged close to the chest wall of a prone subject.

CAD simulations were used to initially estimate any increase in imaged breast volumes using limited angle acquisition techniques. The simulations were then followed by quantative evaluation of medium to high contrast images reconstructed using limited angle and vertical shifting techniques, and using SdNR and contrast quality metrics. Observer studies were then used to determine the effectiveness of using both limited angle and vertical shifting trajectories to visualize low-contrast spherical objects similar

to small lesions embedded in glandular tissue.

The cumulative finding from the observer studies for both limited angle and vertical shifting techniques indicates that both limited angle and vertical shifting trajectories may be feasible to produce minimal volumetric image degradation, compared to a simple-circular, full 360° data set. Trajectories that involve acquiring approximately 300° of projection data seem particularly useful. Using these trajectories may therefore allow increased viewing of the chest wall by circumventing physical restrictions caused by the the design of the patient bed and the designs of the imaging components. Visibility of small low-contrast objects becomes significantly affected when approximately 120° or more of projection data is removed from the full projection data set or vertically shifted on either side of the patient's axis. An approximate 300° scan or better may be achieved by using an x-ray source with a narrower profile in the lateral orientation such as an end-on, or unipolar x-ray tube design to reduce the required angular range of removed projections.

Despite the ability of observers to maintain visualization of spheres, there were definite degradations in the image quality of reconstructed spheres associated with using reduced angles. However, previously acquired patient data that was reconstructed with limited angle tomography methods did not suffer as expected from a loss of projections, and this is encouraging from a practical point of view. If these novel trajectories are able to capture lesions closer to the chest wall, then even though these lesions may be of slightly lower visual quality and possessing associated artifacts, this may be considered preferable to missing them altogether if it is the only way to get them into the FOV.

It should be emphasized that the results of this set of observer studies into the feasibility of using vertical shifting techniques and/or limited angle tomography to increase the amount of breast and chest wall coverage should not be overstated. These observer studies tested the ability to observe a known number lesions in a known arrangement against a uniform background. Based on the results of the observer study, the feasibility of using the techniques should therefore be seen more as tentative, but not conclusive.

Future work should determine how these trajectories are affected when using irregular shaped, low-contrast objects, when there are more observers and/or cases to view, or when tested using a more difficult imaging task than the case tested in this work.

Chapter 7

7. Concluding Remarks

During the course of this thesis work, the independent and separate CT and SPECT systems dedicated to breast cancer imaging have merged into a unique integrated SPECT-CT dual-modality imaging system, complete with a custom designed patient bed, which is capable of routinely imaging human volunteer subjects. The evolution of the imaging system is shown in Figure 7.1, with the separate SPECT and CT devices being combined into the initial prototype SPECT-CT imaging device, then imaging a volunteer subject in one of the early patient trials performed in the MMI Lab. The final photograph is of the system in its current form.

Early work in this thesis centered on investigating the effect of ultra-thick filtration techniques for uncompressed breast imaging. A wide range of candidate metals were tested under various practical operating conditions to measure their effect on the characteristics of the x-ray beam to be employed in the breast CT system. The results of this extensive set of simulations and empirical experiments reinforced the advantages of using ultra–thick K-edge beam filtration techniques for uncompressed breast imaging. A tungsten target x-ray tube, K-edge beam filtration using a 100th VL of cerium metal, and a tube voltage of 60 kVp enabled the generation of a quasi-monochromatic x-ray beam with minimal beam hardening, and a mean beam energy of approximately 36 keV (see Figure 7.2). This mean beam energy is within a range of beam energies advantageous for optimizing the dose efficiency of uncompressed breast imaging.
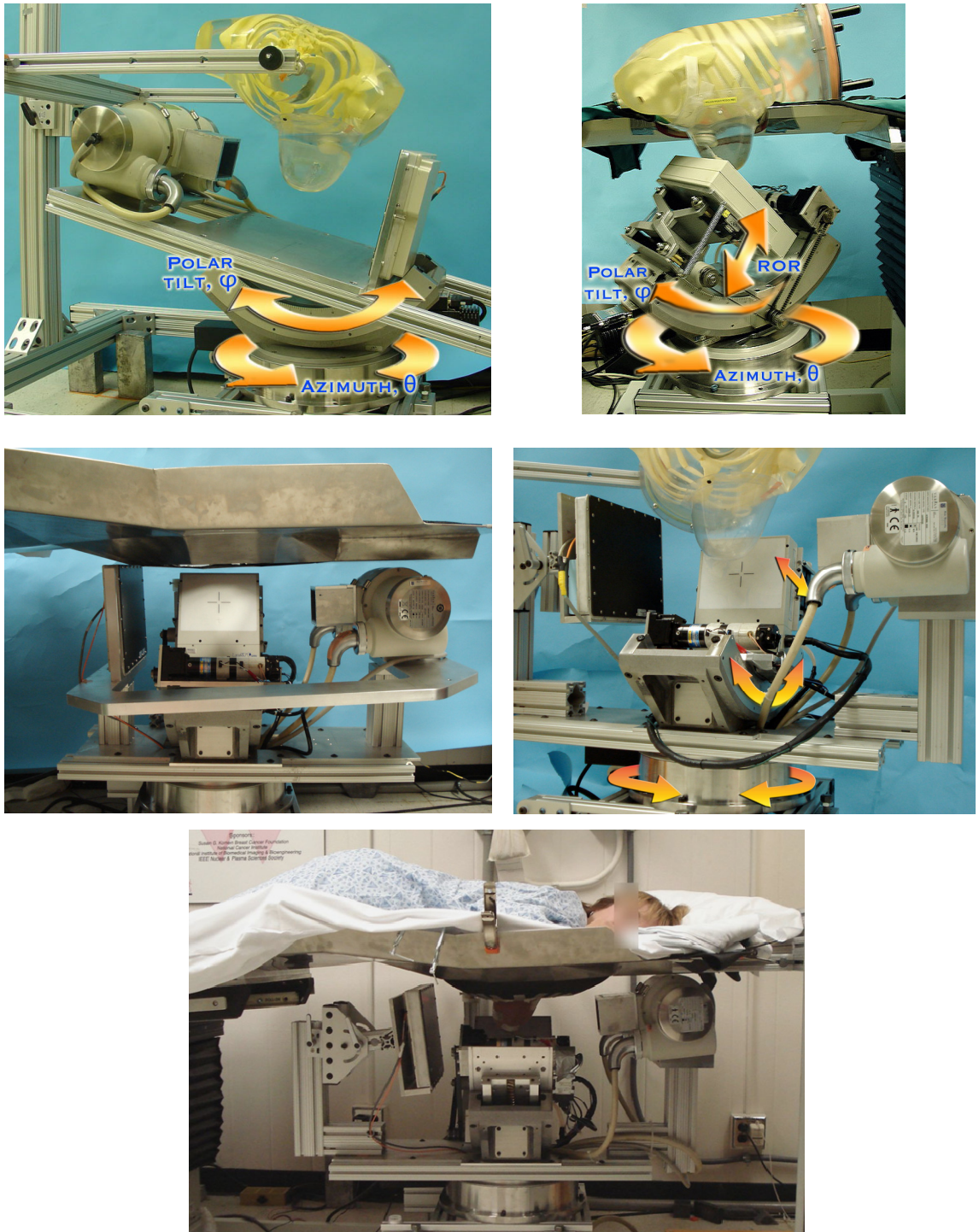
Figure 7.1 Stages in the development of the hybrid SPECT-CT imaging device. (Clockwise from top left) The independent CT and (top right) independent SPECT systems were each capable of motion in a 3D hemisphere about anthropomorphic phantoms. (Middle right) The initial hybrid SPECT-CT device retained full 3D positioning for the integrated SPECT system, but the integrated CT system was restricted to circular motion at a fixed height above the horizontal. (Bottom) Photograph of a volunteer undergoing dual-modality breast imaging using the initial prototype system. (Middle left) The integrated imaging system as currently configured, with the x-ray source and detector connected by a thick U-shaped arm to increase accuracy in the relative positioning of the source and detector.

While cerium at 100th VL is used as the filter material for all imaging tasks in the current system, the experiments carried out in this thesis and in previous work demonstrate that some filters may yield better results than others depending on the characteristics of the breast being imaged, e.g. a very dense glandular breast versus a breast with considerably more adipose composition,. Thus developing a mechanism to allow for efficient swapping of the beam filter types will further optimize the use of k-edge filters for breast CT.
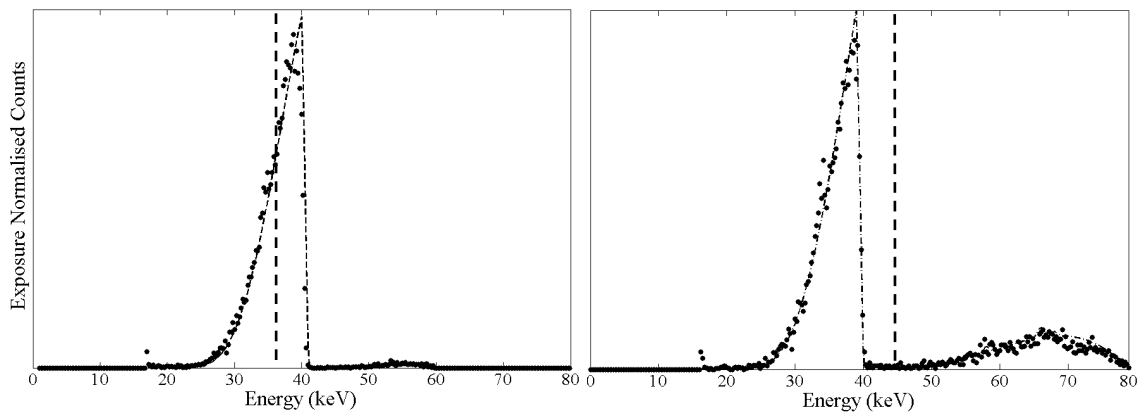
Figure 7.2: Images of simulated (line) and measured (points) output spectra for a 200th VL Ce-filtered x-beam and a tube voltage of (left) 60 kVp and (right) 80kVp. The mean beam energy for each spectrum is also indicated with the dashed line. The filtered 60kVp beam has a FWTM of approximately 15% and a mean beam energy of 36 keV, which is an optimal area for uncompressed breast imaging. The 80 kVp spectrum has a more bimodal appearance, and the mean beam energy (~45 keV) shifts outside the optimal range for breast CT imaging.

Other beneficial characteristics of the cerium-filtered beam employed in the breast CT system were investigated in this thesis research by empirically measuring the dose absorbed by the uncompressed breast during a full breast CT scan. A novel technique using radiochromic film was employed to initially measure the dose absorbed by materials that mimic 100% glandular and fatty breast tissue in a range of geometric and

anthropomorphic phantom shapes. Ultimately, the radiation dose absorbed by an uncompressed cadaver breast during imaging by the breast CT device was measured using this novel radiochromic film technique (Figure 7.3). The results of this experiment found that the breast CT system successfully images the uncompressed cadaver breast at dose levels, 3-5 mGy, that are well below those of the suggested US federal limits for mammography. It determined that the dose is not uniformly distributed in the breast volume, but is concentrated at the peripheries, and also increases as the breast tapers towards the nipple. Another finding was that radiochromic film is also a relatively easy dosimetric technique to employ, compared to moisture-sensitive TLDs, and in the future it may be further used to help optimize the tomographic imaging technique for breasts of different compositions.
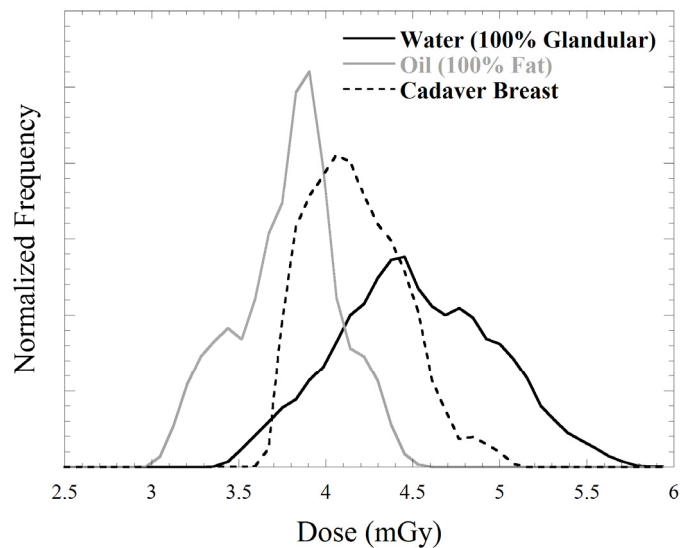
Figure 7.3: Summary of the dose measurements made using the radiochromic film in the anthropomorphic phantom containing water (mimicking 100% glandular breast tissue), oil (mimicking 100% fatty breast tissue), and the cadaver breast. Average measured dose for the three setups are 4.5 mGy, 3.8 mGy and 4.2 mGy, respectively.

In preparation for integrating the separate SPECT and CT imaging devices into a single, hybrid device with a common field of view, complementary studies were performed to measure image contamination of one modality by x-ray or γ-ray photons from the other modality. After extensive investigations, the overall results of the studies indicate that cross contamination will likely not be of great concern in the integrated SPECT-CT imaging system. In the case of emission imaging, the relatively large difference between the 36 keV mean beam energy employed in CT imaging and the 140 keV γ-ray photon employed in SPECT imaging enables effective energy windowing of the SPECT data that eliminates contamination from the CT source, despite the substantially higher x-ray flux that also causes summed events of higher average energy. Results typical of those shown in Table 7.1 indicated a <2% level of photopeak contamination in the SPECT image across several different breast sizes and activity setups.

Table 7.1 Maximum and minimum photopeak contamination for the 1500mL breast across all (0-60°) polar angles at each azimuthal angle

| X-ray Exposure (mAs) | Energy Window (%) | Photopeak contamination per x-ray exposure (%) | | | | | |
| | | -15° azimuth | | 0° azimuth | | +10° azimuth | |
		Min.	Max.	Min.	Max.	Min.	Max.
2.5 mAs	Open	0.6	0.6	0.6	0.9	0.6	0.6
	±3	-	0.3	0.1	0.2	-	0.3
	±5	0.1	0.4	0.1	0.5	0.2	0.3
	±8	0.3	0.5	0.2	0.7	0.3	0.5
5.0 mAs	Open	0.8	1.1	1.3	2.5	0.9	1.4
	±3	-	0.3	0.1	0.3	-	0.3
	±5	0.1	0.3	0.1	0.4	0.1	0.3
	±8	0.2	0.4	0.3	0.6	0.3	0.5
10.0 mAs	Open	2.2	3.1	2.3	3.3	1.7	3.3
	±3	-	0.2	-	0.2	-	0.1
	±5	0.1	0.2	0.2	0.4	0.2	0.2
	±8	0.3	0.4	0.3	0.5	0.3	0.4

Any transmission contamination that was apparent in emission images acquired using an open energy window was removed when progressively tightening the image energy window (Figure 7.4). In the case of transmission imaging, the flux of the x-ray beam is so large, even after passing through a thick glandular breast, that the flux of the emitted ^{99m}Tc γ-ray photons is a tiny fraction of that of the x-ray beam flux. Quantative results from emission source contamination of the transmission image were equivocal, with some results suggesting a definite decrease in image metrics with increasing image contamination, while other studies indicated little or no effect in response to large increases in emission activity.
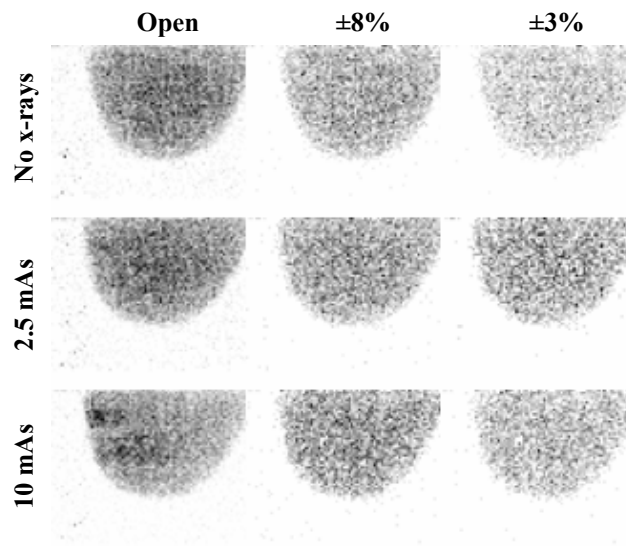
Figure 7.4: Emission projection images of a 1500mL breast (top) without contaminating x-ray exposure, (middle) with a 2.5 mAs exposure, and (bottom) a 10mAs exposure. 10mAs is 4X the standard x-ray exposure used in our lab. Energy windows shown are (left) an open window, (middle) ±8%, and (right) ±3%. Note how the image contamination is windowed out as the energy window tightens.

An observer study indicated no change in the ability to visualize small 5mm spheres in a low contrast environment, even with the presence of an overly large amount (16mCi) of ^{99m}Tc activity in the vicinity of the x-ray detector. Although further investigations may

be undertaken to elucidate the exact level of emission contamination in the x-ray image, the effect of the overall contamination has so far proven to be minimal and may likely remain so in future iterations of the system design.

The next step employed computer aided design techniques to help integrate the separate SPECT and CT systems onto a common gantry, capable of acquiring dual-modality tomographic data of a pendant breast in the systems' common field of view. This was successfully done, but to progress the system as a viable clinical device, it was necessary to custom design a comfortable bed that also enabled dual-modality prone patient imaging. The novel bed design, shown in Figure 7.5, was designed primarily to allow the prototype integrated SPECT and CT systems acquire projection data below the prone patient (see Figure 7.1). The patient bed was used in the initial human volunteer trials that occurred in the MMI Lab. Results from the small number of trials indicated that the bed is successful in terms of this primary task, but issues involving effective patient positioning remain. Inherent shortcomings in the design of the CT imaging components (i.e. large dead zones) means that the tiered bed design falls short of enabling imaging of the patient's chest wall by the CT system.

The next generation of the integrated SPECT-CT system will likely re-establish full 3D positioning capability to the integrated CT system (see Figure 7.6), thus allowing the CT system to overcome many of the physical and geometric obstacles that are involved in trying to image a prone patient on a bed.
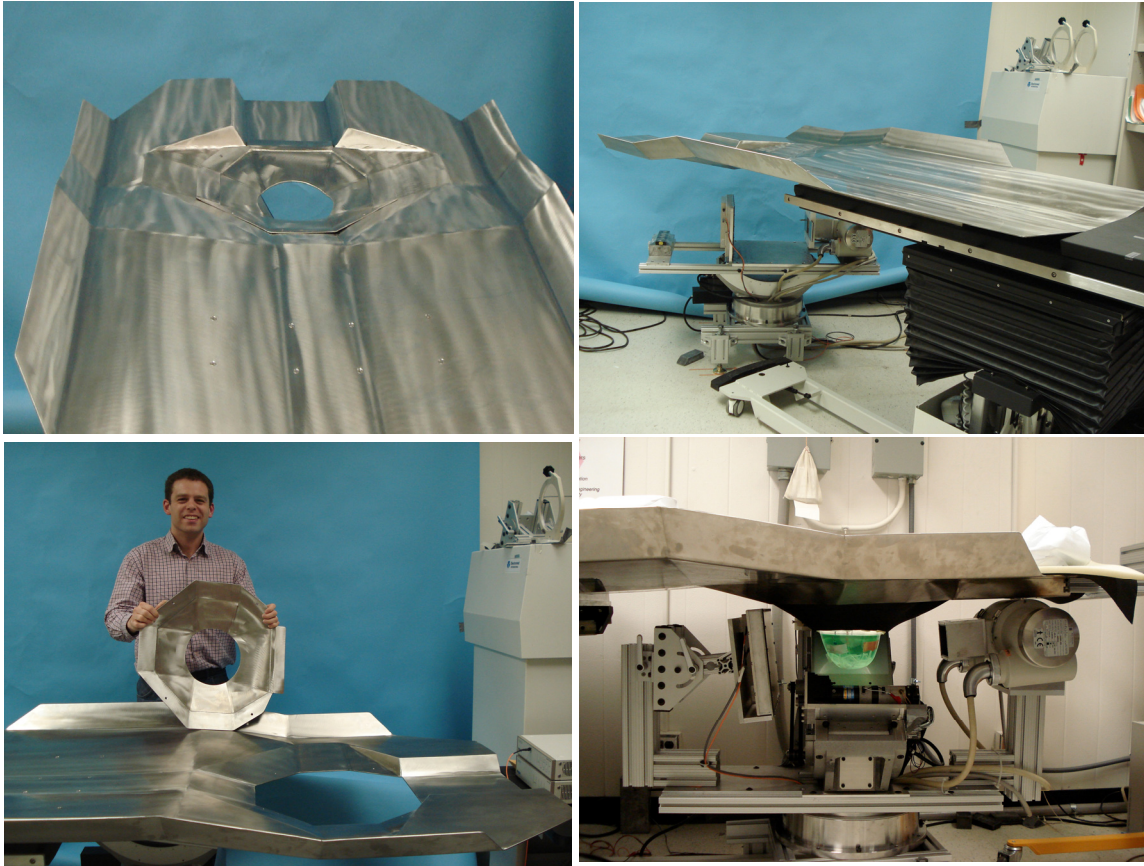
Figure 7.5: Photographs of the custom designed patient bed. (Top left) A photo down the long axis of the bed, showing the angled sides and octagonal torso section. (Top right) The stainless steel bed attached to the *Biodex* bed positioning system. (Bottom left) The author with the torso insert removed from the bed, showing the enlarged hole in the bed to allow the breast and chest wall of the patient to extend more into the x-ray cone beam field of view. (Bottom Right) The original integrated CT system imaging an anthropomorphic breast phantom in the common FOV. The phantom is filled with dye-infused water, and supported by a neoprene layer that sags under the weight of the phantom, bringing the phantom more into the field of view of the cone beam.

The ability to tilt in the polar direction for cone beam CT will also improve the quality of reconstructed 3D breast volumes and may potentially increase the imaged volume of the patient's breast and chest wall. Regaining this additional degree of positioning freedom for the CT system will necessitate the design of a new patient bed to take advantage of the powerful positioning ability of the dual-modality system. A concept design of a bed

to facilitate the tilting trajectories with a next generation CT system is shown in Figure 7.7.

Horizontal axis of rotation
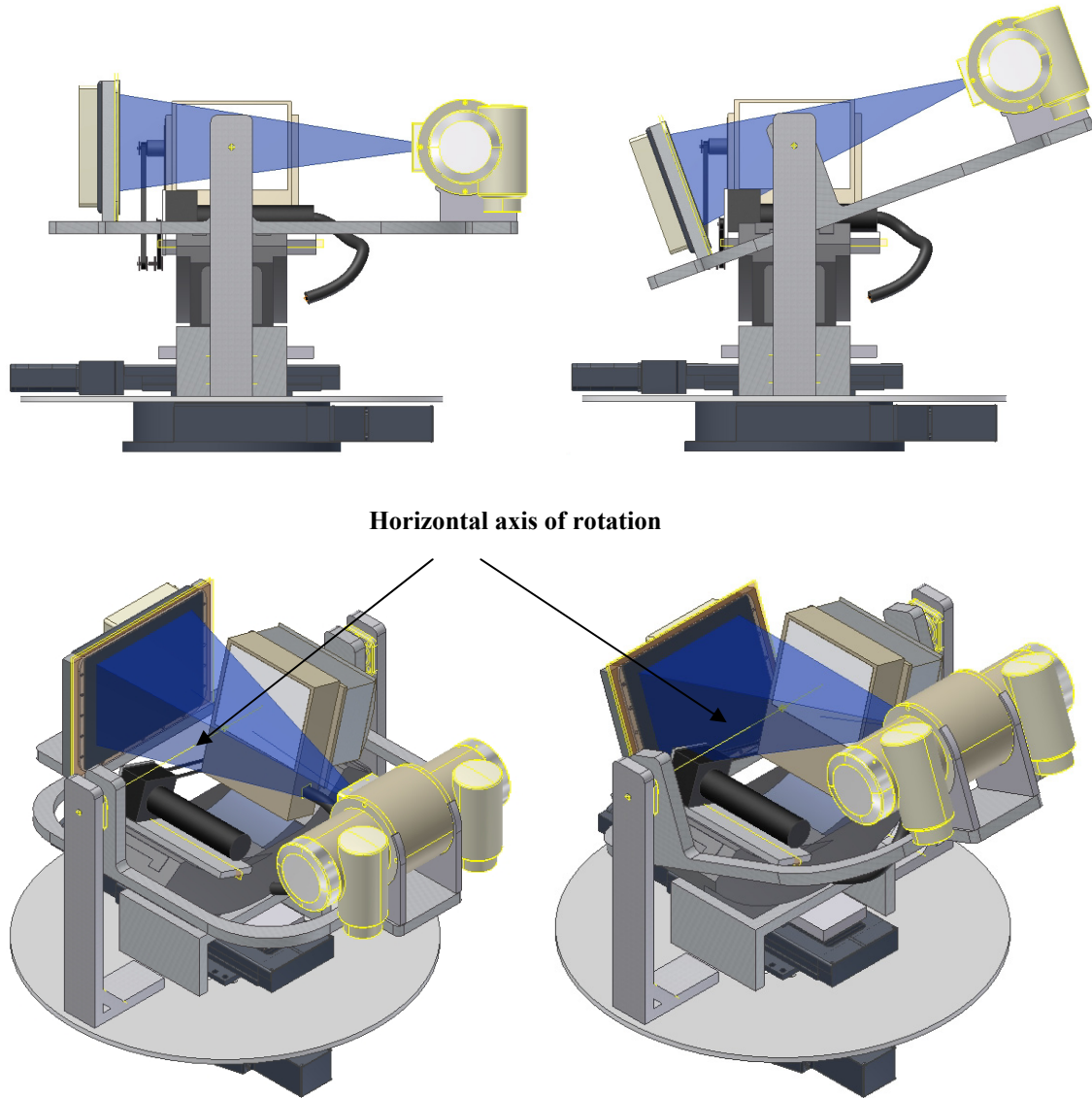
Figure 7.6: CAD concept designs from side-on and oblique perspectives of a next generation integrated SPECT-CT system. The concept includes a CT system (with the same components that are in the current integrated CT system) that can tilt in the polar direction via a see-saw type mechanism about a horizontal axis of rotation through the isocenter of the CT system. The tilted x-ray cone beam reinforces the increase in imaged breast volume compared to the non-tilted system. The other yellow highlights apparent in the image are due to the rendering of the 3D CAD model.

The concept bed design employs a narrowed torso section (20cm at its narrowest) for the patient to lie on at an angle. The bed also employs narrow, angled sides to protect the patient while also allowing the next generation CT system, composed of a narrow profile, end-on x-ray tube and a large 40 x 30 cm detector, to tilt in the polar direction.
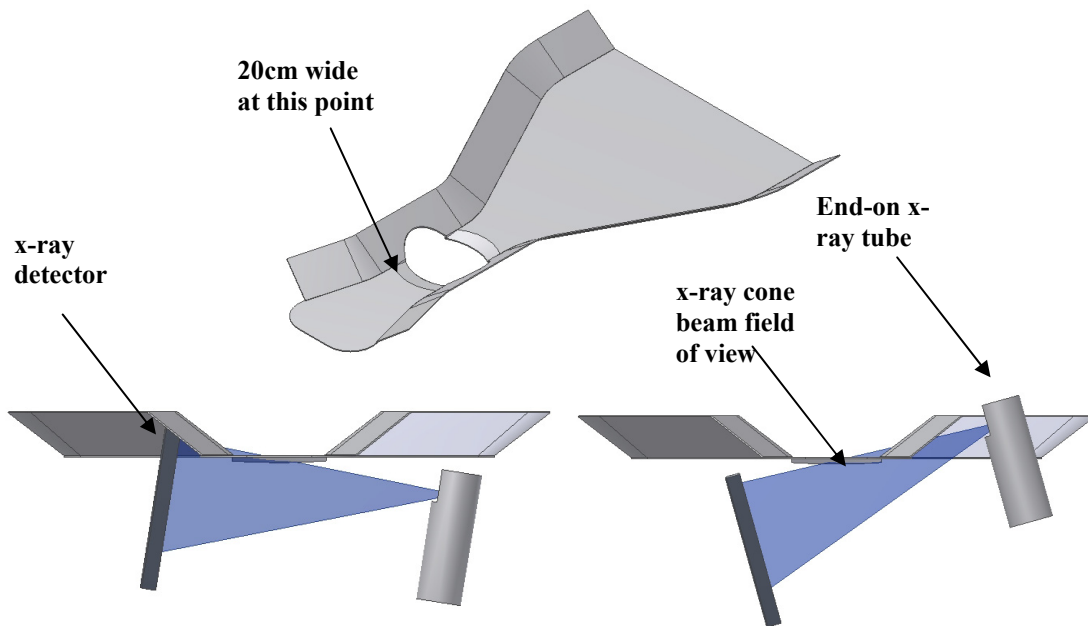
Figure 7.7: Concept design of a 2nd generation bed to allow a narrow edge detector and end-on x-ray tube to tilt in the polar direction. This will enable improved cone beam image quality and increase the imaged volume of breast tissue. The bed is shown (top) from an oblique angle above the bed and (bottom) from a front-on perspective, with a unipolar tube and narrow edge detector tilting the cone beam field of view in the polar direction.

The final design of the bed will also depend on the selection of x-ray source and detector components.

Increasing the imaged breast volume with the current integrated CT system was the subject of the final section of thesis research. This section investigated the feasibility of using two trajectories, limited angle tomography and vertical system shifting, to

overcome restricted viewing of the patient's breast volume in the initial integrated CT system. Results from these early studies suggest that the two novel imaging trajectories, in conjunction with iterative reconstruction techniques, are indeed viable methods that can be used to increase the imaged volume of breast and chest wall tissue. However, a more extensive followup using irregular shaped objects of various sizes in future studies may better establish the viable limits of using limited angle tomography or vertical system shifting in the CT system.

Over the course of the last number of years, great progress has been made to bring the independent SPECT and CT systems up to the current stage of integrated development. The system has already shown itself to be capable of imaging patients effectively using low-dose CT and powerful SPECT imaging in a compact, common field of view machine. While the appropriate place for this imaging system in the diagnostic and treatment environments has yet to be determined, early indications are that it may serve a useful role in areas such as imaging of women with a high risk of breast cancer, in treatment planning, and in monitoring response to therapy. A next step is to build on the success of early patient dual-modality imaging trials conducted during the course of this thesis research, and to undertake larger scale patient imaging trials using the newly integrated SPECT-CT system with the improved bed design. This author is hopeful that these trials will expose the benefits of using the dual-modality SPECT-CT imaging system to improve the detection and diagnosis of breast cancer, and help improve the outcomes for women whose lives are threatened by this disease.

Bibliography

[1]   A. Jemal, R. Siegel, E. Ward, Y. Hao, J. Xu, and M. J. Thun, "Cancer Statistics, 2009," *CA Cancer J Clin*, vol. 59, pp. 225-249, 2009.

[2]   "Cancer Prevention & Early Detection Facts and Figures " *American Cancer Society*, 2009.

[3]   J. G. Elmore, K. Armstrong, C. D. Lehman, and S. W. Fletcher, "Screening for Breast Cancer," *JAMA,* vol. 293, pp. 1245-1256, 2005.

[4]   O. Osen, P.C. Gotsche, "Cochrane review on screening for breast cancer with mammography," *Lancet,* vol. 358, p. 3, 2001.

[5]   A. Karellas and S. Vedantham, "Breast cancer imaging: A perspective for the next decade," *Medical Physics,* vol. 35, pp. 4878-4897, 2008.

[6]   D. Saslow, C. Boetes, W. Burke, S. Harms, M. O. Leach, C. D. Lehman, E. Morris, E. Pisano, M. Schnall, S. Sener, R. A. Smith, E. Warner, M. Yaffe, K. S. Andrews, C. A. Russell, and G. for the American Cancer Society Breast Cancer Advisory, "American Cancer Society Guidelines for Breast Screening with MRI as an Adjunct to Mammography," *CA: A Cancer Journal for Clinicians,* vol. 57, pp. 75-89, 2007.

[7]   H. D. Nelson, K. Tyne, A. Naik, C. Bougatsos, B. K. Chan, and L. Humphrey, "Screening for Breast Cancer: An Update for the U.S. Preventive Services Task Force," *Annals of Internal Medicine,* vol. 151, pp. 727-737, 2009.

[8]   E. D. Pisano, C. Gatsonis, E. Hendrick, M. Yaffe, J. K. Baum, S. Acharyya, E. F. Conant, L. L. Fajardo, L. Bassett, C. D'Orsi, R. Jong, and M. Rebner, "Diagnostic performance for digital versus film mammography for breast-cancer screening," *The New England Journal of Medicine,* vol. 353, pp. 1773-1783, 2005.

[9]   D. B. Kopans, *Breast Imaging*, 3rd ed. Philadelphia: J.B. Lippincott Company, 2006.

[10]   A. Poulos and M. Rickard, "Compression in mammography and the perception of discomfort," *Australasian Radiology,* vol. 41, pp. 247-252, 1997.

[11]   M. D. L. Carney P.A., Yankaskas B.C., "Individual and combined effects of age, breast density, and hormone replacement therapy use on the accuracy of screening mammography," *Annals of Internal Medicine,* vol. 138, p. 8, 2003.

[12]   P. Russo, T. Coppola, G. Mettivier, M. C. Montesi, and A. Lauria, "Distribution of Absorbed Dose in Cone-Beam Breast Computed Tomography with Radiochromic Films," *IEEE Nuclear Science Symosium and Medical Imaging,* 2009.

[13]   W. T. Yang, S. Carkaci, L. Chen, C.-J. Lai, A. Sahin, G. J. Whitman, and C. C. Shaw, "Dedicated Cone-Beam Breast CT: Feasibility Study with Surgical Mastectomy Specimens," *Am. J. Roentgenol.,* vol. 189, pp. 1312-1315, 2007.

[14]   S. J. Glick, "Breast CT," *Annual Review of Biomedical Engineering,* vol. 9, pp. 501-526, 2007.

[15]   J. M. Boone, T. R. Nelson, K. K. Lindfors, and J. A. Siebert, "Dedicated breast CT: radiation dose and image quality evaluation," *Radiology,* vol. 221, pp. 657-667, 2001.

[16]   A. Kwan, N. Shah, G. Burkett, J. A. Seibert, K. K. Lindfors, T. R. Nelson, and J. M. Boone, "Progress in the development of a dedicated breast CT scanner," *Proc. SPIE,* vol. 5368, pp. 304-310, 2004.

[17]   J. M. Boone, A. L. C. Kwan, T. R. Nelson, N. Shah, G. Burkett, J. A. Seibert, K. K. Lindfors, and G. Ross, "Performance assessment of a pendant-geometry CT scanner for breast cancer detection," in *SPIE Medical Imaging Conference*, San Diego, CA, 2005, pp. 319-323.

[18]   K. K. Lindfors, J. M. Boone, T. R. Nelson, K. Yang, A. L. C. Kwan, and D. F. Miller, "Dedicated Breast CT: Initial Clinical Experience," *Radiology,* 2008.

[19]   R. Ning, B. Chen, D. Conover, L. McHugh, J. .Cullinan, and R. Yu, "Flat panel detector-based cone beam volume CT mammography imaging: preliminary phantom study," *Proc. SPIE,* vol. **4320**, pp. 601-610, 2001.

[20]   B. Chen and R. Ning, "Cone-beam volume CT mammographic imaging: feasibility study," *Med. Phys.,* vol. 29, pp. 755-770, 2002.

[21]   R. Ning, Y. Yu, D. L. Conover, X. Lu, H. He, Z. Chen, L. Schiffhauer, and J. Cullinan, "Preliminary system characterization of flat-panel-detector-based cone-beam CT for breast imaging," *2004 SPIE Med Imag Conf,* vol. 5368, pp. 292-303, 2004.

[22]   E. Warner, H. Messersmith, P. Causer, A. Eisen, R. Shumak, and D. Plewes, "Systematic Review: Using Magnetic Resonance Imaging to Screen Women at High Risk for Breast Cancer," *Annals of Internal Medicine,* vol. 148, pp. 671-679, 2008.

[23]   L. Bartella, C. S. Smith, D. D. Dershaw, and L. Liberman, "Imaging Breast Cancer," *Radiologic Clinics of North America,* vol. 45, pp. 45-67, 2007.

[24]   W. A. Berg, J. D. Blume, J. B. Cormack, E. B. Mendelson, D. Lehrer, M. Bohm-Velez, E. D. Pisano, R. A. Jong, W. P. Evans, M. J. Morton, M. C. Mahoney, L. Hovanessian Larsen, R. G. Barr, D. M. Farria, H. S. Marques, K. Boparai, and for the ACRIN Investigators,

"Combined Screening With Ultrasound and Mammography vs Mammography Alone in Women at Elevated Risk of Breast Cancer," *JAMA,* vol. 299, pp. 2151-2163, 2008.

[25]   T. M. Kolb, J. Lichy, and J. H. Newhouse, "Comparison of the Performance of Screening Mammography, Physical Examination, and Breast US and Evaluation of Factors that Influence Them: An Analysis of 27,825 Patient Evaluations," in *Radiology* vol. 225, ed, 2002, pp. 165-175.

[26]   N. Duric, P. Littrup, L. Poulo, A. Babkin, R. Pevzner, E. Holsapple, O. Rama, and C. Glide, "Detection of breast cancer with ultrasound tomography: First results with the Computed Ultrasound Risk Evaluation (CURE) prototype," *Medical Physics,* vol. 34, pp. 773-785, 2007.

[27]   A. Kapur, P. Carson, J. Eberhard, M. Goodsitt, K. Thomenius, M. Lokhandwalla, D. Buckley, M. Roubidoux, M. Helvie, R. Booi, G. LeCarpentier, R. Erkamp, H. Chan, J. Fowlkes, J. Thomas, and C. Landberg, "Combination of digital mammography with semi-automated 3D breast ultrasound," *Technology of Cancer Research Treatment,* vol. 3, p. 9, 2004.

[28]   L. T. Niklason, B. T. Christian, L. E. Niklason, D. B. Kopans, D. E. Castleberry, B. H. Opsahl- Ong, C. E. Landberg, P. J. Slanetz, A. A. Giardino, R. Moore, D. Albagli, M. C. DeJule, P. F. Fitzgerald, D. F. Fobare, B. W. Giambattista, R. F. Kwasnick, J. Liu, S. J. Lubowski, G. E. Possin, J. F. Richotte, C. Y. Wei, and R. F. Wirth, "Digital tomosynthesis in breast imaging," vol. 205, ed, 1997, pp. 399-406.

[29]   D. Gur, G. S. Abrams, D. M. Chough, M. A. Ganott, C. M. Hakim, R. L. Perrin, G. Y. Rathfon, J. H. Sumkin, M. L. Zuley, and A. I. Bandos, "Digital Breast Tomosynthesis: Observer Performance Study," *Am. J. Roentgenol.,* vol. 193, pp. 586-591, 2009.

[30]   S. P. Poplack, T. D. Tosteson, C. A. Kogel, and H. M. Nagy, "Digital Breast Tomosynthesis: Initial Experience in 98 Women with Abnormal Digital Screening Mammography," *Am. J. Roentgenol.,* vol. 189, pp. 616-623, 2007.

[31]   J. T. Dobbins and D. J. Godfrey, "Digital x-ray tomosynthesis: current state of the art and clinical potential," *Physics in Medicine and Biology,* vol. 48, pp. R65-R106, 2003.

[32]   J. T. Dobbins, "Tomosynthesis imaging: At a translational crossroads," *Medical Physics,* vol. 36, pp. 1956-1967, 2009.

[33]   I. Khalkhali, J. K. Baum, J. Villanueva-Meyer, S. L. Edell, L. G. Hanelin, C. E. Lugo, R. Taillefer, L. M. Freeman, C. E. Neal, A. M. Scheff, J. L. Connolly, S. J. Schnitt, M. J. Houlihan, J. S. Sampalis, and S. B. Haber, "[99m]Tc sestamibi breast imaging for the examination of patients with dense and fatty breasts: multicenter study," *Radiology,* vol. 222, pp. 149-155, 2002.

[34]   R. a. Hussain and J. R. b. Buscombe, "A meta-analysis of scintimammography: an evidence-based approach to its clinical utility," *Nuclear Medicine Communications,* vol. 27, pp. 589-594, 2006.

[35]   M. Liberman, F. Sampalis, D. S. Mulder, and J. S. Sampalis, "Breast Cancer Diagnosis by Scintimammography: A Meta-analysis and Review of the Literature," *Breast Cancer Research and Treatment,* vol. 80, pp. 115-126, 2003.

[36]   A. D. Waxman, "The role of 99mTc methoxyisobutylisonitrile in imaging breast cancer," *Seminars in Nuclear Medicine,* vol. 27, pp. 40-54, 1997.

[37]   C. B. Hruska, S. W. Phillips, D. H. Whaley, D. J. Rhodes, and M. K. O'Connor, "Molecular Breast Imaging: Use of a Dual-Head Dedicated Gamma Camera to Detect Small Breast Tumors," *Am. J. Roentgenol.,* vol. 191, pp. 1805-1815, 2008.

[38]   C. B. Hruska, J. C. Boughey, S. W. Phillips, D. J. Rhodes, D. L. Wahner-Roedler, D. H. Whaley, A. C. Degnim, and M. K. O'Connor, "Scientific Impact Recognition Award: Molecular breast imaging: A review of the Mayo Clinic experience," *The American Journal of Surgery,* vol. 196, pp. 470-476, 2008.

[39]   M. K. O'Connor and B. J. Kemp, "Single-photon emission computed tomography/computed tomography: basic instrumentation and innovations," *Semin Nucl Med,* vol. 36, pp. 258-66, Oct 2006.

[40]   M. K. O'Connor, S. W. Phillips, C. B. Hruska, D. J. Rhodes, and D. A. Collins, "Molecular Breast Imaging: Advantages and Limitations of a Scintimammographic Technique in Patients with Small Breast Tumors," *The Breast Journal,* vol. 13, pp. 3-11, 2007.

[41]   K. Scheidhauer, C. Walter, and M. D. Seemann, "FDG PET and other imaging modalities in the primary diagnosis of suspicious breast lesions," *European Journal of Nuclear Medicine and Molecular Imaging,* vol. 31, pp. S70-S79, 2004.

[42]   Y. Zhang, R. Ramirez, H. Li, S. Liu, S. An, C. Wang, H. Baghaei, W.-H. Wong, and M.-L. Jan, "The development of a low-cost large-area high-resolution breast positron emission mammography (PEM) camera," *J Nucl Med Meeting Abstracts,* vol. 50, 2009.

[43]   L. MacDonald, J. Edwards, T. Lewellen, D. Haseley, J. Rogers, and P. Kinahan, "Clinical Imaging Characteristics of the Positron Emission Mammography Camera: PEM Flex Solo II," *J Nucl Med,* vol. 50, pp. 1666-1675, 2009.

[44]   R. R. Raymond and et al., "The positron emission mammography/tomography breast imaging and biopsy system (PEM/PET): design, construction and phantom-based measurements," *Physics in Medicine and Biology,* vol. 53, p. 637, 2008.

[45] E. L. Rosen, T. G. Turkington, M. S. Soo, J. A. Baker, and R. E. Coleman, "Detection of Primary Breast Carcinoma with a Dedicated, Large-Field-of-View FDG PET Mammography Device: Initial Experience," *Radiology*, vol. 234, pp. 527-534, 2005.

[46] R. Ribeiro, C. Abreu, P. Almeida, F. Balau, P. Bordalo, N. C. Ferreira, S. Fetal, F. Fraga, P. Lecoq, M. Martins, N. Matela, R. Moura, C. Ortigão, L. Peralta, S. Ramos, P. Rato, P. Rodrigues, A. I. Santos, A. Trindade, and J. Varela, "Breast imaging with a dedicated PEM," *Nuclear Instruments and Methods in Physics Research Section A: Accelerators, Spectrometers, Detectors and Associated Equipment*, vol. 527, pp. 87-91, 2004.

[47] W. A. Berg, I. N. Weinberg, D. Narayanan, M. E. Lobrano, E. Ross, L. Amodei, L. Tafra, L. P. Adler, J. Uddo, W. S. III, and E. A. Levine, "High-Resolution Fluorodeoxyglucose Positron Emission Tomography with Compression ("Positron Emission Mammography") is Highly Accurate in Depicting Primary Breast Cancer," *The Breast Journal*, vol. 12, 2006.

[48] E. L. Rosen, W. B. Eubank, and D. A. Mankoff, "FDG PET, PET/CT, and Breast Cancer Imaging," *Radiographics*, vol. 27, pp. S215-S229, 2007.

[49] Y. Seo, C. Mari, and B. H. Hasegawa, "Technological Development and Advances in Single-Photon Emission Computed Tomography/Computed Tomography," *Seminars in nuclear medicine*, vol. 38, pp. 177-198, 2008.

[50] S. R. Cherry, "Multimodality *in vivo* imaging systems: Twice the Power or Double the Trouble?," *Annual Review of Biomedical Engineering*, vol. 8, pp. 35-62, 2006.

[51] D. W. Townsend, "Multimodality imaging of structure and function," *Physics in Medicine and Biology*, vol. 53, pp. R1-R39, 2008.

[52] P. E. Kinahan, B. H. Hasegawa, and T. Beyer, "X-ray based attenuation correction for positron emission tomography/computed tomography scanners," *Seminars in Nuclear Medicine*, vol. 33, pp. 166-179, 2003.

[53] Y. Seo, K. H. Wong, M. Sun, B. L. Franc, R. A. Hawkins, and B. H. Hasegawa, "Correction of photon attenuation and collimator response for a body-contouring SPECT/CT imaging system," *J Nucl Med*, vol. 46, pp. 868-877, 2005.

[54] S. R. Cherry, "Multimodality Imaging: Beyond PET/CT and SPECT/CT," *Seminars in Nuclear Medicine*, vol. 39, pp. 348-353, 2009.

[55] W. C. Barber, K. Iwata, B. H. Hasegawa, P. R. Bennett, L. J. Cirignano, and K. S. Shah, "A single CdZnTe detector for simultaneous CT/SPECT imaging," *Nuclear Instruments and Methods in Physics Research Section A: Accelerators, Spectrometers, Detectors and Associated Equipment*, vol. 505, pp. 595-598, 2003.

[56]   B. H. Hasegawa, K. H. Wong, K. Iwata, W. C. Barber, A. B. Hwang, A. E. Sakdinawat, M. Ramaswamy, D. C. Price, and R. A. Hawkins, "Dual-modality imaging of cancer with SPECT/CT," *Tech. Canc. Res. Treatment,* vol. 1, pp. 449-458, 2002.

[57]   X. Wu, J. K. Brown, K. Kalki, and B. H. Hasegawa, "Characterization and correction of pulse pile-up in simultaneous emission--transmission computed tomography," *Medical Physics,* vol. 23, pp. 569-575, 1996.

[58]   I. van der Ploeg, R. Valdés Olmos, B. Kroon, and O. Nieweg, "The Hybrid SPECT/CT as an Additional Lymphatic Mapping Tool in Patients with Breast Cancer," *World Journal of Surgery,* vol. 32, pp. 1930-1934, 2008.

[59]   I. van der Ploeg, R. Valdés Olmos, B. Kroon, E. Rutgers, and O. Nieweg, "The hidden sentinel node and SPECT/CT in breast cancer patients," *European Journal of Nuclear Medicine and Molecular Imaging,* vol. 36, p. 6, 2008.

[60]   D. Delbeke, H. Schöder, W. H. Martin, and R. L. Wahl, "Hybrid Imaging (SPECT/CT and PET/CT): Improving Therapeutic Decisions," *Seminars in Nuclear Medicine,* vol. 39, pp. 308-340, 2009.

[61]   S. Bowen, A. Chaudhari, Y. Wu, N. Packard, G. Burkett, L. Fu, J. Qi, J. Boone, S. Cherry, and R. Badawi, "First human images from a dedicated breast PET/CT scanner," *J Nucl Medicine Meeting Abstracts,* vol. 49, 2008.

[62]   S. L. Bowen, Y. Wu, A. J. Chaudhari, L. Fu, N. J. Packard, G. W. Burkett, K. Yang, K. K. Lindfors, D. K. Shelton, R. Hagge, A. D. Borowsky, S. R. Martinez, J. Qi, J. M. Boone, S. R. Cherry, and R. D. Badawi, "Initial Characterization of a Dedicated Breast PET/CT Scanner During Human Imaging," *J Nucl Med,* vol. 50, pp. 1401-1408, 2009.

[63]   J. T. Bushberg, J. A. Seibert, E. M. L. Jr., and J. M. Boone, *The Essential Physics of Medical Imaging,* 2 ed. Philadelphia, PA: Lippincott Williams & Williams, 2002.

[64]   D. B. Husarik and H. C. Steinert, "Single-Photon Emission Computed Tomography/Computed Tomography for Sentinel Node Mapping in Breast Cancer," *Seminars in Nuclear Medicine,* vol. 37, pp. 29-33, 2007.

[65]   J. Maublant, M. de Latour, D. Mestas, A. Clemenson, S. Charrier, V. Feillel, G. Le Bouedec, P. Kaufmann, J. Dauplat, and A. Veyre, "Technetium-99m-Sestamibi Uptake in Breast Tumor and Associated Lymph Nodes," *J Nucl Med,* vol. 37, pp. 922-925, 1996.

[66]   R. L. Birdwell, C. E. Mountford, and J. D. Iglehart, "Molecular Imaging of the Breast," *Am. J. Roentgenol.,* vol. 193, pp. 367-376, 2009.

[67]   H. H. Barrett and W. Swindell, *Radiological imaging: the theory of image formation, detection, and processing* vol. 1: Academic Press, Inc., 1981.

[68]   S. Cherry, J. A. Sorensen, and M. E. Phelps, *Physics in Nuclear Medicine*, 3rd. ed.: Elsevier Science, 2003.

[69]   D. L. Gunter, "Collimator Design for Nuclear Medicine," in *Emission Tomography: The Fundamentals of PET and SPECT*, M. N. Wernick and J. N. Aarsvold, Eds., ed: Elsevier Academic Press, 2004.

[70]   D. N. Wagenaar, "CdTe and CdZnTe semiconductor detectors for nuclear medicine imaging," in *Emission Tomography: The Fundamentals of PET and SPECT*, ed: Elsevier, 2004.

[71]   M. J. Tapiovaara and R. Wagner, "SNR and DQE analysis of broad spectrum X-ray imaging," *Physics in Medicine and Biology,* vol. 30, p. 519, 1985.

[72]   K. Koedooder and H. W. Venema, "Filter materials for dose reduction in screen-film radiography," *Phys. Med. Biol. ,* vol. **31**, pp. 585-600, 1986.

[73]   S. J. Glick, S. Thacker, X. Gong, and B. Liu, "Evaluating the impact of x-ray spectral shape on image quality in flat-panel CT breast imaging," *Medical Physics,* vol. 34, pp. 5-24, 2007.

[74]   D. R. Dance, A. Thilander-Klang, M. Sandborg, C. L. Skinner, A. Castellano-Smith, and G. Alm-Carlsson, "Influence of anode/filter material and tube potential on contrast, signal-to-noise ratio and average absorbed dose in mammography: a Monte Carlo study," *Brit. J. Radiol.,* vol. **73**, pp. 1056-1067, 2000.

[75]   R. L. McKinley, E. Samei, C. N. Brzymialkiewicz, M. P. Tornai, and C. E. Floyd, "Measurements of an optimized beam for x-ray computed mammotomography," in *SPIE Medical Imaging Conference*, San Diego, CA, 2004, pp. 311-319.

[76]   A. G. Haus, C. E. Metz, J. T. Chiles, and K. Rossmann, "The effect of x-ray spectra from molybdenum and tungsten target tubes on image quality in mammography," *Radiology,* vol. 118, pp. 705-709, 1976.

[77]   A. G. Haus and M. Yaffe, "Screen-film and digital mammography. Image quality and radiation dose considerations," *Radiologic Clinics of North America,* vol. 38, p. 18, 2000.

[78]   X. Wu, E. L. Gingold, G. T. Barnes, and D. M. Tucker, "Normalized average glandular dose in molybdenum target-rhodium filter and rhodium target-rhodium filter mammography," *Radiology,* vol. 193, pp. 83-89, 1994.

[79]   R. L. McKinley, M. P. Tornai, E. Samei, and M. L. Bradshaw, "Development of an optimal x-ray beam for dual-mode emission and transmission mammotomography," *Nucl. Instr. Meth. Phys. Res. A,* vol. 527, pp. 102-109, 2003.

[80]   R. L. McKinley, M. P. Tornai, E. Samei, and M. L. Bradshaw, "Simulation study of a quasi-monochromatic beam for x-ray computed mammotomography," *Med. Phys.,* vol. 31, pp. 800-813, 2004.

[81]   M. L. Bradshaw, R. L. McKinley, M. P. Tornai, and E. Samei, "Simulation Study of Quasi-Monochromatic X-ray Beam Performance for X-ray Computed Mammotomography Given Various Breast Compositions and Lesion Sizes," in *IEEE Medical Imaging Conference*, Portland, OR, 2003.

[82]   R. L. McKinley, M. P. Tornai, C. N. Archer, E. Samei, and J. E. Bowsher, "Quasi-monochromatic beam measurements for dedicated cone-beam mammotomography of an uncompressed breast," in *7th International Workshop on Digital Mammography*, Durham, NC, 2004.

[83]   R. L. McKinley, M. P. Tornai, E. Samei, and M. L. Bradshaw, "Initial study of quasi-monochromatic beam performance for x-ray computed mammotomography," *IEEE Medical Imaging Conference,* vol. 4, pp. 2999-3003, 2003.

[84]   R. L. McKinley, M. P. Tornai, E. Samei, and M. L. Bradshaw, "Development of an Optimal X-ray Beam for Dual-Mode Emission and Transmission Mammotomography," in *2nd International Conf. on Imaging Technologies in Biomedical Sciences*, Milos, Greece, 2003.

[85]   R. L. McKinley, M. P. Tornai, E. Samei, and M. L. Bradshaw, "Optimizing Beam Quality for x-ray Computed Mammotomography (CmT)," *Proc. SPIE: Phys. Med. Imag.,* vol. 5030, pp. 575-584, 2003.

[86]   R. L. McKinley, M. P. Tornai, E. Samei, and M. L. Bradshaw, "Initial study of quasi-monochromatic beam performance for x-ray computed mammotomography," *IEEE Trans. Nucl. Sci.,* vol. 52, pp. 1243-1250, 2005.

[87]   S. J. Cutler, P. Madhav, K. L. Perez, D. J. Crotty, and M. P. Tornai, "Comparison of reduced angle and fully 3D acquisition sequencing and trajectories for dual-modality mammotomography," in *IEEE Nucl Sci Symp & Med Imag Conf*, Honolulu, HI, USA, 2007.

[88]   J. M. Boone, N. Shah, and T. R. Nelson, "A comprehensive analysis of DgN_{CT} coefficients for pendant-geometry cone-beam breast computed tomography," *Medical Physics,* vol. 31, pp. 226-235, 2004.

[89]   N. Mail, D. J. Moseley, J. H. Siewerdsen, and D. A. Jaffray, "The influence of bowtie filtration on cone-beam CT image quality," *Medical Physics,* vol. 36, pp. 22-32, 2009.

[90]   F. H. Attix, *Introduction to Radiological Physics and Radiation Dosimetry*: Wiley & Sons, 1986.

[91]   M. J. Butson, P. K. N. Yu, T. Cheung, and P. Metcalfe, "Radiochromic film for medical radiation dosimetry," *Materials Science and Engineering: R: Reports,* vol. 41, pp. 61-120, 2003.

[92]   G. F. Knoll, *Radiation detection and measurement*, 3rd ed.: John Wiley & Sons, Inc., 2000.

[93]   M. Bertram, J. Wiegert, and G. Rose, "Scatter correction for cone-beam computed tomography using simulated object models," in *2006 SPIE Medical Imaging Conference*, San Diego, CA, 2006.

[94]   M. Endo, T. Tsunoo, N. Nakamori, and K. Yoshida, "Effect of scattered radiation on image noise in cone beam CT," *Med Phys*, vol. 28, pp. 469-74, Apr 2001.

[95]   G. H. Glover, "Compton scatter effects in CT reconstructions," *Med. Phys.*, vol. 9, pp. 860-867, 1982.

[96]   H. Kanamori and et al., "Effects of scattered X-rays on CT images," *Physics in Medicine and Biology*, vol. 30, p. 239, 1985.

[97]   A. L. C. Kwan, J. M. Boone, and N. Shah, "Evaluation of x-ray scatter properties in a dedicated cone-beam breast CT scanner," *Med Phys*, vol. 32, pp. 2967-2975, 2005.

[98]   J. H. Siewerdsen and D. A. Jaffray, "Cone-beam computed tomography with a flat-panel image: magnitude and effects of x-ray scatter," *Med Phys*, vol. 28, pp. 220-231, 2001.

[99]   C. N. Brzymialkiewicz, R. L. McKinley, and M. P. Tornai, "Towards patient imaging with dedicated emission mammotomography," *IEEE Nucl Sci Symp & Med Imag Conf*, vol. 3, pp. 1519-1523, 2005.

[100]   C. N. Brzymialkiewicz, M. P. Tornai, R. L. McKinley, and J. E. Bowsher, "3D data acquisition sampling strategies for dedicated emission mammotomography for various breast sizes," *IEEE Nucl Sci Symp & Med Imag Conf*, vol. 4, pp. 2596-2600, 16-22 Oct. 2004 2004.

[101]   J. Hsieh, *Computed Tomography: Principles, Design, Artifacts, and Recent Advances*: SPIE Press, 2003.

[102]   H. E. Johns and J. R. Cunningham, *Physics in Radiology*: Charles C. Thomas, 1983.

[103]   D. R. Dance, C. L. Skinner, and G. Alm Carlsson, "Breast dosimetry," *Applied Radiation and Isotopes*, vol. 50, pp. 185-203, 1999.

[104]   L. Bassett, C. D'Orsi, C. Lee, P. Butler, R. Jong, and B. Monsees, "Practice guidelines for the performance of screening and diagnostic mammography," 2008.

[105]   R. v. Engen, "Addendum on Digital Mammography to Chapter 3 of the: European Guidelines for Quality Assurance in Mammography Screening," 4.0 ed, 2006.

[106]   D. J. Brenner and E. J. Hall, "Computed Tomography -- An Increasing Source of Radiation Exposure," *N Engl J Med*, vol. 357, pp. 2277-2284, 2007.

[107]   F. A. J. Mettler, B. R. Thomadsen, M. Bhargavan, D. B. Gilley, J. E. Gray, J. A. Lipoti, J. McCrohan, T. T. Yoshizumi, and M. Mahesh, "Medical radiation exposure in the U.S: in 2006: Preliminary results," *Health Physics*, vol. 95, pp. 502-507, 2008.

[108]   G. R. Hammerstein, D. W. Miller, D. R. White, M. E. Masterson, H. Q. Woodard, and J. S. Laughlin, "Absorbed radiation dose in mammography," *Radiology*, vol. 130, pp. 485-491, 1979.

[109]   R. L. McKinley and M. P. Tornai, "Preliminary investigation of dose for a dedicated mammotomography system," *Proc SPIE: Phys Med Imag*, vol. 6142, pp. 60-70, 2006.

[110]   R. L. McKinley, M. P. Tornai, C. E. Floyd, and E. Samei, "A contrast-detail comparison of computed mammotomography and digital mammography," in *SPIE Medical Imaging Conference: Physics of Medical Imaging*, San Diego, CA, USA, 2007.

[111]   F. M. Khan, *The Physics of Radiation Therapy*, 3rd ed.: Lippincott Williams & Wilkins, 2003.

[112]   J. M. Boone, "Normalized glandular dose (DgN) coefficients for arbitrary x-ray spectra in mammography: Computer-fit values of Monte Carlo derived data," *Medical Physics*, vol. 29, pp. 869-875, 2002.

[113]   D. R. Dance, "Monte-Carlo calculation of conversion factors for the estimation of mean glandular breast dose," *Physics in Medicine and Biology*, vol. 35, p. 1211, 1990.

[114]   L. Stanton, J. L. Day, S. D. Brattelli, D. A. Lightfoot, M. A. Vince, and R. E. Stanton, "Comparison of ion chamber and TLD dosimetry in mammography," *Medical Physics*, vol. 8, pp. 792-798, 1981.

[115]   S. C. Thacker and S. J. Glick, "Normalized glandular dose (DgN) coefficients for flat-panel CT breast imaging," *Physics in Medicine and Biology*, vol. 49, p. 5433, 2004.

[116]   K. Arshak and O. Korostynska, *Advanced materials and techniques for radiation dosimetry*. Boston: Artech House, 2006.

[117]   C. G. Soares, "New developments in radiochromic film dosimetry," *Radiat Prot Dosimetry*, vol. 120, pp. 100-6, 2006.

[118]   A. Niroomand-Rad, C. R. Blackwell, B. M. Coursey, K. P. Gall, J. M. Galvin, W. L. McLaughlin, A. S. Meigooni, R. Nath, J. E. Rodgers, and C. G. Soares, "Radiochromic film dosimetry: recommendations of AAPM Radiation Therapy Committee Task Group 55. American Association of Physicists in Medicine," *Med Phys*, vol. 25, pp. 2093-115, Nov 1998.

[119]   Y. Zhu, A. S. Kirov, V. Mishra, A. S. Meigooni, and J. F. Williamson, "Quantitative evaluation of radiochromic film response for two-dimensional dosimetry," *Medical Physics*, vol. 24, pp. 223-231, 1997.

[120] A. Rink, I. A. Vitkin, and D. A. Jaffray, "Characterization and real-time optical measurements of the ionizing radiation dose response for a new radiochromic medium," *Medical Physics,* vol. 32, pp. 2510-2516, 2005.

[121] S. Devic, N. Tomic, Z. Pang, J. Seuntjens, E. B. Podgorsak, and C. G. Soares, "Absorption spectroscopy of EBT model GAFCHROMIC™ film," *Medical Physics,* vol. 34, pp. 112-118, 2007.

[122] R. Ning, D. Conover, Y. Yu, Y. Zhang, W. Cai, R. Betancourt-Benitez, and X. Lu, "A novel cone beam breast CT scanner: system evaluation," in *Medical Imaging 2007: Physics of Medical Imaging,* San Diego, CA, USA, 2007.

[123] R. L. McKinley, "Development and characterization of a dedicated computed mammotomography system," Ph.D. Thesis, Biomedical Engineering, Duke University, Durham, NC, 2006.

[124] A. L. C. Kwan, J. M. Boone, K. Yang, and S. Huang, "Evaluation of the spatial resolution characteristics of a cone-beam breast CT scanner," *Med Phys,* vol. 34, pp. 275-281, 2007.

[125] M. P. Tornai, R. L. McKinley, C. N. Brzymialkiewicz, P. Madhav, S. J. Cutler, D. J. Crotty, J. E. Bowsher, E. Samei, and C. E. Floyd, "Design and development of a fully-3D dedicated x-ray computed mammotomography system," *Proc SPIE: Phys Med Imag,* vol. 5745, pp. 189-197, 2005.

[126] A. R. Cowen, S. M. Kengyelics, and A. G. Davies, "Solid-state, flat-panel, digital radiography detectors and their physical imaging characteristics," *Clinical Radiology,* vol. 63, pp. 487-498, 2008.

[127] C. W. E. v. Eijk, "Inorganic scintillators in medical imaging," *Physics in Medicine and Biology,* vol. 47, p. R85, 2002.

[128] E. E. Ovechkina, V. Gaysinskiy, S. R. Miller, C. Brecher, A. Lempicki, and V. V. Nagarkar, "Multiple doping of CsI:Tl crystals and its effect on afterglow," *Radiation Measurements,* vol. 42, pp. 541-544, 2007.

[129] J. H. Siewerdsen and D. A. Jaffray, "Cone-beam computed tomography with a flat-panel imager: Effects of image lag," *Medical Physics,* vol. 26, pp. 2635-2647, 1999.

[130] W. Kalender and Y. Kyriakou, "Flat-detector computed tomography (FD-CT)," *European Radiology,* vol. 17, pp. 2767-2779, 2007.

[131] W. Zhao, G. DeCrescenzo, S. O. Kasap, and J. A. Rowlands, "Ghosting caused by bulk charge trapping in direct conversion flat-panel detectors using amorphous selenium," *Medical Physics,* vol. 32, pp. 488-500, 2005.

[132] A. K. Bloomquist, M. J. Yaffe, G. E. Mawdsley, D. M. Hunter, and D. J. Beideck, "Lag and ghosting in a clinical flat-panel selenium digital mammography system," *Medical Physics*, vol. 33, pp. 2998-3005, 2006.

[133] S. N. Ahmed, *Physics and Engineering of Radiation Detection*: Aacademic Press, 2007.

[134] J. H. Radon, "Ueber die Bestimmng von Funktionen durch Ihre Integralwerte laengs gewisser Mannigfaltigkeiten," *Ber. vor Saechs Akad Wiss* vol. 69, p. 16, 1917.

[135] L. A. Feldkamp, L. C. Davis, and J. W. Kress, "Practical cone-beam algorithm," *J Opt Soc A*, vol. 1, pp. 612-619, 1984.

[136] Y. Ye and G. Wang, "Filtered backprojection formula for exact image reconstruction from cone-beam data along a general scanning curve," *Med. Phys.*, vol. 32, pp. 42-48, 2005.

[137] J. Bian, N. J. Packard, K. Yang, D. Xia, J. M. Boone, and X. Pan, "Non-circular scans and image reconstruction for breast CT," in *Medical Imaging: Physics of Medical Imaging*, San Diego, CA, USA, 2008.

[138] D. Yang, R. Ning, D. Conover, and Y. Yu, "Reconstruction implementation based on a flat panel detector cone beam breast CT," San Diego, CA, USA, 2006.

[139] A. Katsevich, "Image reconstruction for the circle and line trajectory," *Physics in Medicine and Biology*, vol. 49, pp. 5059-5072, 2004.

[140] C. N. Archer, M. P. Tornai, and R. L. McKinley, "Orbits for nuclear medicine dedicated SPECT," in *7th International Workshop on Digital Mammography*, Durham, NC, 2004.

[141] P. Madhav, D. J. Crotty, R. L. McKinley, and M. P. Tornai, "Evaluation of tilted cone-beam CT orbits in the development of a dedicated hybrid mammotomograph," *Physics in Medicine and Biology*, vol. 54, pp. 3659-3676, 2009.

[142] R. L. McKinley, C. N. Brzymialkiewicz, P. Madhav, and M. P. Tornai, "Investigation of cone-beam acquisitions implemented using a novel dedicated mammotomography system with unique arbitrary orbit capability," *Proc SPIE: Phys Med Imag*, vol. 5745, pp. 609-617, 2005.

[143] H. Erdogan and J. A. Fessler, "Ordered subsets algorithms for transmission tomography," *Phys Med Biol*, vol. 44, pp. 2835-2851, 1999 1999.

[144] F. J. Beekman and C. Kamphius, "Ordered subsets reconstruction for x-ray CT," *Phys. Med. Biol.*, vol. 46, pp. 1835-1844, 2001.

[145] D. L. Lalush and M. N. Wernick, "Iterative Image Reconstruction," in *Emission Tomography: The Fundamentals of PET and SPECT*, J. N. Aarsvold and M. N. Wernick, Eds., ed: Elsevier Science, 2004.

[146] C. N. Brzymialkiewicz, "Development and evaluation of a dedicated emission mammotomography system," Ph. D. Thesis, Biomedical Engineering, Duke University, 2005.

[147] C. N. Brzymialkiewicz, M. P. Tornai, R. L. McKinley, and J. E. Bowsher, "Evaluation of fully 3D emission mammotomography with a compact cadmium zinc telluride detector," *IEEE Trans. Med. Imag.,* vol. 24, pp. 868-877, 2005.

[148] C. N. Brzymialkiewicz, M. P. Tornai, R. L. McKinley, S. J. Cutler, and J. E. Bowsher, "Performance for dedicated emission mammotomography for various breast shapes and sizes," *Phys Med Biol,* vol. 51, pp. 5051-5064, 2006.

[149] R. L. McKinley, M. P. Tornai, C. N. Brzymialkiewicz, P. Madhav, E. Samei, and J. E. Bowsher, "Analysis of a novel offset cone-beam transmission imaging system geometry for accommodating various breast sizes," *Medica Physica,* vol. XXI, pp. 46-53, 2006.

[150] M. P. Tornai, C. N. Brzymialkiewicz, R. L. McKinley, J. E. Bowsher, and E. Samei, "Development of Dedicated 3D Molecular Mammotomography with SPECT and Quasi-Monochromatic X-ray Computed Mammotomography," in *Workshop on Alternatives to Mammography*, 2004.

[151] M. P. Tornai, R. L. McKinley, M. L. Bradshaw, C. N. Brzymialkiewicz, and E. Samei, "Effects of uncompressed breast composition and thickness on image quality using a quasi-monochromatic beam for computed mammotomography," in *7th Int. Workshop on Digital Mammography*, Durham, NC, 2004.

[152] D. J. Crotty, R. L. McKinley, and M. P. Tornai, "Experimental spectral measurements of heavy K-edge filtered beams for x-ray computed mammotomography," *Physics in Medicine and Biology,* vol. 52, pp. 603-616, 2007.

[153] P. C. Johns and M. J. Yaffe, "X-ray characterization of normal and neoplastic breast tissues," *Phys. Med. Biol.,* vol. 32, pp. 675-695, 1987.

[154] J. H. Hubbell and S. M. Seltzer, "Tables of x-ray mass attenuation coefficients and mass energy-absorption coefficients 1 keV to 20 meV for elements z = 1 to 92 and 48 additional substances of dosimetric interest," 1995.

[155] D. Chapman, W. Thomlinson, R. E. Johnston, D. Washburn, E. Pisano, N. Gmür, Z. Zhong, R. Menk, F. Arfelli, and D. Sayers, "Diffraction enhanced x-ray imaging," *Physics in Medicine and Biology,* vol. 42, pp. 2015-2025, 1997.

[156] M. Gambaccini, A. Fantini, G. D. Domenico, N. Sabba, A. Taibi, A. Tuffanelli, G. Zavattini, D. Bollini, E. Castelli, R. Pani, and A. D. Guerra, "Development of a quasi-monochromatic CT system for breast cancer study with combined emission-transmission tomography," *IEEE Trans. Nucl. Sci. ,* vol. 48, pp. 703-706, 2001.

[157]   P. Baldelli and et al., "Quasi-monochromatic x-rays for diagnostic radiology," *Physics in Medicine and Biology,* vol. 48, p. 3653, 2003.

[158]   P. Silvia and et al., "Breast tomography with synchrotron radiation: preliminary results," *Physics in Medicine and Biology,* vol. 49, p. 1739, 2004.

[159]   P. Baldelli, A. Taibi, A. Tuffanelli, M. C. Gilardoni, and M. Gambaccini, "A prototype of a quasi-monochromatic system for mammography applications," *Physics in Medicine and Biology,* vol. 50, pp. 2225-2240, 2005.

[160]   B. Alberto and et al., "High-resolution CT by diffraction-enhanced x-ray imaging: mapping of breast tissue samples and comparison with their histo-pathology," *Physics in Medicine and Biology,* vol. 52, p. 2197, 2007.

[161]   E. Castelli, F. Arfelli, D. Dreossi, R. Longo, T. Rokvic, M. A. Cova, E. Quaia, M. Tonutti, F. Zanconati, A. Abrami, V. Chenda, R. H. Menk, E. Quai, G. Tromba, P. Bregant, and F. de Guarrini, "Clinical mammography at the SYRMEP beam line," *Nuclear Instruments and Methods in Physics Research Section A: Accelerators, Spectrometers, Detectors and Associated Equipment,* vol. 572, pp. 237-240, 2007.

[162]   E. Storm, "Calculated Bremsstrahlung Spectra from Thick Tungsten Targets," *Physical Review A,* vol. 5, p. 2328, 1972.

[163]   E. Storm, "Emission of Characteristic L and K Radiation from Thick Tungsten Targets," *Journal of Applied Physics,* vol. 43, pp. 2790-2796, 1972.

[164]   C. Dodge and M. Flynn, "Advanced Integral Method for the Simulation of Diagnostic X-Ray Spectra," *Medical Physics,* vol. 33, pp. 1983-1983, 2006.

[165]   P. Madhav, S. J. Cutler, D. C. Crotty, K. L. Perez, R. L. McKinley, L. Wilke, T. Wong, and M. P. Tornai, "Pilot Patient Studies Using a Dedicated Dual-Modality SPECT-CT System for Breast Imaging " presented at the 2008 AAPM, Houston TX, 2008.

[166]   H. Delis, G. Spyrou, L. Costaridou, G. Tzanakos, and G. Panayiotakis, "Suitability of new anode materials in mammography: Dose and subject contrast considerations using Monte Carlo simulation," *Medical Physics,* vol. 33, pp. 4221-4235, 2006.

[167]   M. Varjonen and P. Strömmer, "Optimizing the Target-Filter Combination in Digital Mammography in the Sense of Image Quality and Average Glandular Dose," ed, 2009, pp. 570-576.

[168]   S. J. Cutler, D. J. Crotty, and M. P. Tornai, "Dynamic laser-guided contouring for dedicated emission mammotomography," in *IEEE Nuclear Science Symposium Conference Record*, 2008, pp. 4789-4793.

[169] J. Hsieh, R. C. Molthen, C. A. Dawson, and R. H. Johnson, "An iterative approach to the beam hardening correction in cone beam CT," *Med Phys*, vol. 27, pp. 23-29, 2000.

[170] B. De Man, J. Nuyts, P. Dupont, G. Marchal, and P. Suetens, "An iterative maximum-likelihood polychromatic algorithm for CT," *Medical Imaging, IEEE Transactions on*, vol. 20, pp. 999-1008, 2001.

[171] R. Redus, "CdTe Measurement of X-Ray Tube Spectra: Escape Events," Amptek Inc., Bedford, MA., Application Note02/04/2008 2008.

[172] P. Russo, A. Lauria, G. Mettivier, and M. C. Montesi, "Dose distribution in cone-beam breast computed tomography: An experimental phantom study," *IEEE Nuclear Science Symposium Conference Record*, pp. 5623-5628, 2008.

[173] J. M. Boone, A. L. C. Kwan, J. A. Seibert, N. Shah, K. K. Lindfors, and T. R. Nelson, "Technique factors and their relationship to radiation dose in pendant geometry breast CT," *Medical Physics*, vol. 32, pp. 3767-3776, 2005.

[174] H. Alva and et al., "The use of a reflective scanner to study radiochromic film response," *Physics in Medicine and Biology*, vol. 47, p. 2925, 2002.

[175] G. Thomas, R. Y. L. Chu, and F. Rabe, "A study of GafChromic XR type R film response with reflective-type densitometers and economical flatbed scanners," *Journal of applied clinical medical physics*, vol. 4, pp. 307-314, 2003.

[176] B. C. Ferreira, M. C. Lopes, and M. Capela, "Evaluation of an Epson flatbed scanner to read Gafchromic EBT films for radiation dosimetry," *Phys Med Biol*, vol. 54, pp. 1073-1085, 2009.

[177] L. Paelinck, W. De Neve, and C. De Wagter, "Precautions and strategies in using a commercial flatbed scanner for radiochromic film dosimetry," *Phys Med Biol*, vol. 52, pp. 231-42, 2007.

[178] S. Devic, J. Seuntjens, E. Sham, E. B. Podgorsak, C. R. Schmidtlein, A. S. Kirov, and C. G. Soares, "Precise radiochromic film dosimetry using a flat-bed document scanner," *Med Phys*, vol. 32, pp. 2245-53, Jul 2005.

[179] S. Devic, N. Tomic, C. G. Soares, and E. B. Podgorsak, "Optimizing the dynamic range extension of a radiochromic film dosimetry system," *Med Phys*, vol. 36, pp. 429-37, Feb 2009.

[180] Y. S. Horwitz, *Thermoluminescence and Thermoluminescent Dosimetry* vol. 3: CRC Press, 1984.

[181] A. Celler, D. Axen, D. Togane, and J. El-Khatib, "Investigation of scatter in SPECT transmission studies," *IEEE Transactions on Nuclear Science*, vol. 47, pp. 1251-1257, 2000.

[182]   P. E. Kinahan, D. W. Townsend, T. Beyer, and D. Sashin, "Attenuation correction for a combined 3D PET/CT scanner," *Med Phys,* vol. 25, pp. 2046-2053, 1998.

[183]   J. A. Patton, D. W. Townsend, and B. F. Hutton, "Hybrid Imaging Technology: From Dreams and Vision to Clinical Devices," *Seminars in Nuclear Medicine,* vol. 39, pp. 247-263, 2009.

[184]   D. W. Townsend, "Dual-modality imaging: combining anatomy and function," *J Nucl Med,* vol. 49, pp. 938-55, Jun 2008.

[185]   T. Beyer, D. W. Townsend, T. Brun, P. E. Kinahan, M. Charron, R. Roddy, J. Jerin, J. Young, L. Byars, and R. Nutt, "A Combined PET/CT Scanner for Clinical Oncology," *J Nucl Med,* vol. 41, pp. 1369-1379, 2000.

[186]   B. L. Franc, P. D. Acton, C. Mari, and B. H. Hasegawa, "Small-Animal SPECT and SPECT/CT: Important Tools for Preclinical Investigation," *J Nucl Med,* vol. 49, pp. 1651-1663, 2008.

[187]   M. P. Tornai, J. E. Bowsher, R. J. Jaszczak, B. C. Pieper, K. L. Greer, P. H. Hardenbergh, and R. E. Coleman, "Mammotomography with Pinhole Incomplete Circular Orbit SPECT," *Journal of Nuclear Medicine,* vol. 44, pp. 583-593, 2003.

[188]   A. Seret, M. Defrise, and D. Blocklet, "180° Pinhole SPET with a tilted detector and OS-EM reconstruction: phantom studies and potential clinical applications," *European Journal of Nuclear Medicine,* vol. 28, pp. 1836-1841, 2001.

[189]   P. Madhav, D. J. Crotty, R. L. McKinley, and M. P. Tornai, "Evaluation of lesion distortion at various CT system tilts in the development of a hybrid system for dedicated mammotomography," *SPIE Med Imag Conf,* vol. 6150, 2007.

[190]   C. N. Archer, M. P. Tornai, J. E. Bowsher, S. D. Metzler, B. C. Pieper, and R. J. Jaszczak, "Implementation and initial characterization of acquisition orbits with a dedicated emission mammotomograph," *IEEE Trans. Nucl. Sci.,* vol. 50, pp. 413-420, 2003.

[191]   M. P. Tornai, R. L. McKinley, S. J. Cutler, D. J. Crotty, and C. N. Brzymialkiewicz, "Anthropomorphic breast phantoms for preclinical imaging evaluation with emission or transmission imaging," *Proc. SPIE,* vol. 5746, pp. 825-834, 2005.

[192]   K. L. Perez, S. J. Cutler, P. Madhav, and M. P. Tornai, "Novel patient optimized acquisition trajectories for dedicated breast SPECT imaging," in *IEEE Nuclear Science Symposium Conference Record.*, 2008, pp. 5629-5634.

[193]   K. L. Perez, S. J. Cutler, and M. P. Tornai, "Empirical effects of angular sampling and background content on image quality in dedicated breast SPECT," in *2007 IEEE Nuclear Science Symposium & Medical Imaging Conference*, Piscataway, NJ, USA, 2007.

[194]   S. J. Boyce and E. Samei, "Imaging properties of digital magnification radiography," *Medical Physics,* vol. 33, pp. 984-996, 2006.

[195]   J. H. Siewerdsen, M. J. Daly, B. Bakhtiar, D. J. Moseley, S. Richard, H. Keller, and D. A. Jaffray, "A simple, direct method for x-ray scatter estimation and correction in digital radiography and cone-beam CT," *Med. Phys.,* vol. 33, pp. 187-197, 2006.

[196]   D. J. Crotty, P. Madhav, R. L. McKinley, and M. P. Tornai, "Investigating novel patient bed designs for use in a hybrid dual modality dedicated 3D breast imaging system," *2007 SPIE Med Imag Conf,* vol. 6150, 2007.

[197]   S. J. Cutler, K. L. Perez, P. Madhav, and M. P. Tornai, "Comparison of 2D scintimammography and 3D dedicated breast SPECT using a compressible breast phantom and lesions of varying size and tracer uptake," in *IEEE Nuclear Science Symposium Conference Record.*, 2008, pp. 5640-5646.

Biography

Place/Date of Birth:

Cork, Ireland   July 26th 1974

Education:

1996	Bachelor of Science in Electrical Engineering, National University of Ireland, Cork, Ireland
2004	Diploma in Financial Management, Association of Chartered and Certified Accountants, London, United Kingdom
2006	Master of Science, Biomedical Engineering, Duke University, Durham, NC
2010	Doctor of Philosophy, Biomedical Engineering, Duke University, Durham, NC

Scholarships/Fellowships/Awards:

2004 – 2005	Engineering Award, Duke University, Durham, NC
2004 – 2005	Biomedical Engineering Fellowship Award, Duke University, Durham, NC
2006	Student Travel Award, SPIE Medical Imaging Conference, San Diego, California
2007	Student Travel Award, Workshop on the Nuclear Radiology of Breast Cancer, Sand Diego, California
2008 – Present	Principal Investigator, Department of Defense Breast Cancer Research Program Pre-Doctoral Traineeship Award (W81XWH-08-1-0352), $90,000 awarded over 3 years
2010	Finalist, Michael B. Merickel Student Paper Award, SPIE Medical Imaging Conference, San Diego, California

Papers Published, Submitted, or in Preparation

[1]   D.J. Crotty, R.L. McKinley, and M.P. Tornai, "Experimental spectral measurements of heavy K-edge filtered beams for x-ray computed mammotomography." *Phys Med Biol*. 52(3): p. 603-616, 2007.

[2]   P. Madhav, D.J. Crotty, R.L. McKinley, and M.P. Tornai, "Evaluation of tilted cone-beam CT orbits in the development of a dedicated hybrid mammotomograph." 54(12): 3659-676, 2009.

[3]   D.J. Crotty, S.L. Brady, D.C. Jackson, G.I. Toncheva, T. Yoshizumi, and M.P. Tornai, "Measurement of the Absorbed Dose in the Uncompressed Breast Using a Dedicated CT Mammotomography System and Radiochromatic Film.", in preparation for submission to *Medical Physics*.

[4]   D.J. Crotty, R.L. McKinley, and M.P. Tornai, "Partial angle and vertical shifting trajectories to increase chest wall imaging in a dedicated CT mammotomography system", in preparation for submission to *Physics in Medicine and Biology*.

[5]   D.J. Crotty, S.J. Cutler, P. Madhav. and M.P. Tornai, "Novel patient bed design for an integrated SPECT-CT imaging device dedicated to breast cancer imaging", in preparation for submission to *Medical Engineering and Physics*.

[6]   D.J. Crotty, R.L. McKinley, and M.P. Tornai, "Transmission source contamination of the emission image in a common field-of-view compact breast SPECT-CT system", submitted to *Phys Med Biol*., in preparation for resubmission.

[7]   D.J. Crotty, RL McKinley, M.P. Tornai. "Investigation of Emission Contamination in the Transmission Image of a Dual-modality Computed Mammotomography System.", in preparation.

[8]   S.J. Cutler, D.J. Crotty, M.P. Tornai. "Dynamic Laser-Guided Contouring for Dedicated Emission Mammotomography.", in preparation.

Conference Proceedings

[9]   D.J. Crotty, C.N. Brzymialkiewicz, R.L. McKinley*,* and M.P. Tornai*.*, "Optimizing orientation of SPECT and CT detectors through quantification of cross contamination in a dual-modality mammotomography system," *IEEE Nuclear Science Symposium & Medical Imaging Conference Record,* 3, 1672-1676, 2005

[10]   D.J. Crotty, C.N. Brzymialkiewicz, R.L. McKinley*,* and M.P. Tornai*.*, "Investigation of emission contamination in the transmission image of a dual-modality computed mammotomography system," *Proceedings of the SPIE: Physics of Medical Imaging,* 6142, 664-674, 2006

[11] D. J. Crotty, S. J. Cutler, R. L. McKinley*,* and M. P. Tornai, "Improved chest wall imaging through combined complex trajectories in dedicated dual-modality SPECT-CT breast molecular imaging." *IEEE Nuclear Science Symposium & Medical Imaging Conference Record*, 6, 5650-5656, 2008

[12] D. J. Crotty, P. Madhav, R. L. McKinley, and M.P. Tornai., "Patient bed design for an integrated SPECT-CT dedicated mammotomography system," *IEEE Nuclear Science Symposium Conference Record*, 6, 3915-3919, 2006.

[13] D. J. Crotty, P. Madhav, R. L. McKinley*,* and M.P. Tornai., "Investigating novel patient bed designs for use in a hybrid dual-modality dedicated 3D breast imaging system," *Proceedings of the SPIE: Physics of Medical Imaging,* 6150H, 2007.

[14] D. J. Crotty, R. L. McKinley, P. Madhav*,* and M.P. Tornai. "Initial investigation of novel trajectories to improve chest wall imaging in a dedicated breast computed tomography system." *Proceedings of the SPIE: Physics of Medical Imaging,* 7258, 72585L-10, 2009.

[15] S. J. Cutler, D. J. Crotty, and M. P. Tornai, "Dynamic laser-guided contouring for dedicated emission mammotomography." *IEEE Nuclear Science Symposium Conference Record,* 6, 4789-4793, 2008

[16] S. J. Cutler, D.J. Crotty, P. Madhav, K.L. Perez, and M.P. Tornai, "Comparison of reduced angle and fully 3D acquisition sequencing and trajectories for dual-modality mammotomography." *IEEE Nuclear Science Symposium Conference Record,* 4044-4050, 2007

[17] P. Madhav, D.J. Crotty, R.L. McKinley, M.P. Tornai, "Initial development of a dual-modality SPECT-CT system for dedicated mammotomography," *IEEE Nuclear Science Symposium & Medical Imaging Conference Record*, 2382 – 86, 2006

[18] P. Madhav, D.J. Crotty, R.L. McKinley, M.P. Tornai. "Evaluation of lesion distortion at various CT system tilts in the development of a hybrid system for dedicated mammotomography." *Proceedings of the SPIE: Physics of Medical Imaging*, 6510, F1-12, 2007

[19] P. Madhav, S.J. Cutler, K.L. Perez*,* D.J. Crotty, .R.L. McKinley, T.Z. Wong, M.P. Tornai, "Initial patient study with dedicated dual-modality SPECT-CT mammotomography," *IEEE Nuclear Science Symposium Conference Record,* 3781-7, 2007

[20] K.L. Perez, P. Madhav, D.J. Crotty, M.P. Tornai, "Analysis of patient bed positioning in SPECT-CT imaging for dedicated mammotomography." *Proceedings of the SPIE: Physics of Medical Imaging*, 6510, 2007.

[21] M.P. Tornai, R.L. McKinley, C.N. Brzymialkiewicz, P. Madhav, S.J. Cutler, D.J. Crotty, J.E. Bowsher, E. Samei, C.E. Floyd , "Design and development of a fully-

3D dedicated x-ray computed mammotomography system," *Proceedings of the SPIE: Physics of Medical Imaging,* 5745, 2005.

[22]　M.P. Tornai, R.L. McKinley, S.J. Cutler, D.J. Crotty, "Anthropomorphic breast phantoms for preclinical imaging evaluation with emission or transmission imaging," *Proceedings of the SPIE: Physics of Medical Imaging,* 5746, 2005.

Presentations

[23]　D.J. Crotty, S.L. Brady, D.C. Jackson, G.I. Toncheva, T. Yoshizumi, and M.P. Tornai. "Investigating the dose distribution in the uncompressed breast with a dedicated CT mammotomography system." Presented at the *SPIE Medical Imaging Conference*, San Diego, 2010.

[24]　D.J. Crotty, C.N. Brzymialkiewicz, R.L. McKinley*,* and M.P. Tornai*.* "Optimizing Orientation of SPECT and CT Detectors Through Quantification of Cross Contamination in a Dual-modality Mammotomography System". Presented at the *IEEE Nucelar Science Symposium and Medical Imaging Conference*, Puerto Rico, 2005.

[25]　D.J. Crotty, R.L. McKinley, and M.P. Tornai, 'Experimental Measurement of Heavy K-edge Beam Filtration beams for x-ray computed mammotomography". Presented at the *SPIE Medical Imaging Conference*, San Diego, 2006

[26]　D.J. Crotty, C.N. Brzymialkiewicz, R.L. McKinley*,* and M.P. Tornai . "Emission Contamination of the Transmission Image in a Dual-modality Computed Mammotomography System". Presented at the *SPIE Medical Imaging Conference*, San Diego, 2006.

[27]　D.J. Crotty, P. Madhav, S.J. Cutler, K.L. Perez, R.L. McKinley, J.E. Bowsher, M.P. Tornai "Development of an Integrated SPECT-CT Imaging System for Enhanced Dual-modality Dedicated Breast Imaging". Presented at the *Duke University Biomedical Engineering Annual Research Retreat*, Myrtle Beach, SC, 2007.

[28]　D.J. Crotty, P. Madhav, S.J. Cutler, K.L. Perez, R.L. McKinley, M.P. Tornai. "Performance of a New Dual-modality Molecular-Anatomical Imaging System Dedicated to Breast Imaging" Presented at the *Duke University Comprehensive Cancer Center Meeting*, Durham NC, 2008

[29]　D.J. Crotty, P. Madhav, K.L. Perez, S.J. Cutler, R.L. McKinley, T. Wong, P.K. Marcom, M.P. Tornai. "3D Molecular Breast Imaging with Dedicated Emission Mammotomography: Results of the First Patient Study." Presented at the *Duke University Center for Molecular and Biomolecular Imaging Meeting*, Durham, NC, 2007.

[30]   P. Madhav, D.J. Crotty, S.J. Cutler, K.L. Perez, R.L. McKinley, M.P. Tornai. "A novel dual-modality SPECT-CT system dedicated to 3D volumetric breast imaging." Presented at the *Duke University Center for Molecular and Biomolecular Imaging Meeting*, Durham, NC, 11-13 March, 2007 and *Duke Frontiers 2007*, Durham, NC, 2007.

[31]   P. Madhav, S.J. Cutler, D.J. Crotty, K.L. Perez, R.L. McKinley, M.P. Tornai. "3D volumetric breast imaging with a dedicated dual-modality SPECT-CT system." Presented at the *2007 Duke Biomedical Engineering Annual Research Retreat*, Myrtle Beach, SC, 2007.

[32]   P. Madhav, S.J. Cutler, D.J. Crotty, K.L. Perez, R.L. McKinley, L. Wilke, T.Z.Wong, M.P. Tornai. "Pilot patient studies using a dedicated dual-modality SPECT-CT system for breast imaging." Presented at the *2008 American Association of Physicists in Medicine Meeting*, Houston, TX, 27-31 Jul. 2008, and published in Med. Phys. 35(6): 2894

[33]   M.P. Tornai, C.N. Brzymialkiewicz, R.L. McKinley, J.E. Bowsher, E. Samei, P. Madhav, S.J. Cutler, D.J. Crotty, C.E. Floyd. "3D molecular breast imaging." Presented at *Duke Frontiers 2005*, Durham, NC, 2005.

[34]   M.P. Tornai, P Madhav, D.J. Crotty, S.J. Cutler, R.L. McKinley, K.L. Perez, J.E. Bowsher. "Initial hybrid SPECT-CT system for dedicated fully-3D breast imaging." Presented at the *2007 Society of Nuclear Medicine Meeting*, Washington, DC, 2007, and published in J. Nucl. Med. 48(5). 2007.

[35]   M.P. Tornai, P. Madhav, D.J. Crotty, S.J Cutler, R.L. McKinley, K.L. Perez, J.E. Bowsher. "Application of volumetric molecular breast imaging with a dedicated SPECT-CT mammotomograph." Presented at the *2007 American Association of Physicists in Medicine Meeting*, Minneapolis, MN, 2007, and published in Med. Phys. 34(6):2597.

[36]   P Madhav, S.J. Cutler, D.J. Crotty, K.L. Perez, R.L. McKinley, P.K. Marcom, T. Wong, M.P. Tornai. "Dedicated Molecular and Anatomical Breast Imaging - Initial Patient Studies." Presented at the *Annual Meeting of the Duke Comprehensive Cancer Center*, March 2008, Durham, NC.

[37]   M.P. Tornai, R.L. McKinley, D.J. Crotty, S.J. Cutler, P. Madhav, K.L. Perez. "Breast Imaging Devices for Screening, Diagnostics and Treatment Monitoring." Presented at *Clinical Directions for Molecular Imaging*, Duke University, Durham, NC, March, 2009.

[38]   D.J. Crotty, D.C. Jackson, S.L. Brady, G.I. Toncheva, C.E. Anderson, T.T. Yoshizumi, M.P. Tornai. "Empirical Measurement of the 3D Dose Distribution in the Uncompressed Breast Using a Dedicated CT Mammotomography System." Presented at the *Annual Meeting of the Duke Comprehensive Cancer Center*, 2009, Durham, NC.